ESPOO 2007 VTT RESEARCH NOTES 2399

Hannu Hänninen, Anssi Brederholm,
Tapio Saukkonen, Hans Gripenberg, Aki Toivonen,
Ulla Ehrnstén & Pertti Aaltonen

Hot cracking and environment-assisted cracking susceptibility of dissimilar metal welds

VTT TIEDOTTEITA – RESEARCH NOTES 2399

Hot cracking and environment-assisted cracking susceptibility of dissimilar metal welds

Hannu Hänninen[1], Anssi Brederholm[1], Tapio Saukkonen[1], Hans Gripenberg[1], Aki Toivonen[2], Ulla Ehrnstén[2] & Pertti Aaltonen[2]

[1] Helsinki University of Technology, Finland
[2] VTT Technical Research Centre of Finland

ISBN 978-951-38-6952-6 (soft back ed.)
ISSN 1235-0605 (soft back ed.)

ISBN 978-951-38-6953-3 (URL: http://www.vtt.fi/publications/index.jsp)
ISSN 1455-0865 (URL: http://www.vtt.fi/publications/index.jsp)

JULKAISIJA – UTGIVARE – PUBLISHER

VTT, Vuorimiehentie 3, PL 1000, 02044 VTT
puh. vaihde 020 722 111, faksi 020 722 4374

VTT, Bergsmansvägen 3, PB 1000, 02044 VTT
tel. växel 020 722 111, fax 020 722 4374

VTT Technical Research Centre of Finland, Vuorimiehentie 3, P.O. Box 1000, FI-02044 VTT, Finland
phone internat. +358 20 722 111, fax +358 20 722 4374

VTT, Kemistintie 3, PL 1000, 02044 VTT
puh. vaihde 020 722 111, faksi 020 722 7002

VTT, Kemistvägen 3, PB 1000, 02044 VTT
tel. växel 020 722 111, fax 020 722 7002

VTT Technical Research Centre of Finland, Kemistintie 3, P.O. Box 1000, FI-02044 VTT, Finland
phone internat. +358 20 722 111, fax +358 20 722 7002

Technical editing Anni Kääriäinen

Edita Prima Oy, Helsinki 2007

Hänninen Hannu, Brederholm, Anssi, Saukkonen, Tapio, Gripenberg, Hans, Toivonen, Aki, Ehrnstén, Ulla & Aaltonen, Pertti. Hot cracking and environment-assisted cracking susceptibility of dissimilar metal welds. Espoo 2007. VTT Tiedotteita – Research Notes 2399. 182 p.

Keywords hot cracking, environment-assisted cracking, nuclear power plants, nickel base alloys, carbon steels, austenitic stainless steels, weldability, dissimilar metal welds, Varestraint tests, residual stress measurement, microstructural analysis, crack initiation, crack growth

Abstract

The operating experience of major nuclear power plant (NPP) pressure boundary components has recently shown that dissimilar metal weld joints can markedly affect the plant availability and safety because of increased incidences of environment-assisted cracking or primary water stress corrosion cracking (EAC, PWSCC) of alloy 600 and corresponding weld metals (alloys 182/82). Alloy 690 and associated weld metals (alloys 152/52) are widely used for repair and replacement of the affected thick-section components. The selection of new materials relies mainly on laboratory results and short-term service experience. The long-term behavior of these materials and their performance in the plant has still to be demonstrated.

Weldability and susceptibility to hot cracking of the studied nickel-base materials was evaluated based on the Varestraint test results obtained with weld metals of different chromium contents. The microstructures and microchemistry of the multi-pass nickel-base alloy welds was studied by FEG-SEM/EDS techniques and were found to be very different from those of the wrought and recrystallized nickel-base materials. Additionally, the weld residual stresses were measured and analyzed by a novel Contour method suitable for through-thickness residual stress determination.

The studied nickel-base material welds were exposed to doped steam test environment and crack initiation susceptibility of them was studied. The results showed the markedly higher susceptibility to EAC of alloy 182 weld metal as compared to the other studied alloys, i.e., alloy 152, 52 and 82.

Preface

The Tekes ERIPARI project carried out during 2003–2006 at Helsinki University of Technology (HUT) and VTT Technical Research Centre of Finland (VTT) is connected to the needs of the nuclear power plant (NPP) industry, but also oil refining, conventional energy production and pulp and paper industries can benefit from the results and the developed expertise on modern dissimilar metal welds (DMW). In the weldability research a modern, versatile, Varestraint test system was built and used for hot cracking testing of present nuclear power plant and oil refinery DMW materials. Techniques were also developed for producing controlled amounts of hot cracking type of defects in test samples for EAC crack initiation studies. Weld residual stresses of DMWs were measured and analyzed with the Contour method suitable for through-thickness residual stress determination for the first time. A full scale DMW mock-up thick-wall weld was prepared for oil refinery applications. The whole manufacturing procedure is documented also as a video film.

Four-point bend tests were carried out in an aggressive doped-steam test environment to enhance the crack initiation with various types of alloy 182, 82, 52 and 152 welds with and without hot cracks, to benchmark their relative EAC susceptibility in NPP applications.

Contents

1. Introduction

This study is part of the national Dissimilar Metal Welding (DMW) project (ERIPARI), where the main objectives were to first review the field experience related to the nickel-base materials and components, where degradation has occurred in the Light Water Reactor (LWR) systems (Hänninen et al., 2006). In general, dissimilar metal welds are used in nuclear power plants and in oil refineries at locations where two different types of materials, e.g., carbon steel and austenitic stainless steel or nickel-base alloy are joined together. Nickel-base weld metals are used throughout the LWRs to join the low alloy steel pressure vessel, the pressurizer and the steam generator nozzles to wrought nickel-base alloy and austenitic stainless steel components. The nickel-base alloy dissimilar metal welds are typically made of alloy 182 and alloy 82. Recently, alloy 52 has been used both in new constructions as well as in repair welding in PWRs, while in BWRs alloy 82 is still considered to be the best choice. The interest in alloys with higher content of chromium is driven by the cracking observed in alloy 182, and recently also in alloy 82.

The number of dissimilar metal welds throughout the LWR plants is large, and their type and design depend on location, materials and welding method. Therefore, for this study some common types of mock-up welds were selected in addition to known weld designs of existing BWR and oil refinery applications. In evaluation of the structural integrity, lifetime and leak-before-break concept application for the DMWs, an excellent understanding of their metallurgical, mechanical and physical properties as well as their damage mechanisms, either hot cracking in welding or EAC during service, is needed.

All the parameters affecting the Environment-Assisted Cracking (EAC) susceptibility of the nickel-base weld metals, which is the major damage mechanism, are not yet known. Weld repairs increase the cracking susceptibility by e.g., increasing the residual stresses, and local residual strains can peak at the fusion lines, being equivalent up to 15…20% room temperature tensile strain in the weldments. Weld defects such as hot cracks, are probably also playing the key role in the crack initiation and growth. Long-term ageing at reactor operating temperatures of these alloys may also markedly affect their microstructure and cracking susceptibility. Thus, several parameters are important when evaluating the manufacturing and performance of nickel-base alloy dissimilar metal welds in Nuclear Power Plant (NPP) and oil refinery conditions. This experimental research program covers the materials, welding, residual stresses, EAC and NDE issues of the dissimilar welds consisting of the presently used nickel-base alloys.

2. Hot cracking of nickel-base dissimilar metal welds

In this study the hot cracking tendency of six different dissimilar metal weld joints were tested by the Varestraint test (CEN ISO/TR 17641-3, 2005). Hot cracking and weld microstructures were studied by optical and scanning electron microscopy (FEG-SEM/EDS). The materials and welds under study are typical for nuclear power plant applications and in the oil and gas industry. In Table 2.1 are presented the chemical compositions of the base materials and filler metals used in manufacturing of the studied dissimilar metal welds.

Table 2.1. Chemical compositions of the base materials and filler metals used in the dissimilar metal welds.

	C	Si	Mn	P	S	Cr	Mo	Ni	Nb	N	Ti	Fe	Al	Co	Cu
Base materials															
S355	< 0,22	< 0,55	< 1,6	< 0,035	<0,035										
42CrMo4	0,42		0,7		0,4	1,05	0,225								
AISI 321	< 0,08					17-19		9-12			5*C-0,7				
AISI 316 NG	< 0,03					16,5-18,5	2,5-3	11-14		0,12-0,22					
SA508 (Grade 2)	0,24	0,21	1,38		0,009	0,16	0,54	0,58		0,014			0,015		0,12
Inconel 600	0,07	0,19	0,21	0,007	0,001	16,3		72,86	Nb+Ta 0,10		0,28	9,44	0,229	0,076	0,13
Inconel 690	0,02	0,04	0,16		0,001	29,46		59,82			0,33	9,96	0,2		<0,01
Filler metals															
E 316L (OK 63.30)	0,02	0,75	0,7	0,013	0,011	18,3	2,7	13							
E 309Mo-17 (OK 67.70)	0,01	0,76	0,6	0,017	0,013	22,6	2,7	13							0,06
E 309 (OK Tigrod 16.51)	0,02	0,89	1,7	0,02	0,01	23,8	0,18	13,7							0,1
E 347 (OK 61.81)	0,07	0,7	1,7	0,021	0,006	19,8	0,1	10	0,61						0,14
AISI 347 (OK Tigrod 16.11)	0,04	0,85	1,4	0,02	0,01	19	0,02	9,5	0,55						0,03
E 347 (OK Band 11.62)	< 0,025	0,4	1,8			20		10	0,7						
AISI 308L (OK Band 11.61)	< 0,025	0,4	1,8			20		10							
AISI 309L (OK Band 11.65)	< 0,025	0,4	1,8			24		13							
Inconel 182 (OK 92.26)	0,03	0,8	6,5	0,01	0,003	15,7		68	1,8		0,1	6,7			< 0,01
Inconel 82 (OK Tigrod 19.85)	0,039	0,03	2,98	0,001	0,004	19,94		72,6	Nb+Ta 2,47		0,34	1		0,01	0,01
Inconel 52	0,03	0,13	0,24	<0,001	<0,001	29,2	0,03	59,28	Nb+Ta <0,02		0,51	9,8	0,72	0,009	0,04
Inconel 52M	0,02	0,09	0,8	0,003	0,001	30,06	0,01	59,54	Nb+Ta 0,83		0,224	8,22	0,11	0,027	0,02
Inconel 52MS	0,014	0,12	0,68	0,004	0,0007	29,53	0,02	60,14	0,78		0,19	8,33	0,13	0,008	0,03
Inconel 152	0,048	0,41	3,48	0,003	0,003	28,74	0,01	55,2	Nb+Ta 1,54		0,09	10,39	0,06	<0,005	<0,01
Inconel 152M	0,0293	0,3276	3,247	<0,001	0,0042	28,98	<0,005	57	Nb+Ta 1,533		0,039	8,75	<0,005	0,0119	<0,005

2.1 Groove geometries, materials and welding of Varestraint test samples

Materials, groove geometries and filler metals were selected to simulate those used in the nuclear power plants (NPP) and oil refineries in Finland. Four similar test specimens were manufactured for each groove geometry. The length of the test specimens was 300 mm, thickness 8 mm and the width varied from 50 to 80 mm, respectively.

2.1.1 Neste Oil dissimilar metal weld

Figure 2.1 presents the groove geometry and materials of the Neste Oil dissimilar metal weld (marked later as Nx).

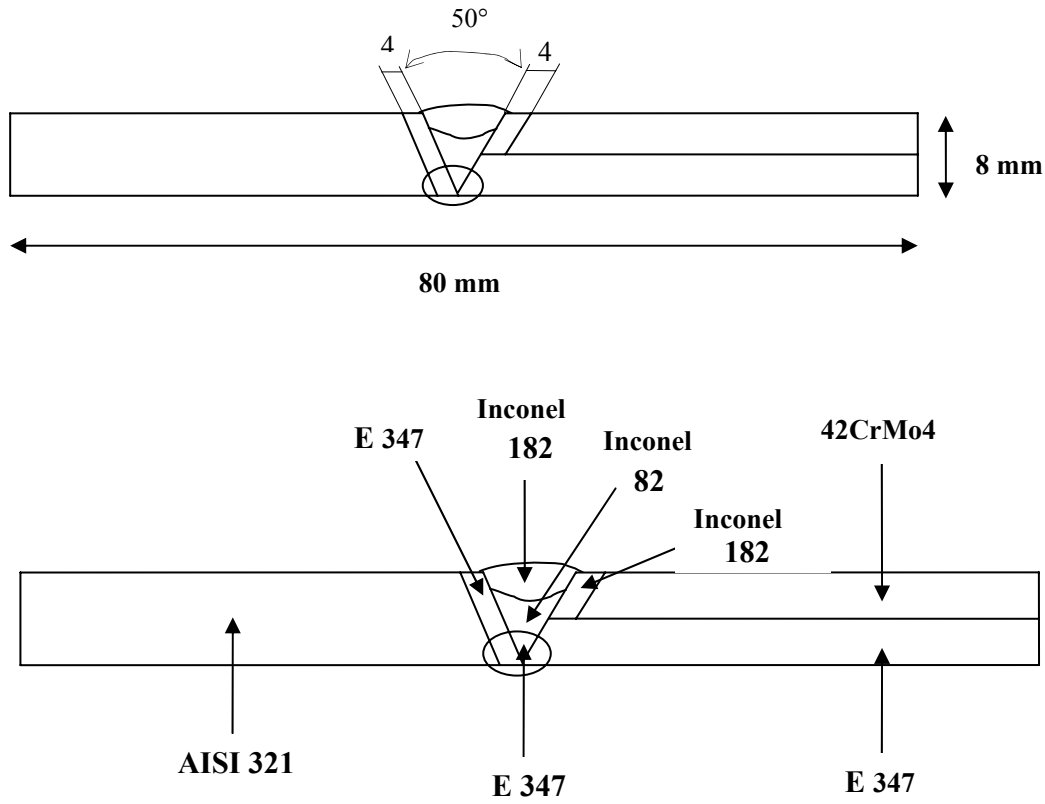

Figure 2.1. Groove geometry and materials of the Neste Oil dissimilar metal weld.

The surface of a ferritic 42CrMo4 steel bar (∅ 80 mm and length 750 mm) was machined to the width of 70 mm (Figure 2.2). After machining, it was clad by submerged arc welding (Figure 2.3) using E 347 filler metal band (OK Band 16.11, width 60 mm and 0,5 mm thickness).

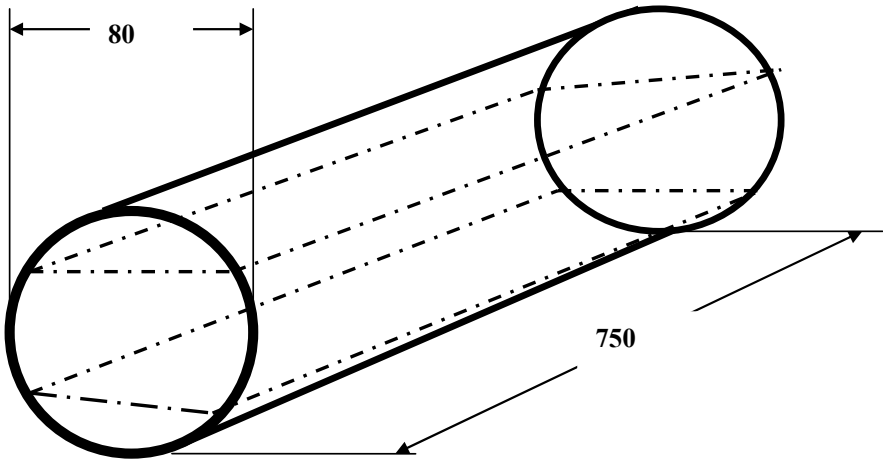

Figure 2.2. A schematic presentation of the 42CrMo4 ferritic steel bar before submerged arc weld cladding.

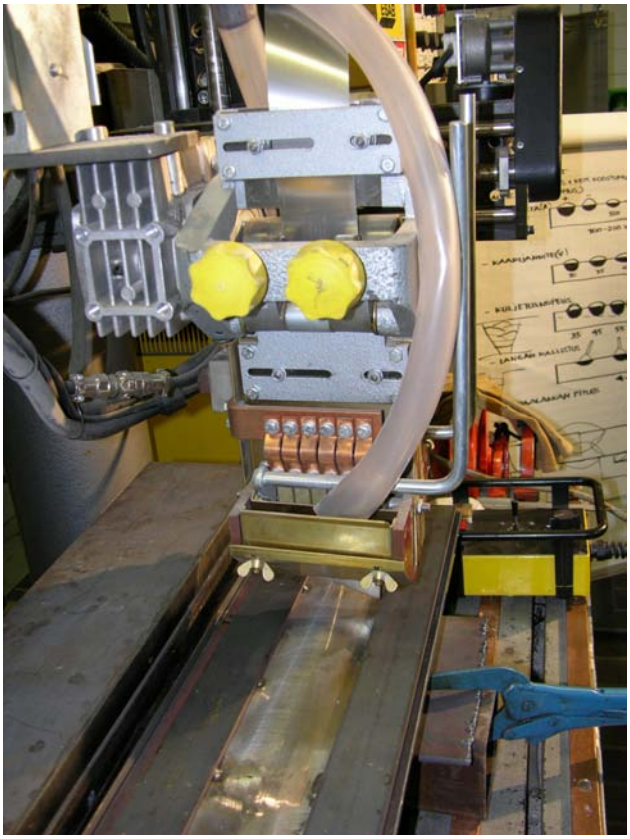

Figure 2.3. Cladding of ferritic 42CrMo4 steel bar by submerged arc welding.

One layer was welded to the surface of the bar, and the thickness of the cladding was 4 mm. After welding, the surface of the weld was machined to the cladding thickness of 3 mm (Figure 2.4).

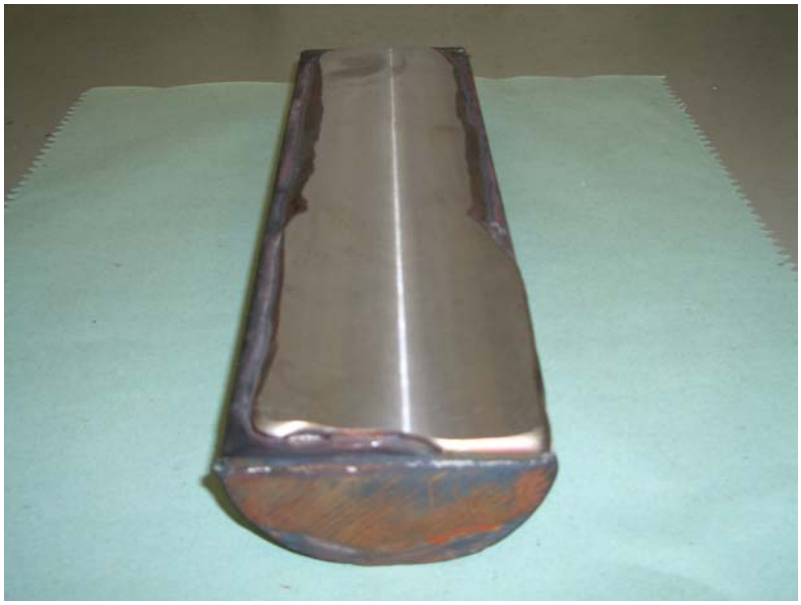

Figure 2.4. Ferritic 42CrMo4 steel bar after cladding and machining.

After machining, an 8 mm thick slice (Figure 2.6) was cut by Wire Electro Discharge Machining (WEDM), as shown in Figure 2.5.

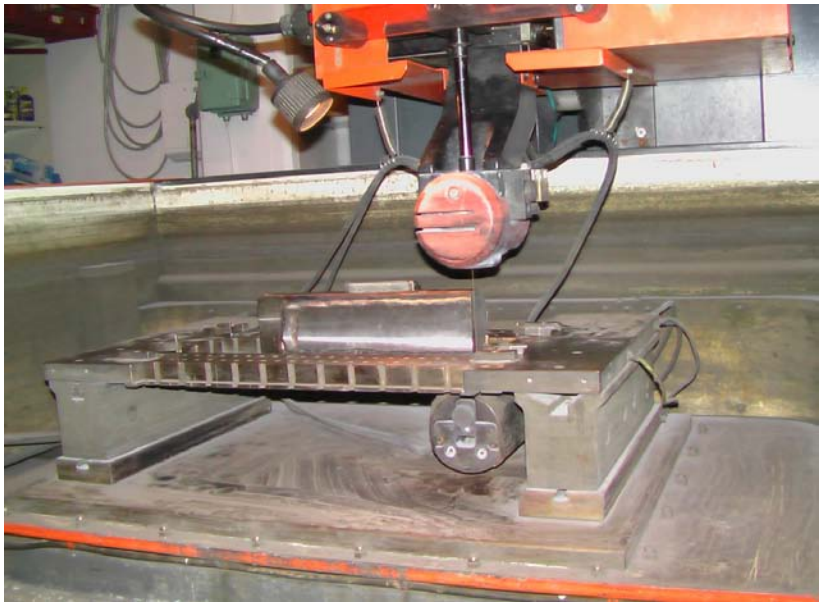

Figure 2.5. Wire Electro Discharge Machining (WEDM).

Figure 2.6. Clad, 8 mm thick slice after cutting from ferritic 42CrMo4 steel bar.

After cutting, a 4 mm deep groove was machined on the ferritic steel side and filled by welding with Inconel 182 type filler metal OK 92.26, and then machined to the final groove geometry. This side of the test specimen was heat treated at 700 °C for 7 h. The other side of the test specimen was AISI 321 stainless steel plate. When the groove

geometry was machined to the plate, it was buttered by E 347 filler metal OK 61.81 to simulate E 347 plate. The reason for this was that plain E 347 type plate was not available. After cladding, the final groove geometry was machined. No heat treatment was made to this side of the test specimen. These two sides were welded together first with E 347 filler metal OK Tigrod 16.11 for the root pass, next pass was made with Inconel 82 type filler metal OK Tigrod 19.85, and the rest of the filling passes were made with Inconel 182 type filler metal OK 92.26.

2.1.2 Fortum Nuclear Service dissimilar metal weld

Figure 2.7 presents the groove geometry and materials of the Fortum Nuclear Service dissimilar metal weld (marked later as Fx).

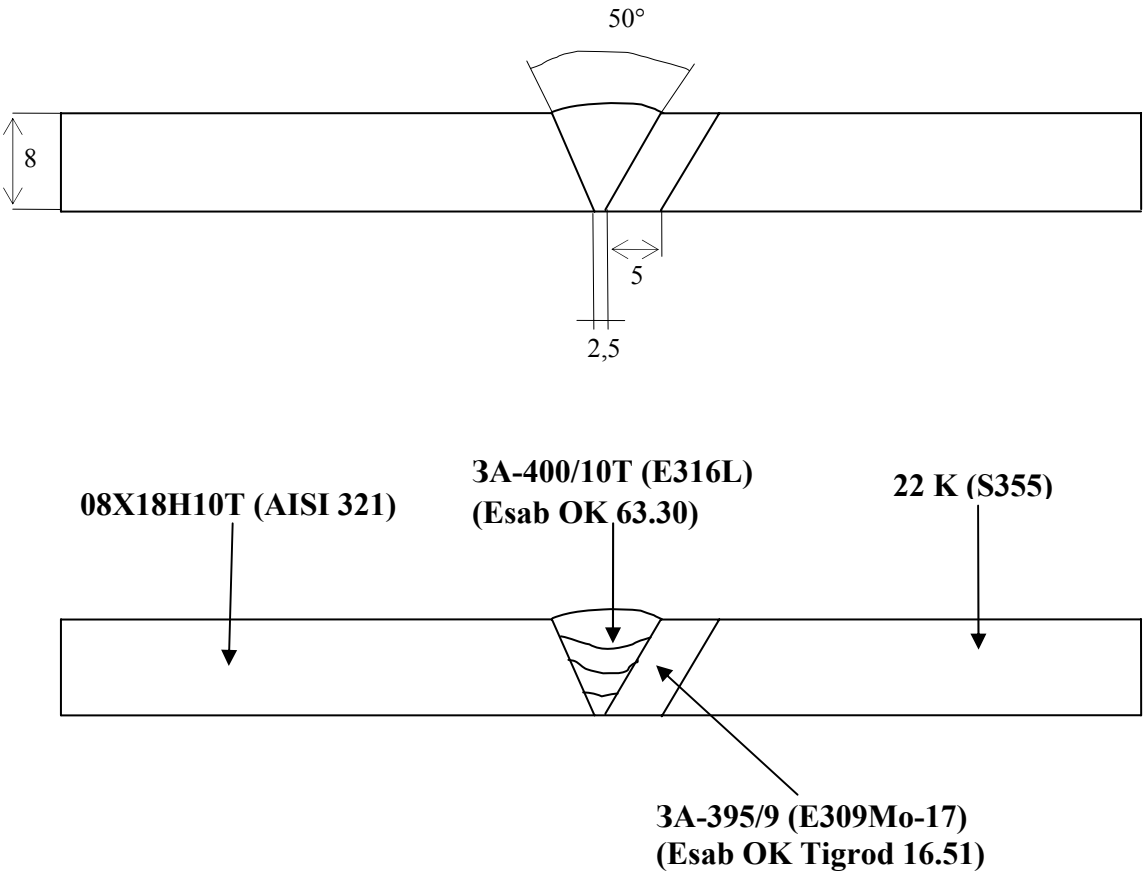

Figure 2.7. Groove geometry and materials of the Fortum Nuclear Service dissimilar metal weld.

The machined groove in the S355 ferritic steel was buttered by austenitic filler metal OK Tigrod 16.51 to the thickness of 6 mm. Final thickness of the buttering after the machining was approximately 5 mm. Welding of the plates together was made with austenitic filler metal OK 63.30. No heat treatment was made to this test specimen.

2.1.3 Mock-up TV dissimilar metal weld

Figure 2.8 presents the groove geometry and materials of the mock-up TV dissimilar metal weld (marked later as TVx).

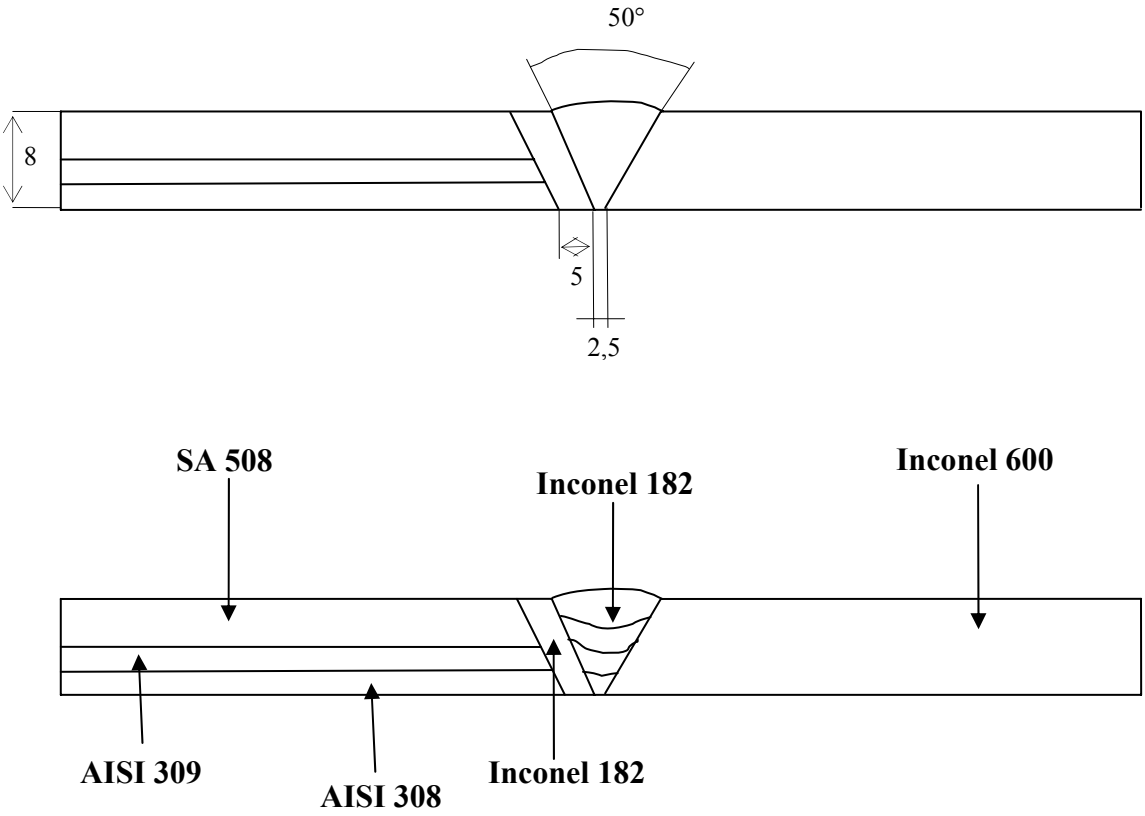

Figure 2.8. Groove geometry and materials of the mock-up TV dissimilar metal weld.

A pressure vessel steel (SA 508 Grade 2) piece obtained from the Ringhals plant (Sweden) (Figure 2.9) was clad with two austenitic stainless steel layers by submerged arc welding.

Figure 2.9. Pressure vessel steel (SA 508 Grade 2) piece.

The pressure vessel steel surface was machined and then the piece was fastened to the jig for cladding. The first layer was welded by austenitic filler metal OK Band 11.65 (width 60 mm and thickness 0,5 mm) with flux OK 10.05. Two passes were welded side by side and the thickness of the cladding was 4 mm (Figure 2.10).

Figure 2.10. First layer of cladding on pressure vessel steel SA 508 Grade 2.

After welding the first cladding layer, it was machined to the thickness of 2 mm and then the second layer of cladding was welded in the same way as the first one, using filler metal OK Band 11.61 (width 60 mm and thickness 0,5 mm). Figure 2.11 shows cladding of the second layer after the first pass.

Figure 2.11. Cladding of the second layer after first pass.

The second layer was then machined to a thickness of 2 mm, for a combined cladding thickness of 4 mm. A 10 mm thick slice was cut by band saw (Figures 2.12 and 2.13) and then machined to the thickness of 8 mm. After cutting the slice, two 80 mm wide, 300 mm long and 8 mm thick pieces were obtained where the groove geometry was machined.

Figure 2.12. Cutting a slice by band saw.

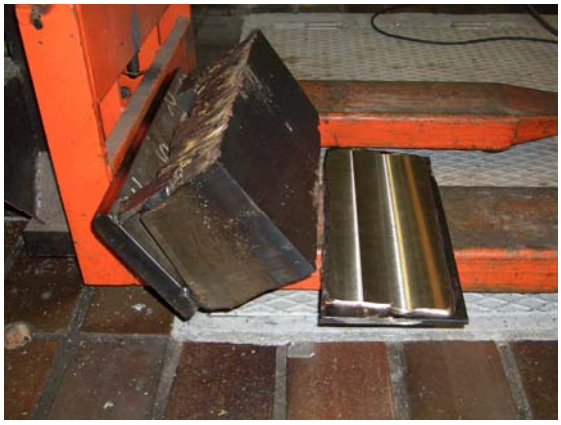

Figure 2.13. Cut slice.

The slice was cut into 45 mm width and a 25° groove was machined. The pressure vessel side of the groove was buttered with Inconel 182. The thickness of the buttering layer was 4 mm. Figure 2.14 shows the groove after the first buttering pass.

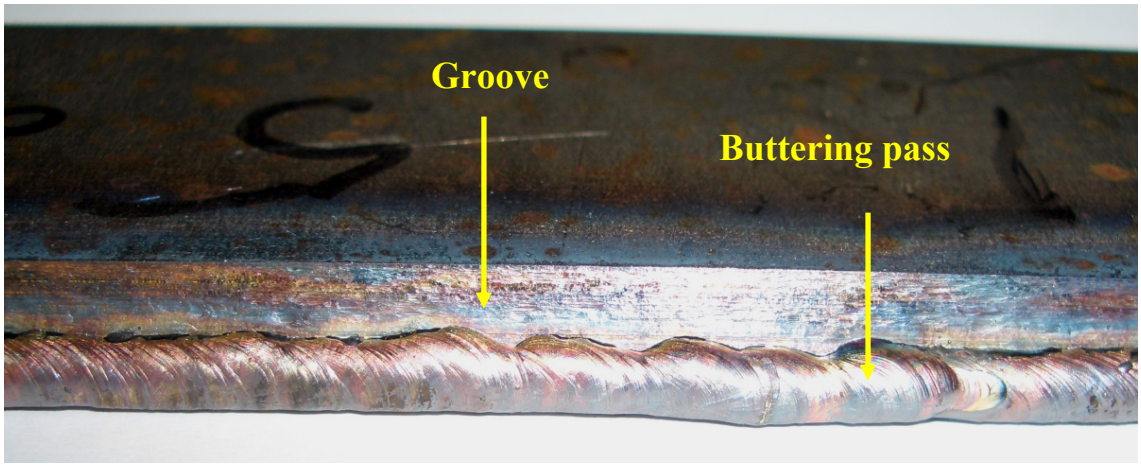

Figure 2.14. Groove after first buttering pass.

After buttering, the groove was machined to the angle of 25° as shown in Figure 2.8. Before final welding, the SA 508 side (with Inconel 182 buttering) of the test specimen was first heat treated at 610 °C for 6 h. The SA 508 side and the Inconel 600 plate were then welded together with Inconel 182 welding electrode, and then resulting test sample was machined to the width of 80 mm.

2.1.4 Mock-up 1 dissimilar metal weld

Figure 2.15 presents the groove geometry and materials of the mock-up 1 dissimilar metal weld (marked later as TU1).

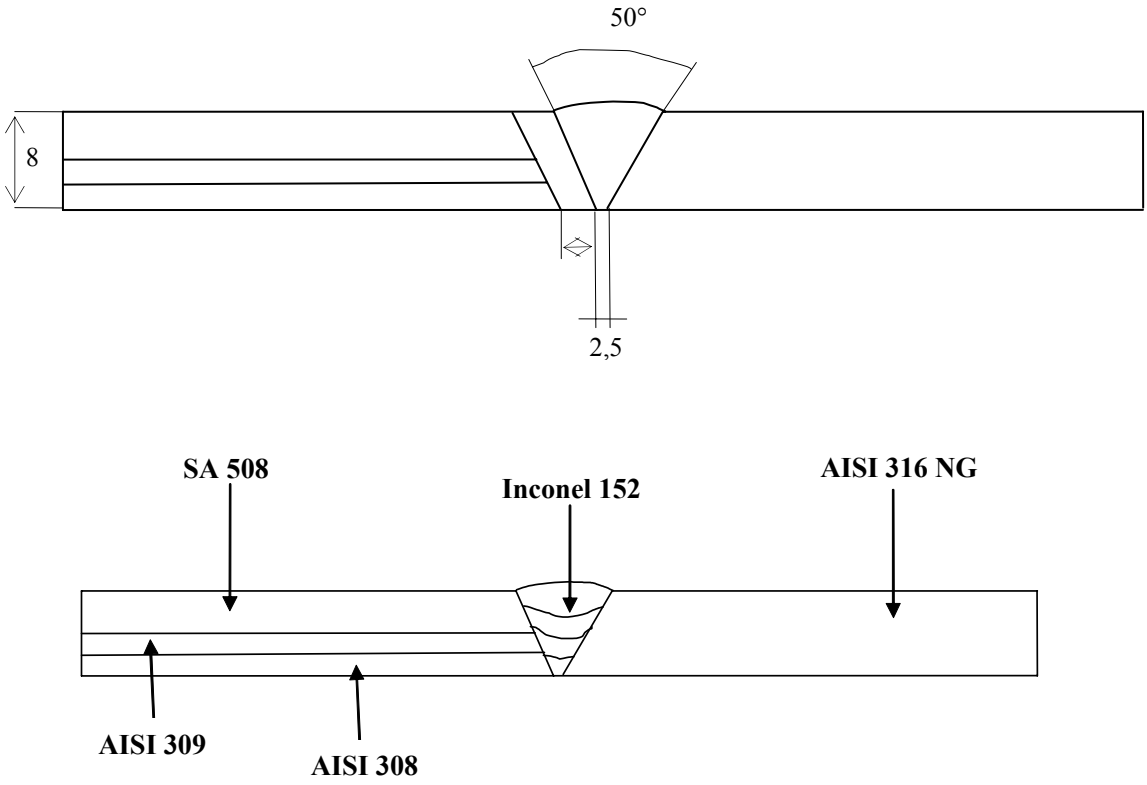

Figure 2.15. Groove geometry and materials of the mock-up 1 dissimilar metal weld.

The cladding of pressure vessel steel SA 508 was done in the same way as in the previous mock-up TV test sample. There is no buttering layer in the groove. The SA 508 side and the AISI 316 NG plate were welded together with Inconel 152 welding electrode, and then the test sample was machined to the width of 80 mm. After welding, the whole test specimen was heat treated at 610 °C for 16 h.

2.1.5 Mock-up 2 dissimilar metal weld

Figure 2.16 presents the groove geometry and materials of the mock-up 2 dissimilar metal weld (marked later as TU2).

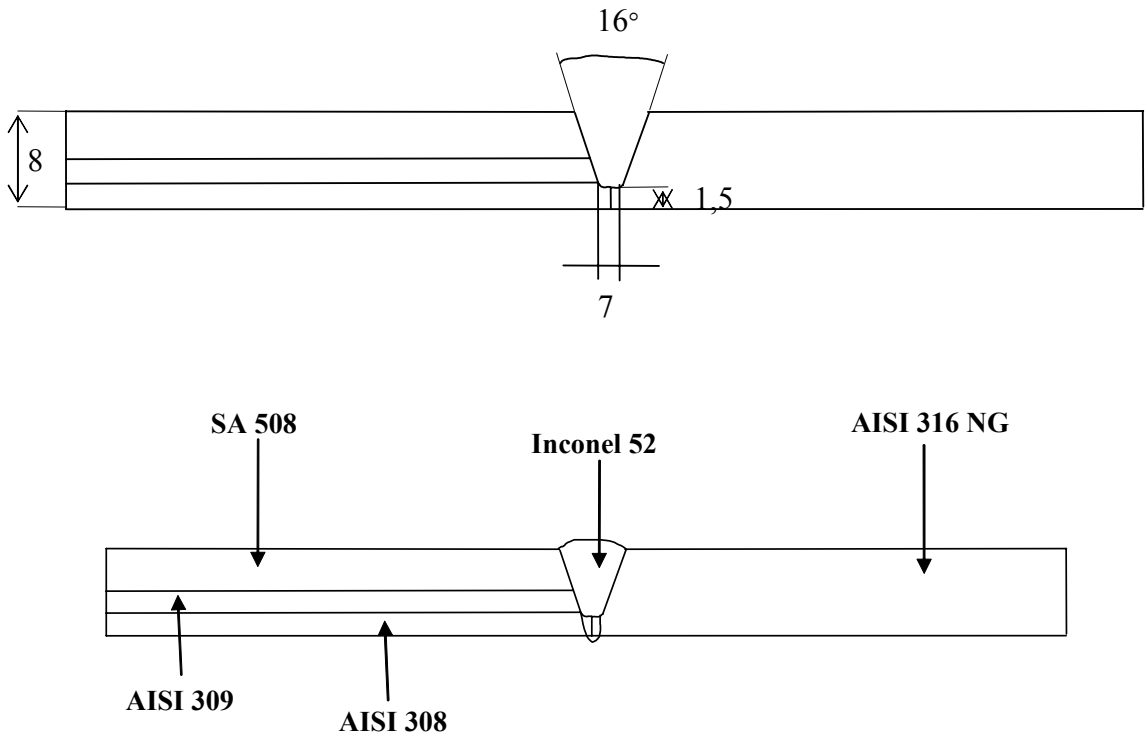

Figure 2.16. Groove geometry and materials of the mock-up 2 dissimilar metal weld.

The cladding of pressure vessel steel SA 508 was made in the same way as in the previous mock-up 1 test sample. The SA 508 side and the AISI 316 NG plate were welded together with Inconel 52 filler metal, and then the test sample was machined to the width of 80 mm. After welding, the whole test specimen was heat treated at 610 °C for 16 h.

2.1.6 Mock-up 3 dissimilar metal weld

Figure 2.17 presents the groove geometry and materials of the mock-up 3 dissimilar metal weld (marked later as TU3).

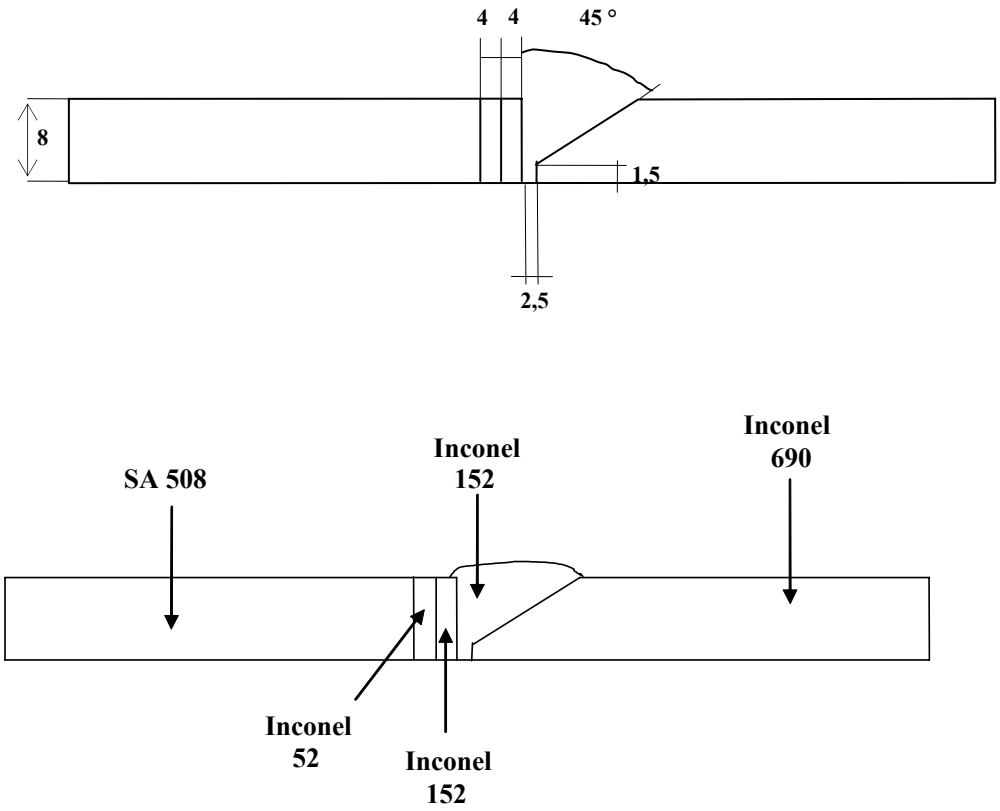

Figure 2.17. Groove geometry and materials of the mock-up 3 dissimilar metal weld.

The thicknesses of the buttering layers of both Inconel 52 and 152 were 3–4 mm. After welding the SA 508 side (with Inconel 52 and 152 buttering) the test specimen was heat treated at 610 °C for 4 h. The SA 508 side and the Inconel 690 plate were welded together with Inconel 152 welding electrode, and then the test sample was machined to the width of 80 mm.

2.2 Varestraint test and testing equipment

In the Varestraint test, a weld is deposited from left to right, as indicated in Figure 2.18. As the arc passes the point marked by A, a pneumatically or hydraulically actuated loading yoke bends the specimen downwards to conform to the radius of curvature of the top surface of the removable die block, B. Meanwhile, the arc travels steadily onwards and is subsequently interrupted in the run-off area at C.

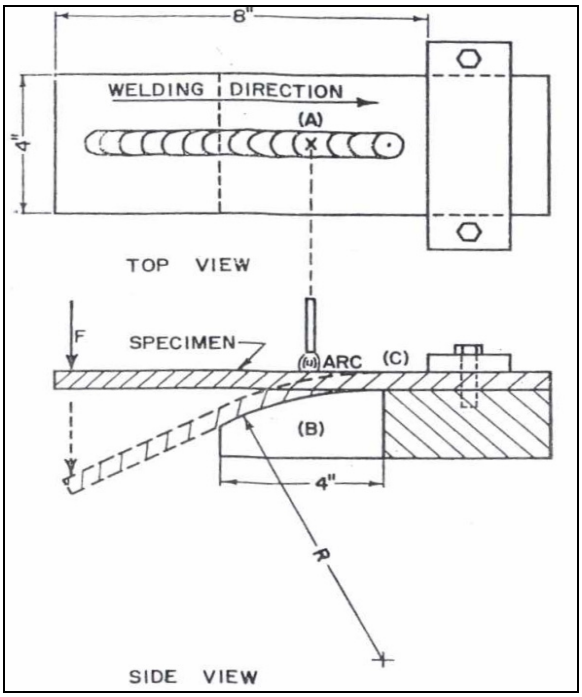

Figure 2.18. Simplified sketch of the operation of the Varestraint testing device.

From the geometry of the system, the nominal value of the suddenly applied, augmented tangential strain in the outer fibre of the test specimen can be calculated as follows:

$$\varepsilon_t = t/2R, \tag{2.1}$$

where

ε_t = augmented tangential strain,
t = specimen thickness, and
R = radius of curvature of the die block.

By substituting the die block with the appropriate radius of curvature, any desired augmented strain can be applied to the weldments at any predetermined instant during the weld deposition.

The Varestraint equipment built for the hot cracking tests is presented in Figures 2.19, 2.20 and 2.21.

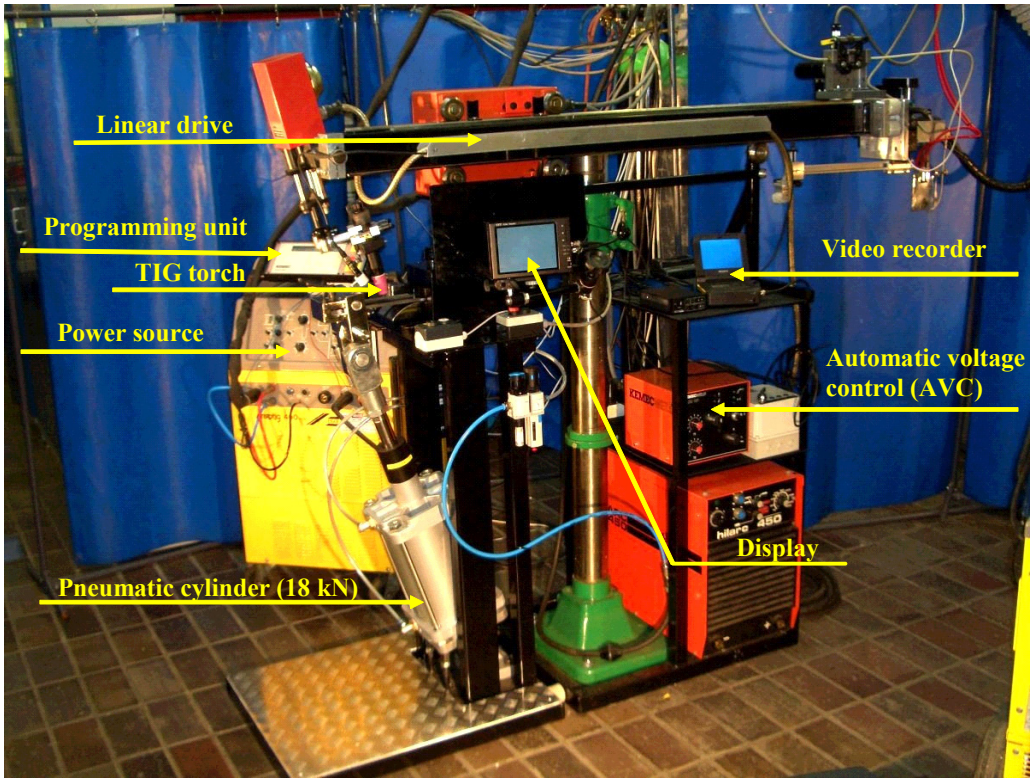

Figure 2.19. General view of Varestraint testing equipment built for hot cracking tests.

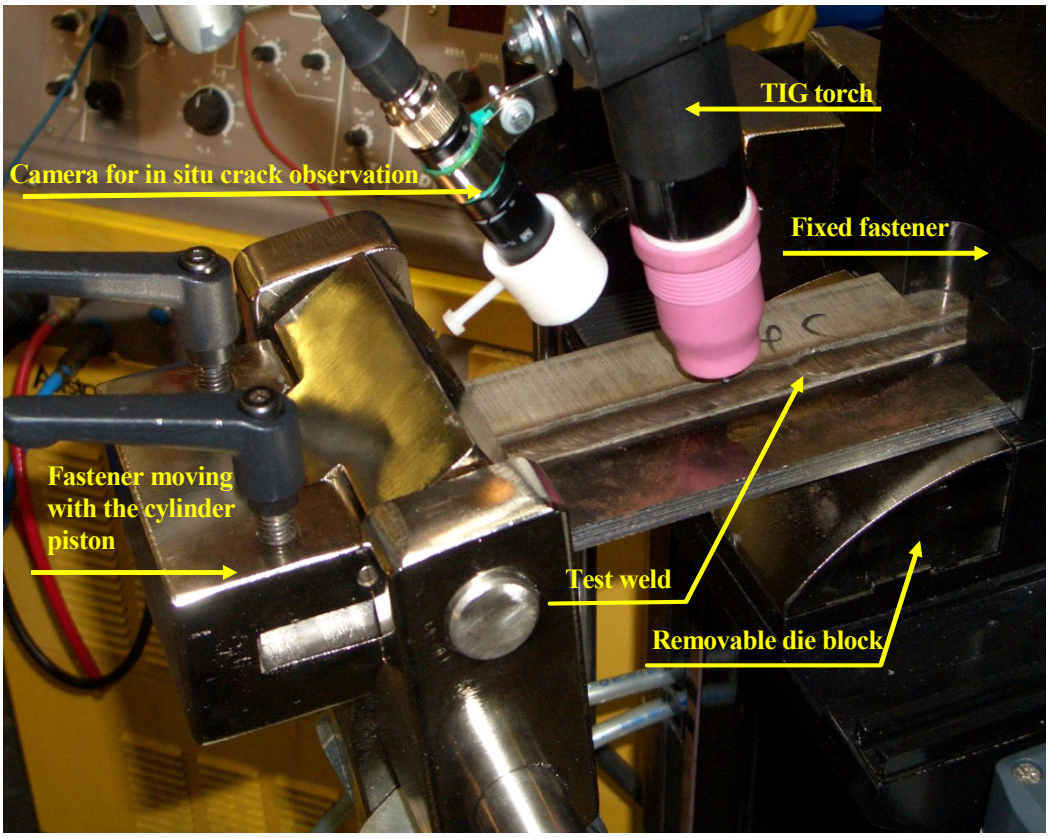

Figure 2.20. Test specimen before bending in Varestraint test.

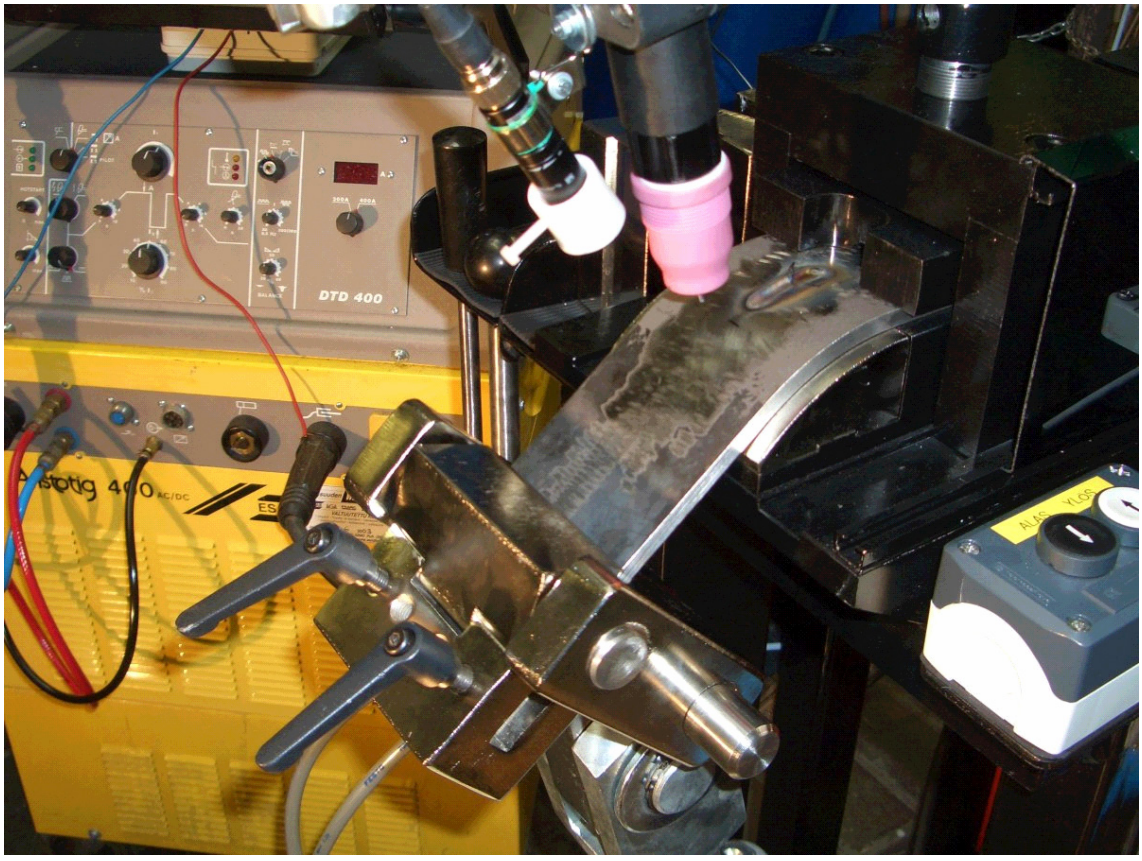

Figure 2.21. Test specimen after bending in Varestraint test.

2.2.1 Results of Varestraint tests

In this study Varestraint specimen thickness was 8 mm and augmented tangential strains used were 0,5, 1, 2, 3 and 4% and the radii of curvature of the die blocks were 800, 400, 200, 133 and 100 mm, respectively.

2.2.1.1 Neste Oil case

In the Neste Oil case, the welding current was 250 A, voltage was 12,5 V, welding speed was 12 cm/min, heat input was 9,4 kJ/cm, welding length was 55 mm and bending speed was 16 mm/s. Bending was done so that tension was in the weld surface side. Figure 2.22 presents the test piece after Varestraint testing utilizing an augmented strain of 4%.

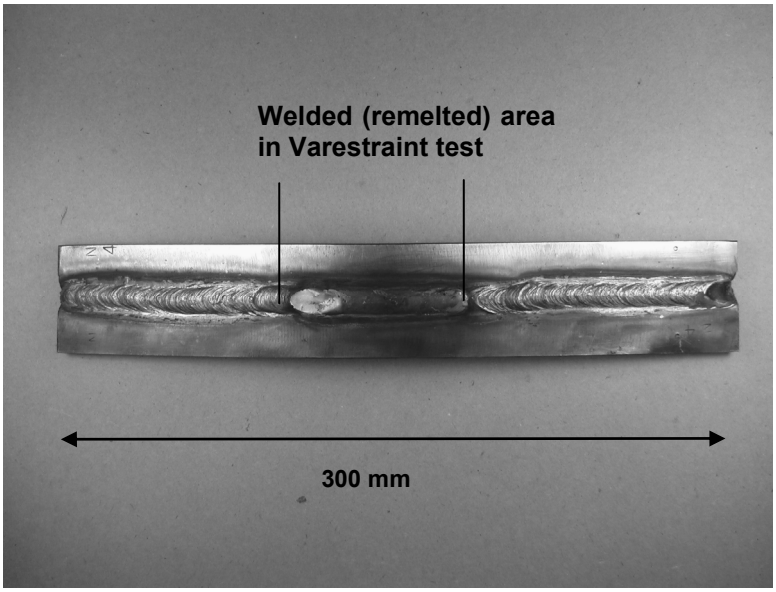

a)

b)

Figure 2.22 (a-b). a) Test piece after Varestraint test. b) By bending augmented strain was 4%.

In Figure 2.23 is the surface of the test piece with hot cracks after Varestraint testing utilizing an augmented strain of 4%.

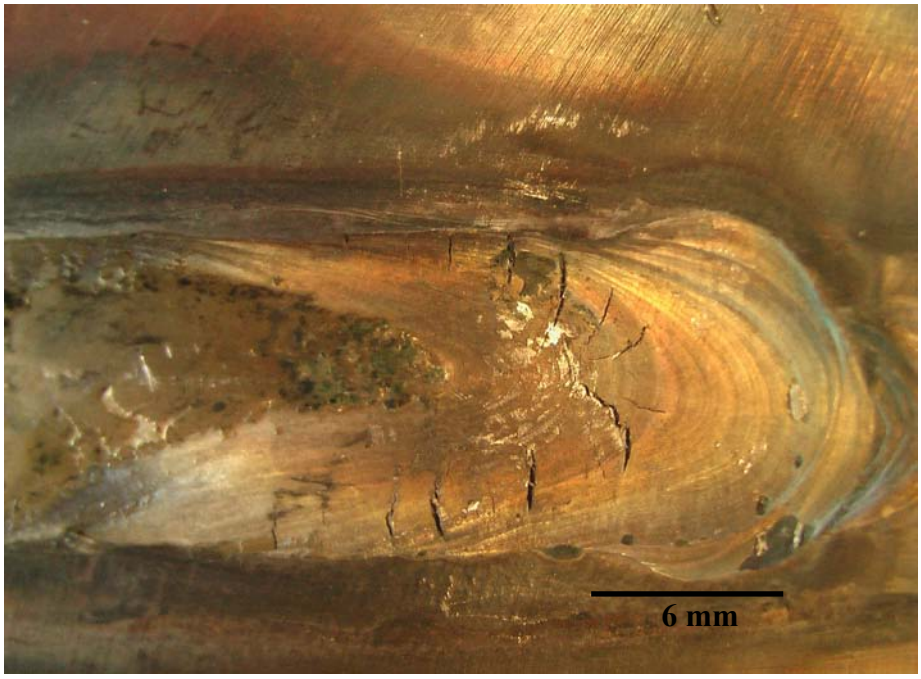

Figure 2.23. Surface of the test piece with hot cracks after Varestraint test. Augmented strain was 4%.

In Figures 2.24–2.28 are presented the calculated crack lengths from the area shown in Figure 2.23 with magnification of 25x and augmented strain of 4% (magnification is determined in standard CEN ISO/TR 17641-3, 2005).

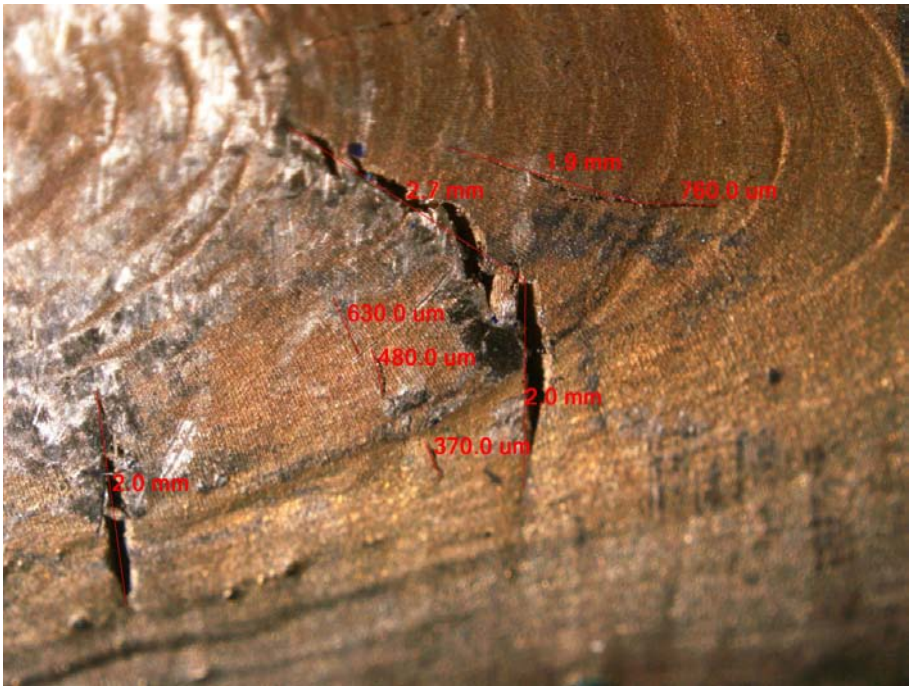

Figure 2.24. Measured crack lengths with magnification of 25x. Augmented strain was 4%.

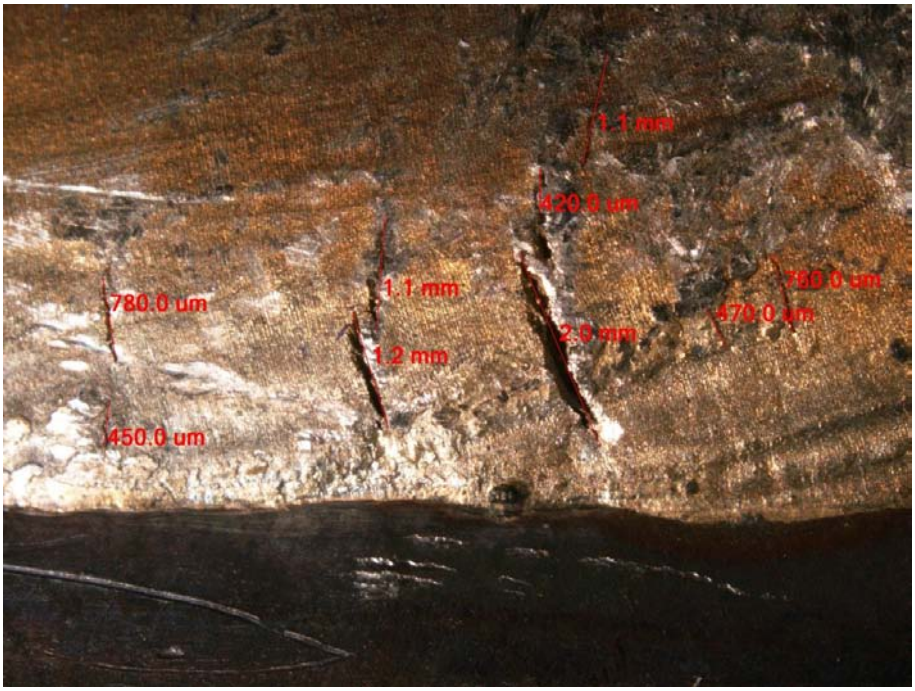

Figure 2.25. Measured crack lengths with magnification of 25x. Augmented strain was 4%.

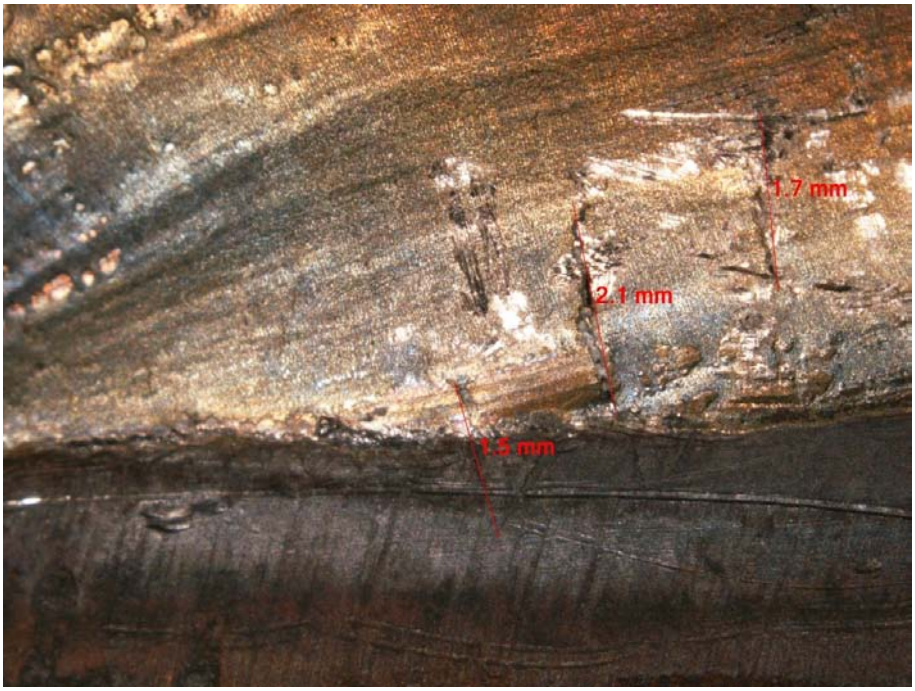

Figure 2.26. Measured crack lengths with magnification of 25x. Augmented strain was 4%.

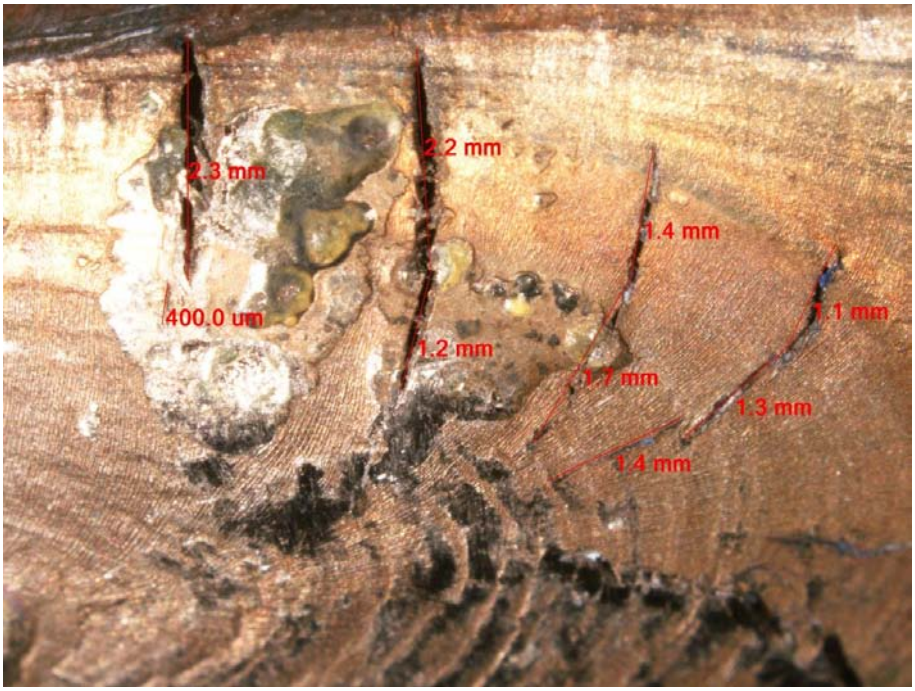

Figure 2.27. Measured crack lengths with magnification of 25x. Augmented strain was 4%.

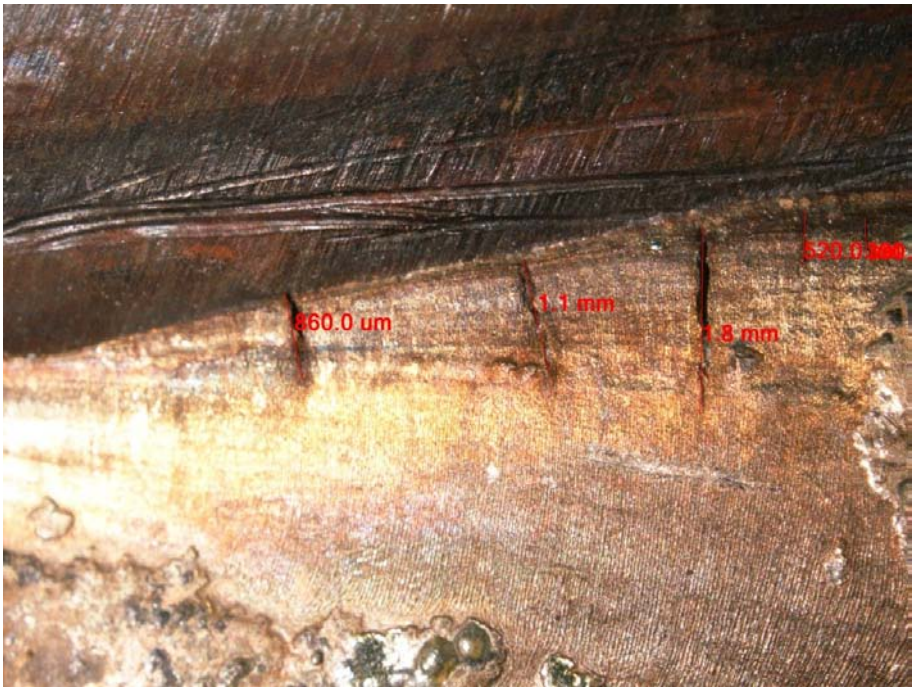

Figure 2.28. Measured crack lengths with magnification of 25x. Augmented strain was 4%.

Total crack length (TCL) of the Neste Oil case Varestraint test with 4% augmented strain was 42 mm and maximum crack length was 3,8 mm.

In Figure 2.29 is the surface of the test piece with hot cracks after Varestraint testing utilizing an augmented strain of 3%.

Figure 2.29. Surface of the test piece with hot cracks after Varestraint test. Augmented strain was 3%.

In Figures 2.30–2.32 are presented measured crack lengths from the area shown in Figure 2.29 with magnification of 25x and augmented strain of 3%.

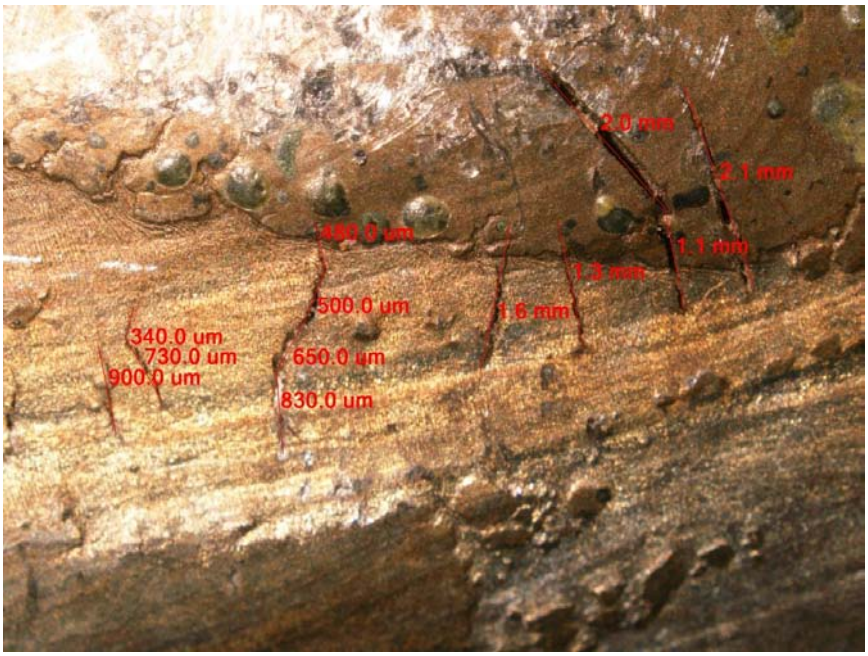

Figure 2.30. Measured crack lengths with magnification of 25x. Augmented strain was 3%.

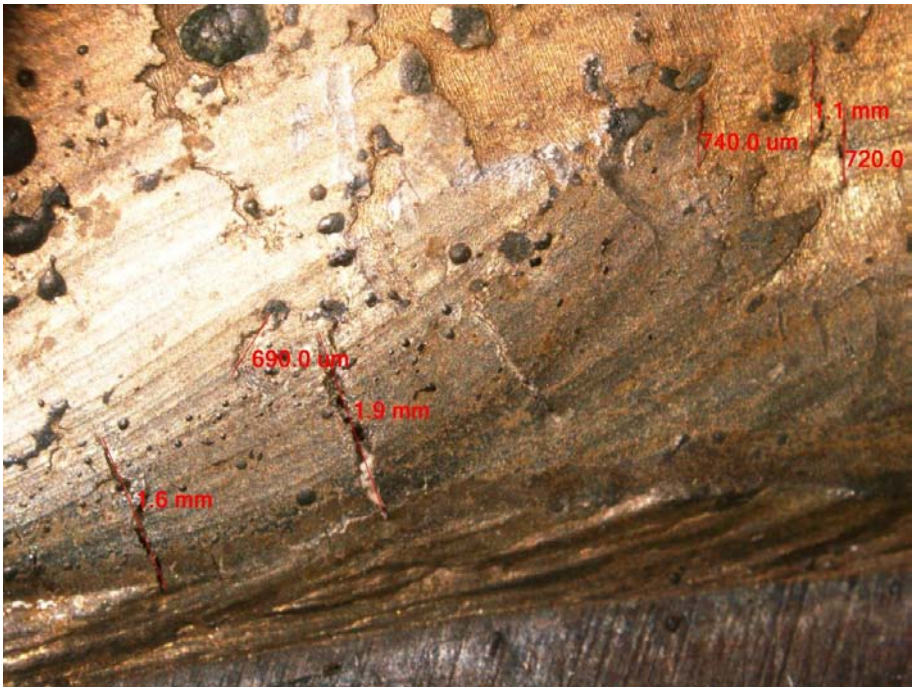

Figure 2.31. Measured crack lengths with magnification of 25x. Augmented strain was 3%.

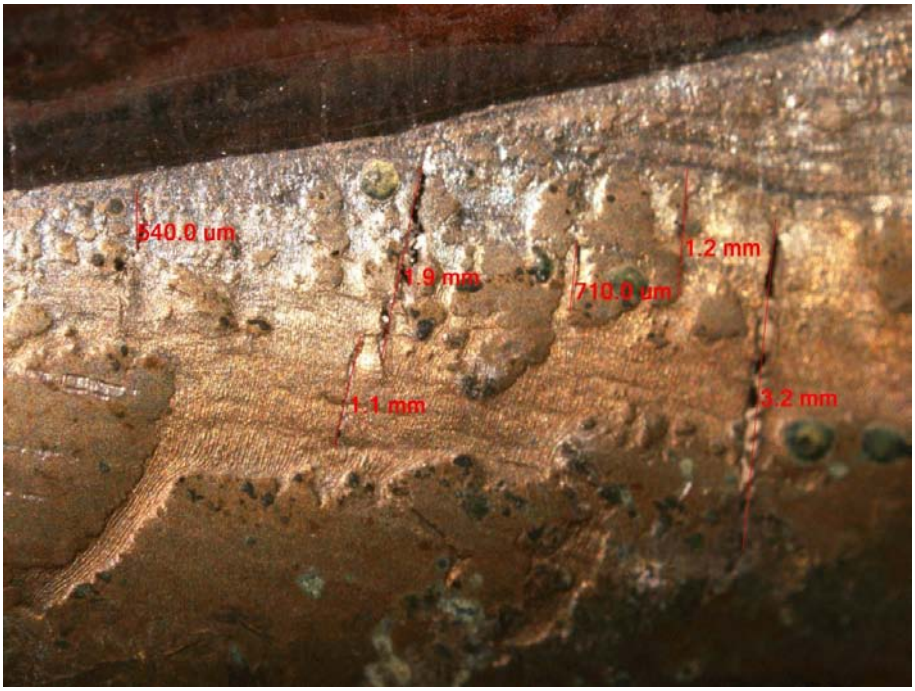

Figure 2.32. Measured crack lengths with magnification of 25x. Augmented strain was 3%.

Total crack length (TCL) of the Neste Oil case Varestraint test with 3% augmented strain was 28 mm and maximum crack length was 3,2 mm.

In Figure 2.33 is the surface of the test piece with hot cracks after Varestraint testing utilizing an augmented strain of 2%.

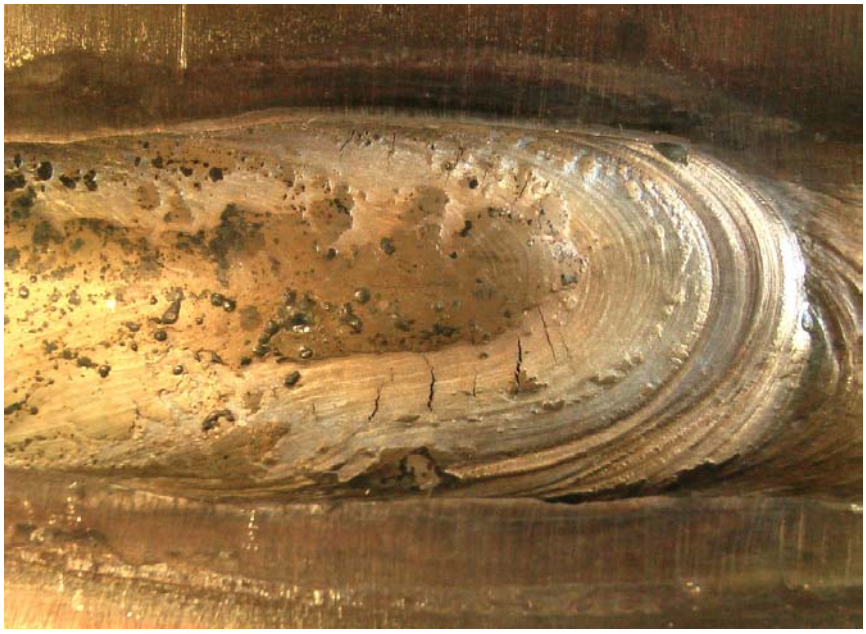

Figure 2.33. Surface of the test piece with hot cracks after Varestraint test. Augmented strain was 2%.

In Figures 2.34–2.36 are presented measured crack lengths from the area shown in Figure 2.33 with magnification of 25x and augmented strain of 2%.

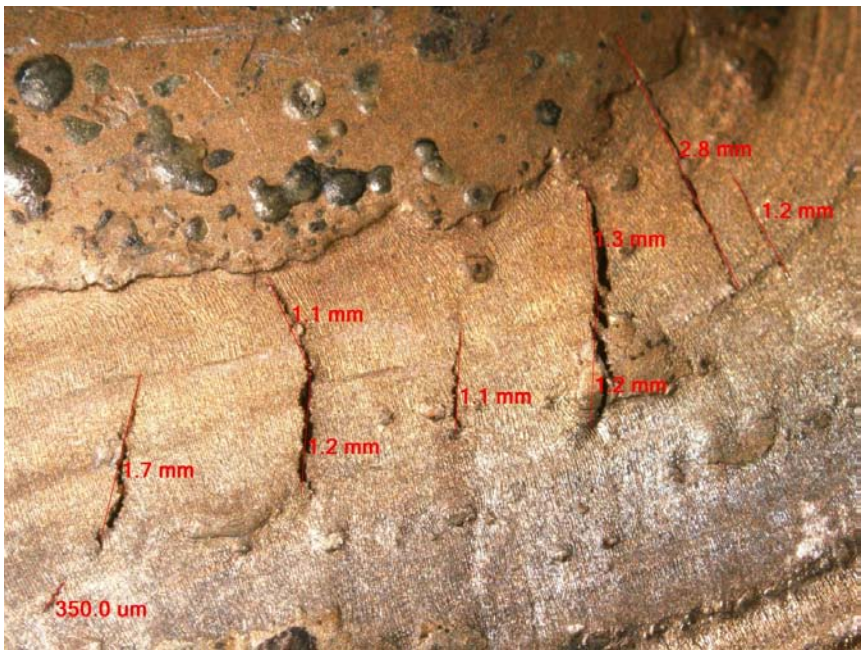

Figure 2.34. Measured crack lengths with magnification of 25x. Augmented strain was 2%.

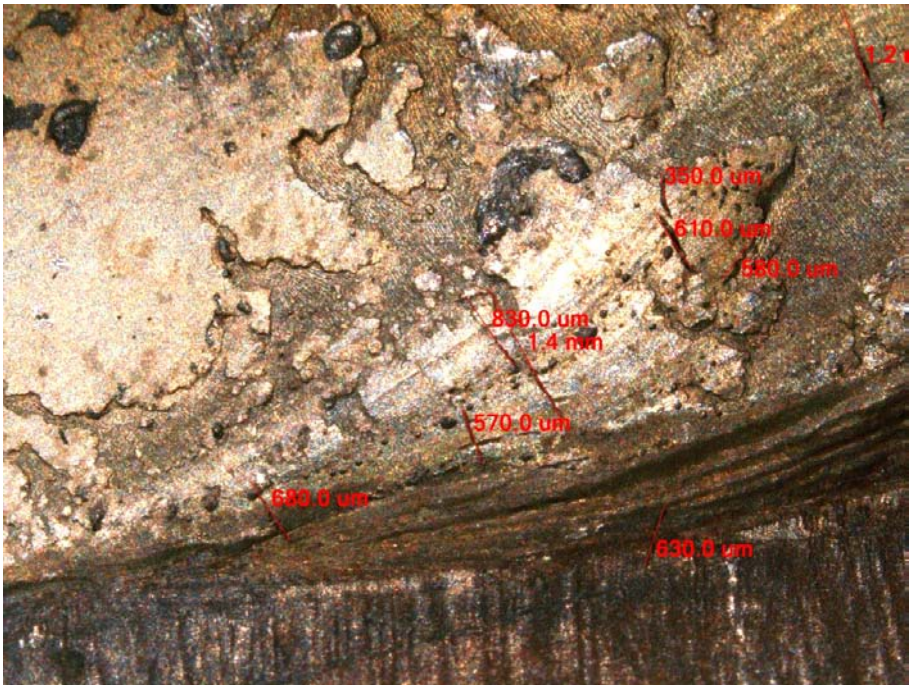

Figure 2.35. Measured crack lengths with magnification of 25x. Augmented strain was 2%.

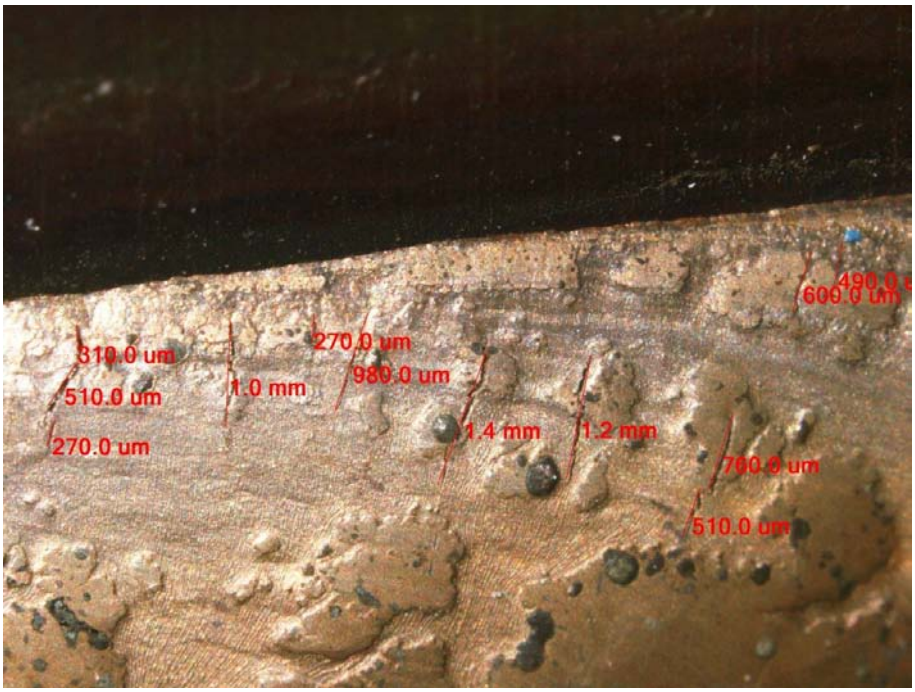

Figure 2.36. Measured crack lengths with magnification of 25x. Augmented strain was 2%.

Total crack length (TCL) of the Neste Oil case Varestraint test with 2% augmented strain was 27 mm and maximum crack length was 2,8 mm.

In Figures 2.37 and 2.38 are presented measured crack lengths with magnification of 25x and augmented strain of 1%.

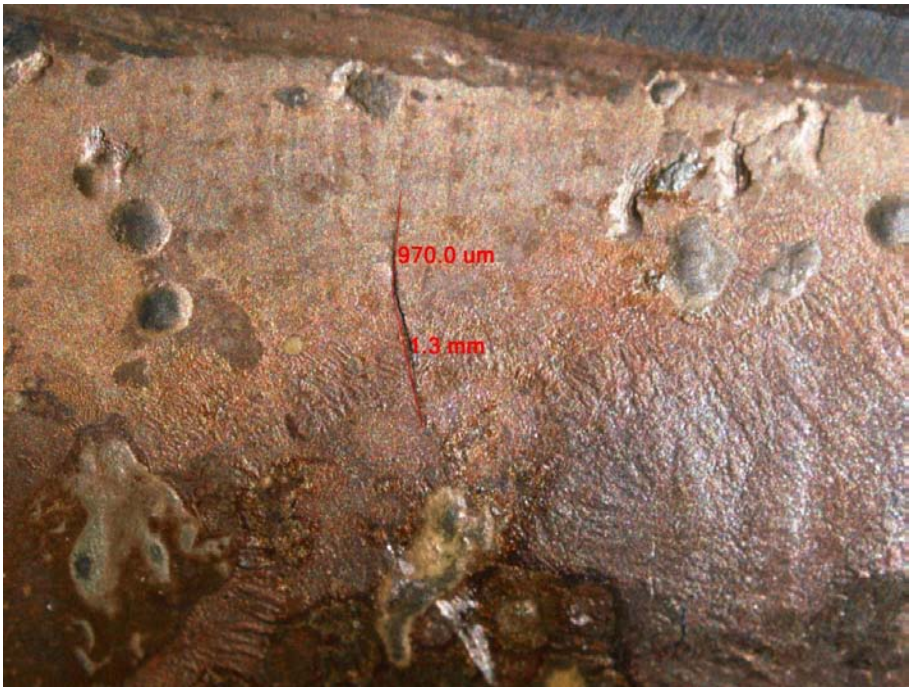

Figure 2.37. Measured crack lengths with magnification of 25x. Augmented strain was 1%.

Figure 2.38. Measured crack lengths with magnification of 25x. Augmented strain was 1%.

Total crack length (TCL) of the Neste Oil case Varestraint test with 1% augmented strain was 4,6 mm and maximum crack length was 2 mm.

2.2.1.2 Fortum case

In the Fortum case, the welding current was 250 A, voltage was 12,5 V, welding speed was 12 cm/min, heat input was 9,4 kJ/cm, welding length was 55 mm and bending speed was 16 mm/s. Bending was done so that tension was in the weld surface side. Figure 2.39 presents the test piece after the Varestraint test. Augmented strain was 4%.

Figure 2.39. Test piece F1 after Varestraint test. Augmented strain was 4%.

The test was repeated with the same parameters. As seen in Figure 2.39 and also in optical microscopy examination, no cracks were observed in these specimens. It was decided that no further tests were necessary to show the low susceptibility to hot cracking of these materials.

2.2.1.3 Mock-up TV case (TV)

In the mock-up TV case, the welding current was 150 A, voltage was 10,5 V, welding speed was 12 cm/min, heat input was 4,7 kJ/cm, welding length was 45 mm and bending speed was 16 mm/s. Bending was done so that tension was in the weld root side. Figure 2.40 presents the test piece after Varestraint testing utilizing an augmented strain of 4%.

Figure 2.40. Test piece TV after Varestraint test. Augmented strain was 4%.

In Figure 2.41 is the surface of the test piece with hot cracks after Varestraint testing utilizing an augmented strain of 4%.

Figure 2.41. Surface of the test piece TV with hot cracks after Varestraint test. Augmented strain was 4%.

In Figures 2.42 and 2.43 are presented measured crack lengths from the area shown in Figure 2.41 with magnification of 25x and augmented strain of 4%.

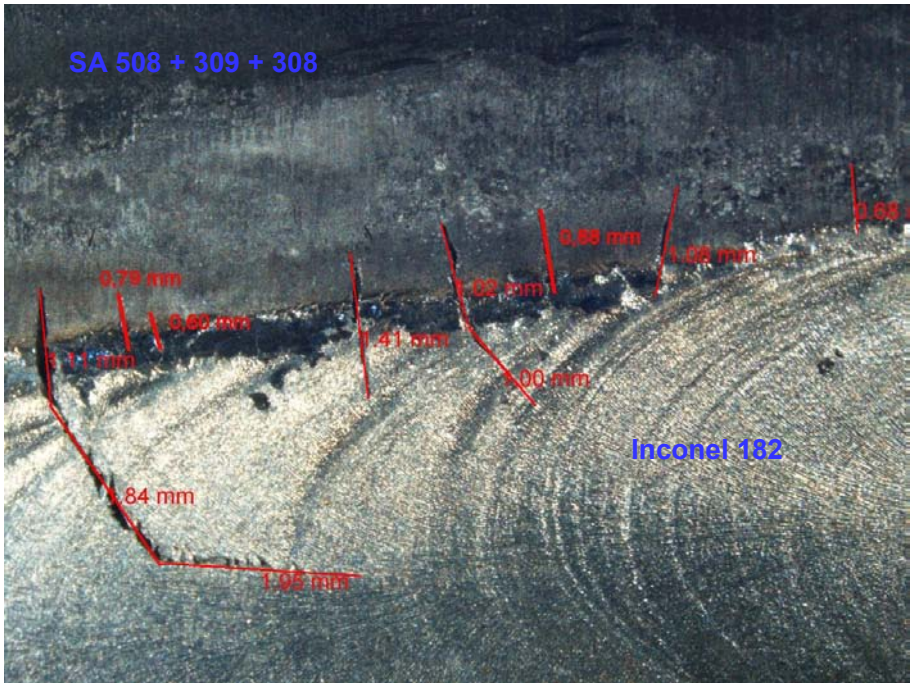

Figure 2.42. Measured crack lengths in TV test piece with magnification of 25x. Augmented strain was 4%.

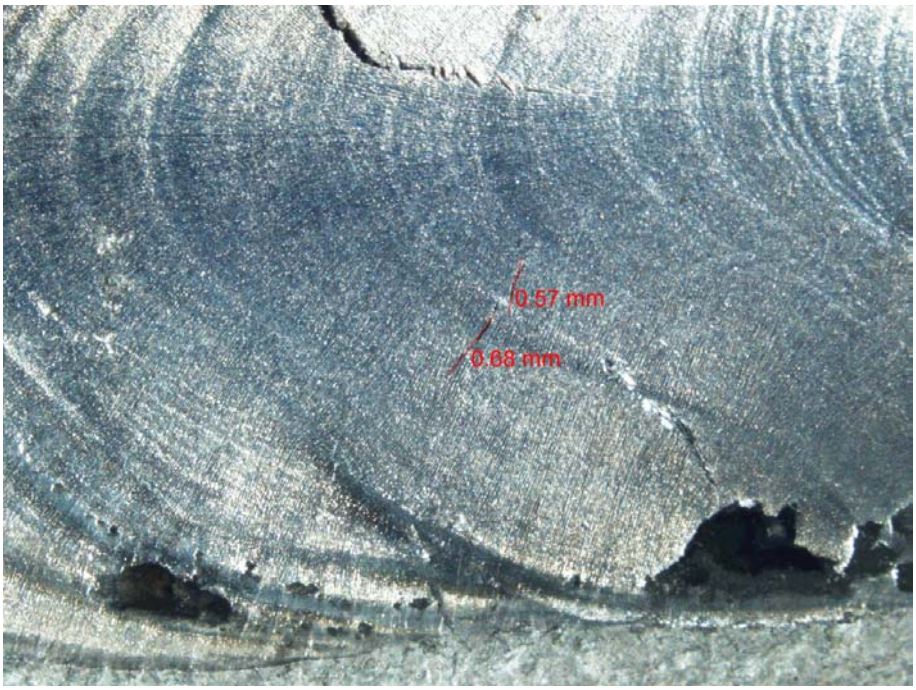

Figure 2.43. Measured crack lengths in TV test piece with magnification of 25x. Augmented strain was 4%.

Total crack length (TCL) of the mock-up TV case Varestraint test made with 4% augmented strain was 13,6 mm and maximum crack length was 4,9 mm.

In Figure 2.44 is the surface of the TV test piece with hot cracks after Varestraint testing utilizing an augmented strain of 3%.

Figure 2.44. Surface of the TV test piece with hot cracks after Varestraint test. Augmented strain was 3%.

In Figures 2.45 and 2.46 are presented measured crack lengths in TV specimens from the area shown in Figure 2.44 with magnification of 25x and augmented strain of 3%.

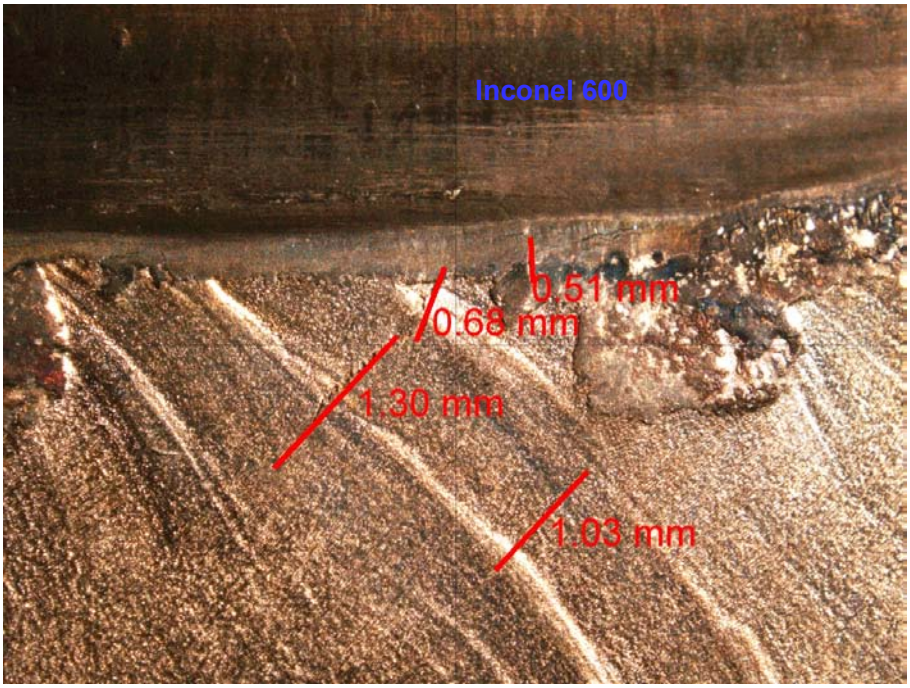

Figure 2.45. Measured crack lengths in TV test piece with magnification of 25x. Augmented strain was 3%.

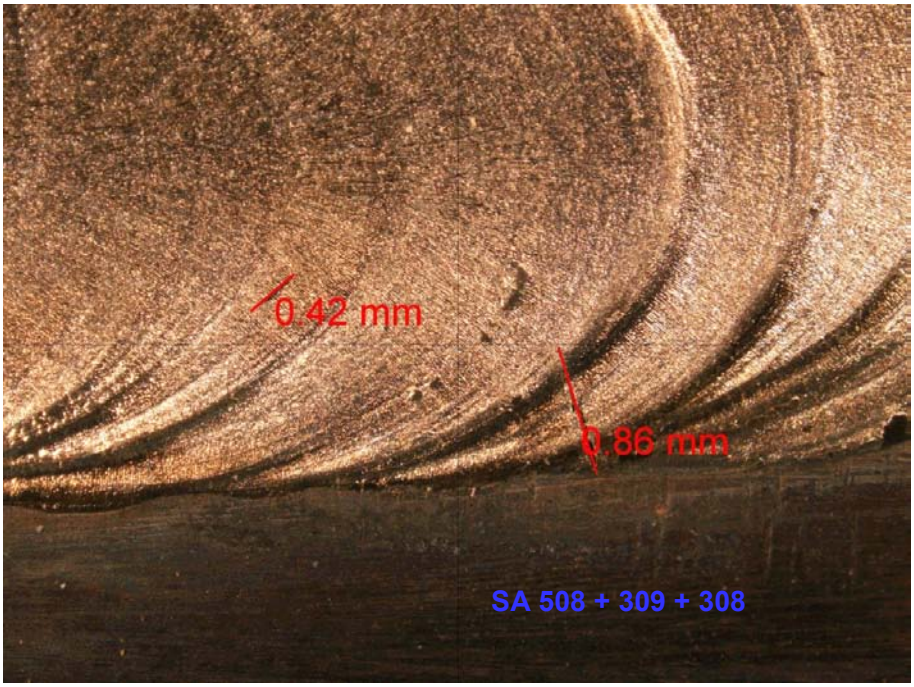

Figure 2.46. Measured crack lengths in TV test piece with magnification of 25x. Augmented strain was 3%.

Total crack length (TCL) of the mock-up TV case Varestraint test with 3% augmented strain was 4,8 mm and maximum crack length was 1,3 mm.

In the Varestraint test made for TV specimen using 2% augmented strain, only short crack was observed, as shown in Figure 2.47.

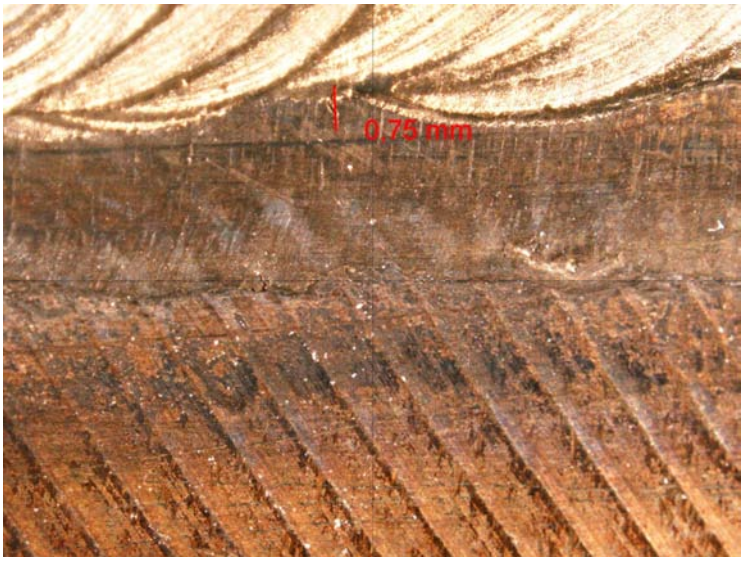

Figure 2.47. Measured crack length in TV test piece with magnification of 25x and augmented strain of 2%.

Total crack length (TCL) of the mock-up TV case Varestraint test with 2% augmented strain was 0,75 mm and maximum crack length was 0,75 mm.

2.2.1.4 Mock-up 1 case (TU1)

In the mock-up 1 case, the welding current was 150 A, voltage was 10,5 V, welding speed was 12 cm/min, heat input was 4,7 kJ/cm, welding length was 45 mm and bending speed was 16 mm/s. Bending was done so that tension was in the weld root side. In Figure 2.48 is the surface side of the mock-up 1 and in Figure 2.49 the root side.

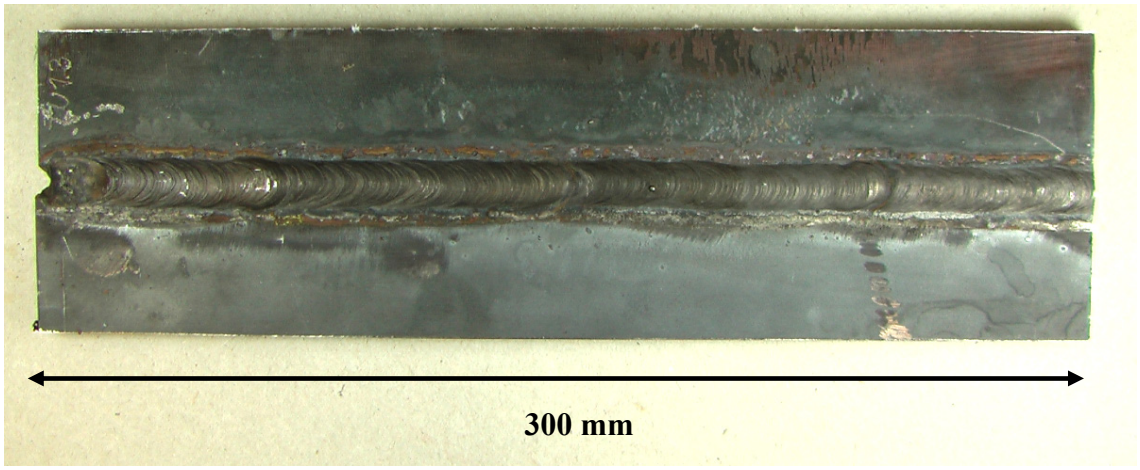

Figure 2.48. Surface side of the as welded mock-up 1.

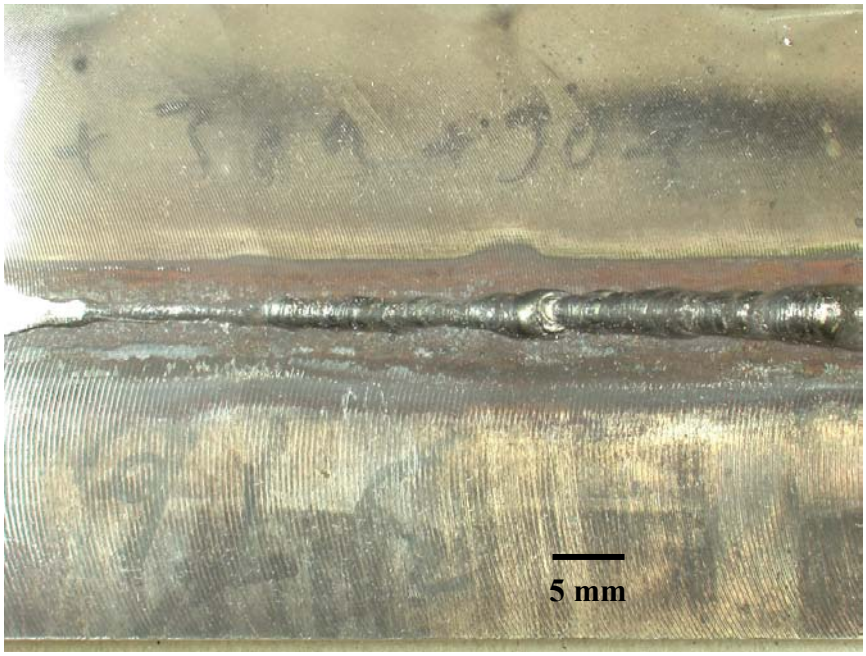

Figure 2.49. Root side of the as welded mock-up 1.

As seen in Figure 2.49, the penetration in the root side is not constant. To eliminate the effect of this on the hot cracking phenomena, the welding area (remelted) in Varestraint test was ground to the level of the surface of the base plate.

In Figure 2.50 is the surface of the test piece with hot cracks after Varestraint testing utilizing an augmented strain of 4%.

Figure 2.50. Root side surface of the test piece in mock-up 1 with hot cracks after Varestraint test. Augmented strain was 4%.

In Figures 2.51–2.54 are presented measured crack lengths from the area shown in Figure 2.50 with magnification of 25x and augmented strain of 4%.

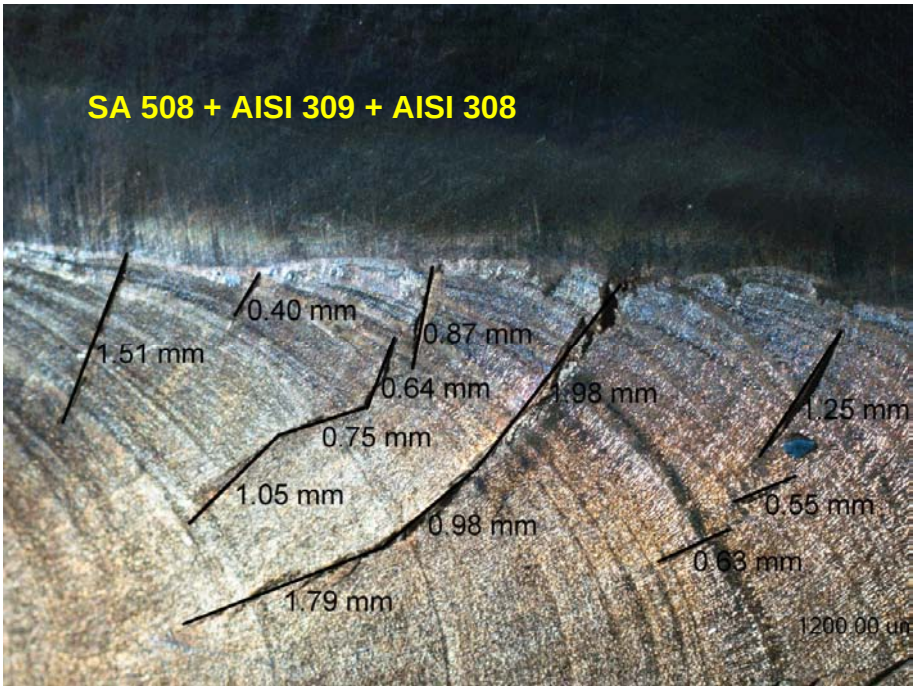

Figure 2.51. Measured crack lengths in mock-up 1 with magnification of 25x and augmented strain of 4%.

Figure 2.52. Measured crack lengths in mock-up 1 with magnification of 25x and augmented strain of 4%.

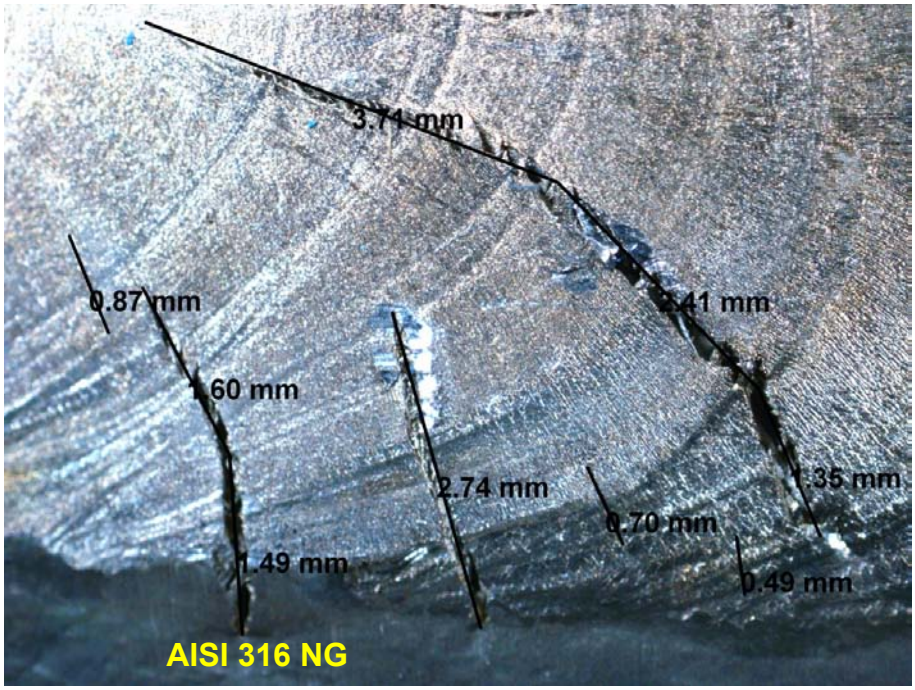

Figure 2.53. Measured crack lengths in mock-up 1 with magnification of 25x and augmented strain of 4%.

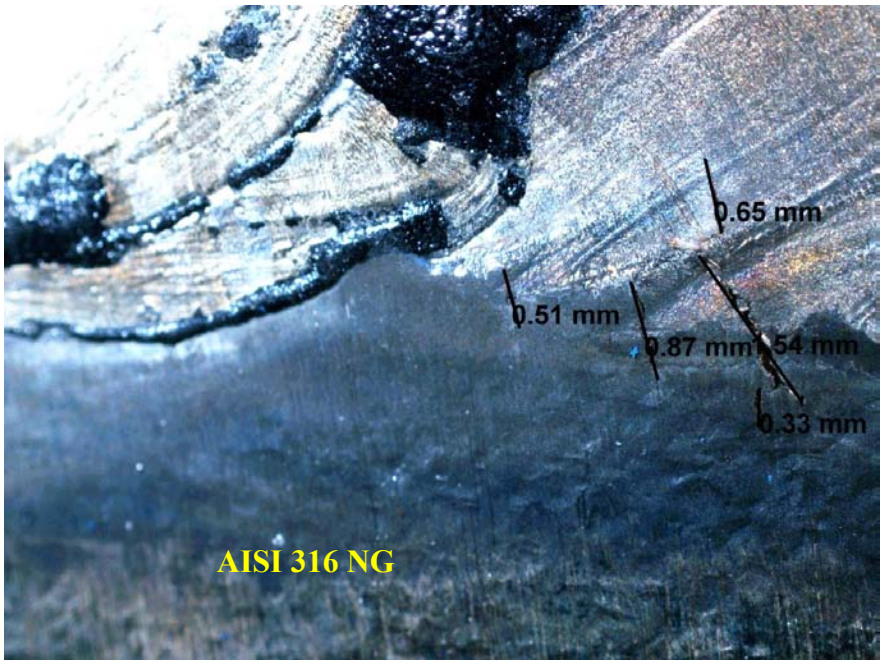

Figure 2.54. Measured crack lengths in mock-up 1 with magnification of 25x and augmented strain of 4%.

Total crack length (TCL) of the mock-up 1 Varestraint test with 4% augmented strain was 37,5 mm and maximum crack length was 7,5 mm.

In Figures 2.55 and 2.56 measured crack lengths with magnification of 25x and augmented strain of 3% are presented.

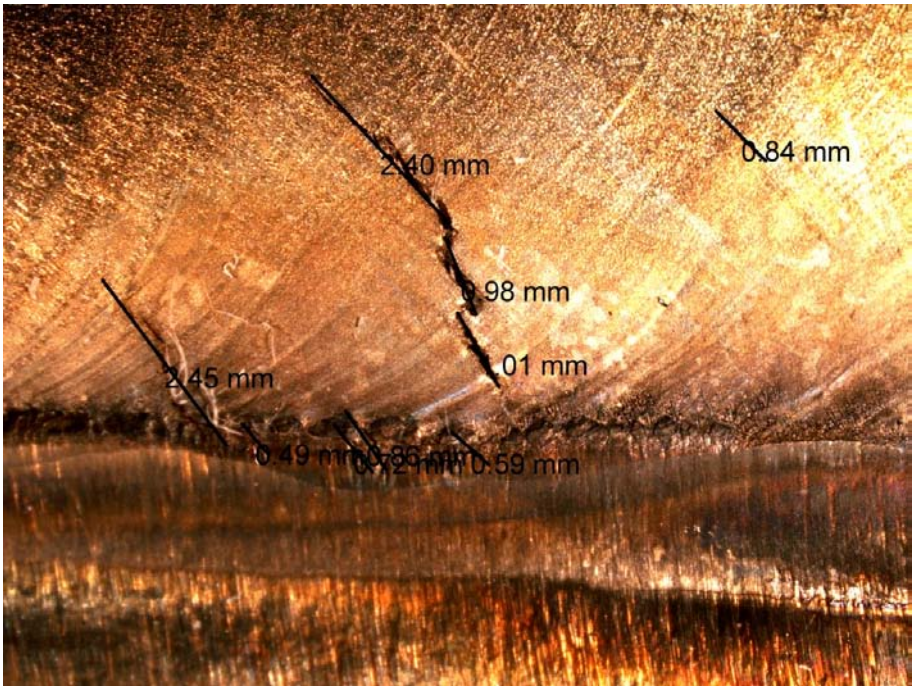

Figure 2.55. Measured crack lengths in mock-up 1 with magnification of 25x and augmented strain of 3%.

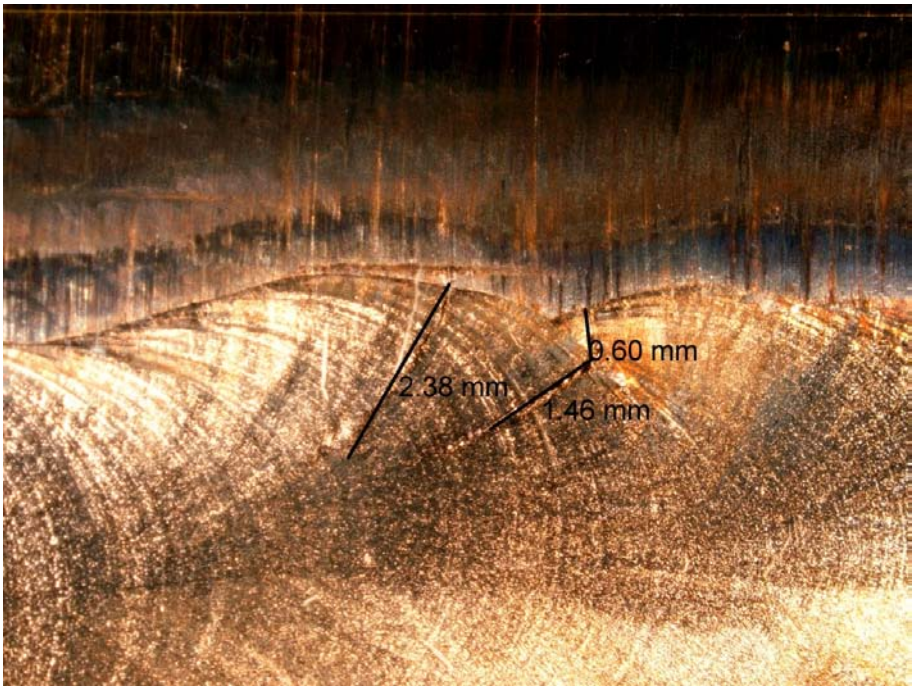

Figure 2.56. Measured crack lengths in mock-up 1 with magnification of 25x and augmented strain of 3%.

In Figure 2.57 measured crack lengths in mock-up 1 with magnification of 25x and augmented strain of 1% are presented.

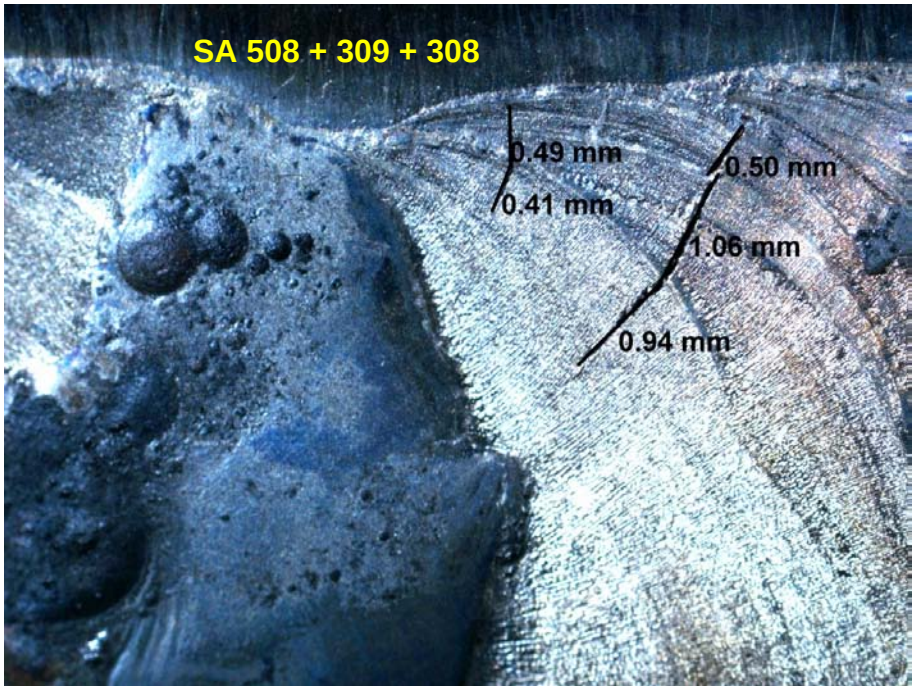

Figure 2.57. Measured crack lengths in mock-up 1 with magnification of 25x and augmented strain of 1%.

Total crack length (TCL) of the mock-up 1 Varestraint test with 1% augmented strain was 3,4 mm and maximum crack length was 2 mm.

Varestraint test was also done for mock-up 1 with augmented strain of 0,5%, but no hot cracks were observed.

2.2.1.5 Mock-up 2 case (TU2)

In the mock-up 2 case, the welding current was 150 A, voltage was 10,5 V, welding speed was 12 cm/min, heat input was 4,7 kJ/cm, welding length was 45 mm and bending speed was 16 mm/s. Bending was done so that tension was in the weld root side. In Figure 2.58 is presented Varestraint test specimen from the weld surface side before the test and in Figure 2.59 the same specimen from the root side.

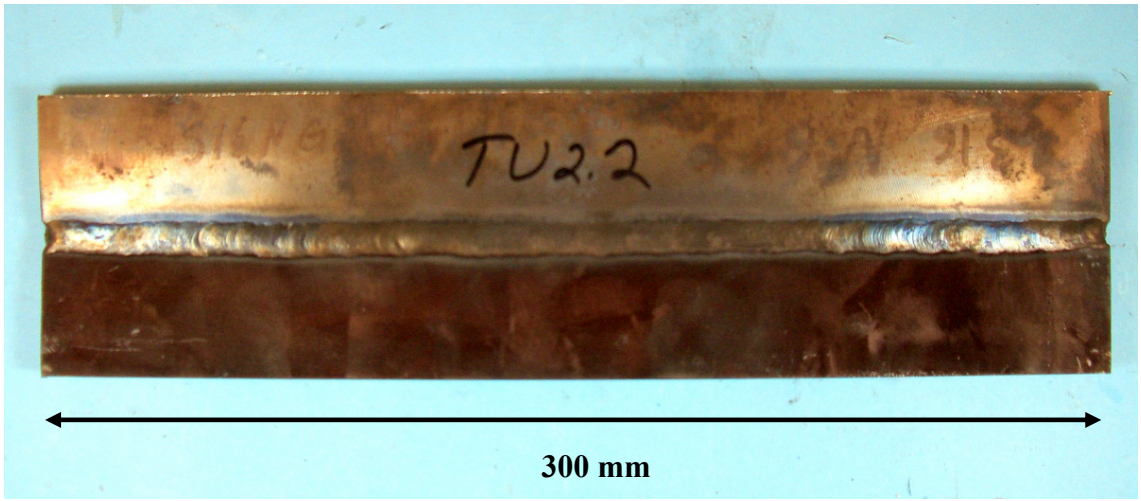

Figure 2.58. Varestraint test specimen mock-up 2 from the weld surface side before the test.

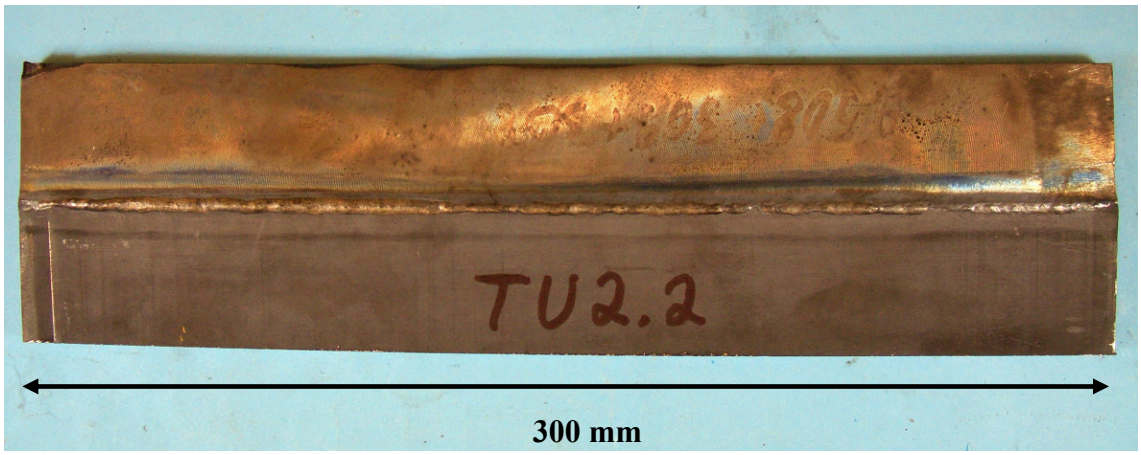

Figure 2.59. Varestraint test specimen mock-up 2 from the weld root side before the test.

In Figures 2.60 and 2.61 are presented measured crack lengths in mock-up 2 with magnification of 25x and augmented strain of 4%.

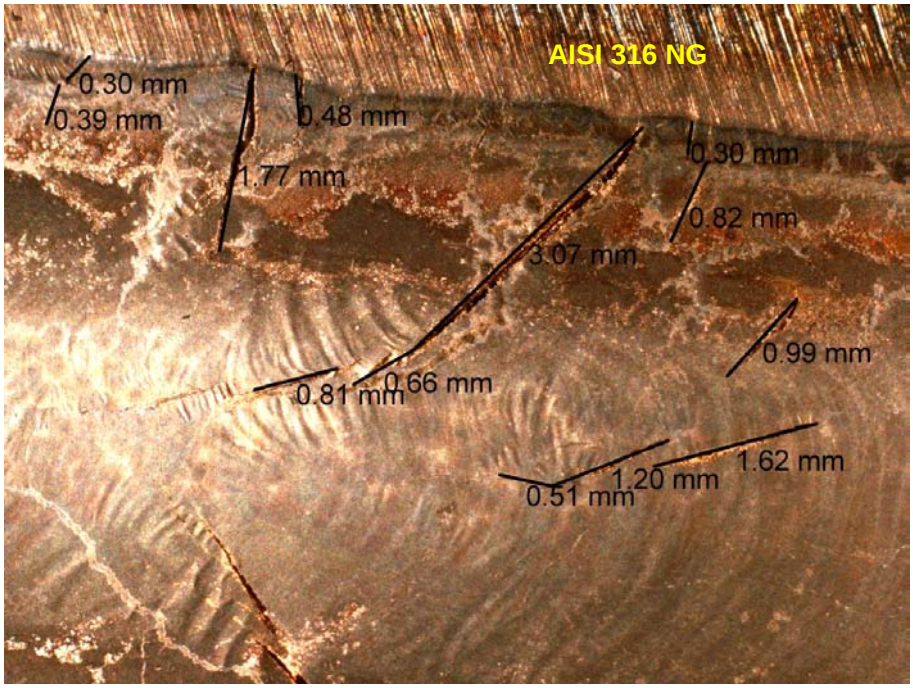

Figure 2.60. Measured crack lengths in mock-up 2 with magnification of 25x and augmented strain of 4%.

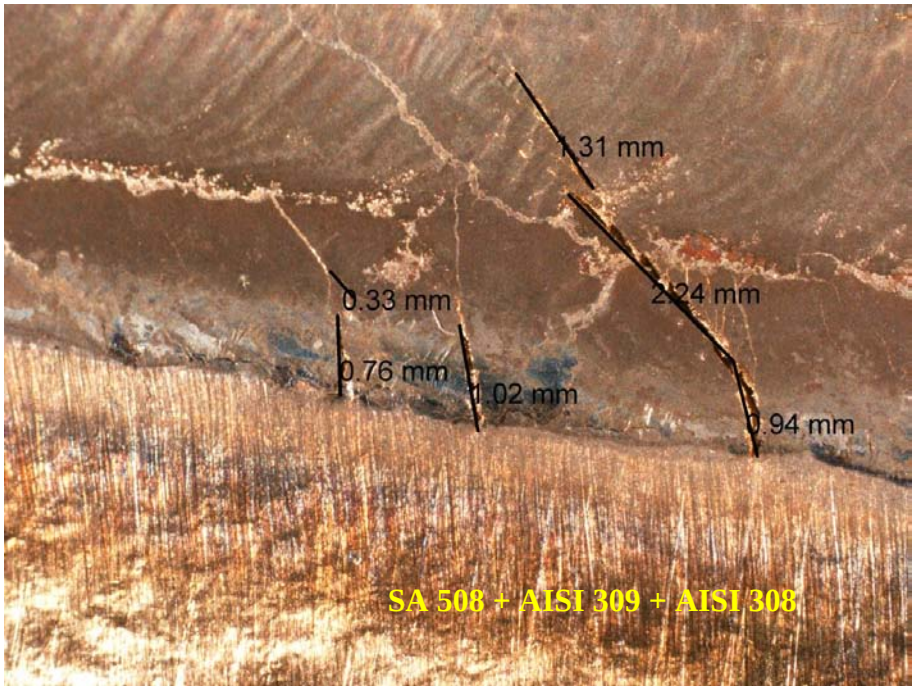

Figure 2.61. Measured crack lengths in mock-up 2 with magnification of 25x and augmented strain of 4%.

Total crack length (TCL) of the mock-up 2 Varestraint test with 4% augmented strain was 19,5 mm and maximum crack length was 3,7 mm.

In Figures 2.62 and 2.63 are presented measured crack lengths in mock-up 2 with magnification of 25x and augmented strain of 3%.

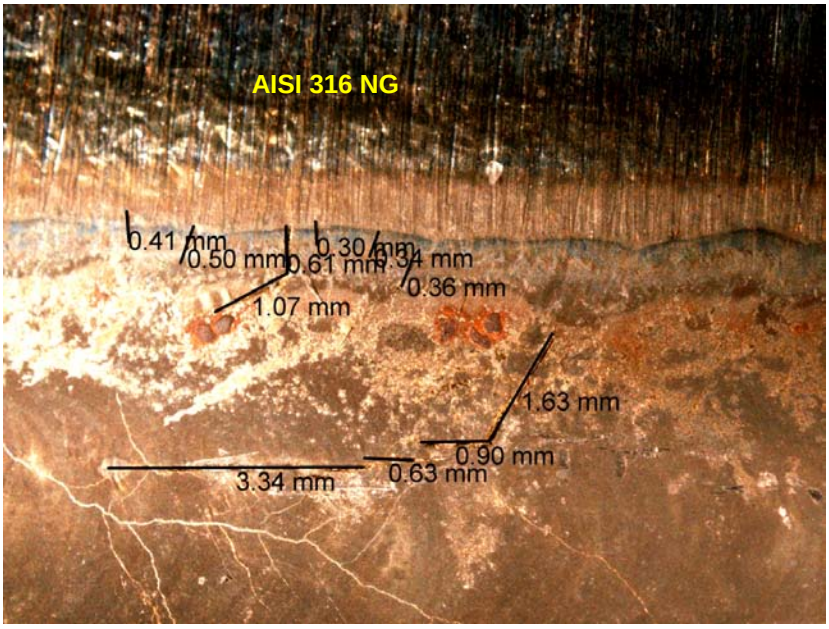

Figure 2.62. Measured crack lengths in mock-up 2 with magnification of 25x and augmented strain of 3%.

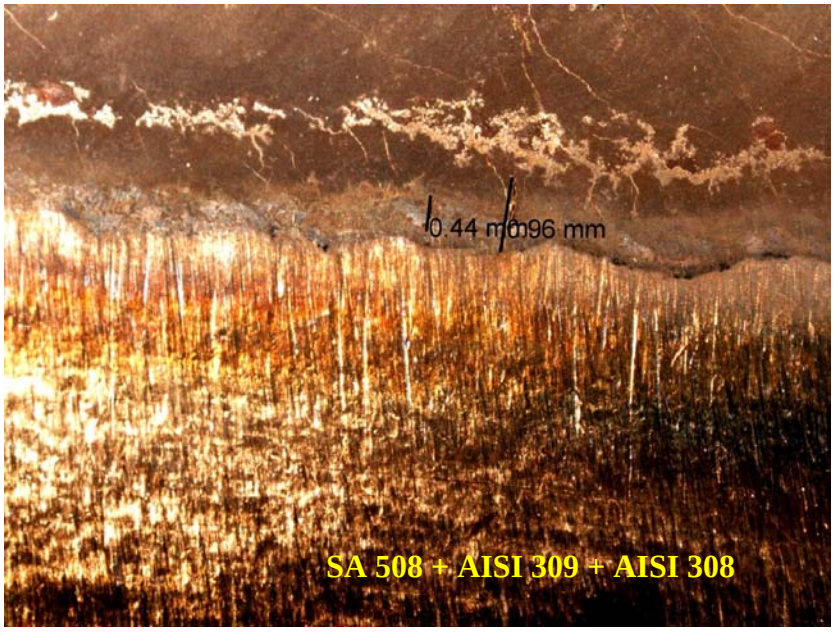

Figure 2.63. Measured crack lengths in mock-up 2 with magnification of 25x and augmented strain of 3%.

Total crack length (TCL) of the mock-up 2 Varestraint test with 3% augmented strain was 11,5 mm and maximum crack length was 3,3 mm.

In Figure 2.64 is presented mock-up 2 Varestraint test specimen from the weld root side after the testing utilizing an augmented strain of 1%.

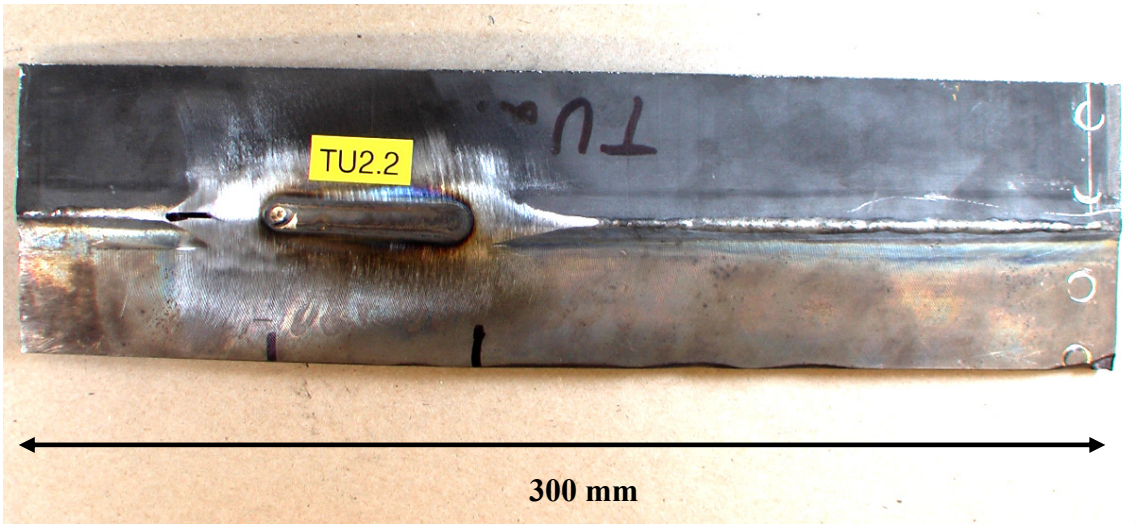

Figure 2.64. Varestraint test specimen mock-up 2 from the weld root side after the test. Augmented strain was 1%.

In Figure 2.65 are presented measured crack lengths in mock-up 2 with magnification of 25x and augmented strain of 1%.

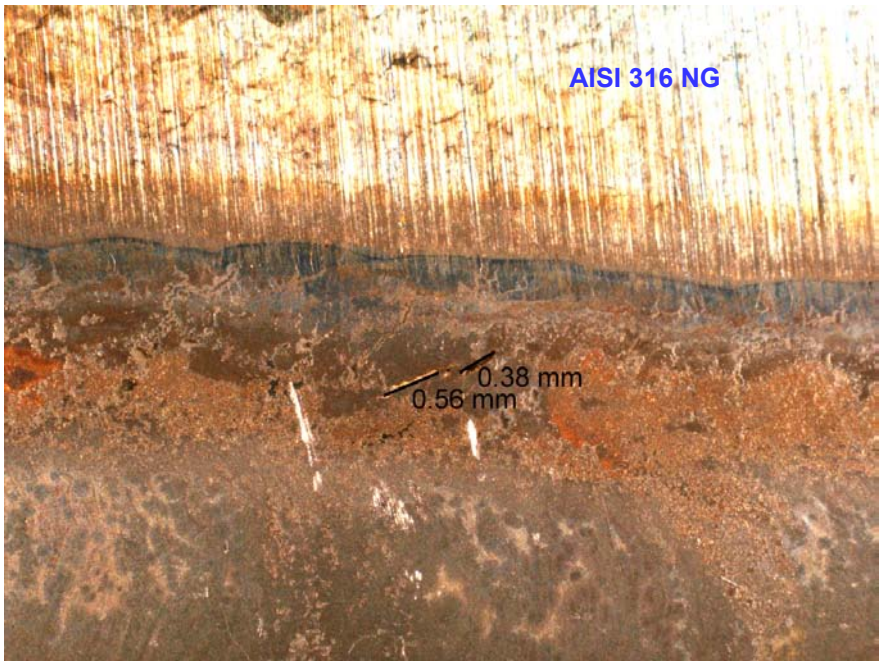

Figure 2.65. Measured crack lengths in mock-up 2 with magnification of 25x and augmented strain of 1%.

Total crack length (TCL) of the mock-up 2 Varestraint test with 1% augmented strain was 0,9 mm and maximum crack length was 0,6 mm.

2.2.1.6 Mock-up 3 case (TU3)

In the mock-up 3 case, the welding current was 150 A, voltage was 10,5 V, welding speed was 12 cm/min, heat input was 4,7 kJ/cm, welding length was 45 mm and bending speed was 16 mm/s. Bending was done so that tension was in the weld root side. In Figures 2.66 and 2.67 are presented measured crack lengths in mock-up 3 with magnification of 25x and augmented strain of 4%.

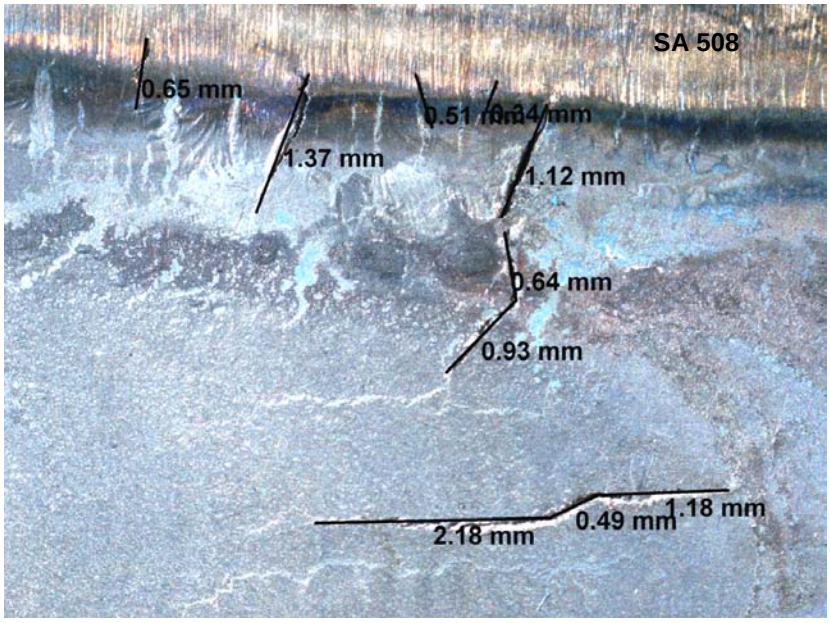

Figure 2.66. Measured crack lengths in mock-up 3 with magnification of 25x and augmented strain of 4%.

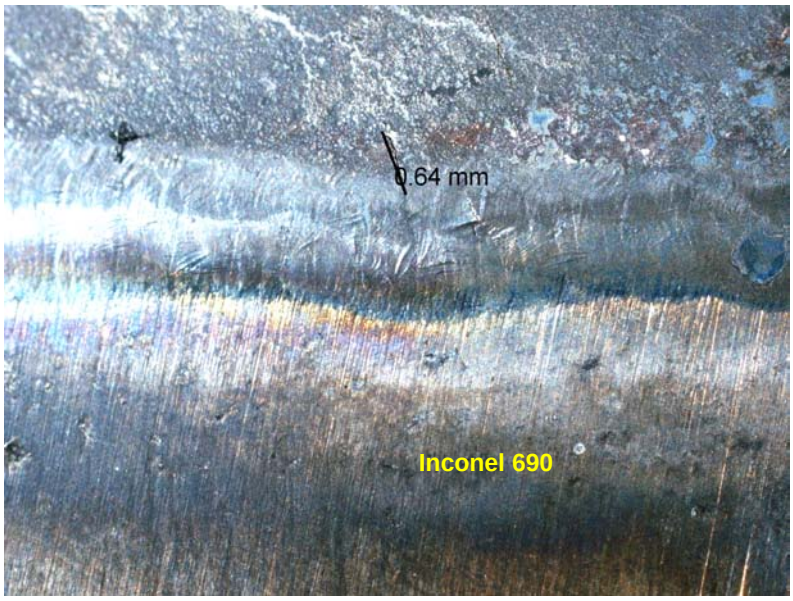

Figure 2.67. Measured crack length in mock-up 3 with magnification of 25x and augmented strain of 4%.

Total crack length (TCL) of the mock-up 3 Varestraint test with 4% augmented strain was 9,8 mm and maximum crack length was 3,9 mm.

In Figure 2.68 is presented measured crack lengths in mock-up 3 with magnification of 25x and augmented strain of 3%.

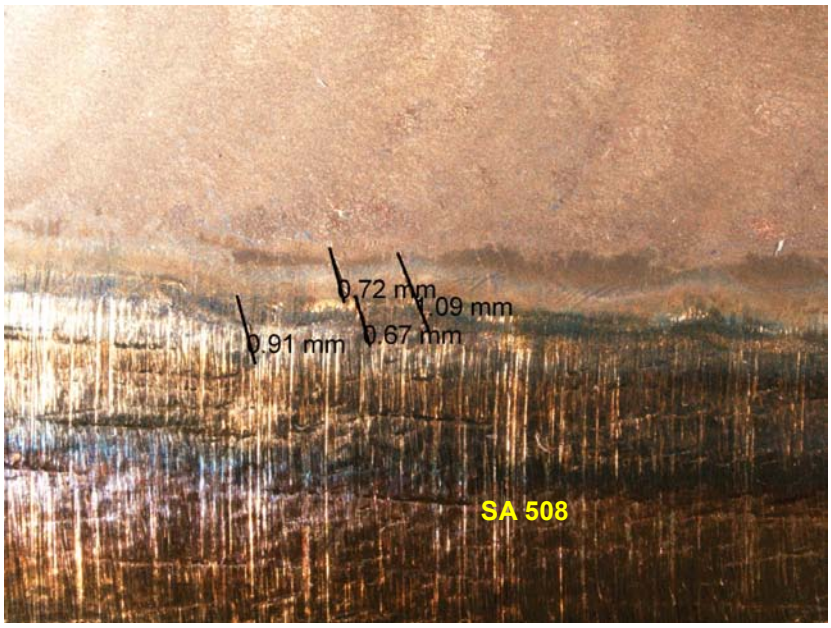

Figure 2.68. Measured crack lengths in mock-up 3 with magnification of 25x and augmented strain of 3%.

Total crack length (TCL) of the mock-up 3 Varestraint test with 3% augmented strain was 3,4 mm and maximum crack length was 1,1 mm.

In Figure 2.69 is presented measured crack length in mock-up 3 with magnification of 25x and augmented strain of 1%.

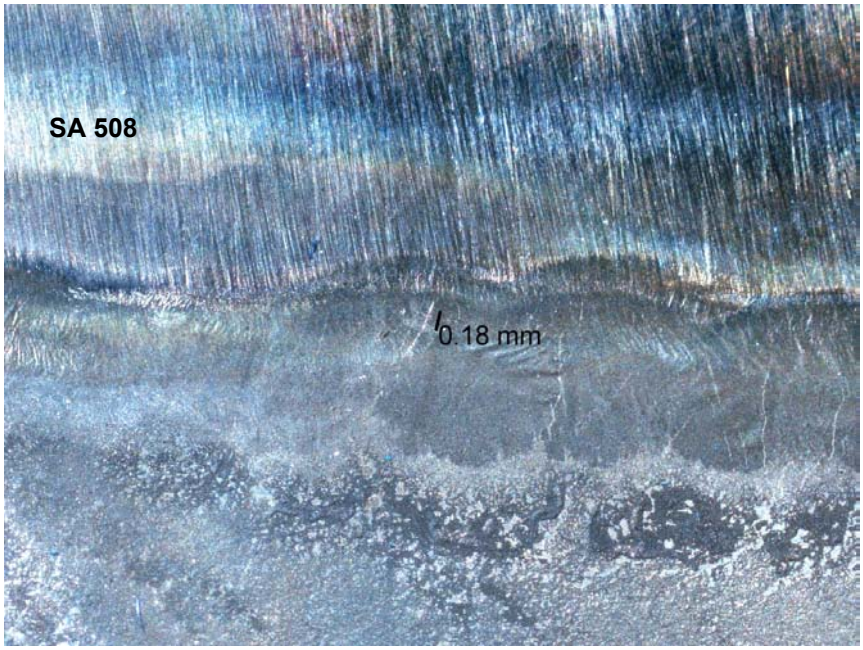

Figure 2.69. Measured crack length in mock-up 3 with magnification of 25x and augmented strain of 1%.

Total crack length (TCL) of the mock-up 3 Varestraint test with 1% augmented strain was 0,2 mm and maximum crack length was 0,2 mm.

2.2.1.7 Summary of the Varestraint tests

In Figure 2.70 is presented total crack lengths of Neste Oil, mock-up TV and mock-ups 1, 2 and 3 and in Figure 2.71 maximum crack lengths with augmented strains of 0%, 0,5%, 1%, 2%, 3% and 4%, respectively. In legend box markings are as follows: case, tension side, filler metal.

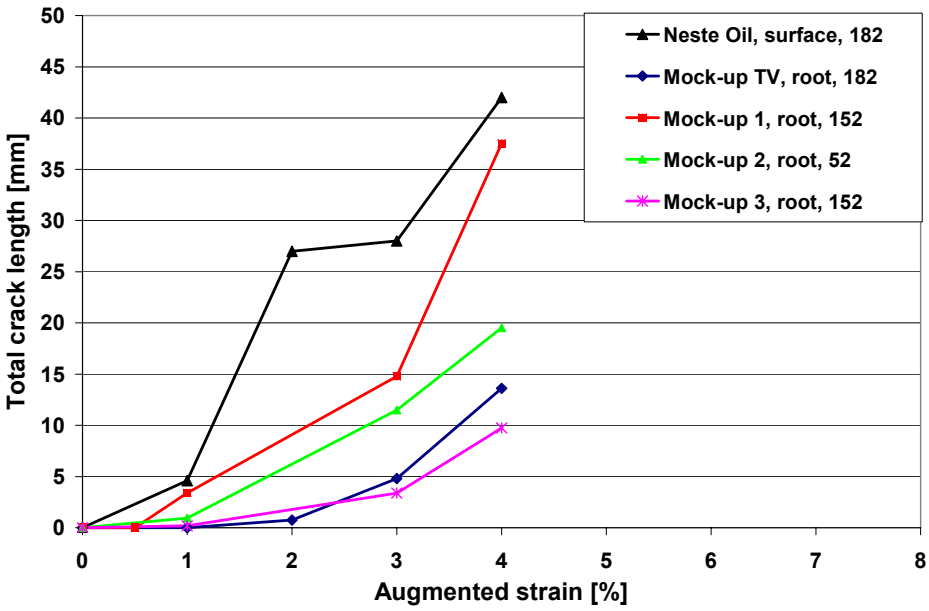

Figure 2.70. Total crack lengths of Neste Oil, mock-up TV and mock-ups 1, 2 and 3.

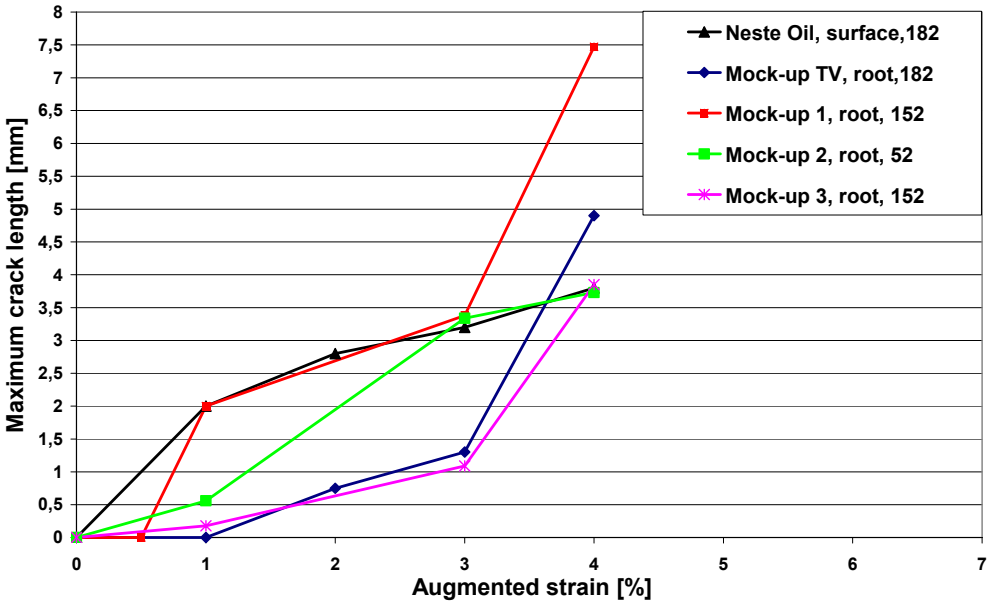

Figure 2.71. Maximum crack lengths of Neste Oil, mock-up TV and mock-ups 1, 2 and 3.

Table 2.2 presents a summary of the welding parameters used in the Varestraint tests.

Table 2.2. Summary of the welding parameters used in Varestraint tests.

	Current [A]	Voltage [V]	Welding speed [cm/min]	Heat input [kJ/cm]
Neste Oil (Inconel 182)	**250**	**12,5**	**12**	**9,4**
Fortum	**250**	**12,5**	**12**	**9,4**
Mock-up TV (Inconel 182)	**150**	**10,5**	**12**	**4,7**
Mock-up 1 (Inconel 152)	**150**	**10,5**	**12**	**4,7**
Mock-up 2 (Inconel 52)	**150**	**10,5**	**12**	**4,7**
Mock-up 3 (Inconel 152)	**150**	**10,5**	**12**	**4,7**

2.3 Varestraint tests of pure weld metals

Figure 2.72 presents the test piece for Varestraint tests of pure weld metals. Base material was AISI 304 plate into which a 20 mm wide, 60 mm long and 4 mm deep groove was machined.

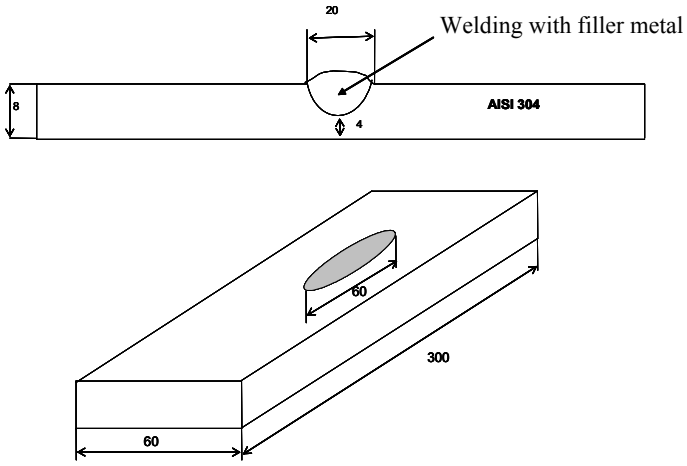

Figure 2.72. Test piece for Varestraint tests of pure weld metals.

After machining the test piece was firmly fastened to avoid distortion while welding the groove with the filler metal. The surface of the weld was then ground to the level of the base metal so that the surface quality was equal in every Varestraint test. Filler metals (supplier in brackets) used in the tests were:

- Inconel 182 (Esab OK 92.26)
- Inconel 82 (Esab Tigrod 19.85)
- Inconel 152 (Special Metals)

- Inconel 152M (Special Metals)
- Inconel 52 (Special Metals)
- Inconel 52M (Special Metals)
- Inconel 52MS (Special Metals).

Table 2.3 presents a summary of the welding parameters used in the pure weld metal Varestraint tests.

Table 2.3. summary of the welding parameters used in the pure weld metal Varestraint tests.

	Current [A]	Voltage [V]	Welding speed [cm/min]	Heat input [kJ/cm]
Inconel 182	**150**	**10,5**	**12**	**4,7**
Inconel 82	**150**	**10,5**	**12**	**4,7**
Inconel 82	**250**	**12,5**	**12**	**9,4**
Inconel 152	**150**	**10,5**	**12**	**4,7**
Inconel 152M	**150**	**10,5**	**12**	**4,7**
Inconel 52	**150**	**10,5**	**12**	**4,7**
Inconel 52M	**150**	**10,5**	**12**	**4,7**
Inconel 52MS	**150**	**10,5**	**12**	**4,7**

Figure 2.73 presents the weld pass sequence for the test specimen utilizing filler metal Inconel 82.

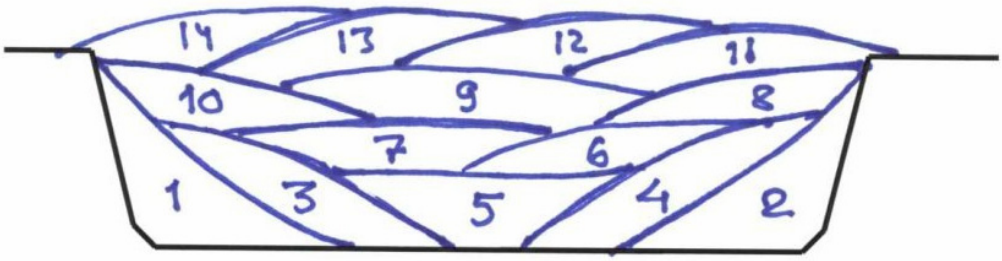

Figure 2.73. Weld pass sequence of the test specimen welded with filler metal Inconel 82.

2.3.1 Results of Varestraint tests of pure weld metals

Welding current in all pure weld metals Varestraint tests (except one additional Inconel 82 specimen) was 150 A, voltage was 10,5 V, welding speed was 12 cm/min, heat input was 4,7 kJ/cm, welding length was 45 mm, bending speed was 16 mm/s and augmented

strain 4%. For some of the filler metals the test was repeated. A summary of all tests is presented in Table 2.3.

Figures 2.74 and 2.75 present the test specimen of Inconel 182 weld after testing with 4% augmented strain. Measured total crack length (TCL) was 19,3 mm.

Figure 2.74. Inconel 182 weld after testing.

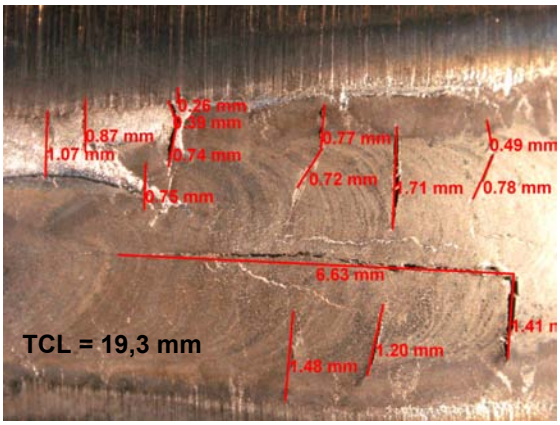

Figure 2.75. Inconel 182 weld after testing. Total crack length (TCL) = 19,3 mm.

Figure 2.76 presents the test specimen of Inconel 82 weld after testing with 4% augmented strain. No cracks were observed.

Figure 2.76. Test specimen of Inconel 82 weld after testing with 4% augmented strain.

Figures 2.77 and 2.78 present the test specimen of Inconel 152 weld after testing with 4% augmented strain. Total crack length (TCL) was 19,3 mm.

Figure 2.77. Inconel 152 weld after testing.

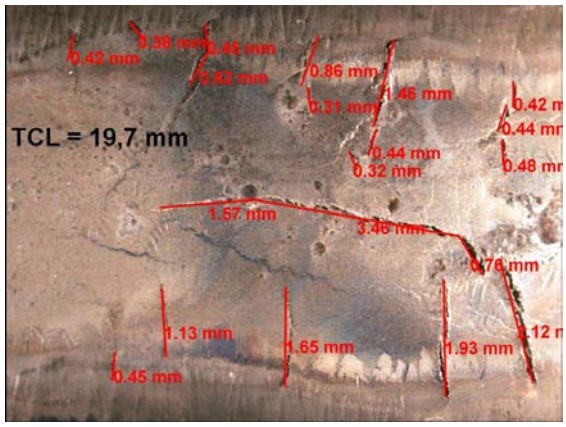

Figure 2.78. Inconel 152 weld after testing. Total crack length (TCL) = 19,7 mm.

Figures 2.79 and 2.80 present the test specimen of Inconel 152M weld after testing with 4% augmented strain. Total crack length (TCL) was 8,1 mm.

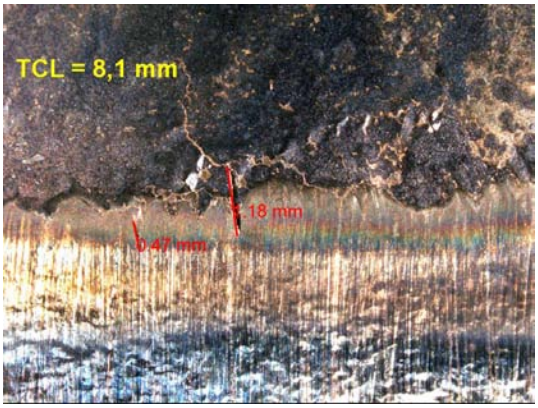

Figure 2.79. Inconel 152M weld after testing.

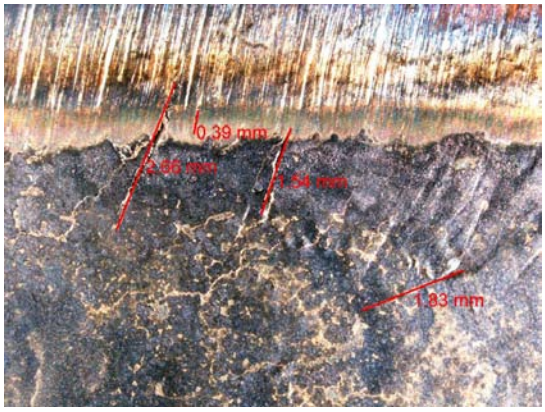

Figure 2.80. Inconel 152M weld after testing. Total crack length (TCL) = 8,1 mm.

Figure 2.81 presents the test specimen of Inconel 52 weld after testing with 4% augmented strain. No cracks were observed.

Figure 2.81. Test specimen of Inconel 52 weld after testing with 4% augmented strain.

Figures 2.82 and 2.83 present the test specimen of Inconel 52M weld after testing with 4% augmented strain. Total crack length (TCL) was 3,1 mm.

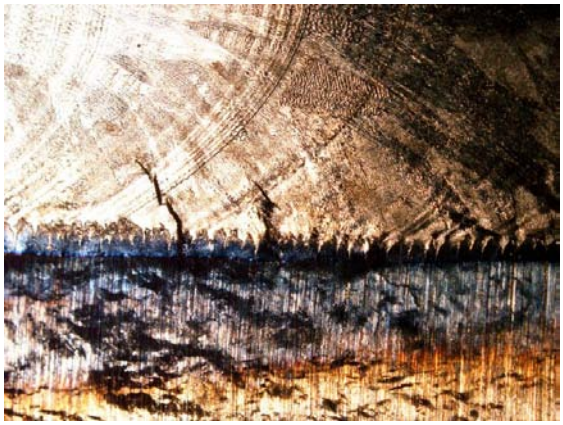

Figure 2.82. Inconel 52M weld after testing.

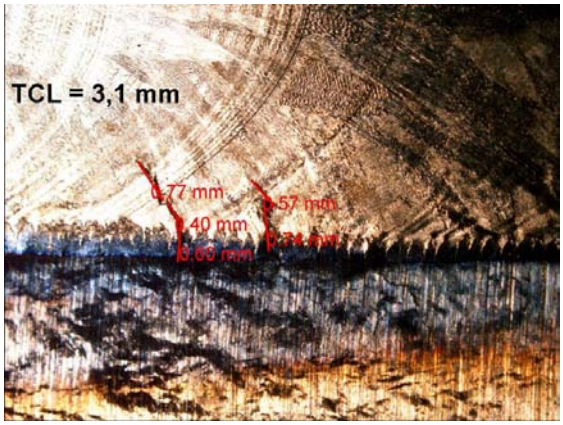

Figure 2.83. Inconel 52M weld after testing. Total crack length (TCL) = 3,1 mm.

Figure 2.84 presents the test specimen of Inconel 52MS weld after testing with 4% augmented strain. No cracks were observed in either the first or second test.

Figure 2.84. Test specimen of Inconel 52MS weld after testing with 4% augmented strain.

Table 2.4 presents summary of all Varestraint tests (augmented strain 4%) made for pure Inconel weld metals.

Table 2.4. Summary of all Varestraint tests (augmented strain was 4%) made for pure Inconel weld metals.

Inconel 182 (Q=4,7 kJ/cm)	**TCL = 19,3 mm / 2nd test -> cracks**
Inconel 82 (Q=4,7 kJ/cm)	**no cracks / 2nd test -> no cracks**
Inconel 82 (Q=9,4 kJ/cm)	**TCL = 32,9 mm**
Inconel 152 (Q=4,7 kJ/cm)	**TCL = 19,7 mm / 2nd test -> cracks**
Inconel 152M (Q=4,7 kJ/cm)	**TCL = 8,1 mm**
Inconel 52 (Q=4,7 kJ/cm)	**no cracks / 2nd test -> no cracks**
Inconel 52M (Q=4,7 kJ/cm)	**TCL = 3,1 mm / 2nd test -> no cracks**
Inconel 52MS (Q=4,7 kJ/cm)	**no cracks / 2nd test -> no cracks**

Weld metal composition was determined by optical emission spectrometery for four welds in order to confirm how "pure" the weld metals were, and if there was excessive dilution between the weld and base materials in the weld centreline region. Analysis was made from the weld surface on the weld centreline. The diameter of analysis area was about 8 mm. Figure 2.85 presents the test pieces used for the analysis.

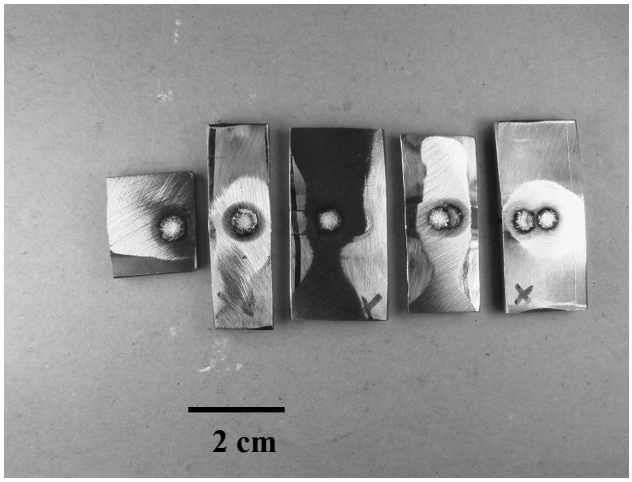

Figure 2.85. Test pieces used for optical emission spectrometer chemical analysis.

In Table 2.5 is presented comparison between optical emission spectrometer analyses and the materials certificate values. The largest differences between the measured data and the certificate values are highlighted by red text.

Table 2.5. Comparison between optical emission spectrometer analyses and certificate values.

	C	Si	Mn	P	S	Cr	Mo	Ni	Nb	Ti	Fe	Al	Cu
TV case (Inconel 182) %	0,03	0,8	6,5	0,01	0,003	15,7		67,5	1,8	0,1	6,7		< 0,01
Analysed %	0,04	0,47	7	0,01	0,01	16,4	0,05	67,49	1,9	0,01	6,6	0,01	0,01
Difference %	**0,01**	**-0,33**	**0,50**	**0,00**	**0,01**	**0,70**	**0,05**	**-0,01**	**0,10**	**-0,09**	**-0,10**	**0,01**	
Inconel 182 (OK 92.26) %	0,03	0,8	7	0,01	0,007	16,5		68	1,8	0,1	5,7		0,02
Analysed %	0,04	0,53	6,7	0,01	0,01	16,2	0,06	61,02	1,6	0,01	13,8	0,01	0,01
Difference %	**0,01**	**-0,27**	**-0,30**	**0,00**	**0,00**	**-0,30**	**0,06**	**-6,98**	**-0,20**	**-0,09**	**8,10**	**0,01**	
Inconel 82 (OK Tigrod 19.85) %	0,039	0,03	2,98	0,001	0,004	19,94		72,6	Nb+Ta 2,47	0,34	1		0,01
Analysed %	0,03	0,14	3,6	0,01	0,01	20	0,05	67,57	2,5	0,23	5,8	0,05	0,01
Difference %	**-0,01**	**0,11**	**0,62**	**0,01**	**0,01**	**0,06**	**0,05**	**-5,03**	**0,03**	**-0,11**	**4,80**	**0,05**	**0,00**
Inconel 152 %	0,048	0,41	3,48	0,003	0,003	28,74	0,01	55,2	Nb+Ta 1,54	0,09	10,39	0,06	<0,01
Analysed %	0,03	0,32	5	0,01	0,01	29,1	0,06	50,75	2	0,04	12,6	0,07	0,01
Difference %	**-0,02**	**-0,09**	**1,52**	**0,01**	**0,01**	**0,36**	**0,05**	**-4,45**	**0,46**	**-0,05**	**2,21**	**0,01**	
Inconel 52 %	0,03	0,13	0,24	<0,001	<0,001	29,2	0,03	59,28	Nb+Ta <0,02	0,51	9,8	0,72	0,04
Analysed %	0,04	0,22	0,51	0,01	0,01	28,2	0,03	55,47	0,04	0,46	14,3	0,7	0,01
Difference %	**0,01**	**0,09**	**0,27**			**-1,00**	**0,00**	**-3,81**		**-0,05**	**4,50**	**-0,02**	**-0,03**

2.4 Residual stress measurements

An important part in the study of the dissimilar metal welds is the measurement of the residual stresses of the welds. It is generally known that the residual stresses in the weldment vary from high tension to compression, depending on the position in the weldment. With conventional methods only discrete points can be measured, but with the Contour method a complete residual stress distribution can be obtained over the whole cross-section measured.

2.4.1 Contour method

The Contour method was developed by Prime (2001) as a powerful tool for mapping the whole stress distribution across an arbitrary section of a part. The method is based on exact sectioning of the part and accurate measuring of the topology of the obtained surface. The 3D-map is used as input data for stress analysis by some finite element (FE) code. A schematic presentation of the steps included in the Contour method is shown graphically in Figure 2.86. A great advantage with the Contour method over the traditional relaxation methods is that it can determine stresses directly from the data without a tedious inversion technique.

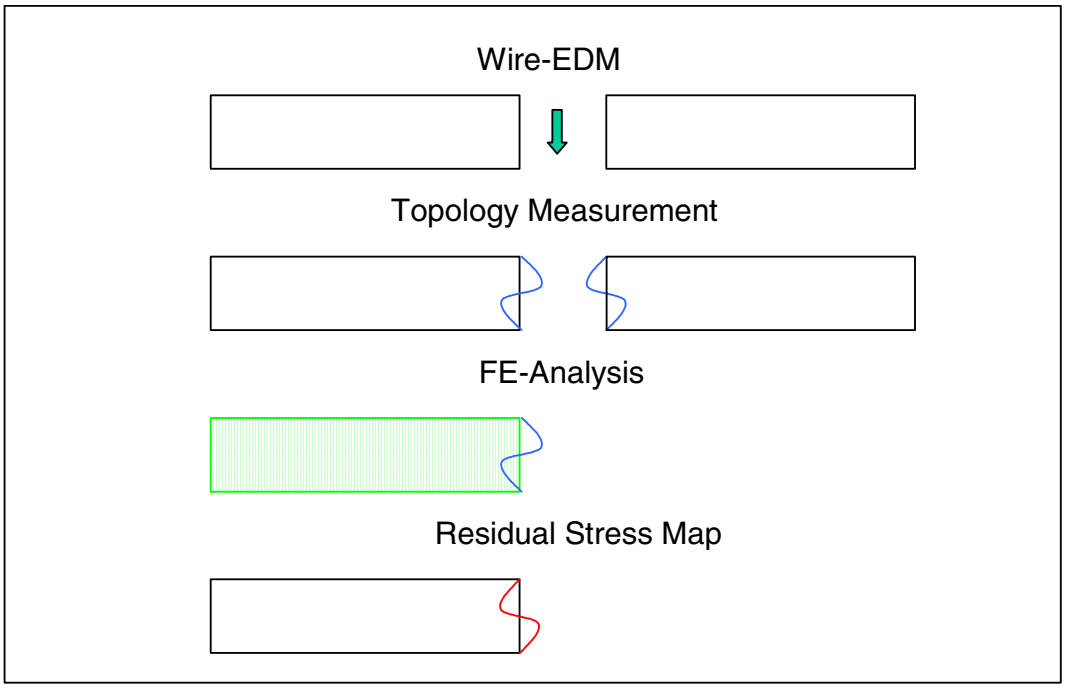

Figure 2.86. The flow-chart for residual stress determination by Contour method.

2.4.2 Measurements and FE-analyses

The residual stress specimen was cut from one of the plates fabricated for the Varestraint tests. The selected plate represented a weld configuration typical for dissimilar metal welds in oil refinery applications, and had been manufactured according to the specifications presented in Chapter 2.1.1. The specimen, having a length of 40 mm, was taken from the end that had been clamped during the Varestraint test, as shown in Figure 2.87. When cutting the plate, the weld longitudinal stresses across the whole surface can be determined.

For accurate utilization of the contour method, it is important that sectioning of the part results in a precisely straight cut and does not interfere with the already cut surfaces.

The best suited method for this is probably wire electric discharge machining (WEDM). In the preparation for sectioning, the specimen was fixed to prevent deformation during machining by WEDM. The cutting procedure is illustrated in Figure 2.87. First, an EDM hole was drilled through the specimen at the position indicated by the broken green line. Then, the EDM cut was made in the direction shown by the red broken line. Finally, the last part of the section, shown by the broken blue line, was cut. The specimen was cut with an AGIECUT 100D WEDM machine using a 100 µm diameter brass wire. Settings normally used for better precision and finer surface finish were used because they also minimize surface distortion.

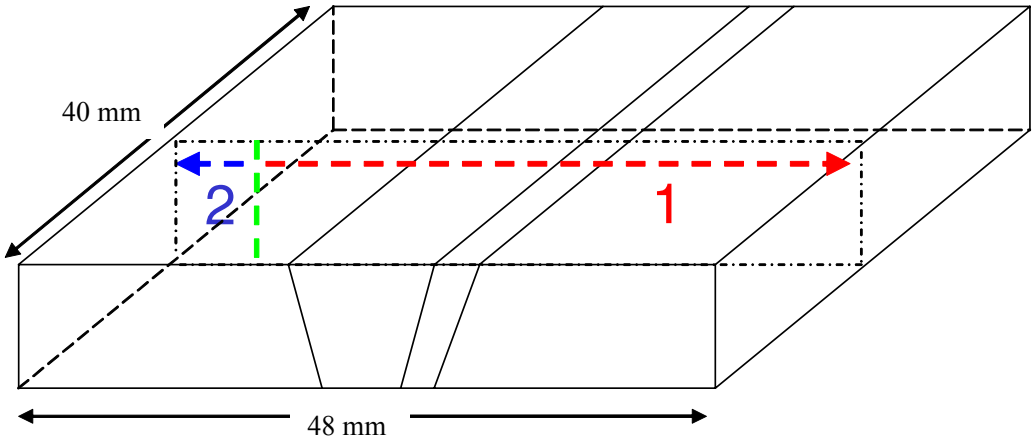

Figure 2.87. The cutting scheme perpendicular to the welding direction.

Both of the obtained surfaces from each half of the original specimen were subjected to topology measurements. The surface topology was measured by a coordinate measurement machine (CMM), which registers the surface through mechanical contact via touch trigger probe. Due to the finite radius of the probe tip, surface roughness is partially filtered out from the measured contour.

The FE-analysis was performed using the Elmer freeware code. The material model was linear elastic assuming isotropic behavior. The shape of the final weld pass and the angular distortion of the welded plate were omitted in the FE-model. The geometry of the specimen half was modeled in 3D as a rectangular block using conventional 8-node brick elements, each node having 3 degrees of freedom. The cross-section of the weldment was divided into three regions, as shown in Figure 2.88, because the three metals have different elastic properties. The Poisson's ratio was 0,3 for all the materials, whereas the elastic modulus was 190, 200 and 210 GPa for the austenitic, nickel-base and ferritic alloy, respectively. The weld groove was buttered with the same nickel-base alloy as the actual weld metal. Therefore, the weld and the buttering were treated as one

material in the FE-model, which is indicated by (2) in Figure 2.88, as compared to the actual layout of the weld shown in Figure 2.1.

The measured contour data from both surfaces was averaged before further filtering by the Shepard function. The conditioned topology data was submitted as displacement boundary conditions to the "wire-cut" face of the FE model.

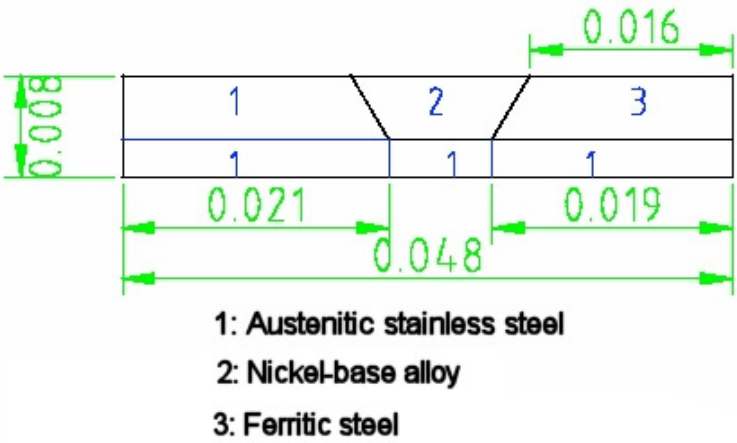

Figure 2.88. The modeled materials in the dissimilar metal weldment. As both weld and buttering were nickel-base alloys, they are shown as one material (2). The dimensions are in m.

The results of the FE-analyses are shown in Figures 2.89 and 2.90, where the residual stresses across the weld in the normal direction to the surface corresponding to the weld longitudinal direction are presented. In Figure 2.89, the numerical values of the residual stress distributions along the topology measurement lines are shown as line-plots. The overall picture of the residual stresses is readily presented as a "stress-map" as shown in Figure 2.90. The Contour analyses showed that high tensile stresses are present in both weld and cladding, which also has been welded. Along the whole austenitic stainless steel cladding, just below the surface (bottom line), the highest tensile stresses are found. Very high tensile stresses are also present in the weld and the buttered ferritic steel.

The difference in the stress distribution between the austenitic stainless and ferritic steel parts is clearly seen. For clarification of the residual stress map a micrograph of the weldment is superimposed on an approximate layout of the modeled geometry at the top of Figure 2.90. Note that the red vertical area in Figure 2.90, about 10 mm from the left edge of the specimen cross-section, is the place of the EDM hole and not an area of high tensile stress.

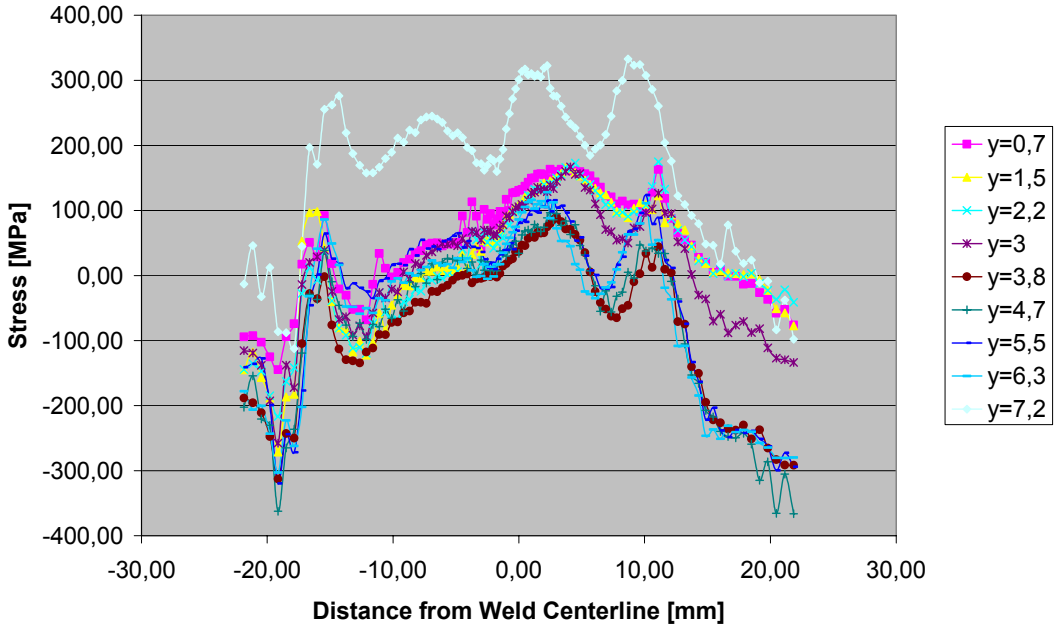

Figure 2.89. An example of the residual stress distributions along the topology measurement lines. The numbers shown in the legend indicate the distance in mm from the upper surface of the specimen.

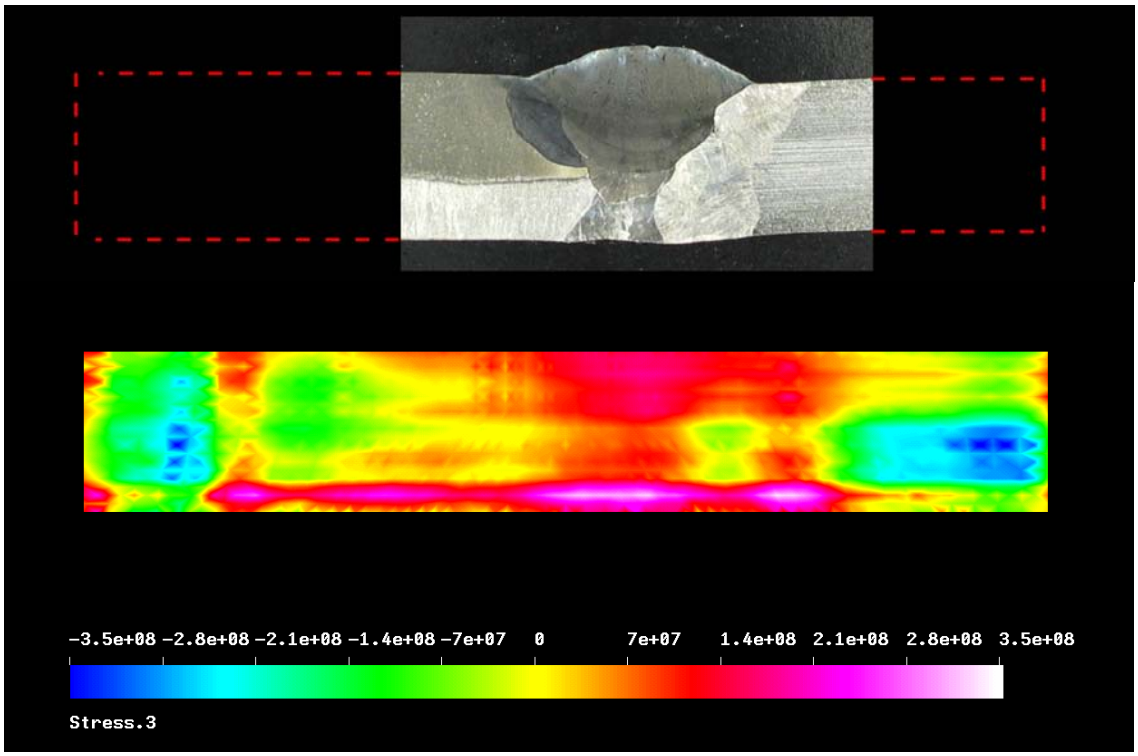

Figure 2.90. The layout of the modeled weldment at the top and the map of the residual stresses of the dissimilar metal weld in the longitudinal direction below. The color code represents a stress range from –350 to 350 MPa.

2.5 Microhardness measurements

Microhardness measurements were made using Vickers hardness and load of 500 g (HV0,5) for Neste Oil and mock-up dissimilar metal welds. Measurements were made according to KTA 3201.3. Two microhardness profiles were made across the weld, one 1,5 mm from the surface and another profile 1,5 mm from the root. Figures 2.91–2.101 present microhardness profiles of the Neste Oil and mock-up dissimilar metal welds. Fusion lines between different weld metals and base materials are marked as red vertical straight lines.

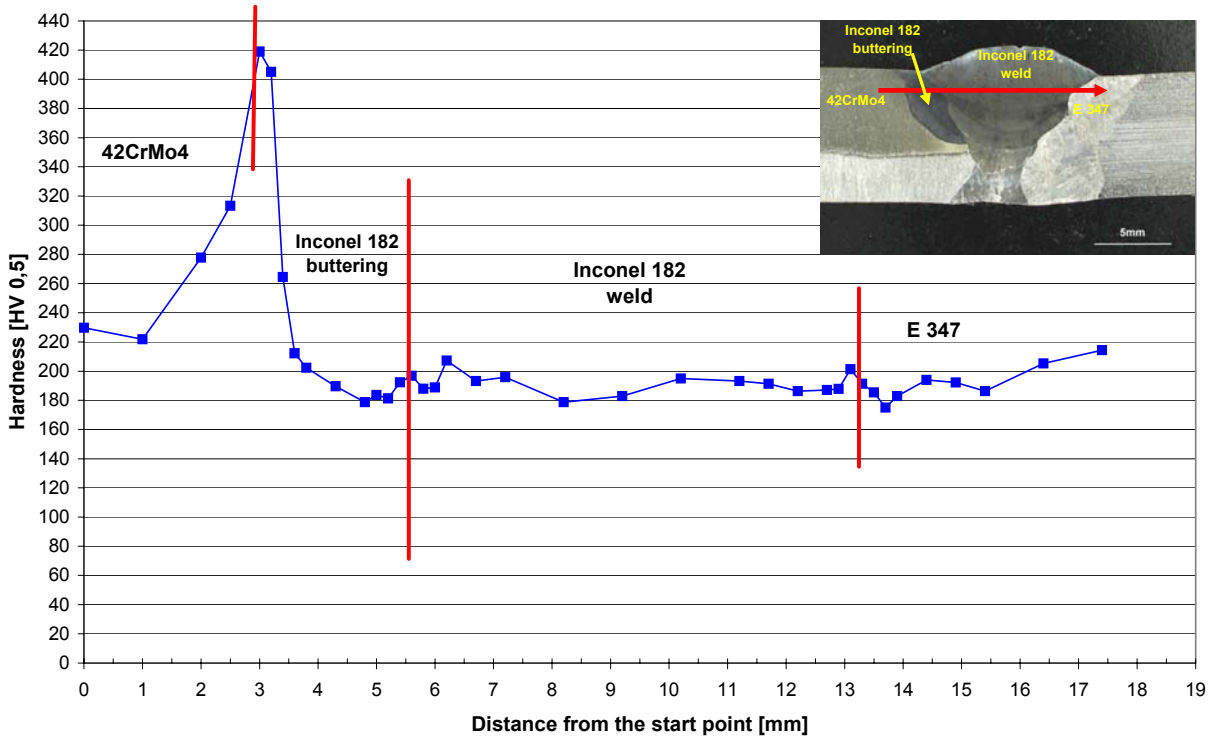

Figure 2.91. Microhardness profile of the Neste Oil dissimilar metal weld (surface side).

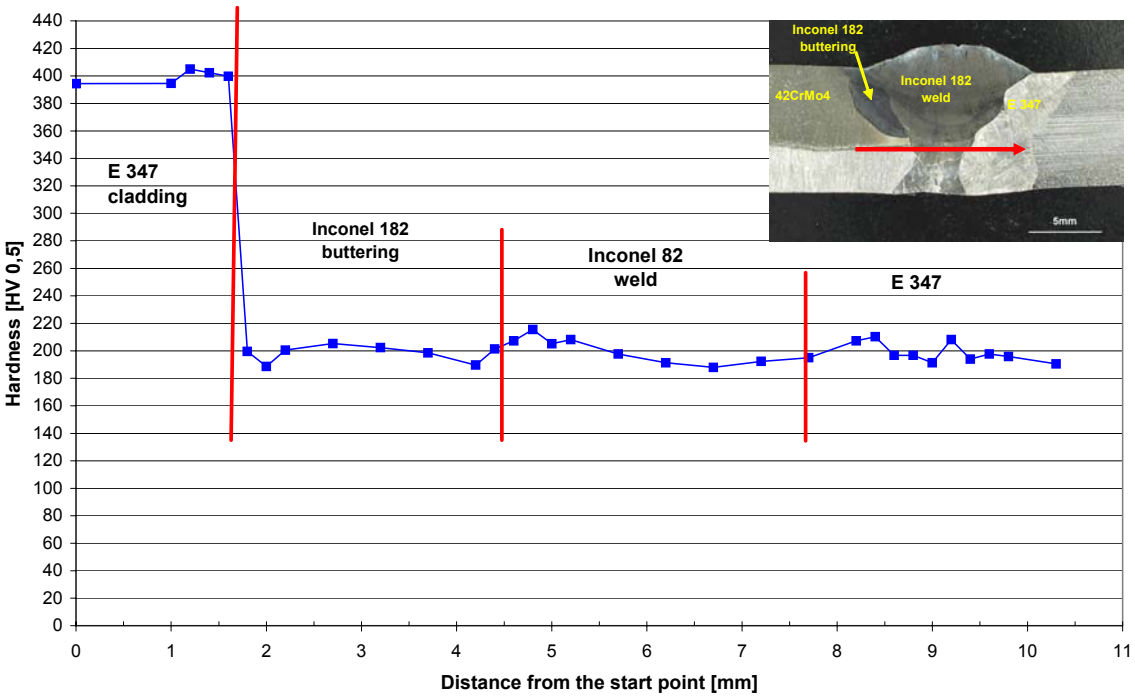

Figure 2.92. Microhardness profile of the Neste Oil dissimilar metal weld (center line).

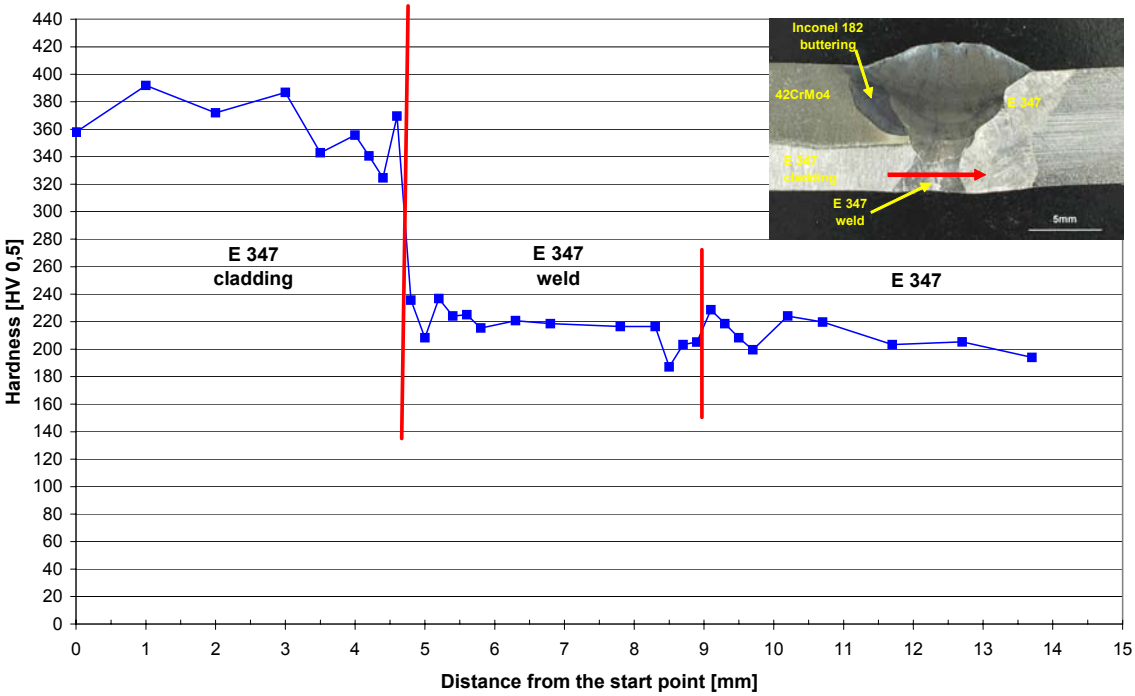

Figure 2.93. Microhardness profile of the Neste Oil dissimilar metal weld (root side).

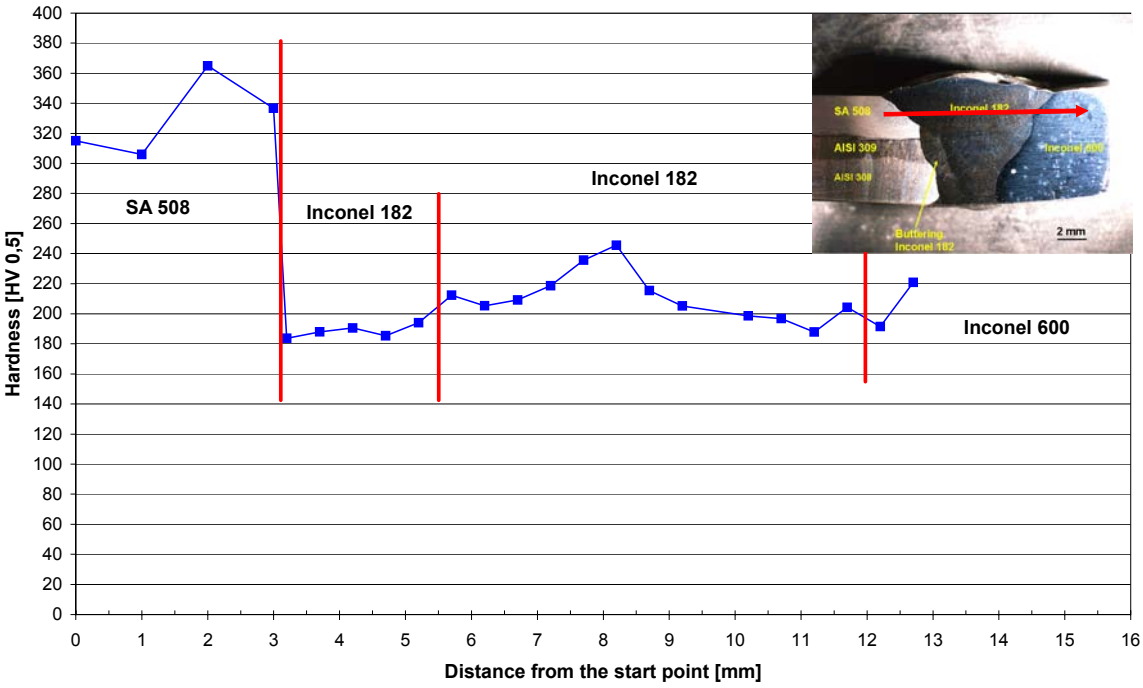

Figure 2.94. Microhardness profile of the mock-up TV dissimilar metal weld (surface side).

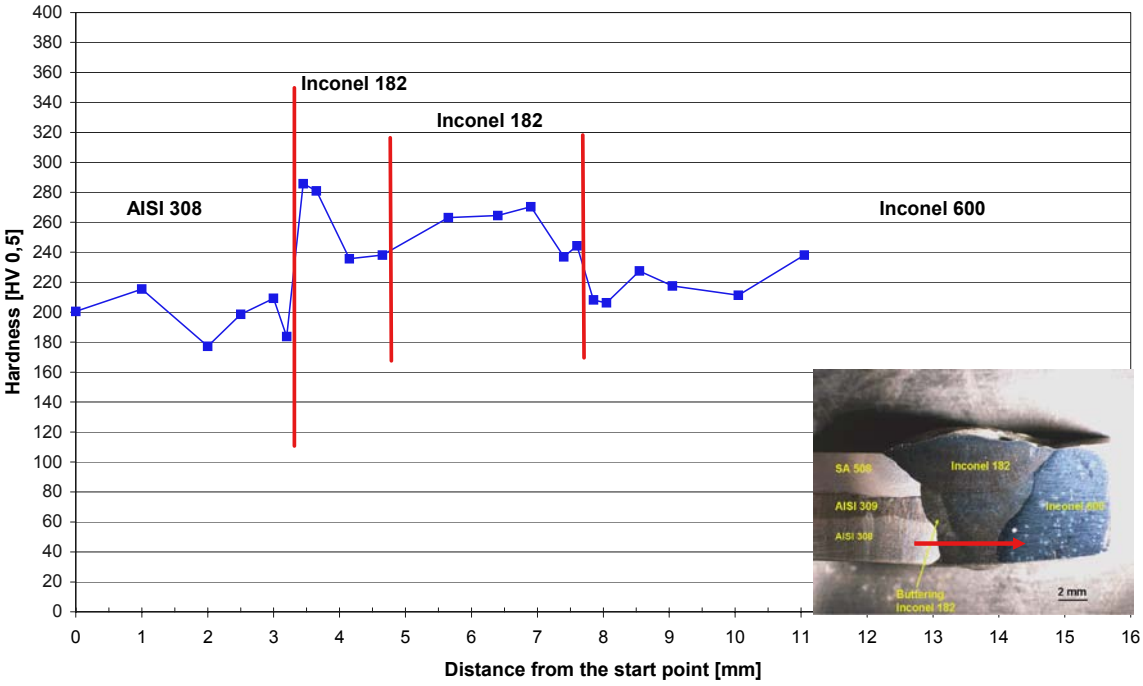

Figure 2.95. Microhardness profile of the mock-up TV dissimilar metal weld (root side).

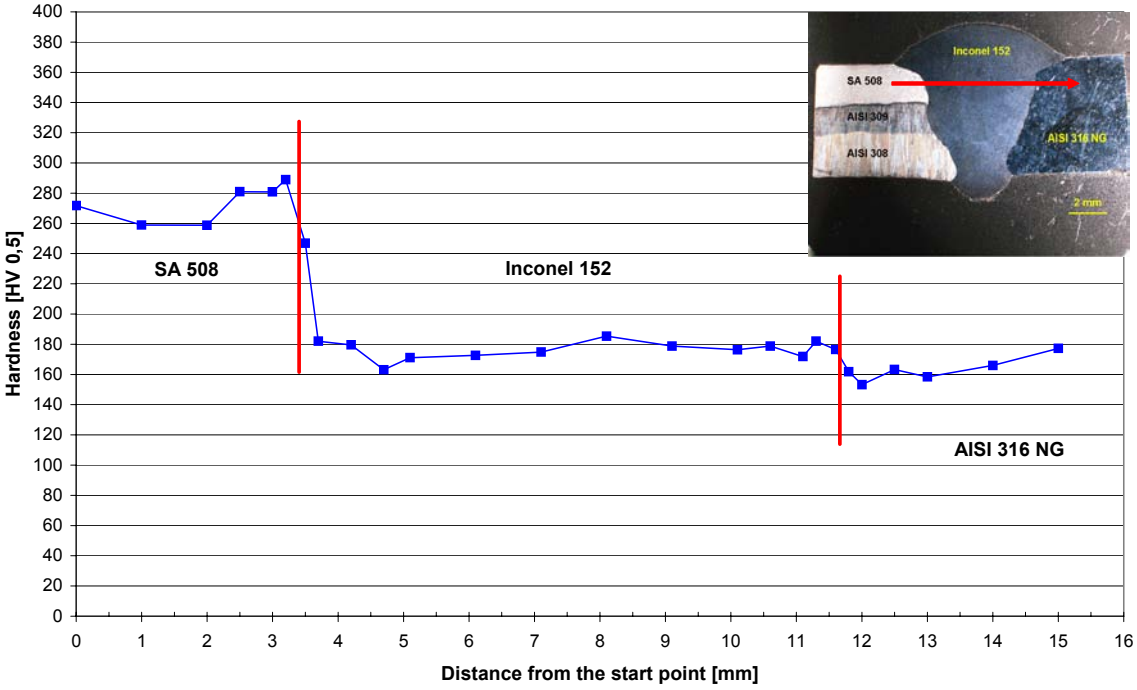

Figure 2.96. Microhardness profile of the mock-up 1 dissimilar metal weld (surface side).

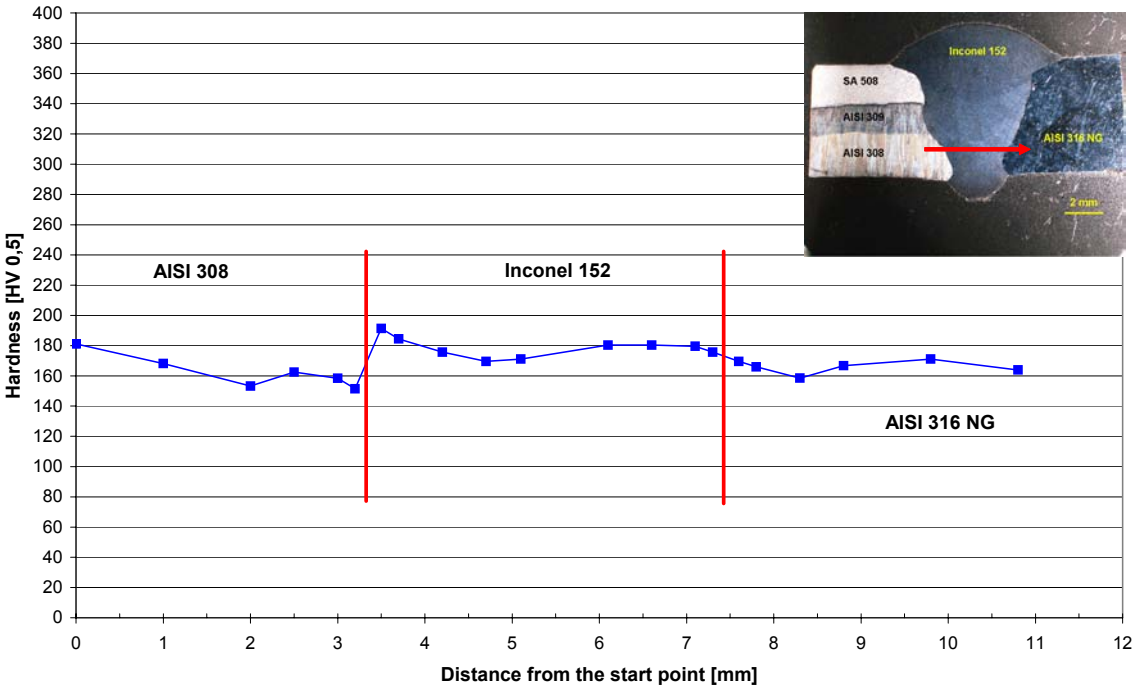

Figure 2.97. Microhardness profile of the mock-up 1 dissimilar metal weld (root side).

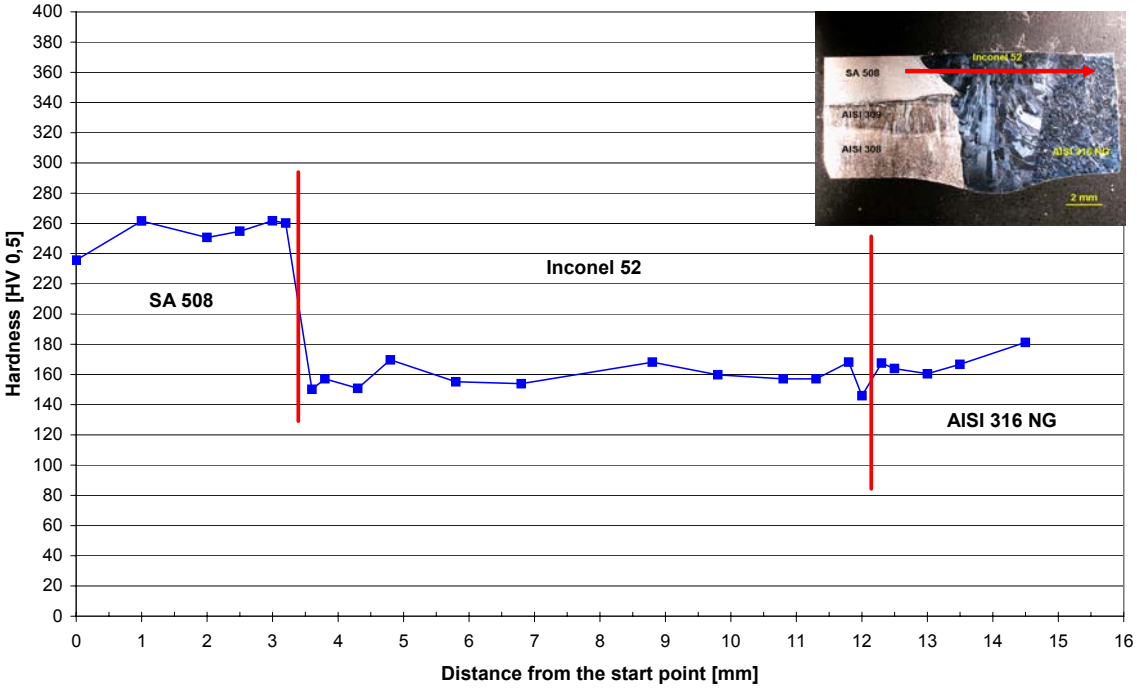

Figure 2.98. Microhardness profile of the mock-up 2 dissimilar metal weld (surface side).

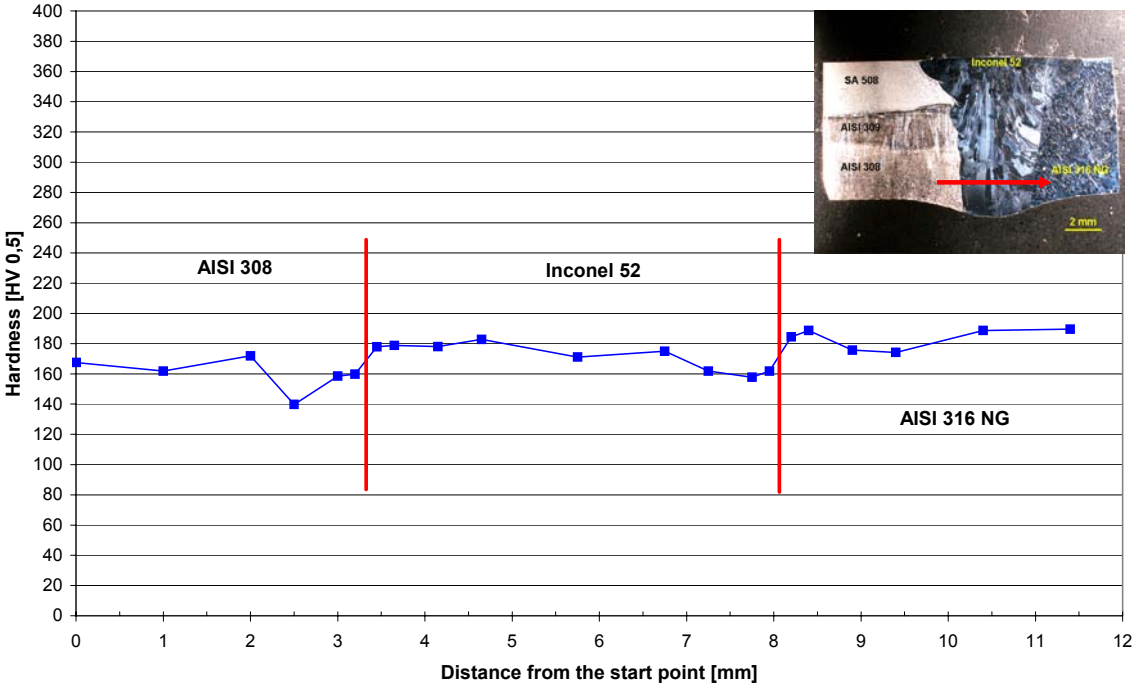

Figure 2.99. Microhardness profile of the mock-up 2 dissimilar metal weld (root side).

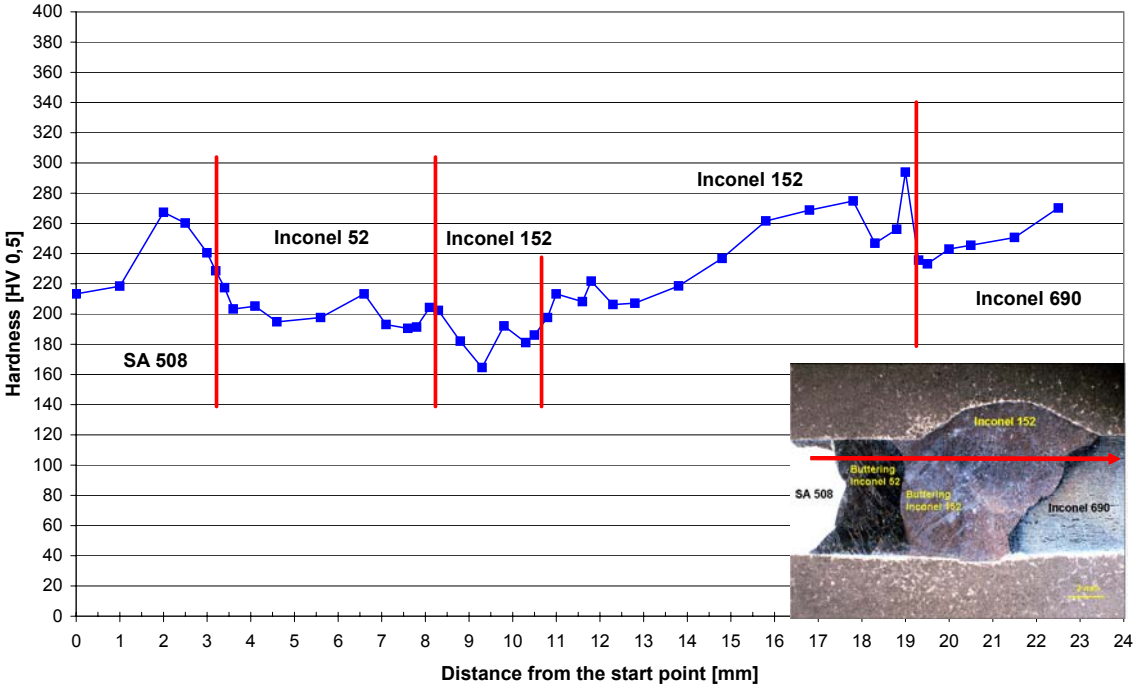

Figure 2.100. Microhardness profile of the mock-up 3 dissimilar metal weld (surface side).

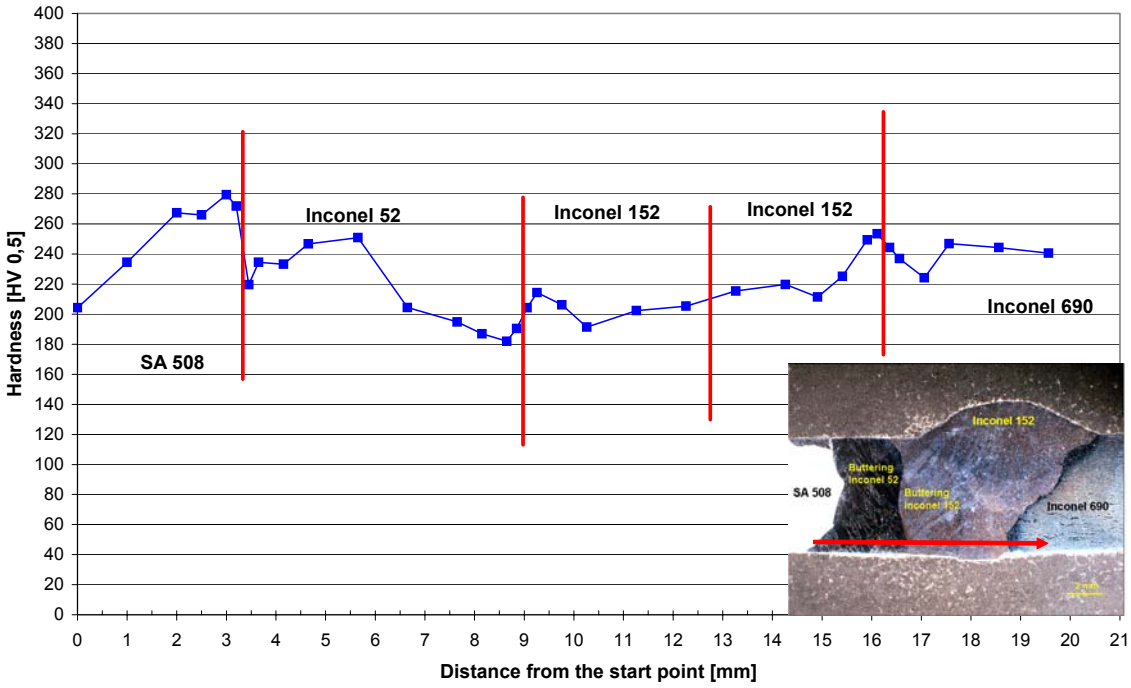

Figure 2.101. Microhardness profile of the mock-up 3 dissimilar metal weld (root side).

2.6 Microstructural analyses of weld metals

Microstructures of the welds and different weld metal boundary zones were examined by optical and scanning electron microscopy (SEM). Cross-sections of the hot cracks formed in Varestraint tests were also analysed by optical metallography and FEG-SEM/EDS.

2.6.1 Neste Oil case

In Figure 2.102 is presented a cross-section of the Neste Oil dissimilar metal weld before the Varestraint test. Plate thickness is 8 mm.

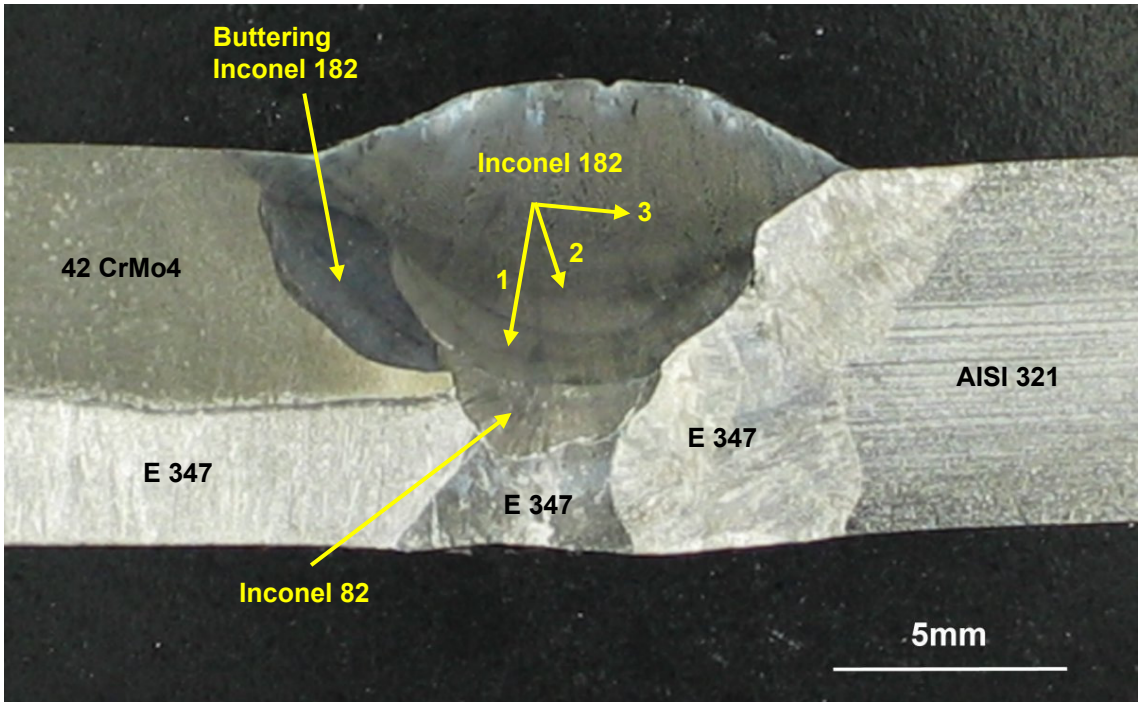

Figure 2.102. Cross-section of Neste Oil dissimilar metal weld.

Figure 2.103 presents the cutting lines of the cross-section of the Neste Oil sample for microstructural examinations.

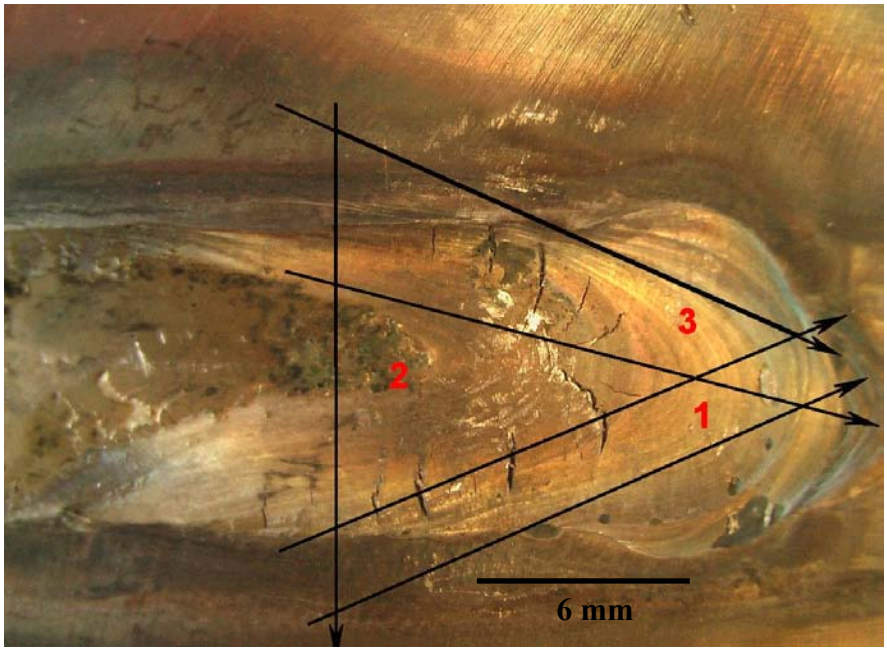

Figure 2.103. Cutting lines of cross-section of Neste Oil sample for microstructural examinations after Varestraint test.

Figure 2.104 presents a cross-section of the Neste Oil weld cracks after Varestraint test.

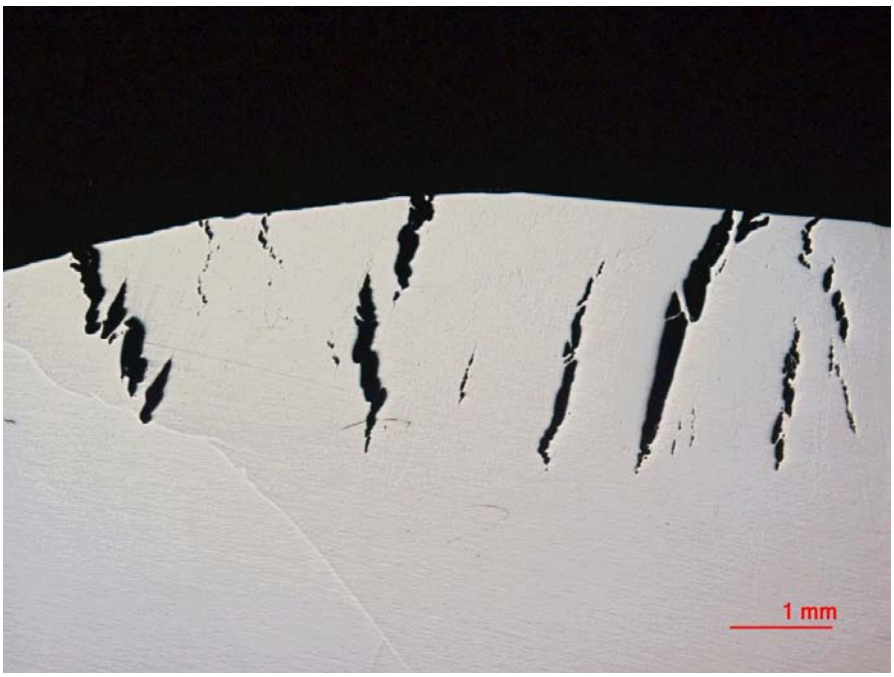

Figure 2.104. Cross-section of Neste Oil weld cracks after Varestraint test.

Figure 2.105 presents scanning electron microscopy (SEM) of the fracture surface of an opened crack.

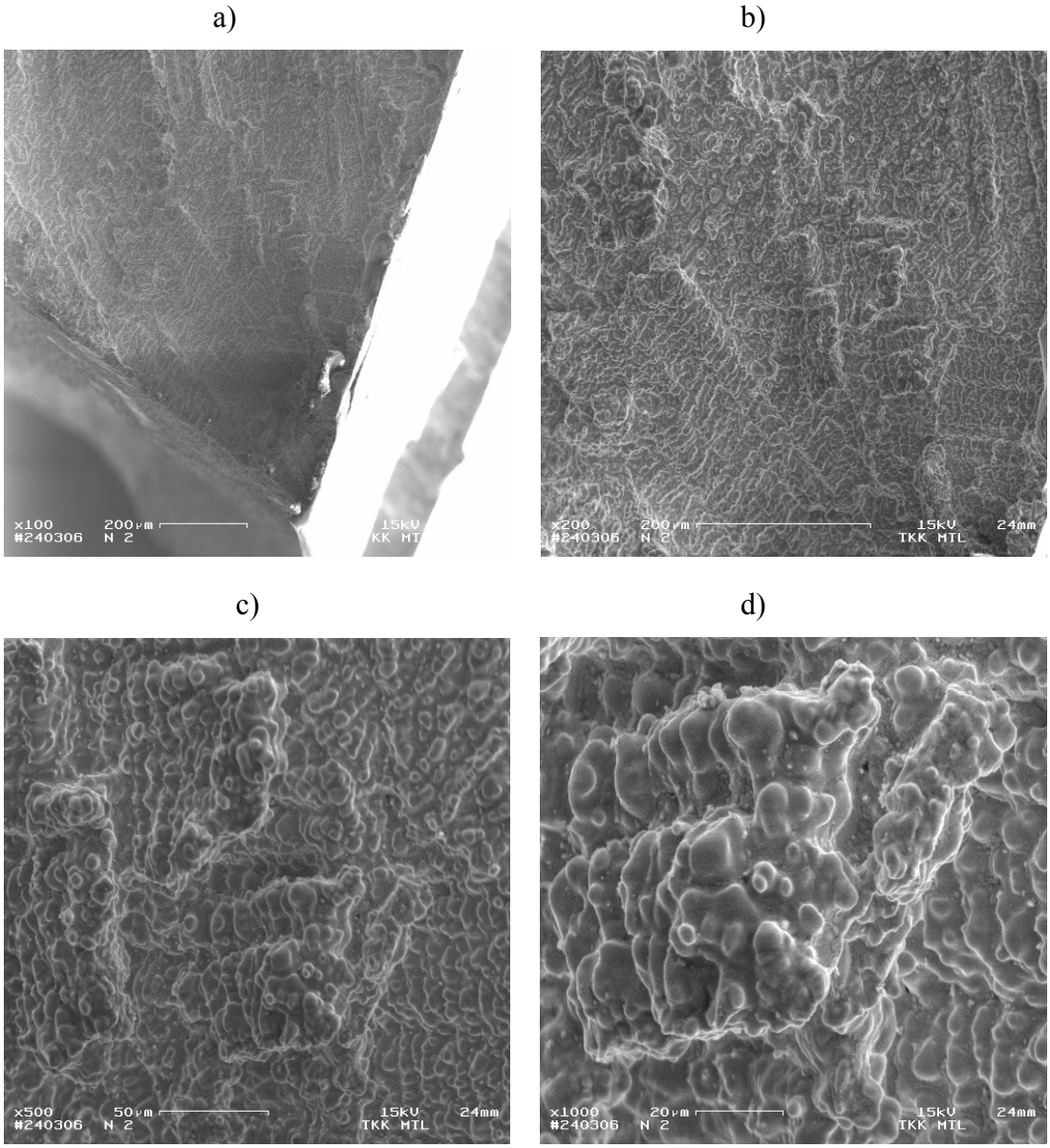

Figure 2.105 (a–d). Scanning electron microscopy (SEM) of the fracture surface of an opened Neste Oil weld crack.

The hot cracks were formed during Varestraint test, when the weld metal was re-melted while bending. It can be seen that the fracture surface is wavy and round shaped which indicates that the cracks are hot cracks.

Figure 2.106 presents optical microscopy of hot cracks.

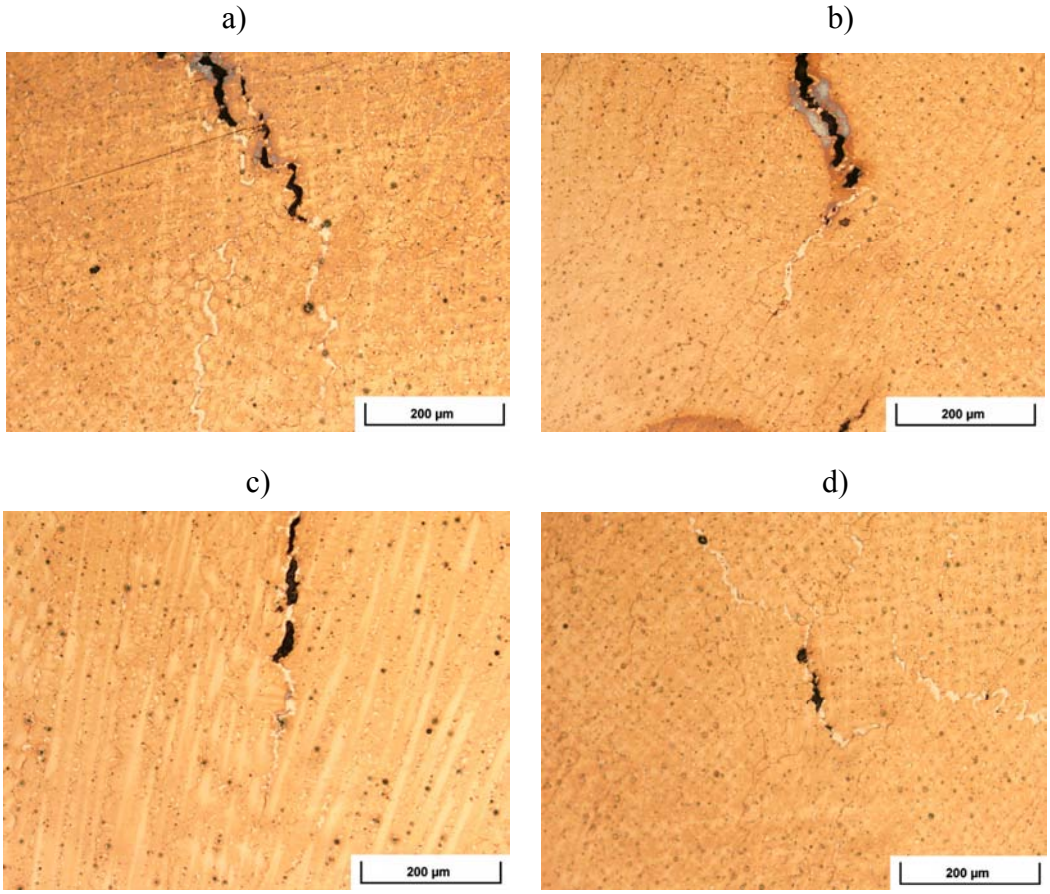

Figure 2.106 (a–d). Optical microscopy of the Neste Oil weld hot cracks (dark areas). Note the white phase ahead of the hot crack tips.

Figure 2.107 presents scanning electron microscopy (SEM) of the Neste Oil weld hot crack tips.

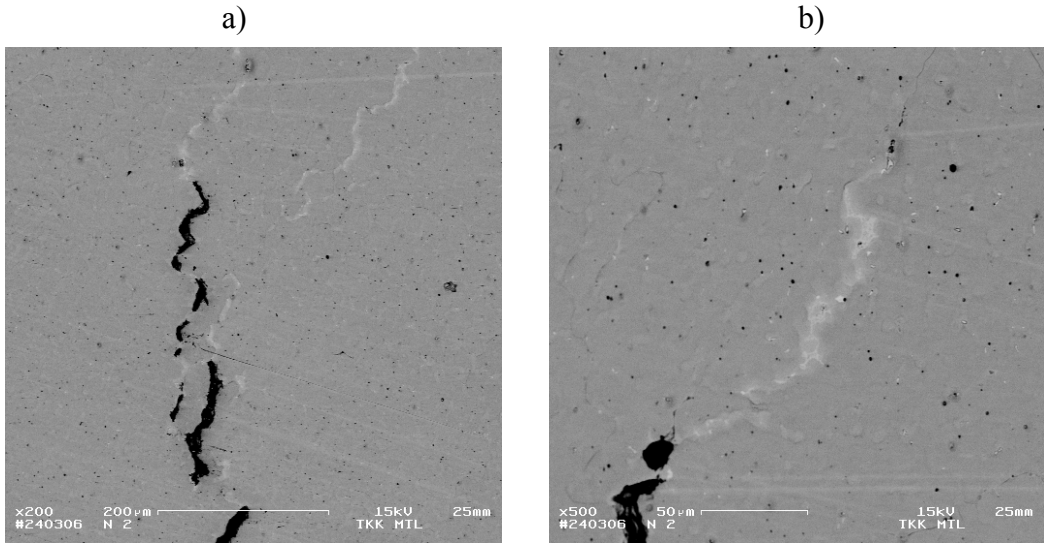

Figure 2.107 (a and b). Scanning electron microscopy (SEM) of the Neste Oil weld hot cracks (dark areas). Note the white phase ahead of the hot crack tips.

Figure 2.108 presents scanning electron microscopy (SEM) of a Neste Oil weld hot crack tip showing details of the irregularly-shaped white phase.

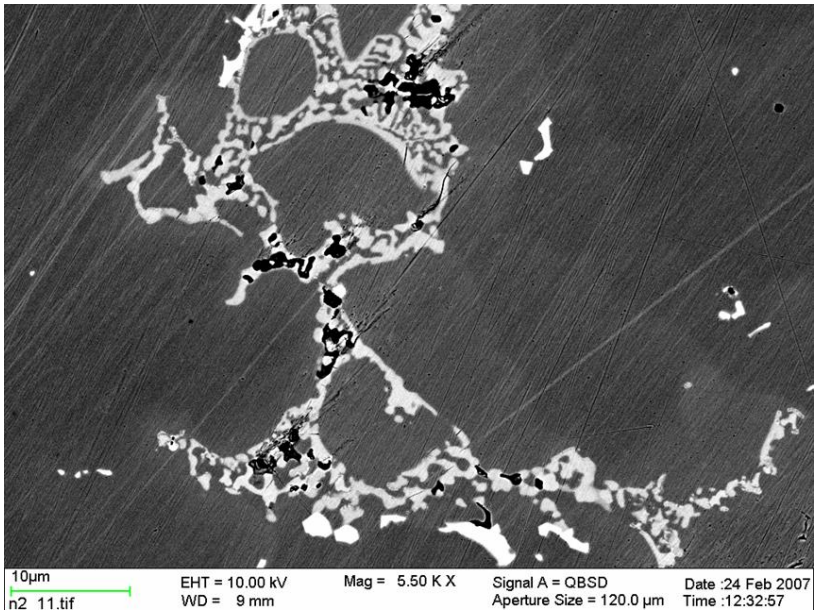

Figure 2.108. Scanning electron microscopy (SEM) of a Neste Oil weld hot crack tip showing details of the white phase with irregular shape.

Figure 2.109 presents scanning electron microscopy (SEM) of the Neste Oil weld hot cracks (dark areas) a) and white phase areas related to the cracks b). Note that there seems to be three different phases present in the BSE-images (white and grey areas on dendrite boundaries and white particles inside the dendrites).

a) b)

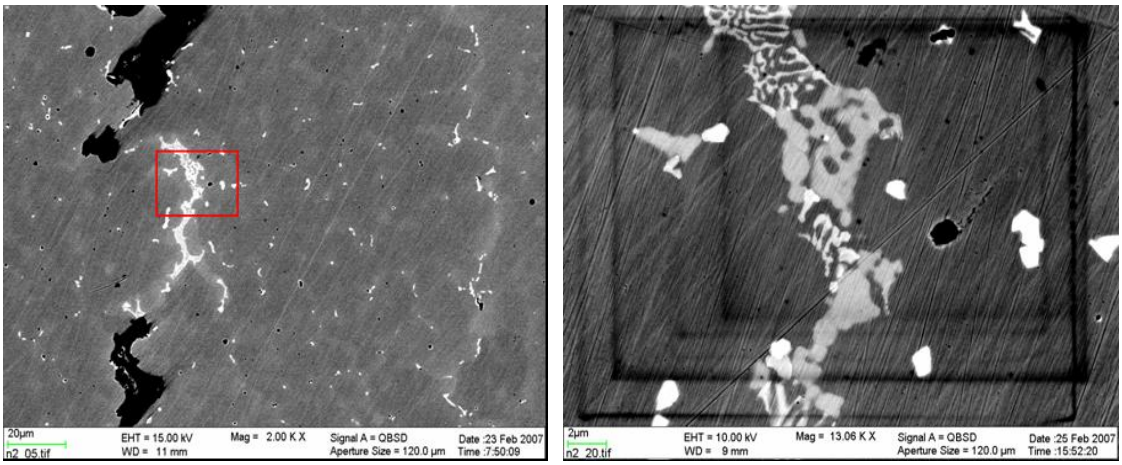

Figure 2.109 (a and b). Scanning electron microscopy (SEM) of the hot cracks (dark areas) a) and white phase areas b).

In both optical and scanning electron microscopy, the white phase areas related to the hot cracks can be clearly seen. These areas were examined by energy dispersive spectrometer (EDS) analysis. Figures 2.110 and 2.111 present EDS analyses and X-ray element maps from the white phase area in the dendrite boundary regions. Region indicated by the rectangle in Figure 2.110 is more carefully analysed in Figure 2.112.

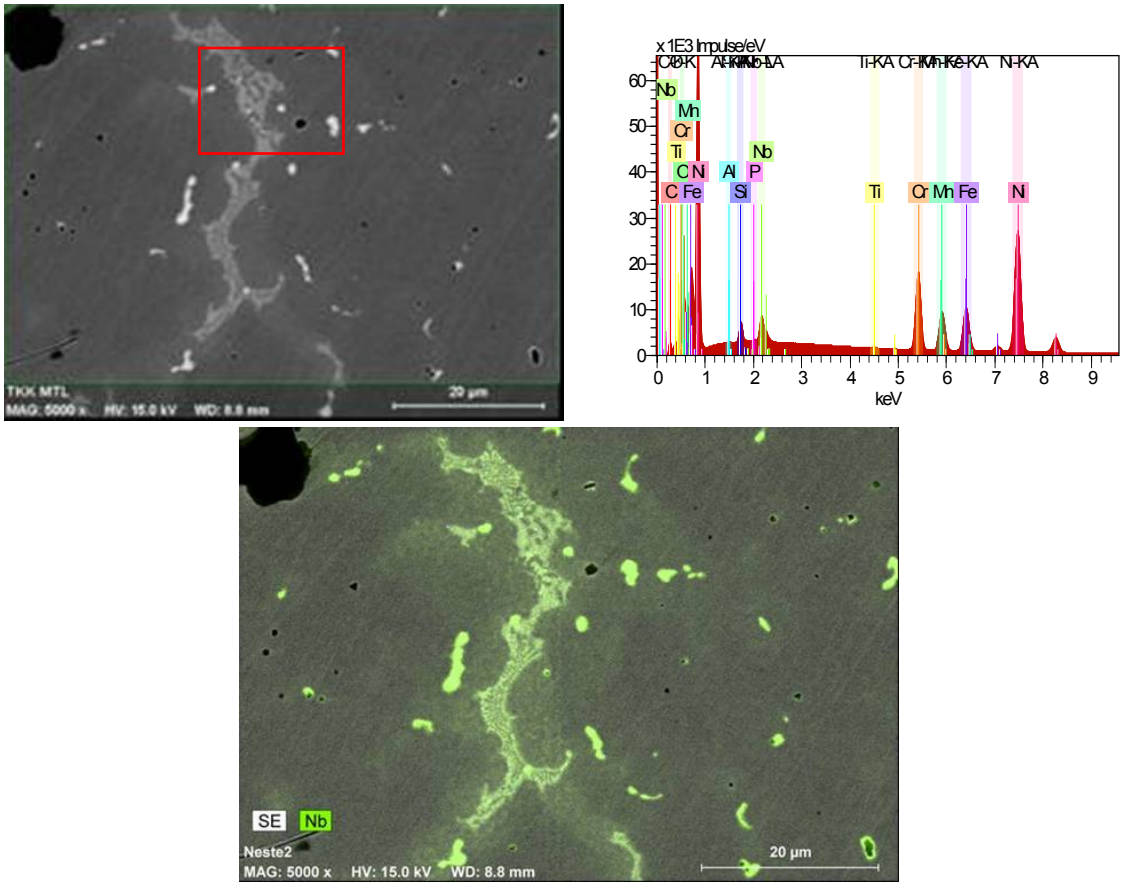

Figure 2.110. EDS analysis of the marked area showing the white phase along the dendrite boundary. Note marked Nb enrichment in the white phase and less enrichment in a wider area along the dendrite boundary.

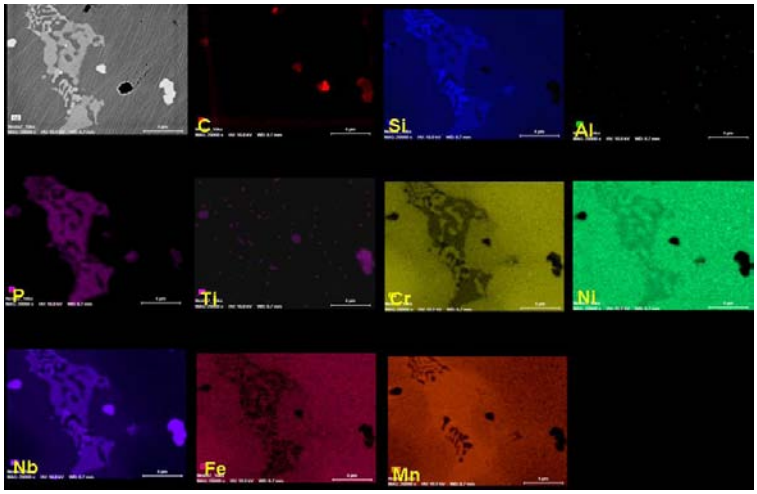

Figure 2.111. X-ray element maps from the white phase area existing ahead of the hot crack.

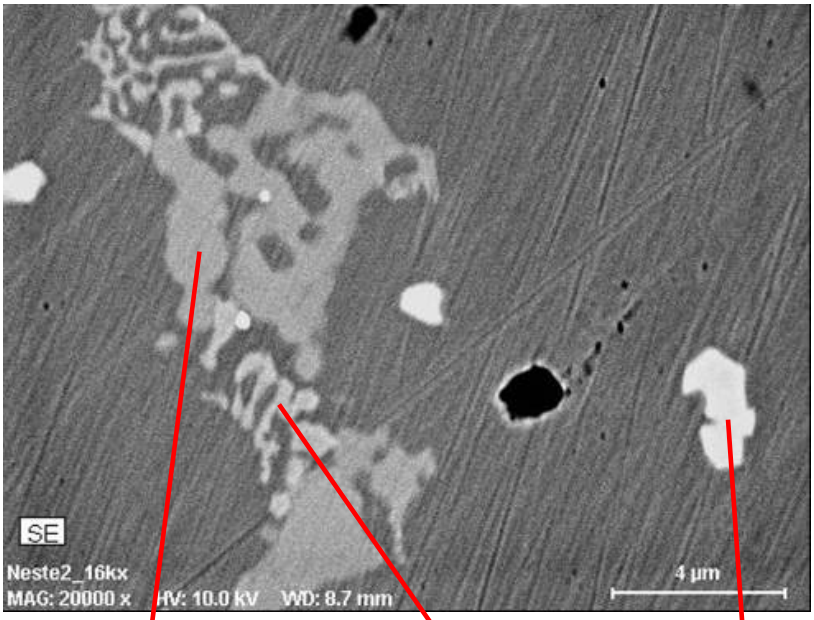

Element	Filler metal wt.%	Grey area wt.%	Enrichment vs. filer metal	Light white area wt.%	Enrichment vs. filer metal	White area wt.%	Enrichment vs. filer metal
Si	0,8	3,4	4,3	6,5	8,1	0	0,0
P	0,01	1,3	130,0	1,3	130,0	0,2	20,0
Ti	0,1	0,04	0,4	0,7	7,0	2,8	28,0
Cr	15,7	5,4	0,3	4,9	0,3	1,4	0,1
Mn	6,5	17,7	2,7	11,8	1,8	1,1	0,2
Fe	6,7	4,7	0,7	4,9	0,7	1,5	0,2
Ni	68	51,4	0,8	49,4	0,7	0	0,0
Nb	1,8	15,2	8,4	20,6	11,4	89,6	49,8

Figure 2.112. SEM image and EDS analyses of the white and grey phase showing Si, Nb, Mn and P enrichment. The spot size in EDS has an interaction diameter about 1 µm, and therefore the surrounding matrix also affects the result.

Study of the cross-sections of the Neste Oil weld (alloy 182) hot cracks reveals a white phase with marked enrichment of Nb, Si, Mn (except the light white phase) and P, which is compensated by depletion of Cr, Fe and Ni. White phase on dendrite boundaries consists of two phases, white and gray, with varying Nb, Si, and Mn contents. Inside and along the dendrites/grains white Nb-rich particles, Nb(C, N), are present. The structure, properties and role of the white interdendritic phase in hot cracking are discussed in the end of this chapter.

The hot crack fracture surfaces that were opened for fractography were further examined and analysed with an FEG-SEM/EDS system. Figures 2.113 and 2.114 present EDS analyses and X-ray element maps for the opened fracture surfaces.

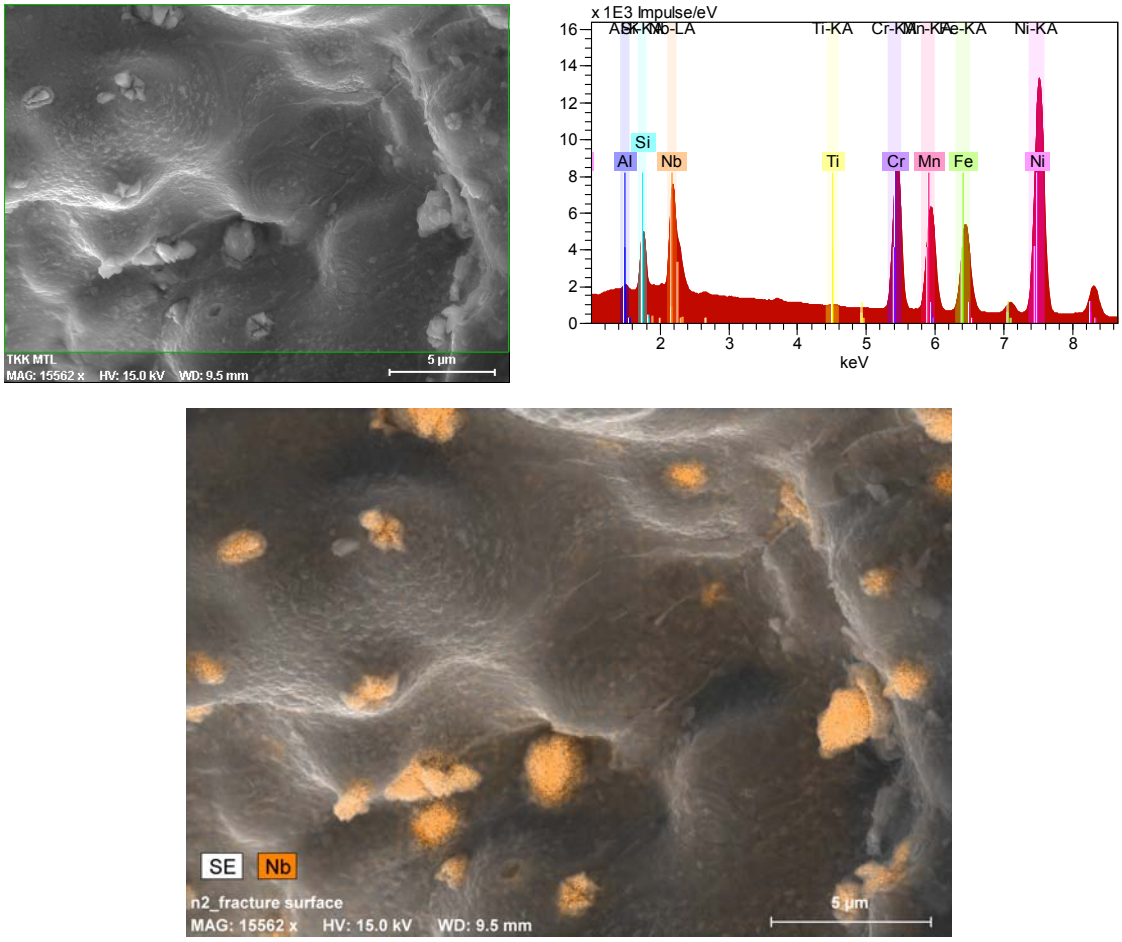

Figure 2.113. EDS analysis of the opened fracture surface showing the Nb(C,N) particles.

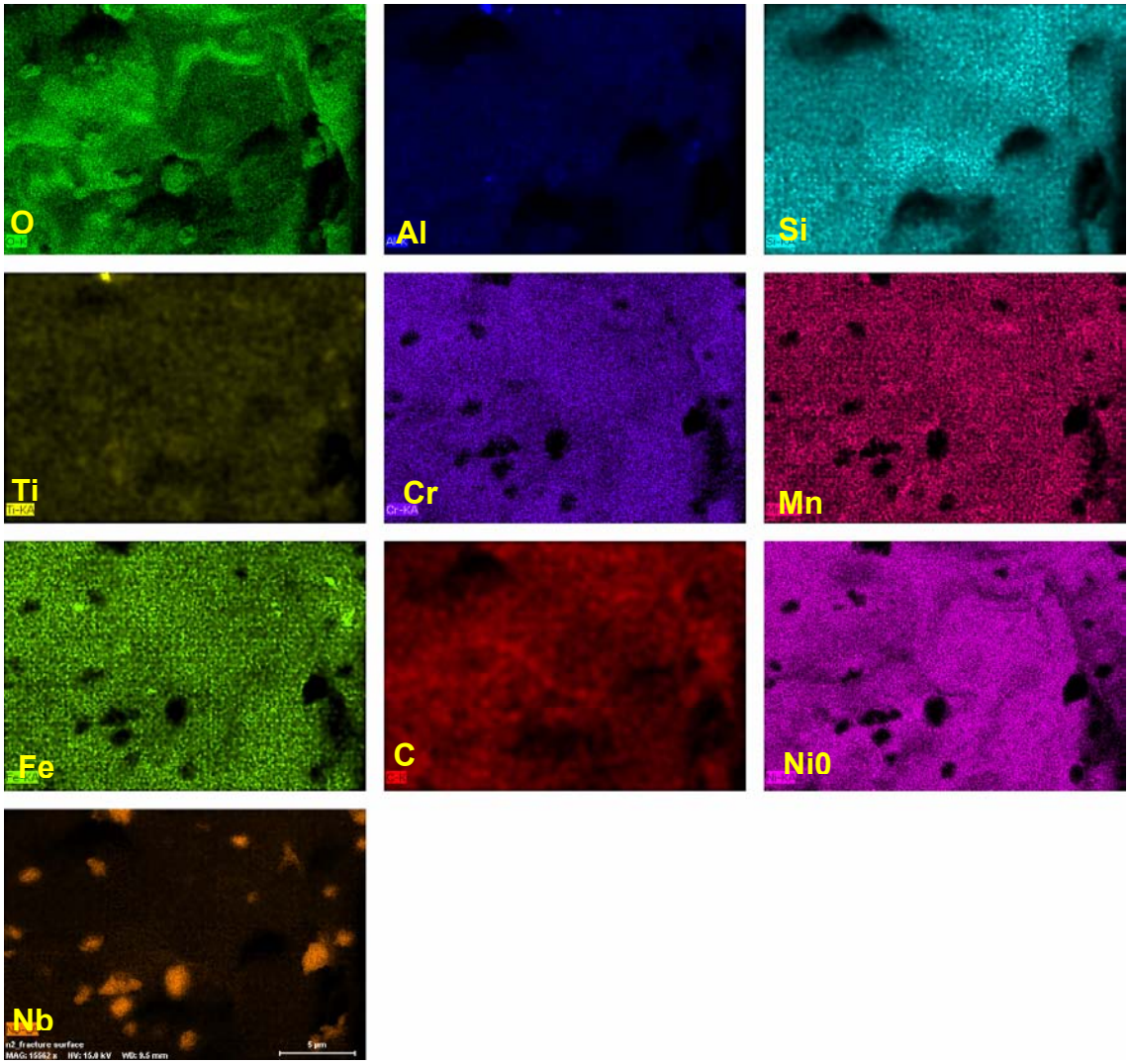

Figure 2.114. X-ray element maps of the opened fracture surface (Figure 2.113) showing element distribution.

Figures 2.115 and 2.116 present EDS analyses and X-ray element maps of the opened fracture surface.

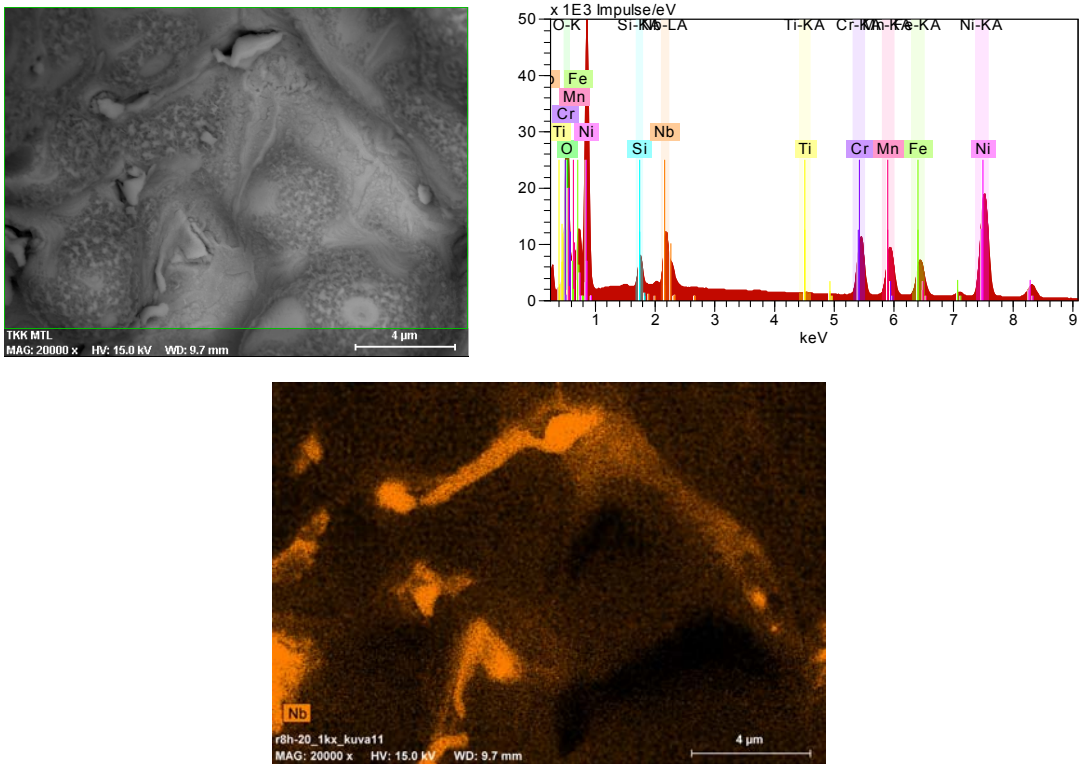

Figure 2.115. EDS analysis of the opened fracture surface with the white phase where Nb enrichment is observed.

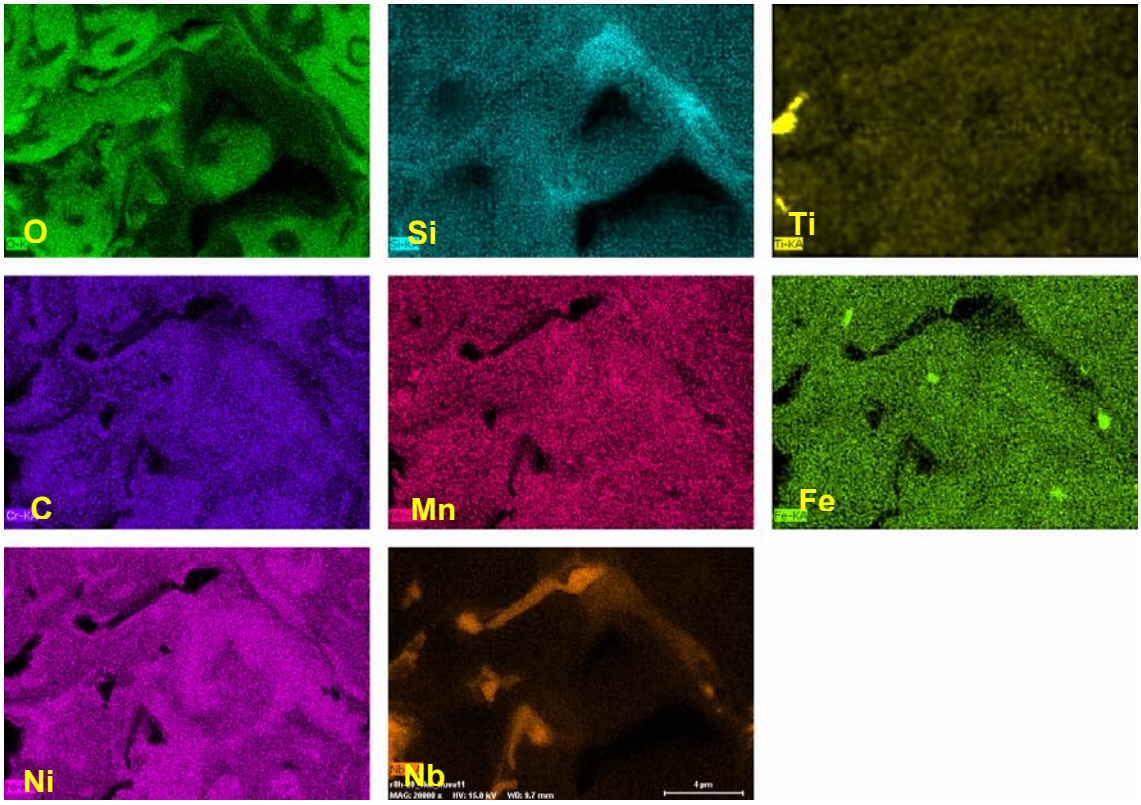

Figure 2.116. X-ray element maps of the opened fracture surface of Figure 2.115.

Figures 2.117 and 2.118 present EDS analyses and X-ray element maps of the opened fracture surface.

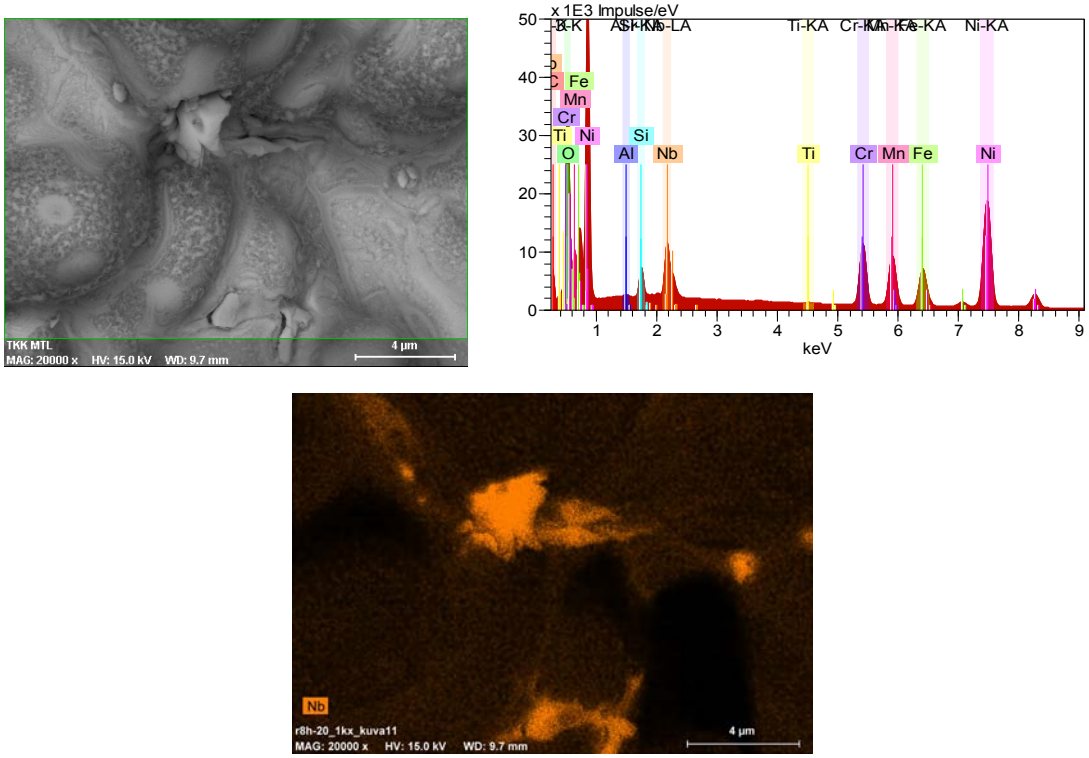

Figure 2.117. EDS analysis of the opened fracture surface with the white phase, showing Nb enrichment in it.

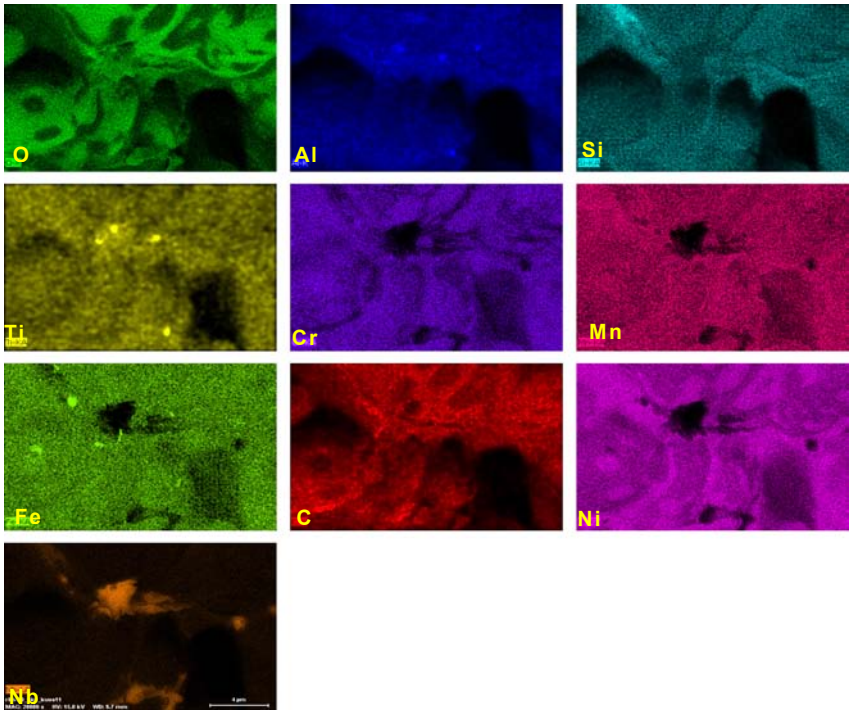

Figure 2.118. X-ray element maps of the opened fracture surface of Figure 2.117.

Study of the fracture surfaces of the Neste Oil weld (alloy 182) hot cracks reveals marked segregation of the same elements on fracture surfaces as seen in the white phase in the cross-section of the hot cracks. On the fracture surface, Nb-rich particles, Nb(C, N), and the white phase are present intermixed in the final microstructure. The white phase exhibits marked enrichment of Nb, Si, Mn, and P, as was also observed in the study of the cross-sections.

2.6.2 Mock-up TV case (TV)

Figure 2.119 presents a cross-section of the TV mock-up dissimilar metal weld before the Varestraint test. Plate thickness is 8 mm.

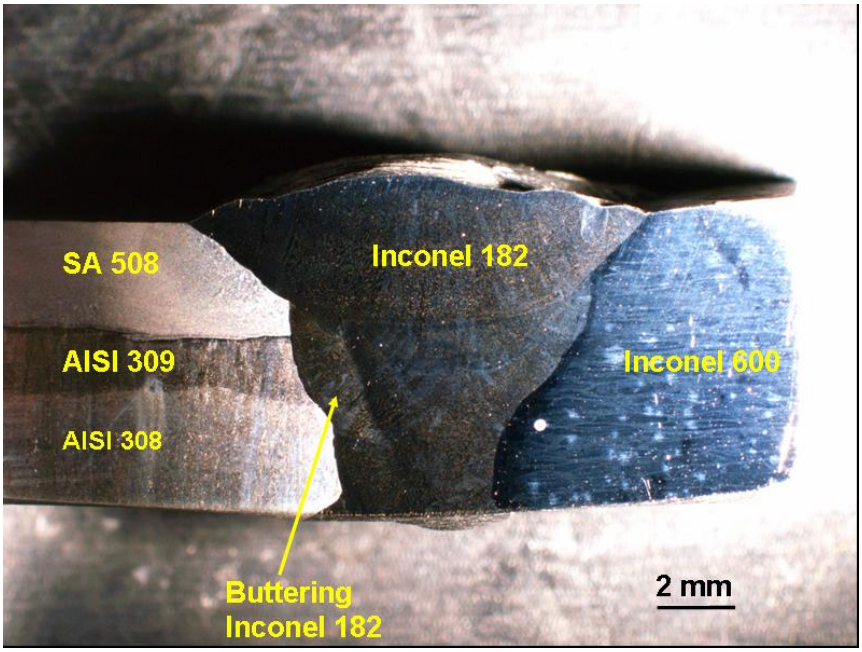

Figure 2.119. Cross-section of the TV mock-up dissimilar metal weld before Varestraint test.

Figures 2.120 and 2.121 present optical microstructures of the weld metals and base material interfaces.

a) b)

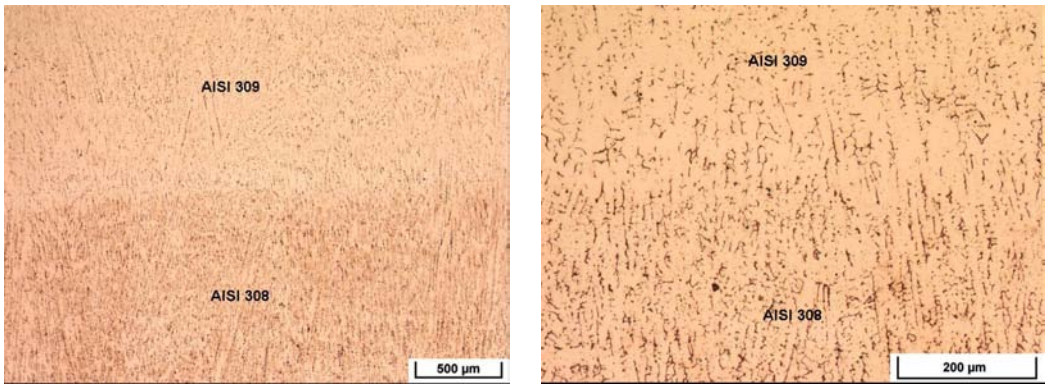

Figure 2.120 (a and b). Fusion line between AISI 309 and AISI 308 weld metals.

a) b)

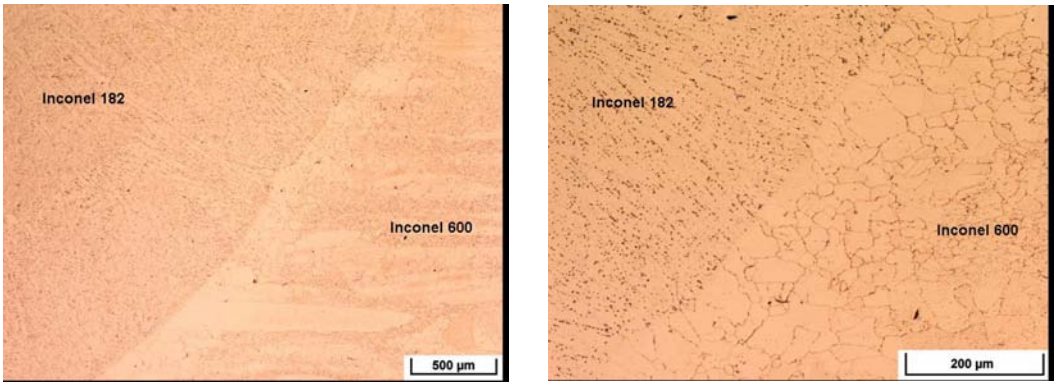

Figure 2.121 (a and b). Fusion line between Inconel 182 weld metal and Inconel 600 base material.

Figure 2.122 presents the cutting line of the cross-section of the TV mock-up sample for microstructural examinations.

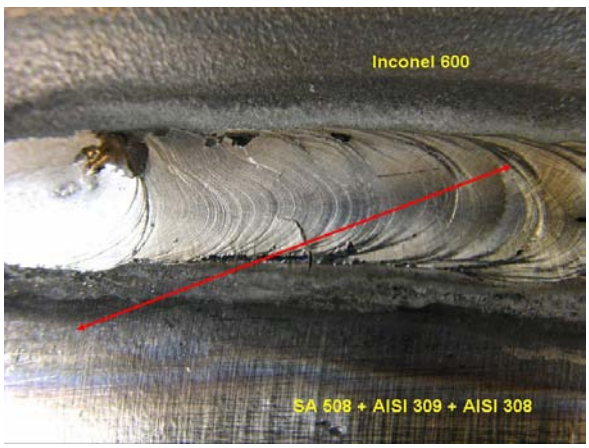

Figure 2.122. Cutting line of the cross-section of TV mock-up sample for microstructural examinations after Varestraint test.

Figure 2.123 presents a cross-section of TV mock-up weld cracks after Varestraint testing.

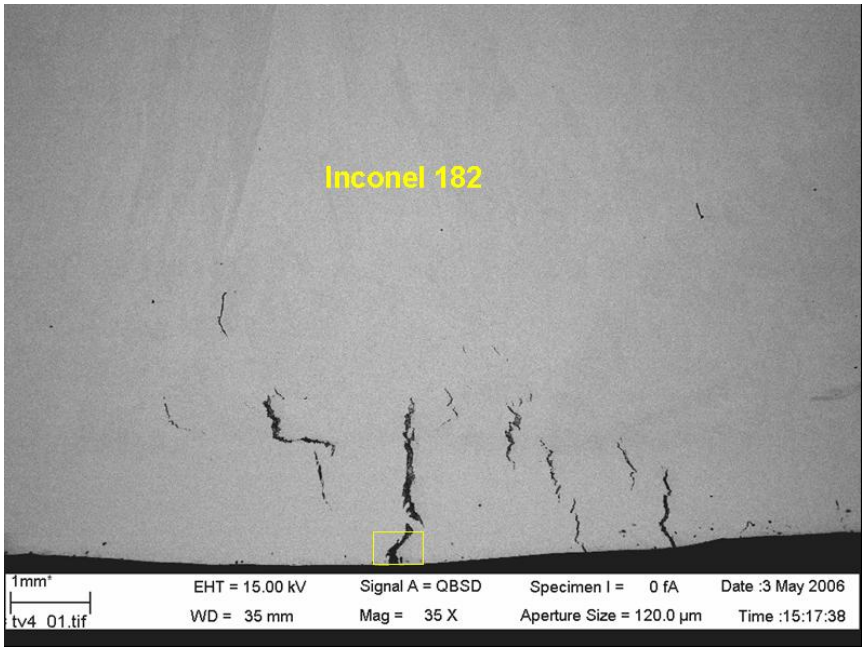

Figure 2.123. Cross-section of TV mock-up weld cracks after Varestraint test.

Figure 2.124 presents scanning electron microscopy (SEM) of the hot crack cross-section, while 2.125 shows an opened crack.

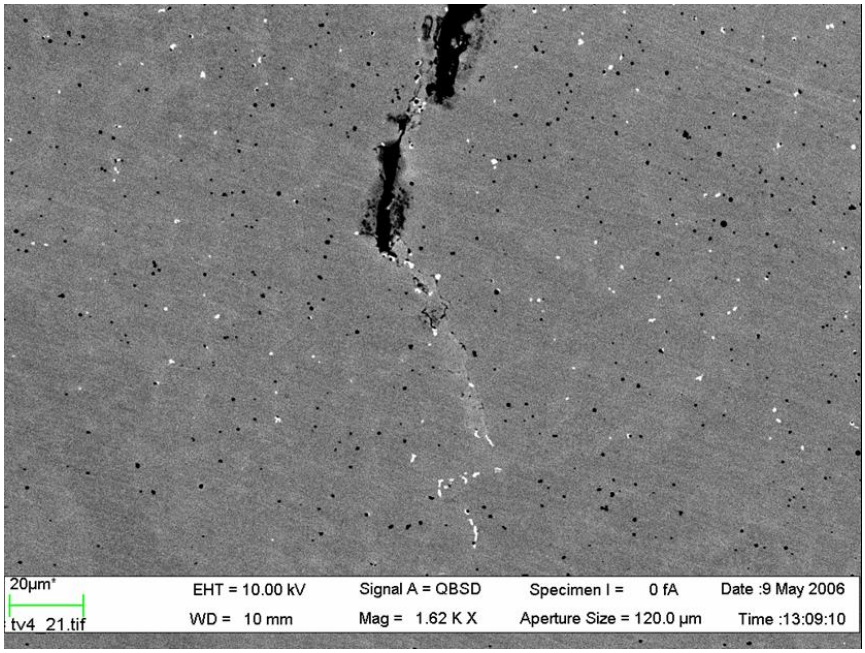

Figure 2.124. Scanning electron microscopy (SEM) of the hot crack cross-section at the crack tip.

Figure 2.126 presents fracture surfaces from the locations marked with rectangles in Figure 2.125.

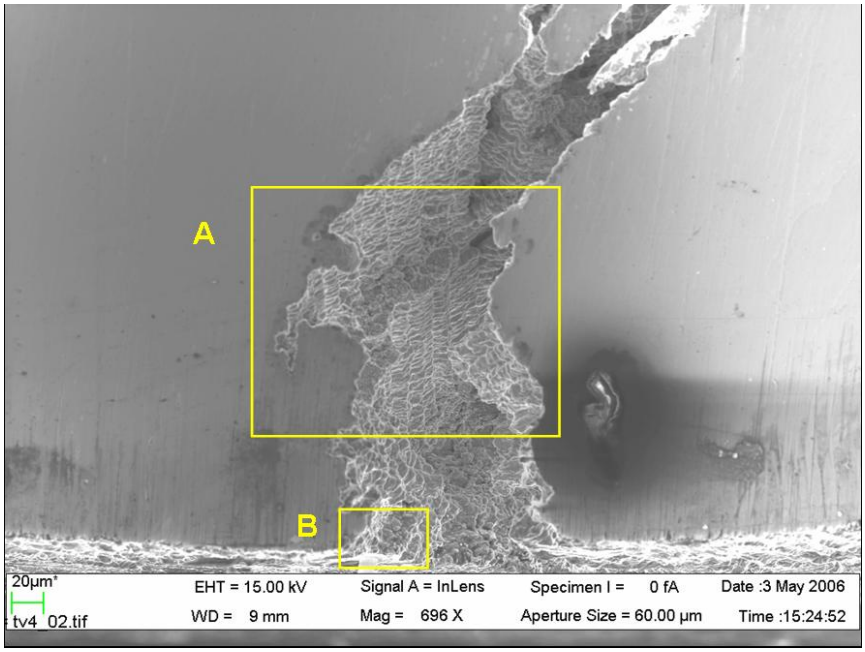

Figure 2.125. Fracture surface of TV mock-up weld crack.

a) b)

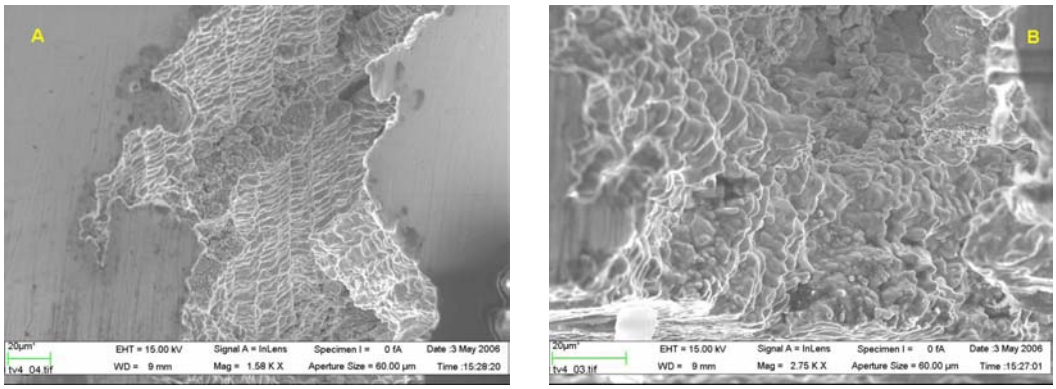

Figure 2.126 (a and b). Fracture surface of mock-up TV weld crack (higher magnification from locations A and B presented in Figure 2.125).

The white phase observed in connection with the Neste Oil weld hot cracks can be seen also in this cross-section. It is also clearly visible on the opened fracture surfaces of the hot cracks, Figure 2.127. Additionally a large number of Nb-rich particles, Nb(C, N), are present on the fracture surface of the hot crack, Figure 2.130.

a) b)

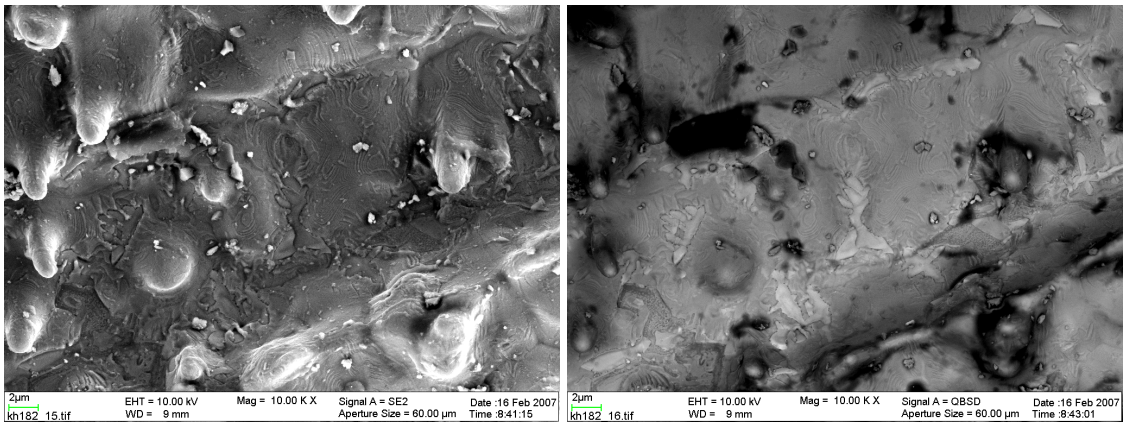

Figure 2.127. Scanning electron microscopy (SEM) of opened fracture surface showing the white phase in the valleys between dendrites.

Figures 2.128 and 2.129 present EDS analysis and X-ray element maps of the opened fracture surface.

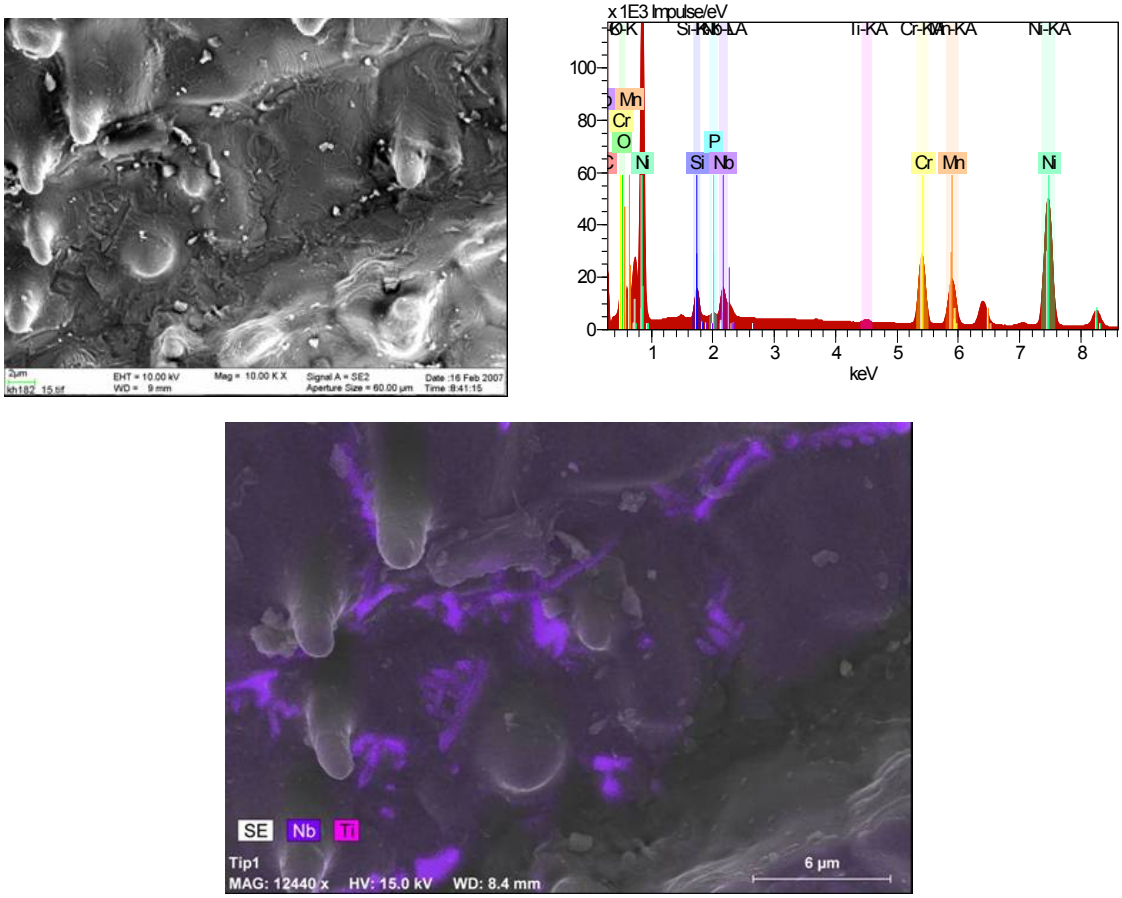

Figure 2.128. EDS analysis of the opened fracture surface showing the marked Nb enrichment of the white phase.

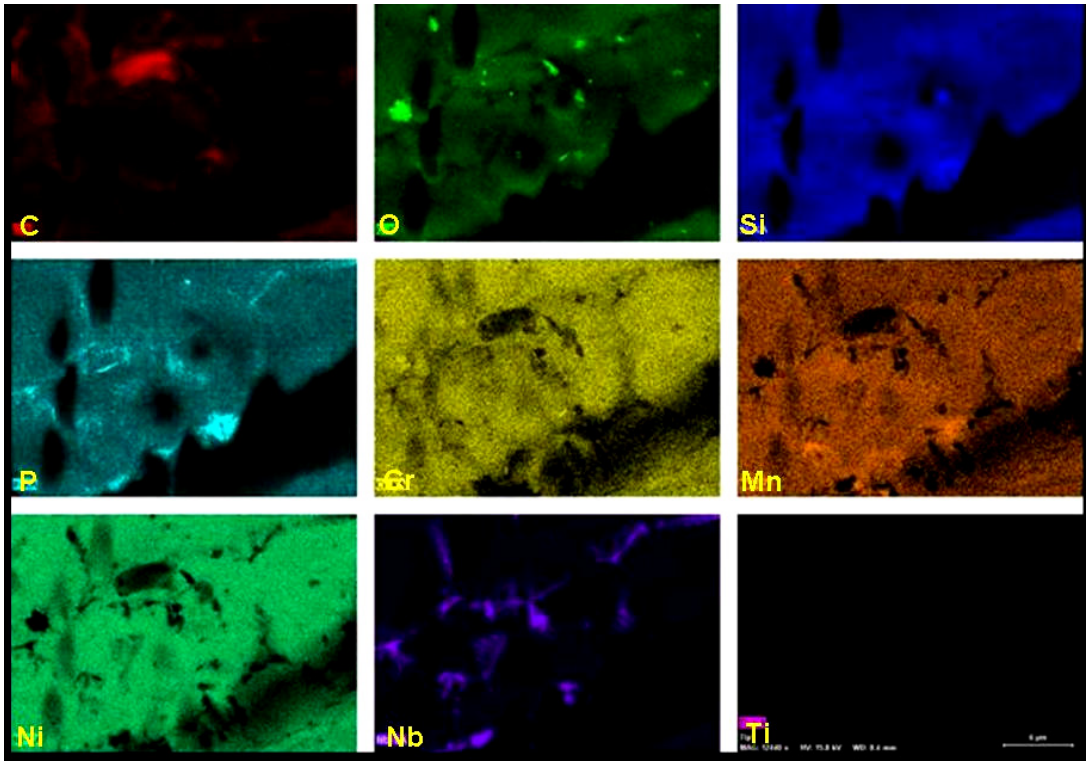

Figure 2.129. X-ray element maps of the opened fracture surface (Figure 2.128) showing the co-enrichment of Nb and Mn, Si as well as P.

Figure 2.130 presents scanning electron microscopy (SEM) of opened fracture surface, where the high density of Nb-rich particles, Nb(C,N), can be observed distinctly separated from the white phase on the hot crack fracture surface.

a) b)

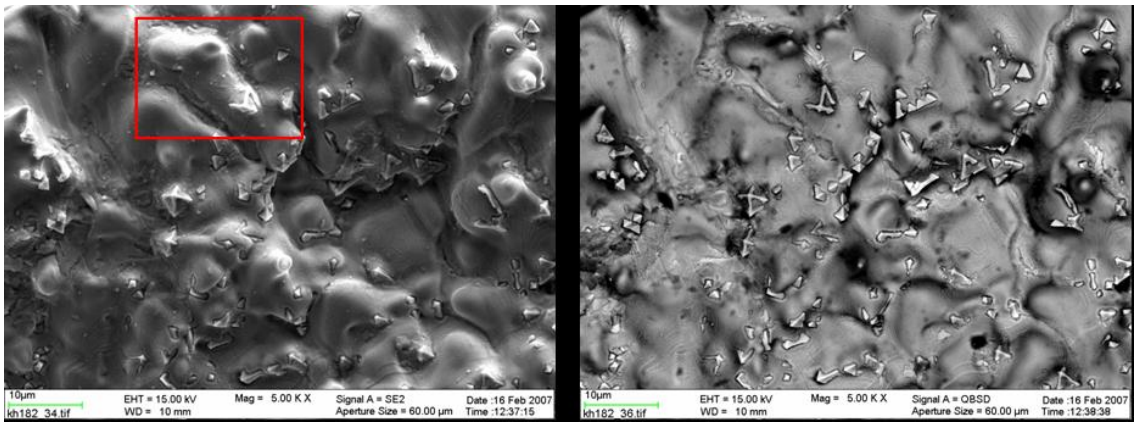

Figure 2.130. Scanning electron microscopy (SEM) of opened fracture surface.

Figures 2.131 and 2.132 present EDS analyses and X-ray element maps of the location marked with a rectangle in Figure 2.130 a).

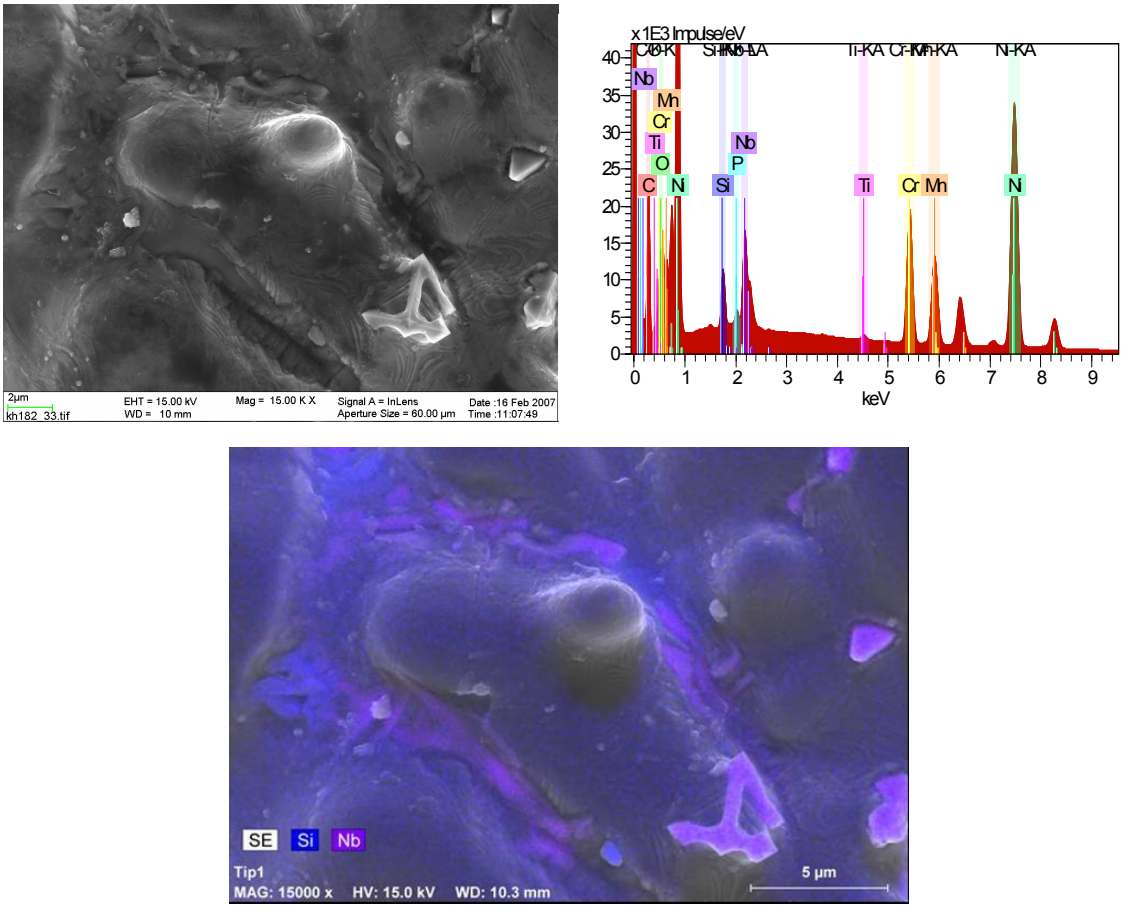

Figure 2.131. EDS analysis of the opened fracture surface showing both the white phase in the valleys between dendrites and the Nb(C,N) particles.

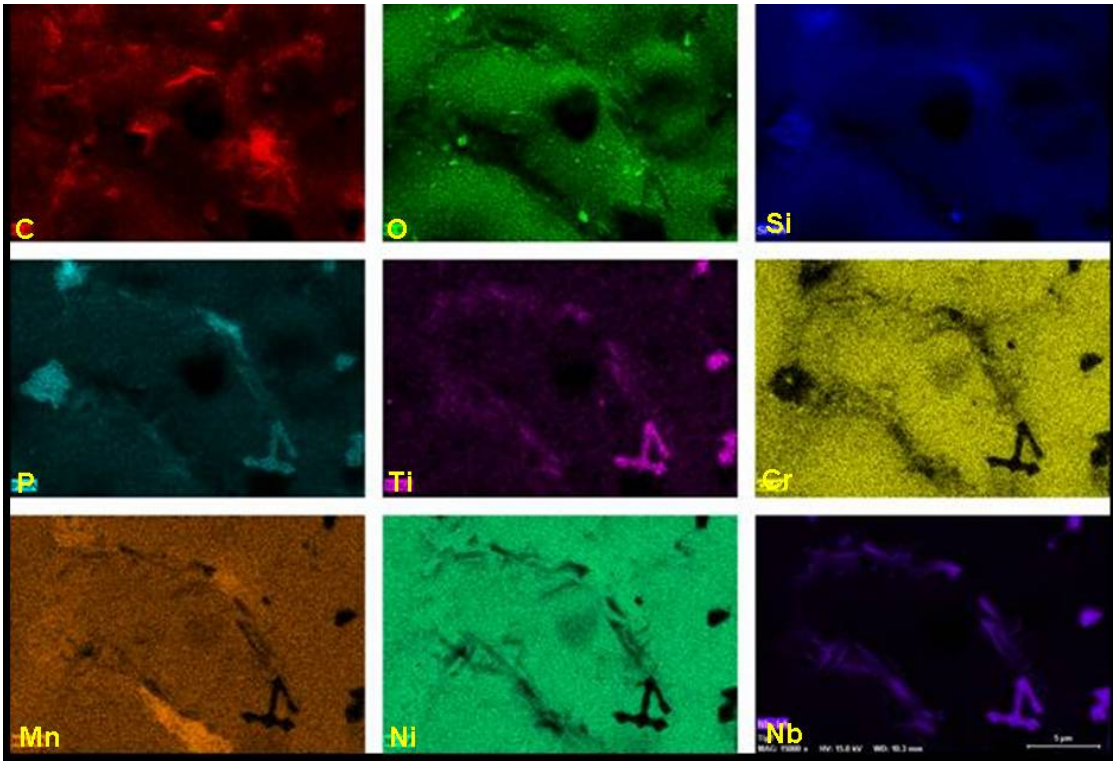

Figure 2.132. X-ray element maps of the opened fracture surface (Figure 2.131). Location marked with a square in Figure 2.130 a).

Figure 2.133 presents scanning electron microscopy (SEM) of opened fracture surface. With a low acceleration voltage of 7 kV the information comes from closer to the surface. The wavy morphology of the fracture surface can be clearly seen, which is an evidence of the molten phase along the grain boundaries during fracture. This suggests that the failure has occurred in the liquid phase rather than by a solid state failure mode, which would produce a smoother intergranular fracture mode. This is an important difference, when hot crack fracture surface is distinguished, e.g., from an EAC fracture surface (see Chapter 3).

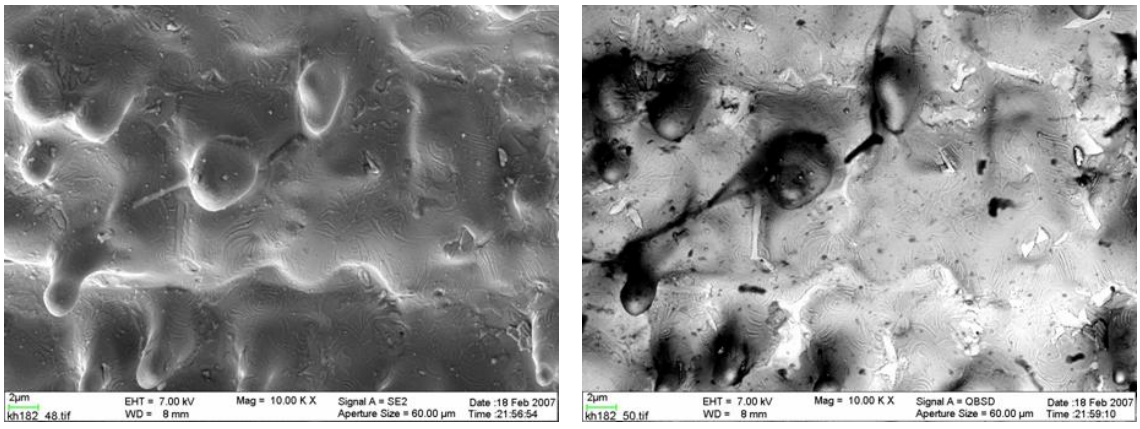

Figure 2.133. Scanning electron microscopy (SEM) of opened fracture surface.

2.6.3 Pure Inconel 82 weld metal

Figure 2.134 presents cracks in pure Inconel 82 weld metal after Varestraint testing (see Chapter 2.3). Alloy 82 showed hot cracking only when welded with the higher heat input (Q = 9,4 kJ/cm).

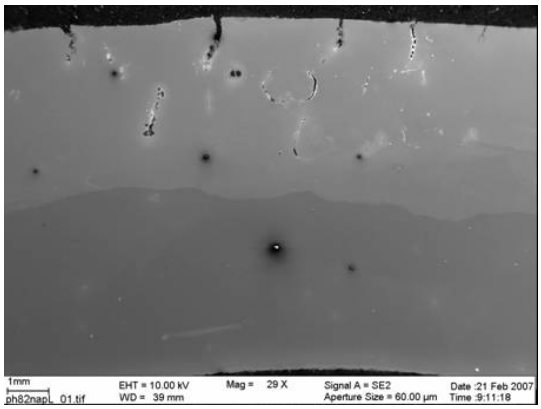

Figure 2.134. Cracks after Varestraint test in pure Inconel 82 weld metal (Q = 9,4 kJ/cm).

Figures 2.135 and 2.136 present EDS analyses and X-ray element maps of a cross-section of a hot crack showing strong Nb segregation.

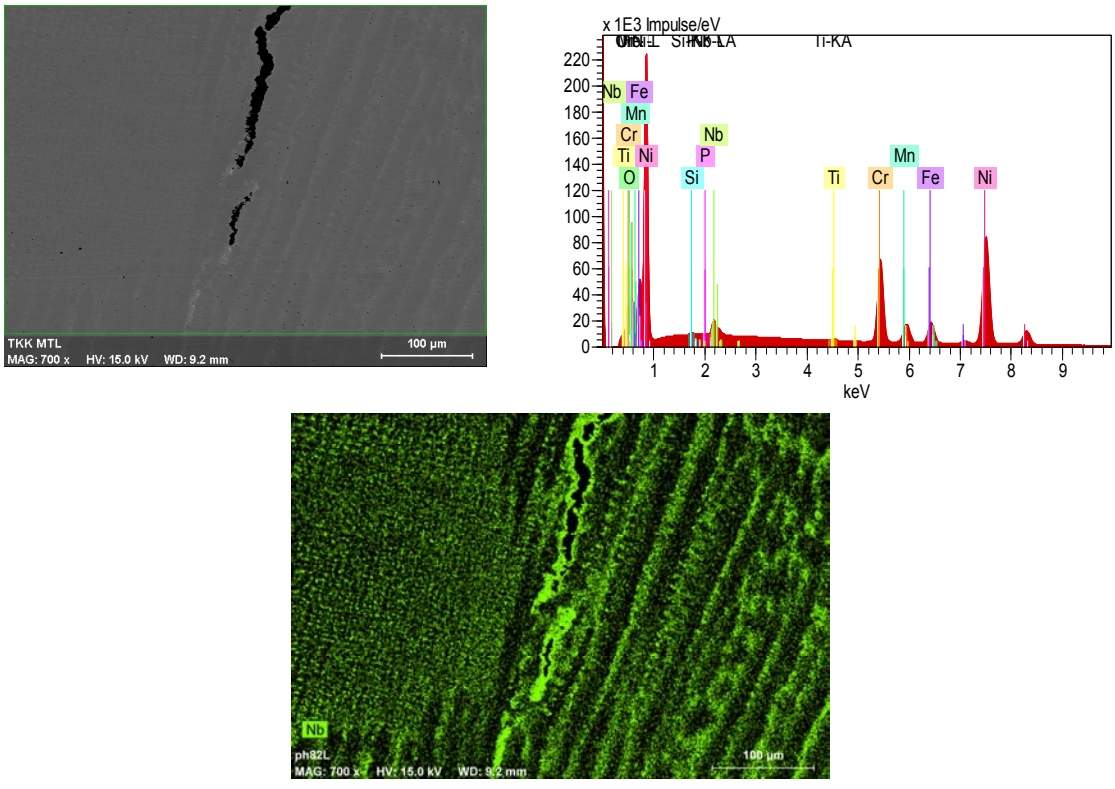

Figure 2.135. EDS analyses of a cross-section of a hot crack in alloy 82, showing strong Nb segregation.

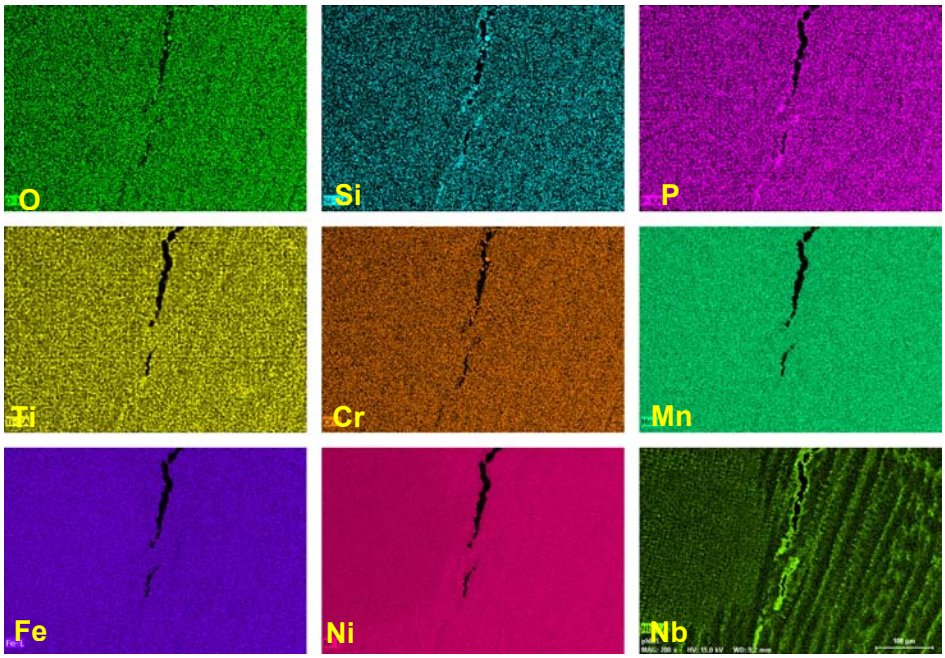

Figure 2.136. X-ray element maps of a cross-section of a hot crack in alloy 82 of Figure 2.135.

Figures 2.137 and 2.138 present EDS analyses and X-ray element maps of a cross-section of a hot crack tip.

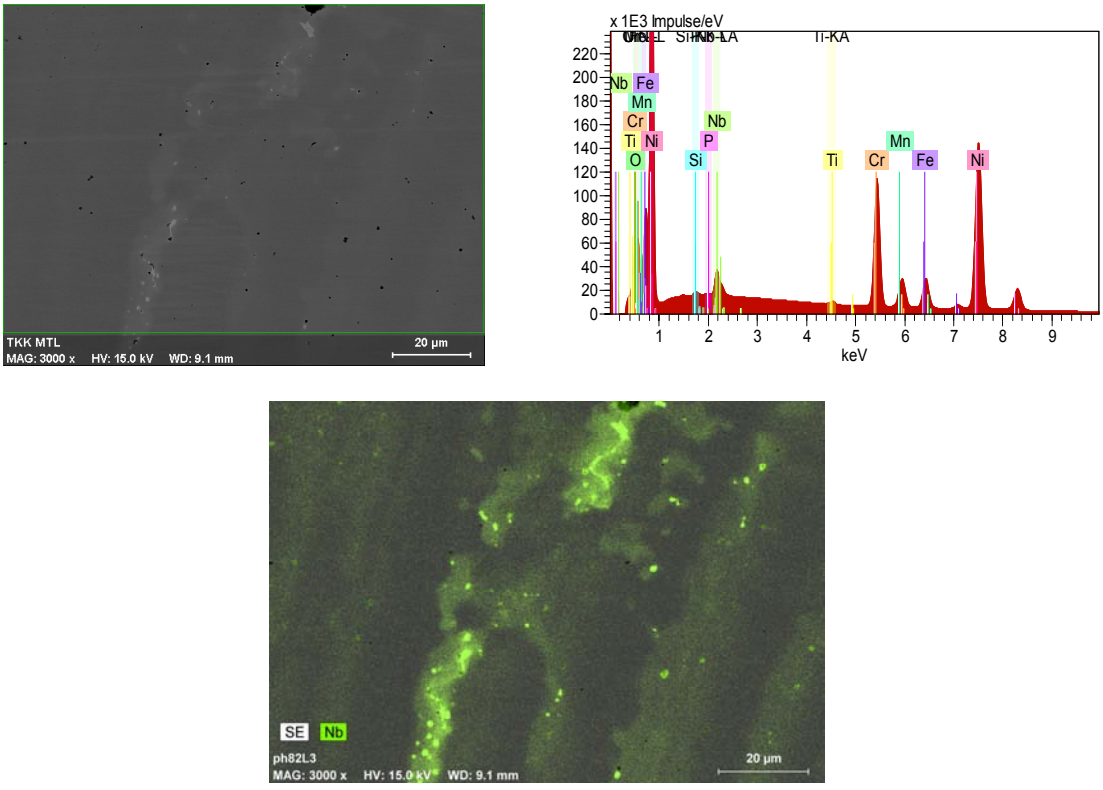

Figure 2.137. EDS analyses of a cross-section of a hot crack tip in alloy 82.

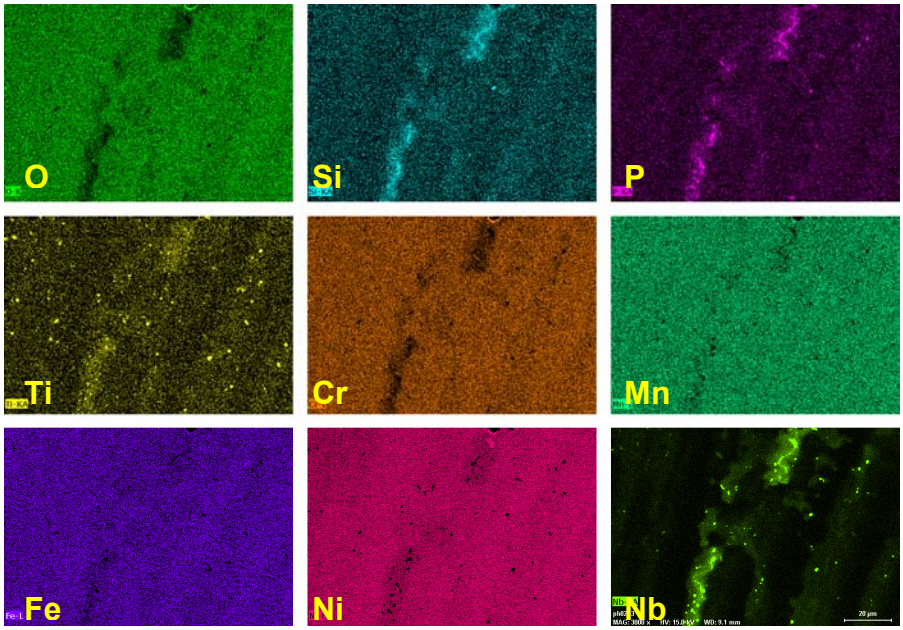

Figure 2.138. X-ray element maps of a cross-section of a hot crack tip in alloy 82 of Figure 2.137.

Figure 2.139 presents scanning electron microscopy (SEM) of the opened fracture surface of alloy 82.

a) b)

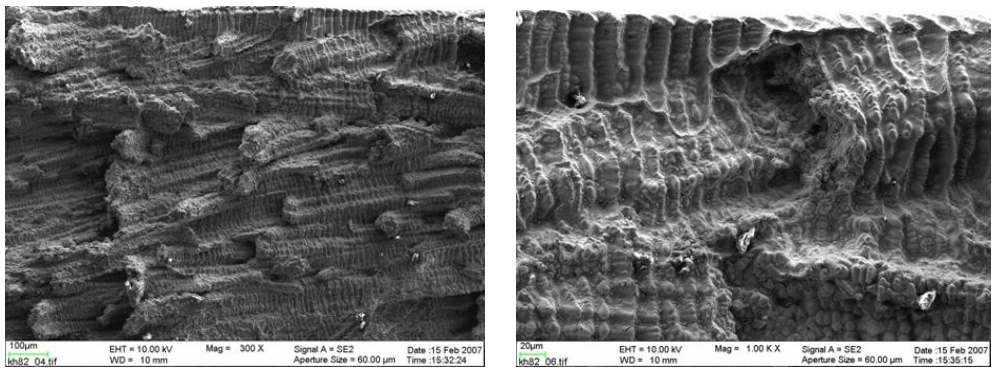

c) d)

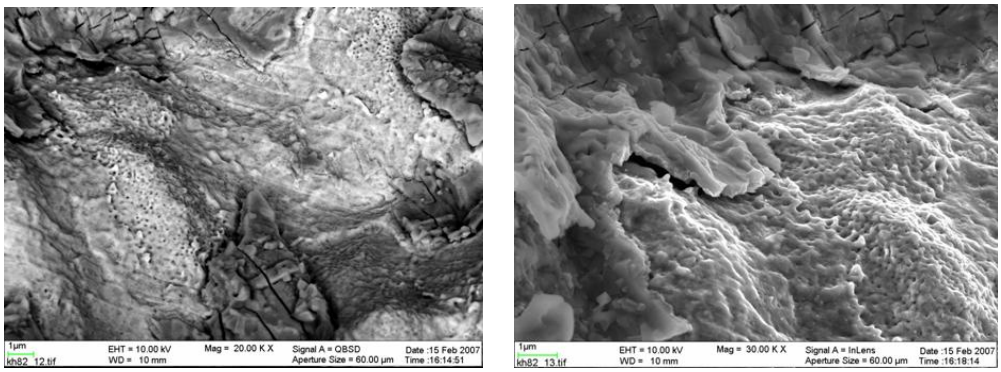

Figure 2.139 (a–d). Scanning electron microscopy (SEM) of opened fracture surface of alloy 82.

In Figure 2.139 d) a thick oxide layer on the fracture surface can be seen. Figure 2.140 and Table 2.5 present EDS analyses of three areas of the oxide layer on the hot crack surface presented in Figure 2.139 d).

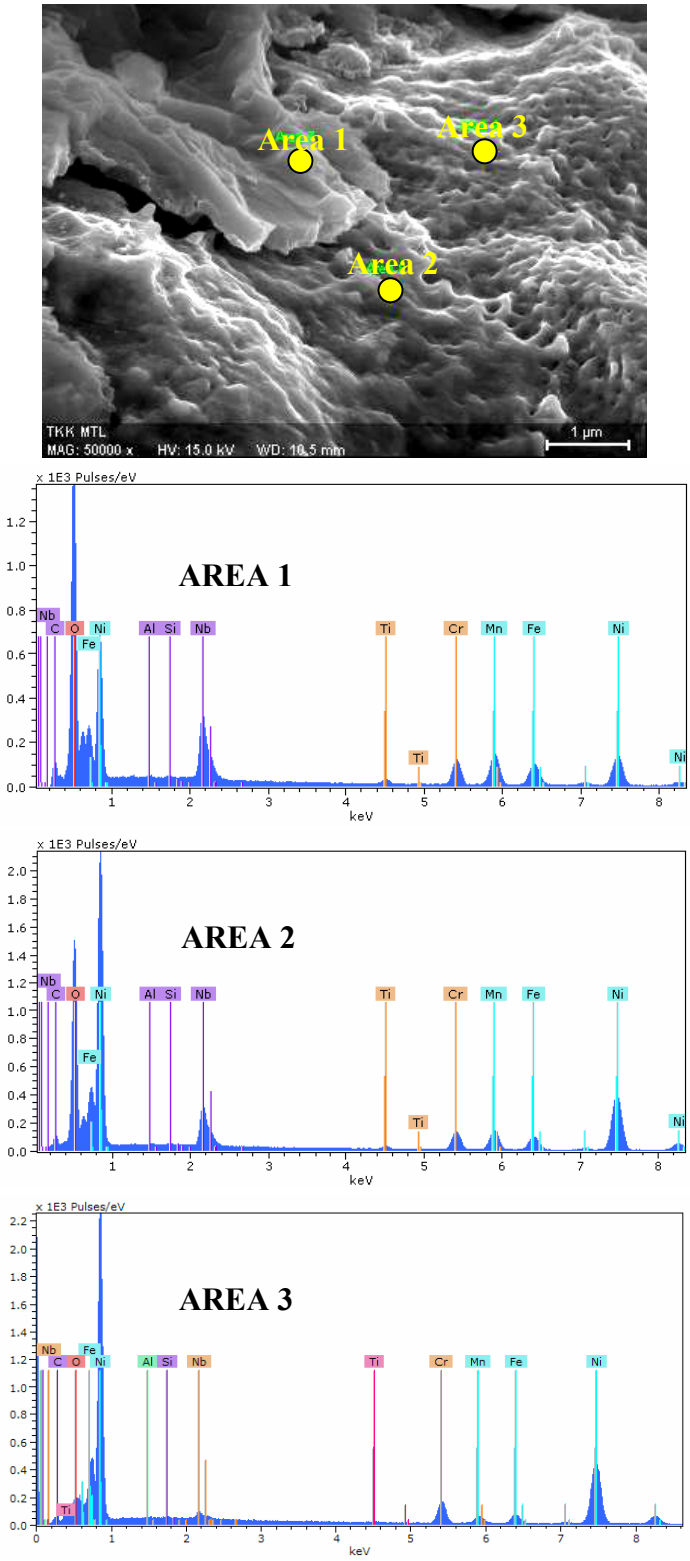

Figure 2.140. EDS analyses of three areas of the oxide layer shown in Figure 2.139 d).

Table 2.5. Chemical compositions from three areas of the oxide layer.

Element	O	Al	Si	Ti	Cr	Mn	Fe	Ni	Nb
Area 1	23,4	0,02	0,18	1,2	8,6	13,4	11,7	30,1	11,6
Area 2	1,4	0,03	0,17	0,3	8,9	2,5	5,9	77,2	3,6
Area 3	1,0	0,04	0,15	0,3	10,0	2,2	5,2	79,2	1,9

Figures 2.141 and 2.142 present EDS analyses and X-ray element maps of the oxide layer of the opened fracture surface.

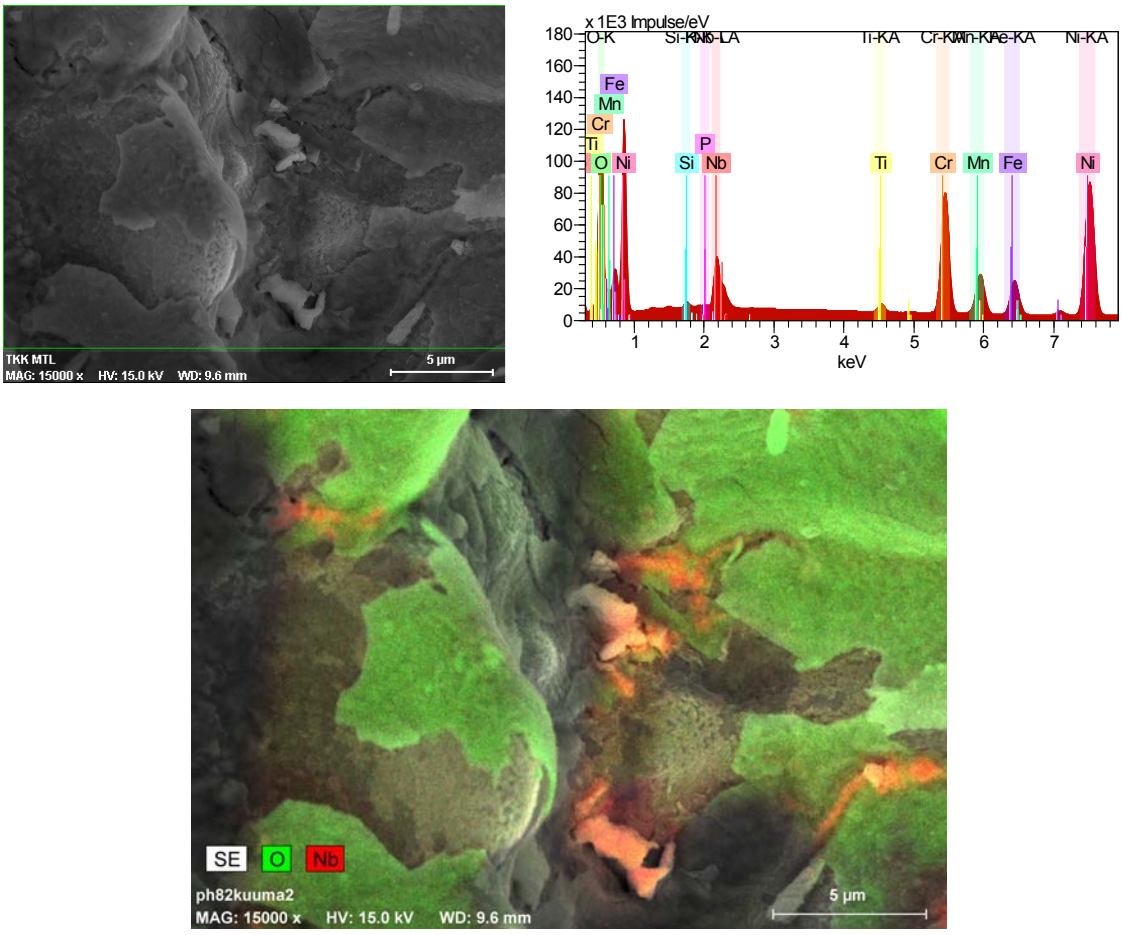

Figure 2.141. EDS analysis of the opened fracture surface of alloy 82 showing distribution of Nb and O.

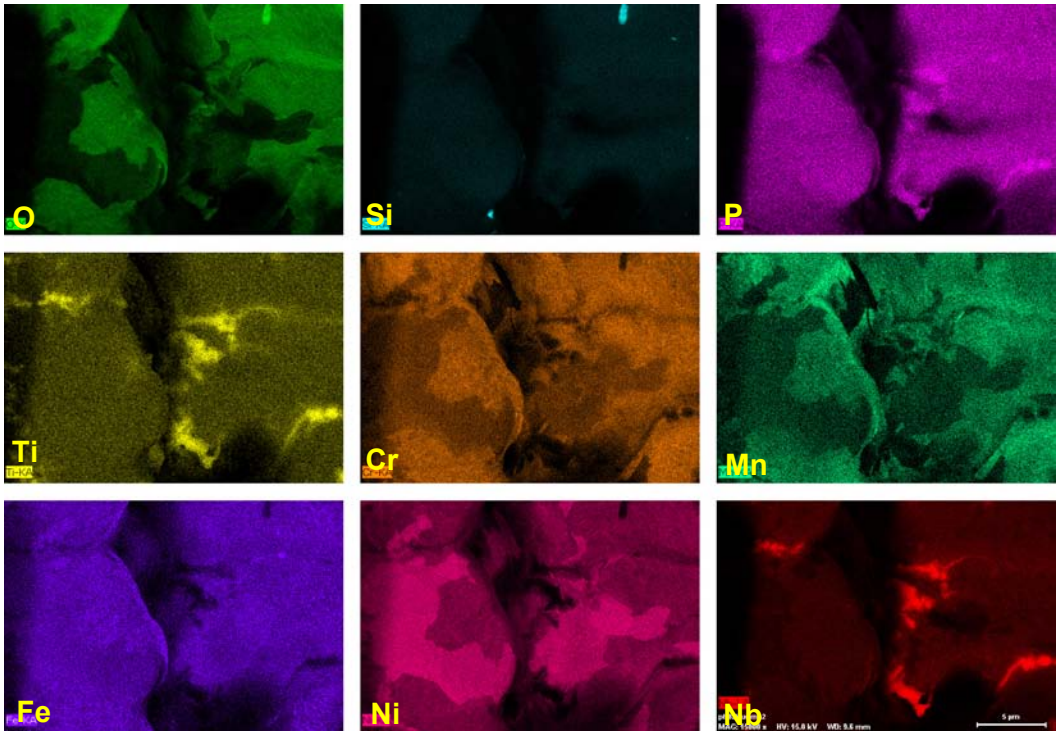

Figure 2.142. X-ray element maps of the opened fracture surface of alloy 82 (Figure 2.141) showing distribution of alloying elements on the fracture surface.

Figure 2.143 presents scanning electron microscopy (SEM) of an opened fracture surface close to the hot crack tip.

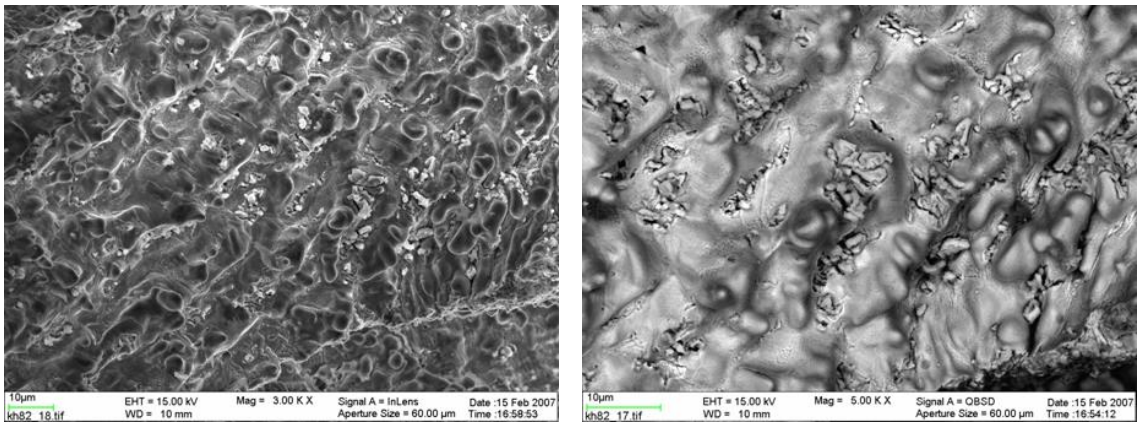

Figure 2.143. Scanning electron microscopy (SEM) of an opened fracture surface.

Figures 2.144 and 2.145 present EDS analyses and X-ray element maps from the opened fracture surface.

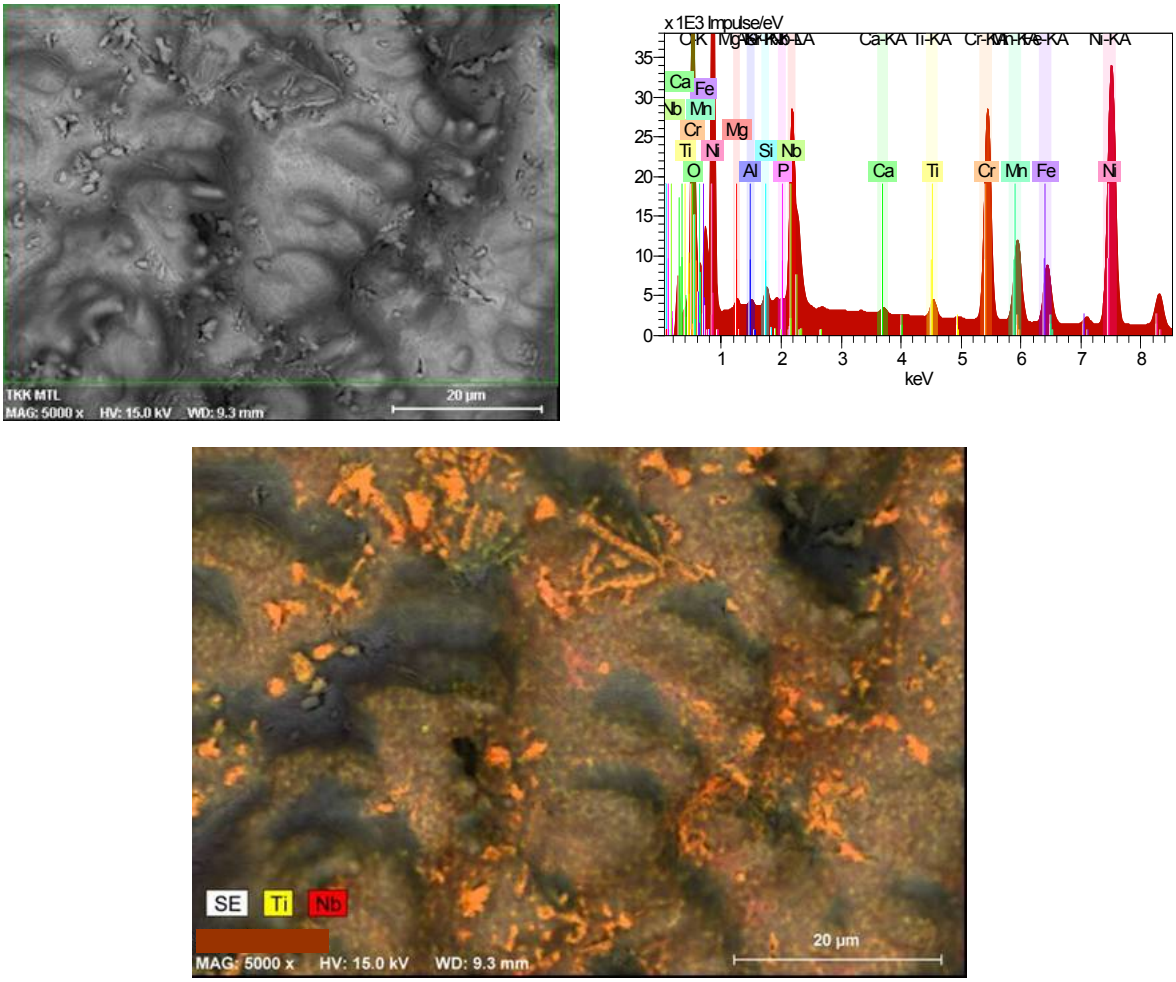

Figure 2.144. EDS analyses of the opened fracture surface of alloy 82 showing distribution of Nb and Ti.

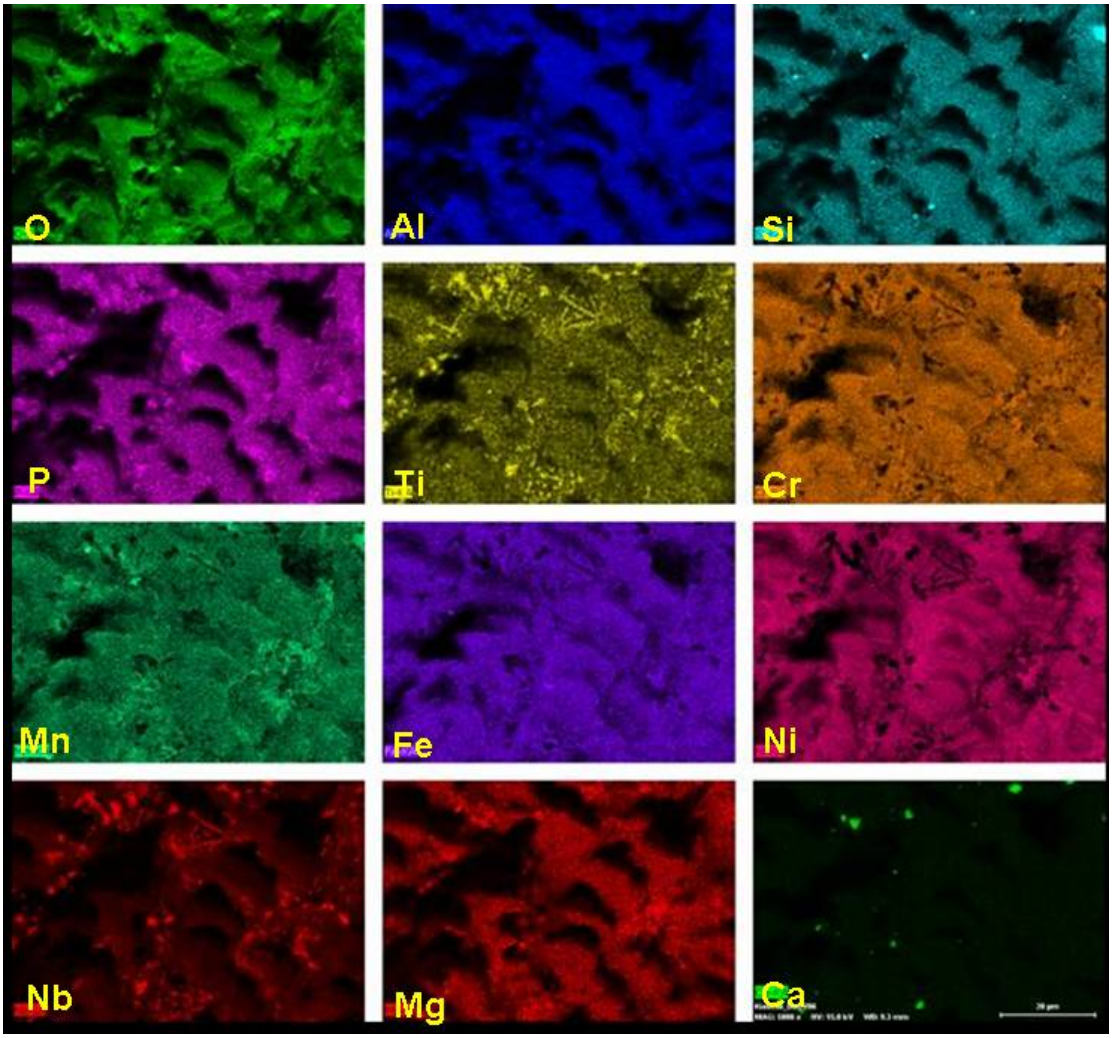

Figure 2.145. X-ray element maps of the opened fracture surface of alloy 82 (Figure 2.144) showing distribution of alloying elements.

Figures 2.146 and 2.147 present EDS analyses and X-ray element maps of a crack on weld pass boundary below the TIG re-melting pass of Inconel 82 weld metal in the Varestraint test.

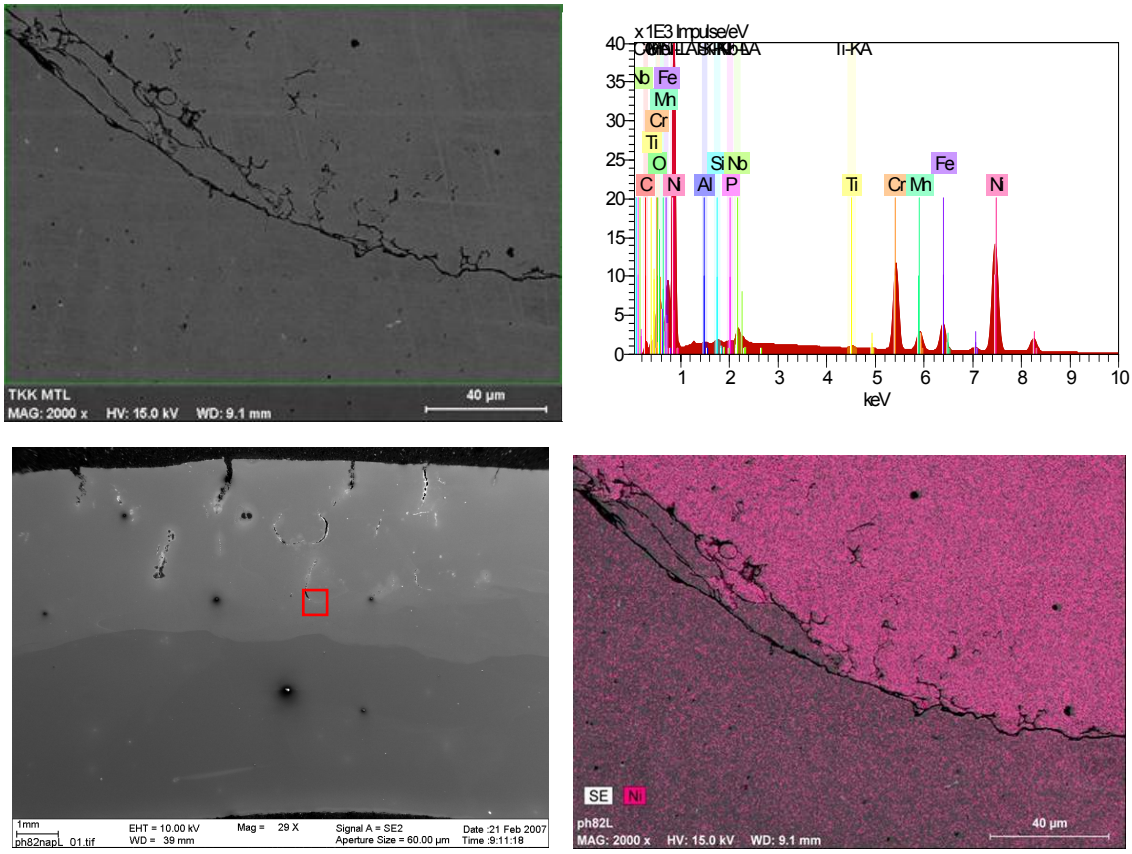

Figure 2.146. EDS analysis of a crack on weld pass boundary below the TIG re-melting pass of Inconel 82 weld metal in the Varestraint test, showing dilution of Ni in the lower pass (detail shows cracking along the boundary between passes 7 and 6 in Figure 2.73).

Pure alloy 82 weld metal hot cracking took place only at higher heat input (Q = 9,4 kJ/cm). The resulting hot cracks were markedly oxidized, probably because of the high heat input and also because of element segregation to the final melt. The chemical composition of the oxide layer shows marked increase of Nb, Mn and Fe, which have a high tendency for oxidation and availability on the fracture surface of a hot crack. Under the oxide layer, the white phase rich in Nb, Mn, Si and P as well as the Nb- and Ti-rich (Ti content 0,34 wt.-%) particles, Nb, Ti(C, N), are also in this alloy clearly visible. In this study of pure weld metal (a groove was filled with a number of weld passes) it was also observed that cracking took place under the weld bead made in the Varestraint test by a liquation cracking mechanism following the boundaries of lower weld passes. The dilution effects probably affect the susceptibility of the boundaries between different weld passes to liquation cracking.

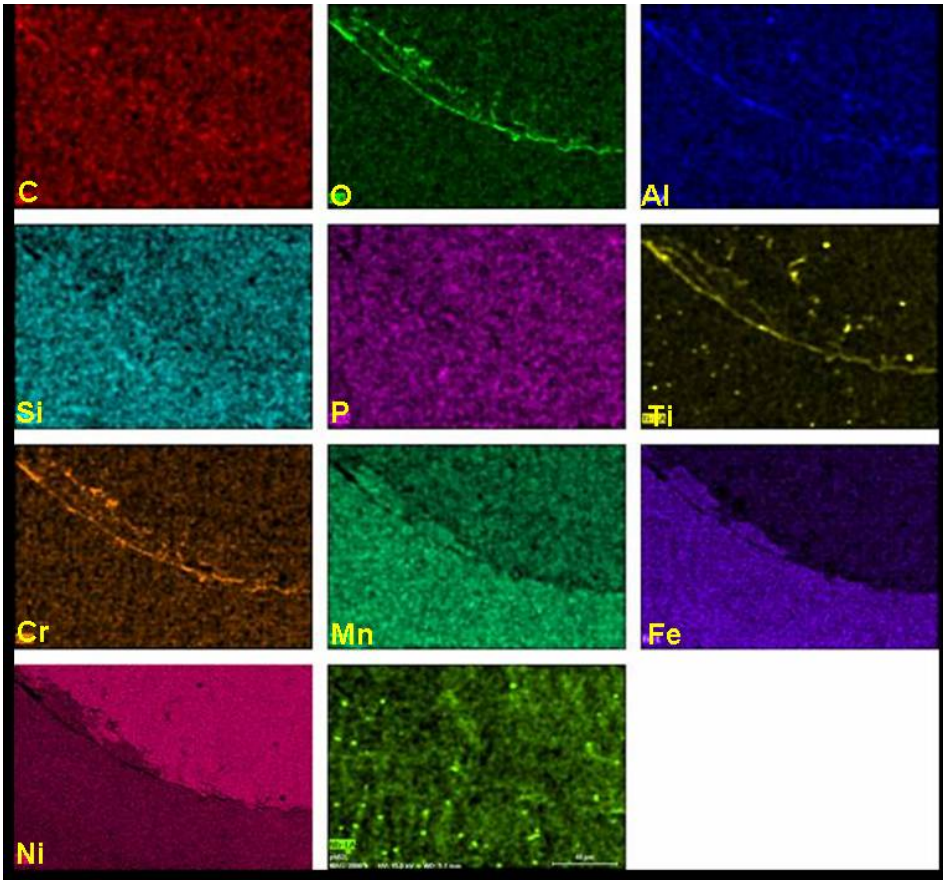

Figure 2.147. X-ray element maps of the weld pass boundary below the TIG re-melting pass of Inconel 82 weld metal in Varestraint test, showing dilution of alloying elements in the lower pass of the filled groove.

2.6.4 Mock-up 1 case (TU1)

Figure 2.148 presents a cross-section of the mock-up 1 dissimilar metal weld before Varestraint testing.

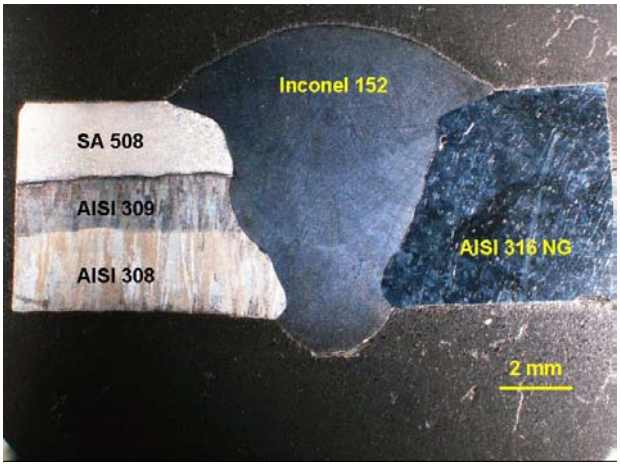

Figure 2.148. Cross-section of the mock-up 1 dissimilar metal weld before Varestraint test.

Figures 2.149–2.153 present optical microstructures of weld metal and base material interfaces.

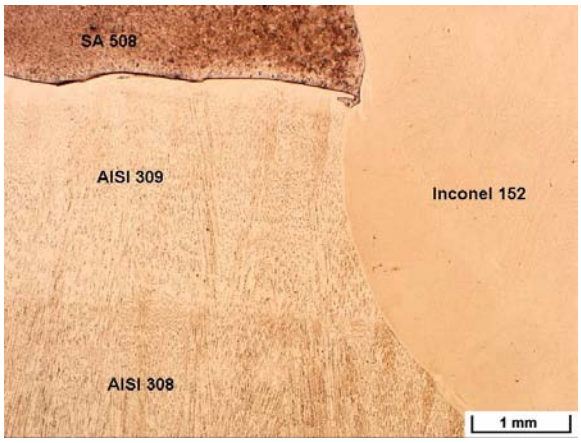

Figure 2.149. Fusion line between pressure vessel steel SA 508, AISI 309 and AISI 308 cladding weld metals and Inconel 152 weld metal.

a) b)

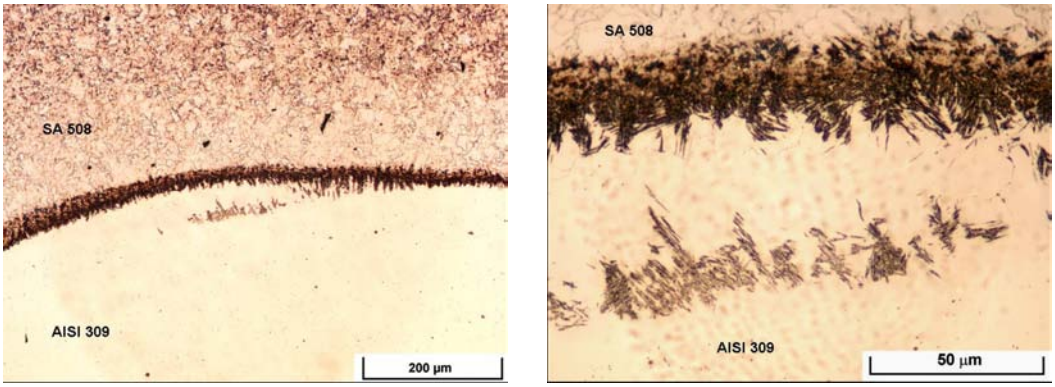

Figure 2.150 (a and b). Fusion line between AISI 309 cladding weld metal and pressure vessel steel SA 508.

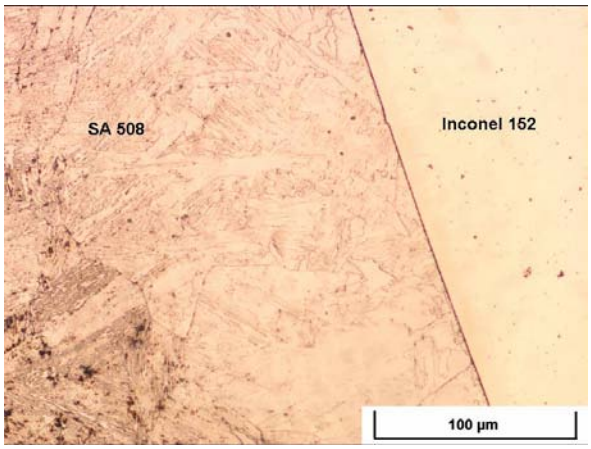

Figure 2.151. Fusion line between pressure vessel steel SA 508 and Inconel 152 weld metal.

a) b)

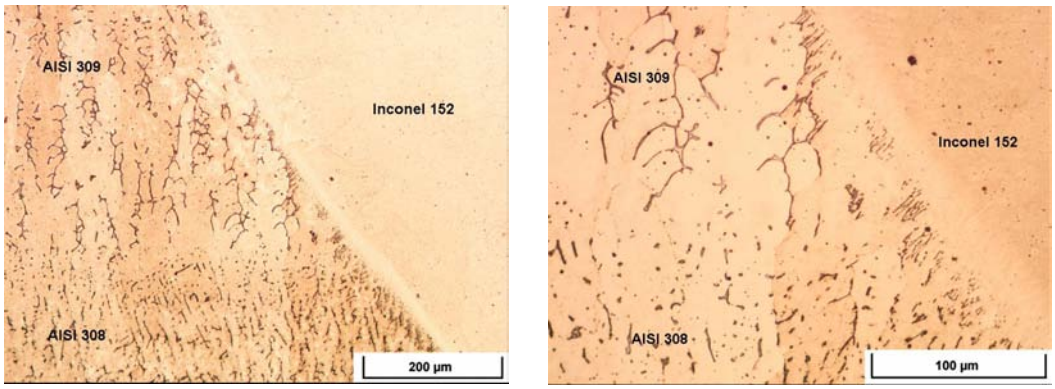

Figure 2.152 (a and b). Fusion line between AISI 309 and AISI 308 cladding weld and Inconel 152 weld metals.

a) b)

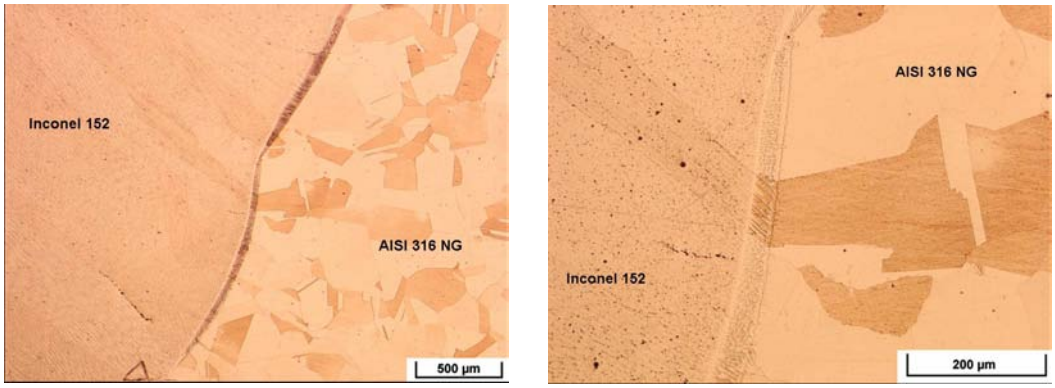

Figure 2.153 (a and b). Fusion line between Inconel 152 weld metal and AISI 316 NG base material.

Figure 2.154 presents the cutting line of the cross-section of the mock-up 1 sample made for microstructural examinations.

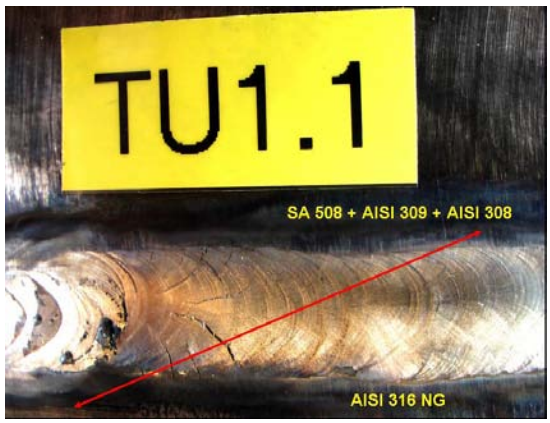

Figure 2.154. Cutting line of cross-section of mock-up 1 sample for microstructural examinations after Varestraint test.

Figure 2.155 presents scanning electron microscopy (SEM) images of cross-section of hot cracks in alloy 152.

a) b)

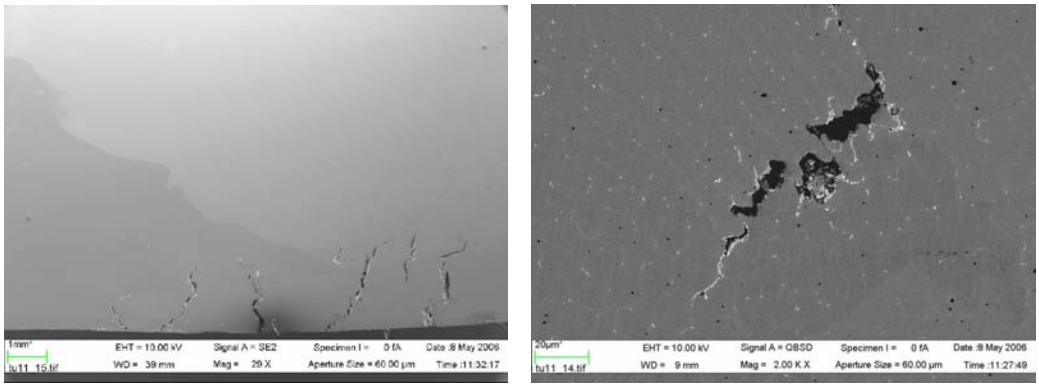

Figure 2.155 (a and b). Scanning electron microscopy (SEM) of hot cracks in alloy 152 weld metal.

Figure 2.156 presents EDS analyses of the white phase ahead of a hot crack from the area marked with a rectangle. In this phase very high segregation of Nb is present together with P, Si and Fe.

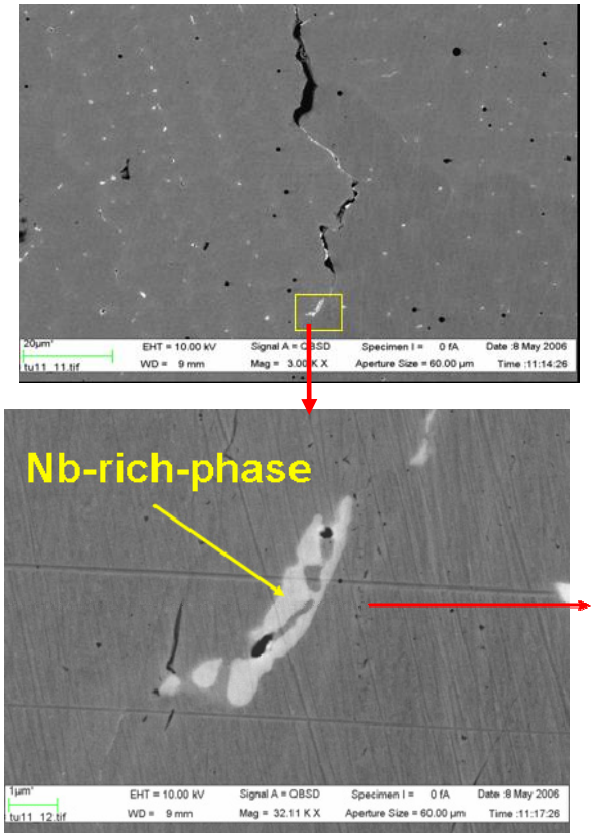

Element	Si	P	Nb	Cr	Fe	Ni
Inconel 152 electrode (wt.-%)	0,4	0,003	1,54	28,7	10,4	55,2
Nb-rich-phase (wt.-%)	1,9	2,7	30,8	18,6	27,4	18,7

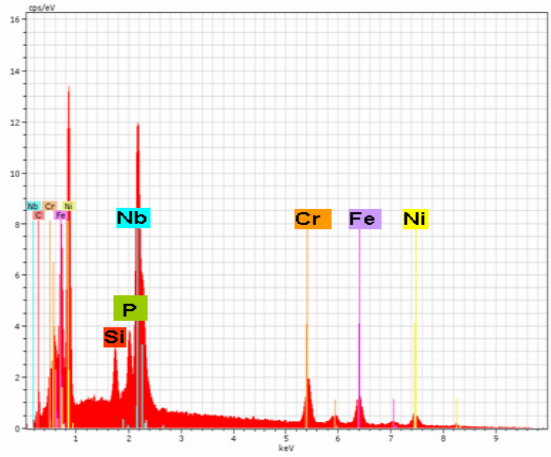

Figure 2.156. EDS analyses of the white phase ahead of a hot crack from the area marked with a square.

Inconel 152 electrode contains niobium (Nb = 1,54 wt.-%) as does also Inconel 182 electrode. It can be seen that hot cracks and the white phase areas related to them in the Inconel 152 weld metal are similar to those in the Inconel 182 of the Neste Oil and TV mock-up hot cracks presented earlier. Figure 2.157 presents additional EDS analyses and X-ray element maps of the cross-section of the hot crack, exhibiting very strong Nb-segregation and co-segregations of Si and Mn to the dendrite boundary.

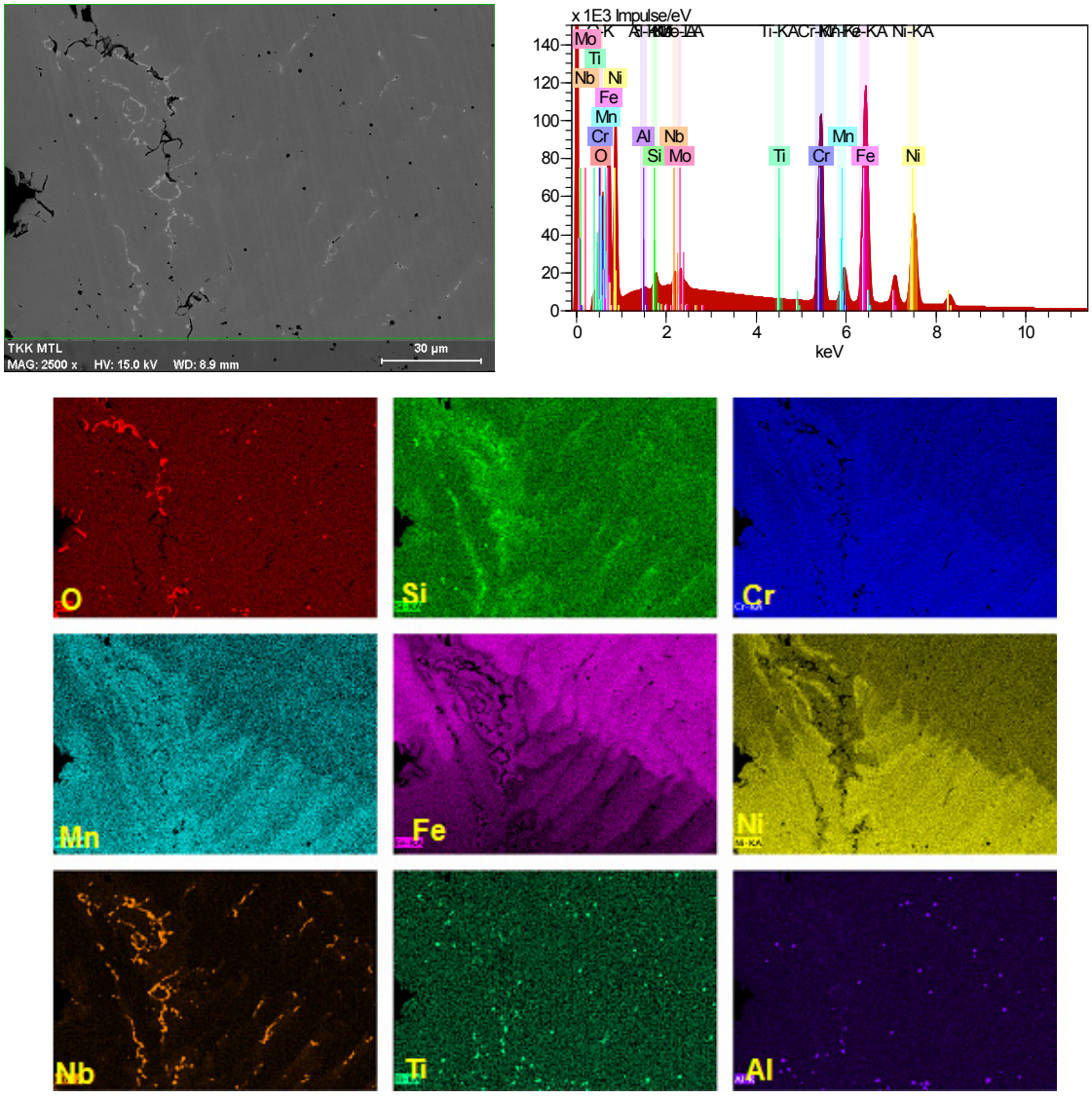

Figure 2.157. EDS analysis and X-ray element maps of the cross-section of a crack showing very high enrichment of Nb in the white phase.

Figures 2.158 and 2.159 present EDS analyses and X-ray element maps of the cross-section of a hot crack.

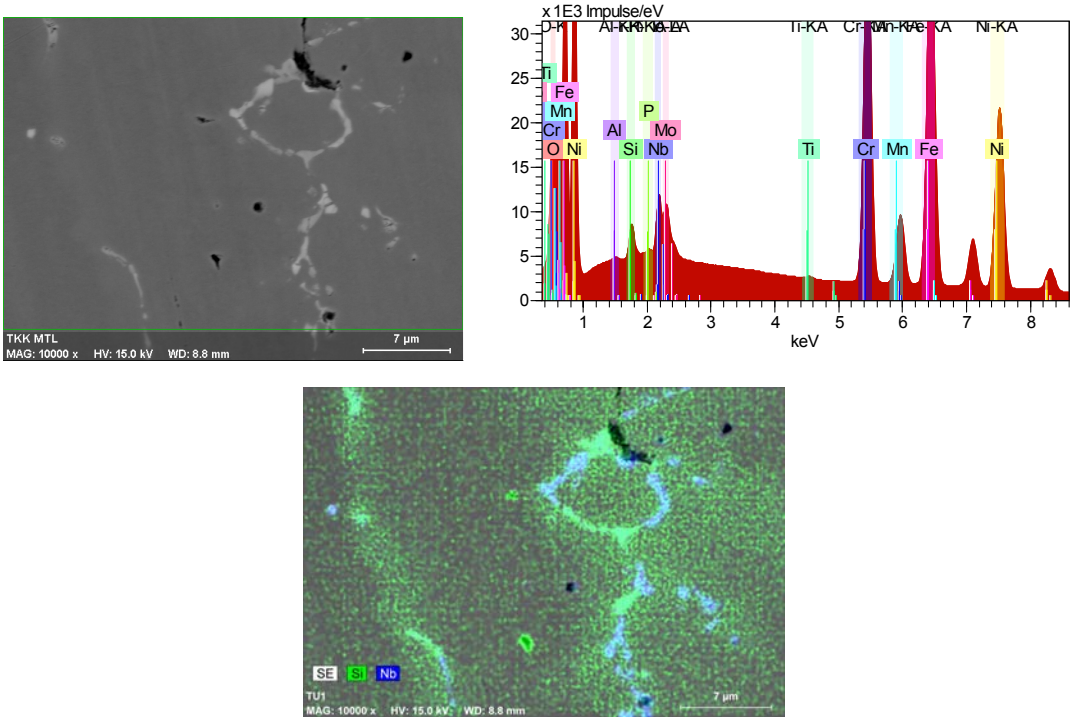

Figure 2.158. EDS analysis from the cross-section area of white phase ahead of a hot crack showing very high enrichment of Nb and Si.

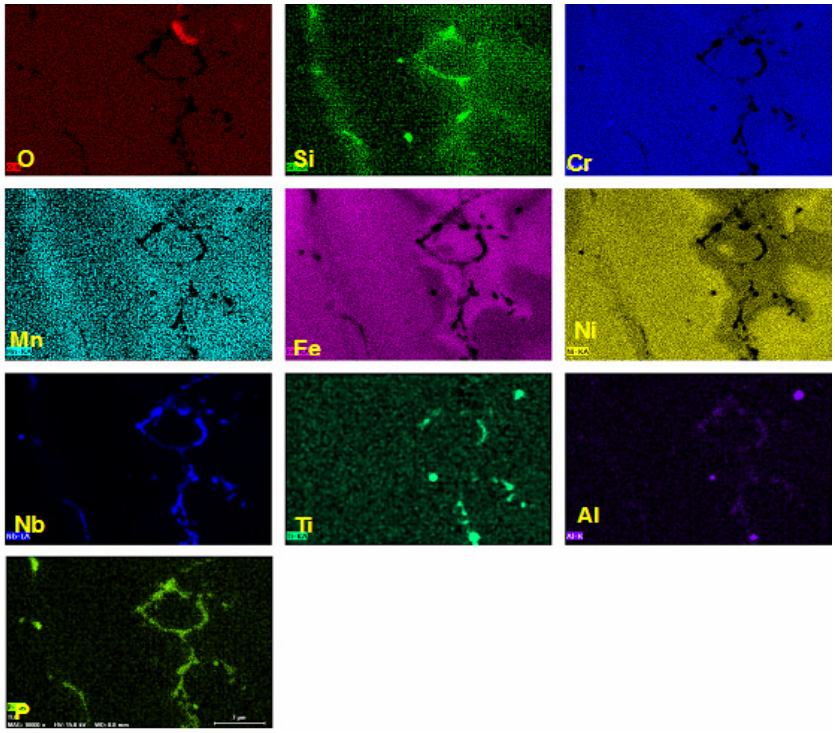

Figure 2.159. X-ray element maps of the cross-section of a hot crack tip area (Figure 2.158). Enrichment of Nb, P, Si, and Mn to the dendrite boundary region and the white phase is clear compensated by depletion of Cr, Ni and Fe. Ti is enriched in Nb, Ti(C, N) particles.

Figure 2.160 presents scanning electron microscopy (SEM) of an opened fracture surface.

a) b)

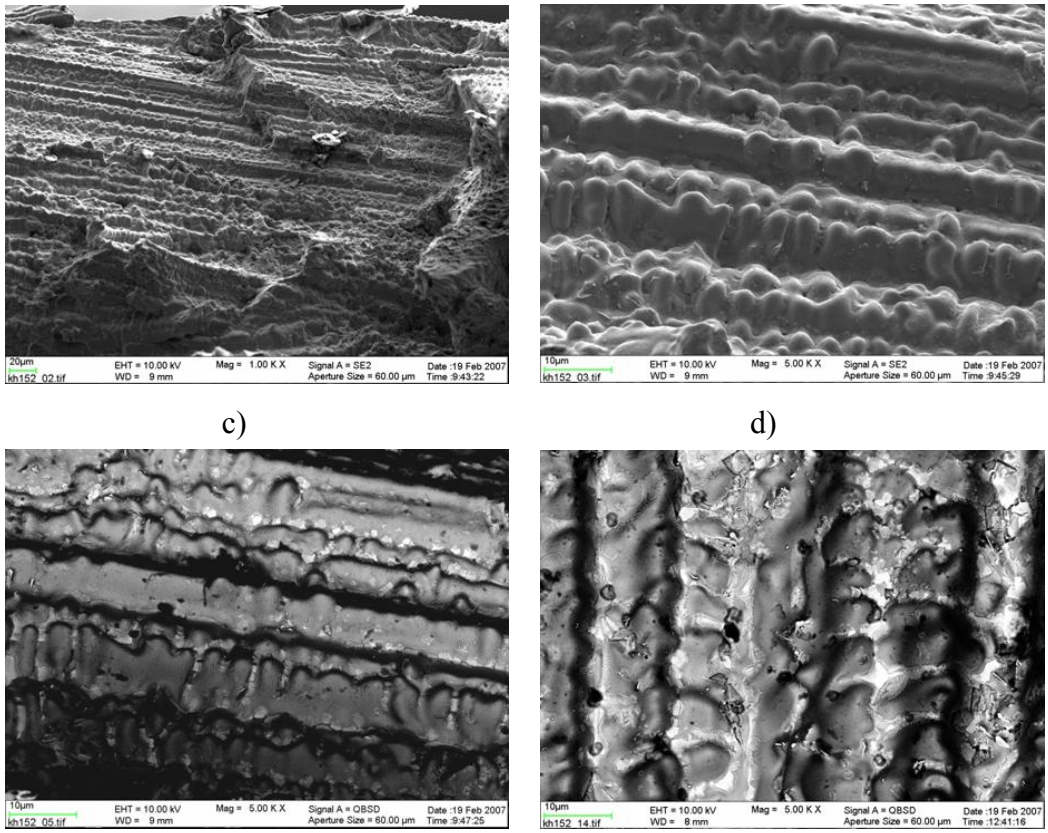

c) d)

Figure 2.160 (a–d). Scanning electron microscopy (SEM) of opened fracture surface showing the presence of white phase on the fracture surface.

Figure 2.161 presents scanning electron microscopy (SEM) of an opened fracture surface, where the presence of the white phase in the valleys between the dendrites is clearly visible.

a) b)

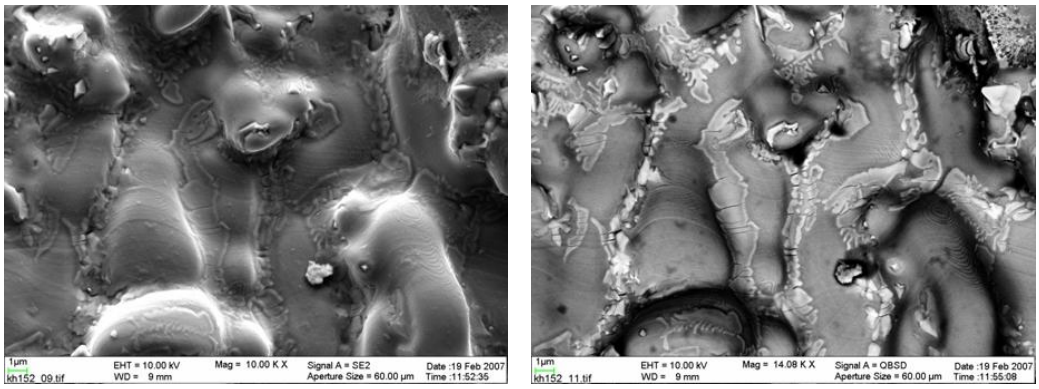

Figure 2.161 (a and b). Scanning electron microscopy (SEM) of opened fracture surface. Note the brittle nature of the lamellar type white phase.

Figures 2.162 and 2.163 present EDS analyses and X-ray element maps of the opened fracture surface.

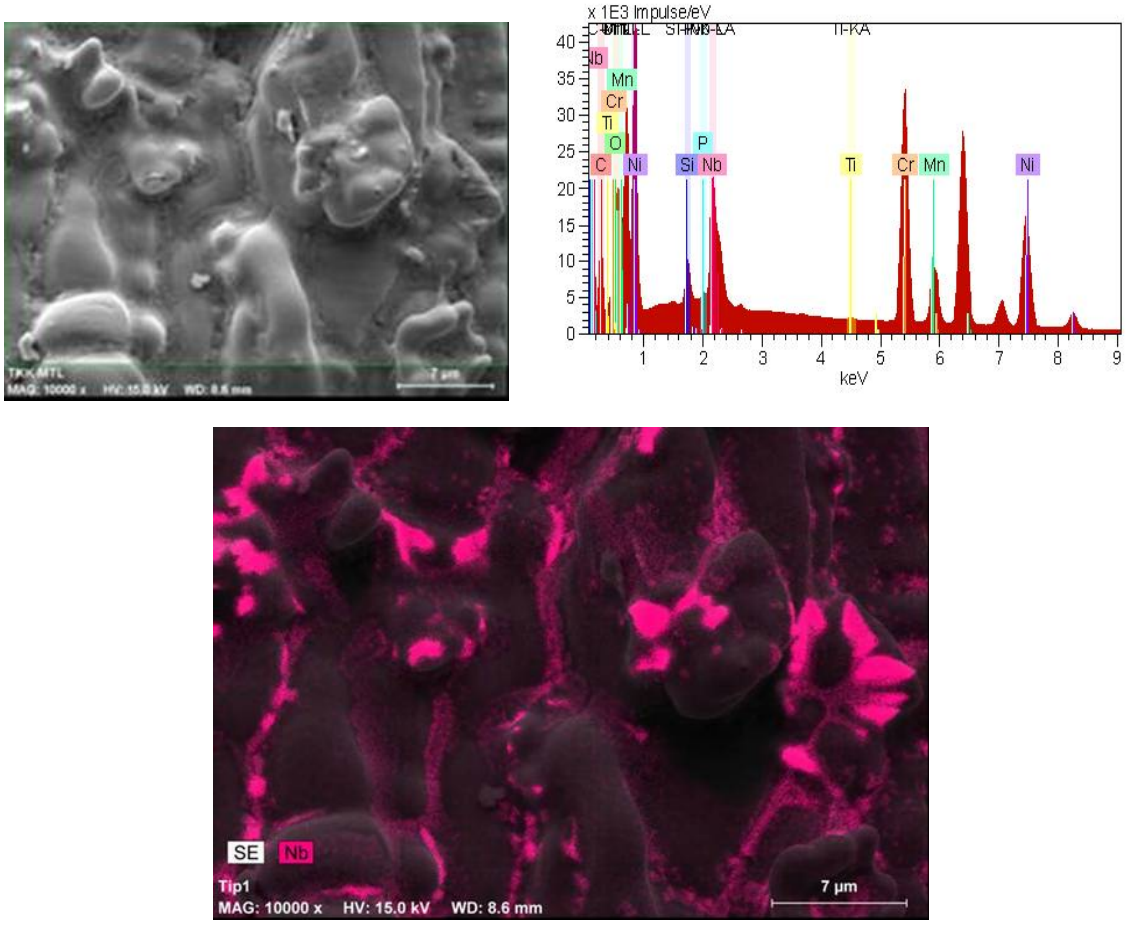

Figure 2.162. EDS analyses of the opened fracture surface showing very high enrichment of Nb.

Alloy 152 weld metal shows similar hot cracking tendency as compared to alloy 182. The Nb-rich white phase is connected to the hot cracks and the phase can be easily found from the cross-sections of the hot cracks as well as from the fracture surfaces (local coverage can be as high as 30%). The dendrite boundaries containing the white phase show, in addition to Nb, a marked increase of Si, Mn and P contents both in the white phase, but also in the wider zone along the dendrite boundaries. Simultaneously, depletion of Cr, Ni and Fe is observed in these zones. In addition to the white phase, plenty of small particles, Nb, Ti(C, N), are present, both in the cross-section as well as on the fracture surfaces.

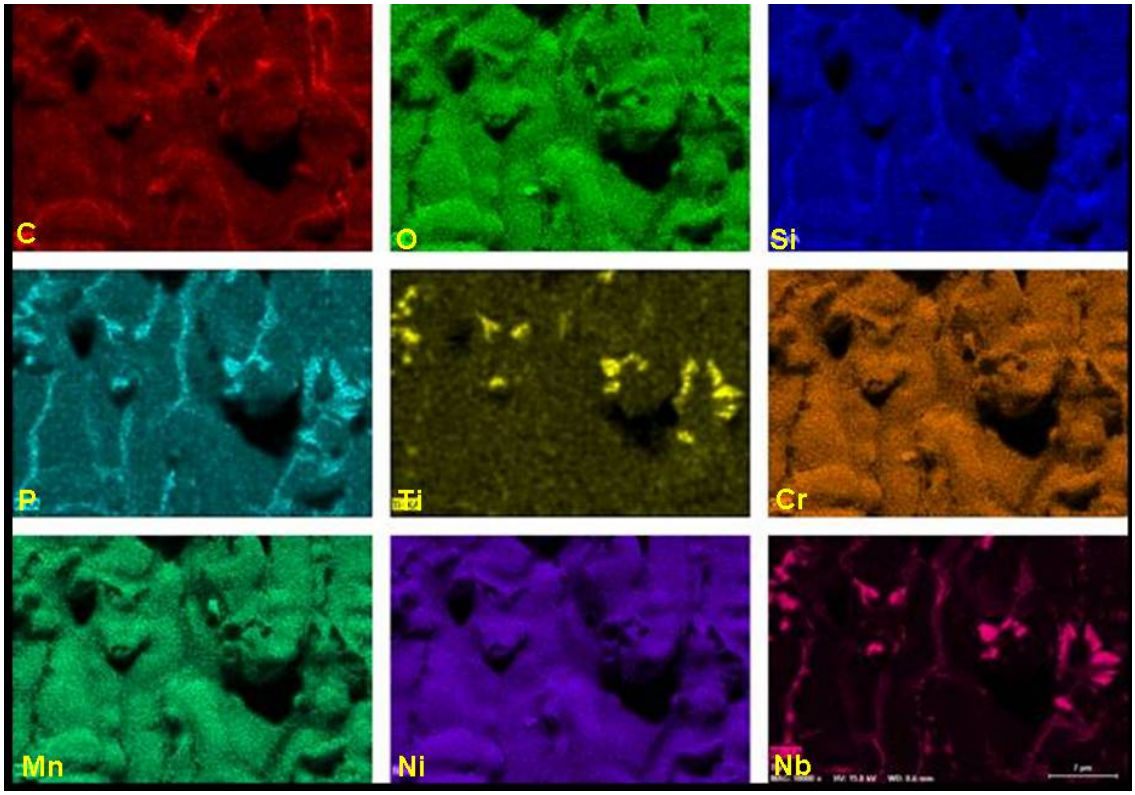

Figure 2.163. X-ray element maps of the opened fracture surface (Figure 2.162) showing that Nb is enriched together with Si, Mn and especially P to the white phase and together with Ti to the particles, Nb, Ti(C, N).

2.6.5 Mock-up 2 case (TU2)

Figure 2.164 presents a cross-section of the mock-up 2 dissimilar metal weld before the Varestraint test.

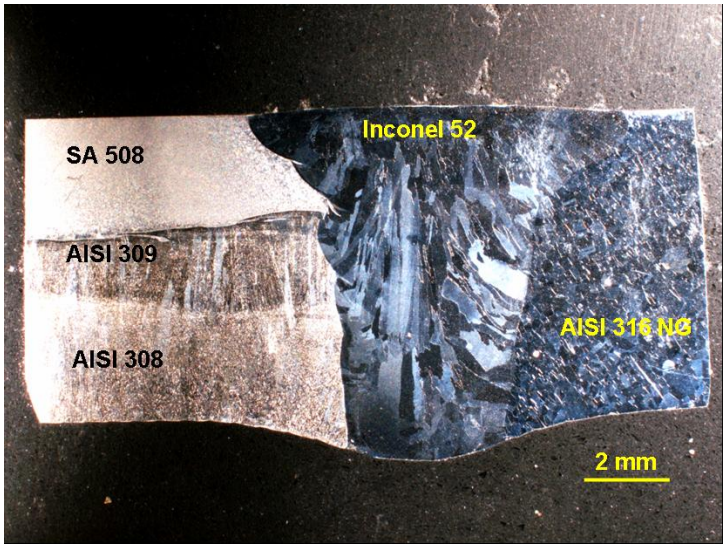

Figure 2.164. Cross-section of the mock-up 2 dissimilar metal weld before Varestraint test.

Figures 2.165–2.167 present microstructures of weld metal and base material interfaces.

Figure 2.165. Fusion line between pressure vessel steel SA 508 and Inconel 52 weld metal.

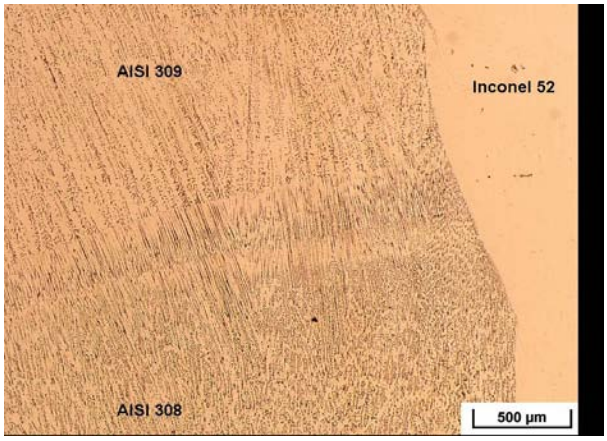

Figure 2.166. Fusion line between AISI 309 and AISI 308 cladding and Inconel 52 weld metal.

a) b)

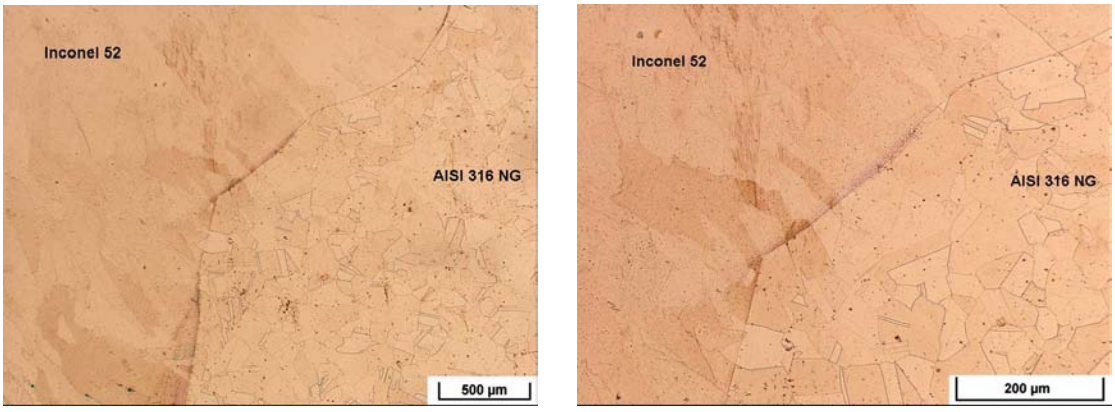

Figure 2.167 (a and b). Fusion line between Inconel 52 weld metal and AISI 316 NG base material.

Figure 2.168 presents the cutting line of the cross-section of mock-up 2 sample for microstructural examinations.

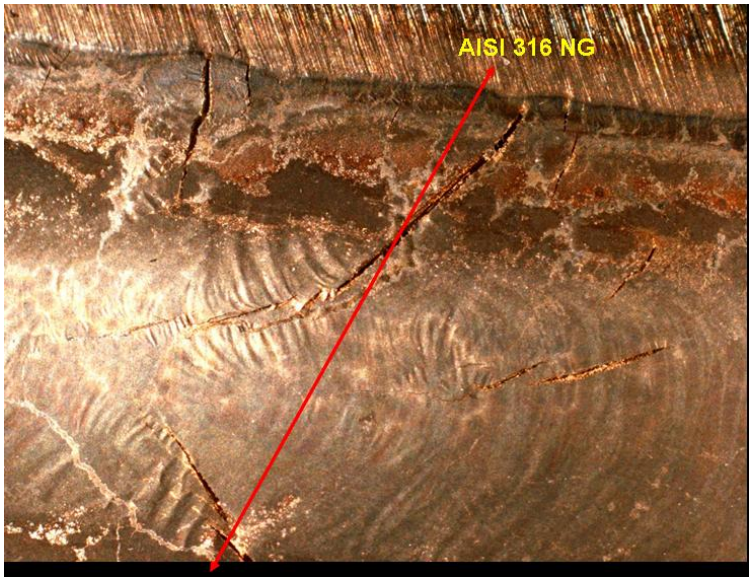

Figure 2.168. Cutting line of cross-section of mock-up 2 sample for microstructural examinations after Varestraint test.

Figures 2.169 and 2.170 present cross-sections of mock-up 2 weld cracks after Varestraint testing. Cracking has also occurred under the TIG re-melting pass of alloy 52 weld metal in the Varestraint test by a liquation cracking mechanism.

a) b)

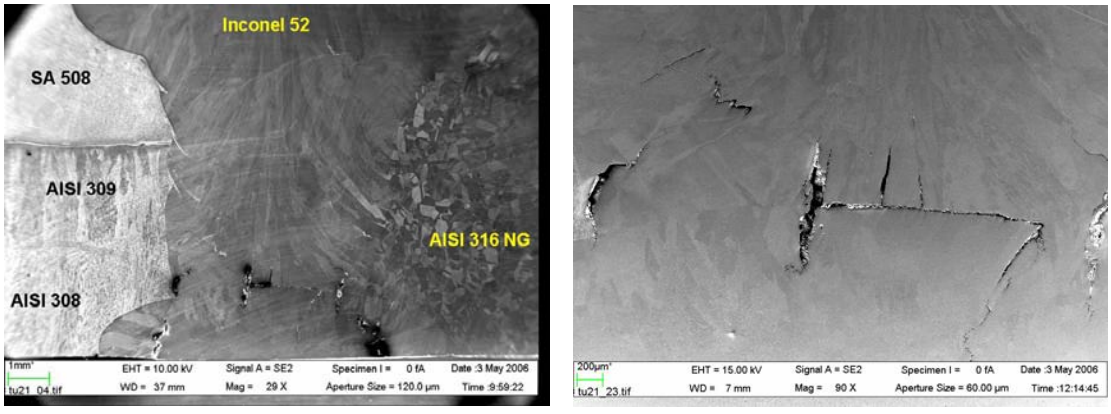

Figure 2.169 (a and b). Cross-section of mock-up 2 weld after Varestraint test.

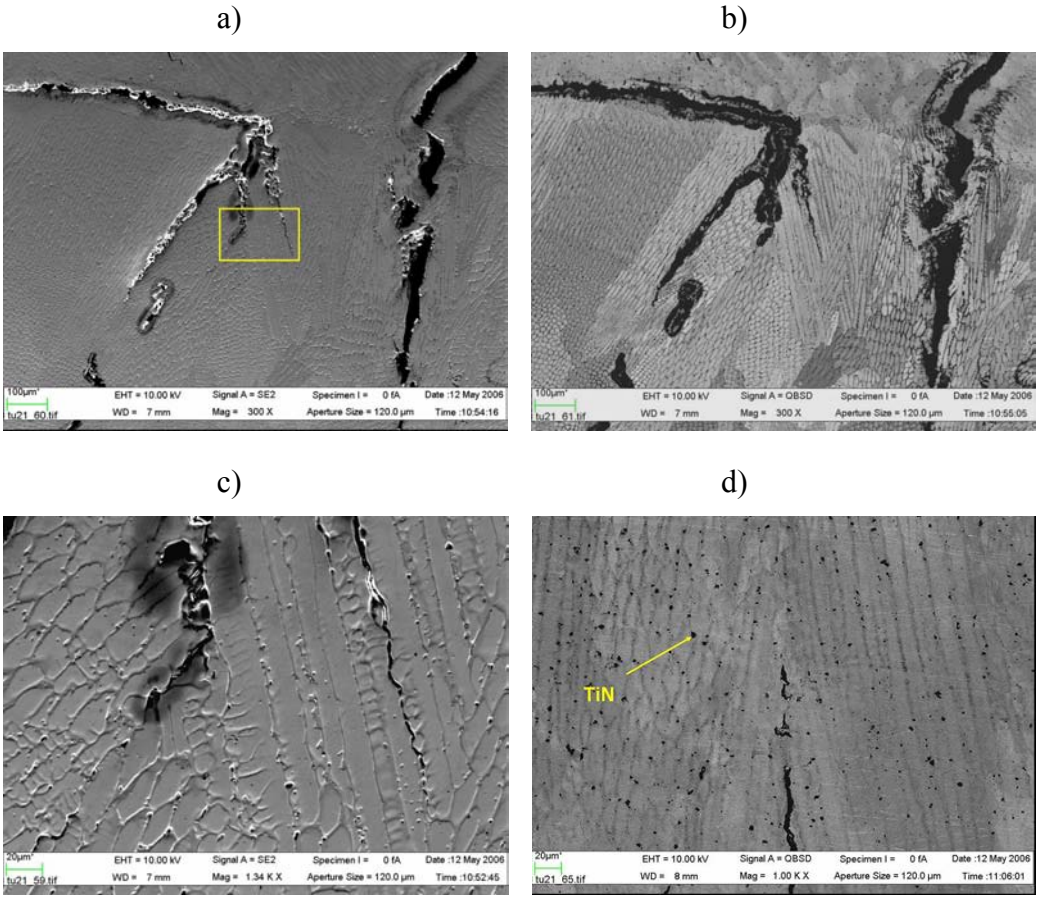

Figure 2.170 (a–d). Scanning electron microscopy (SEM) of the hot cracks.

Filler metal Inconel 52 containing Ti (0,51 wt.-%) does not contain niobium unlike alloys 182 and 152, and thus, in alloy 52 hot cracks form along the dendrite boundaries even without the existence of the white Nb-rich phases. However, a lot of small particles (TiN) have formed along the dendrite boundaries.

Figure 2.171 presents scanning electron microscopy (SEM) of an opened fracture surface.

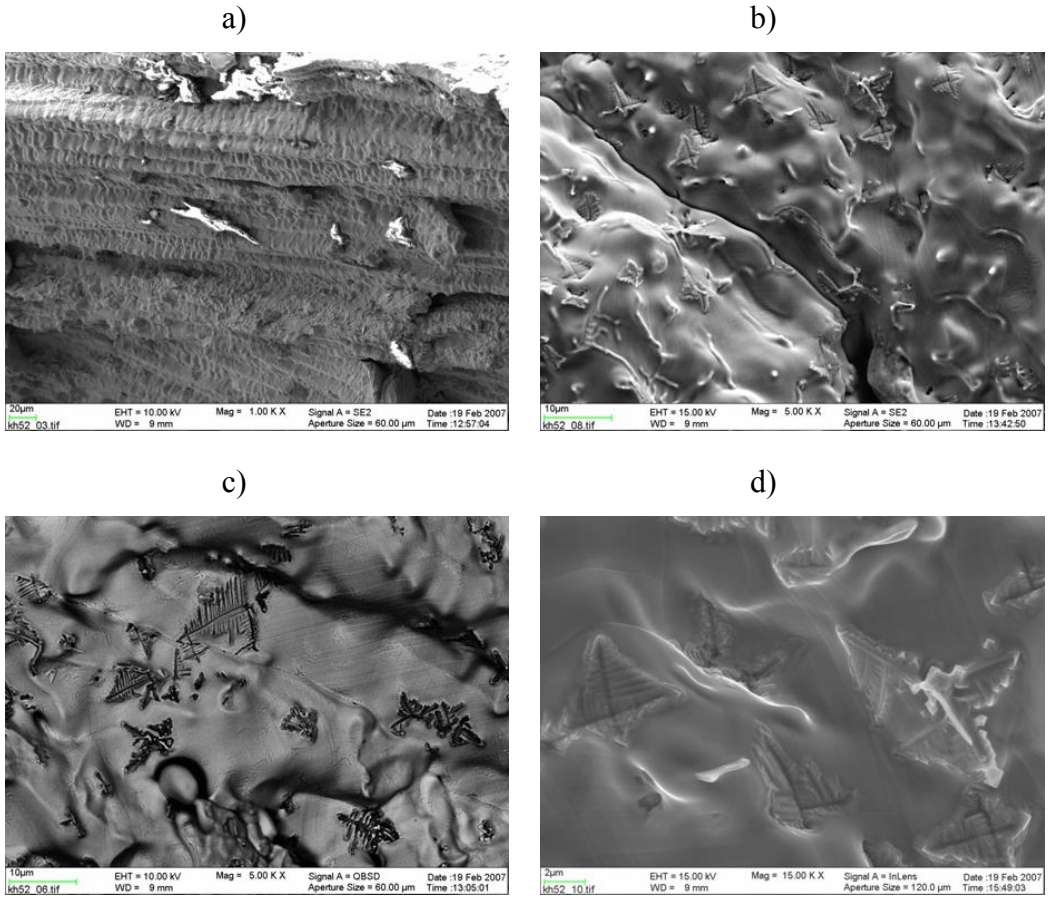

Figure 2.171 (a–d). Scanning electron microscopy (SEM) of an opened fracture surface showing large amount of precipitates.

Figures 2.172–2.176 present EDS analyses and X-ray element maps of the opened fracture surface.

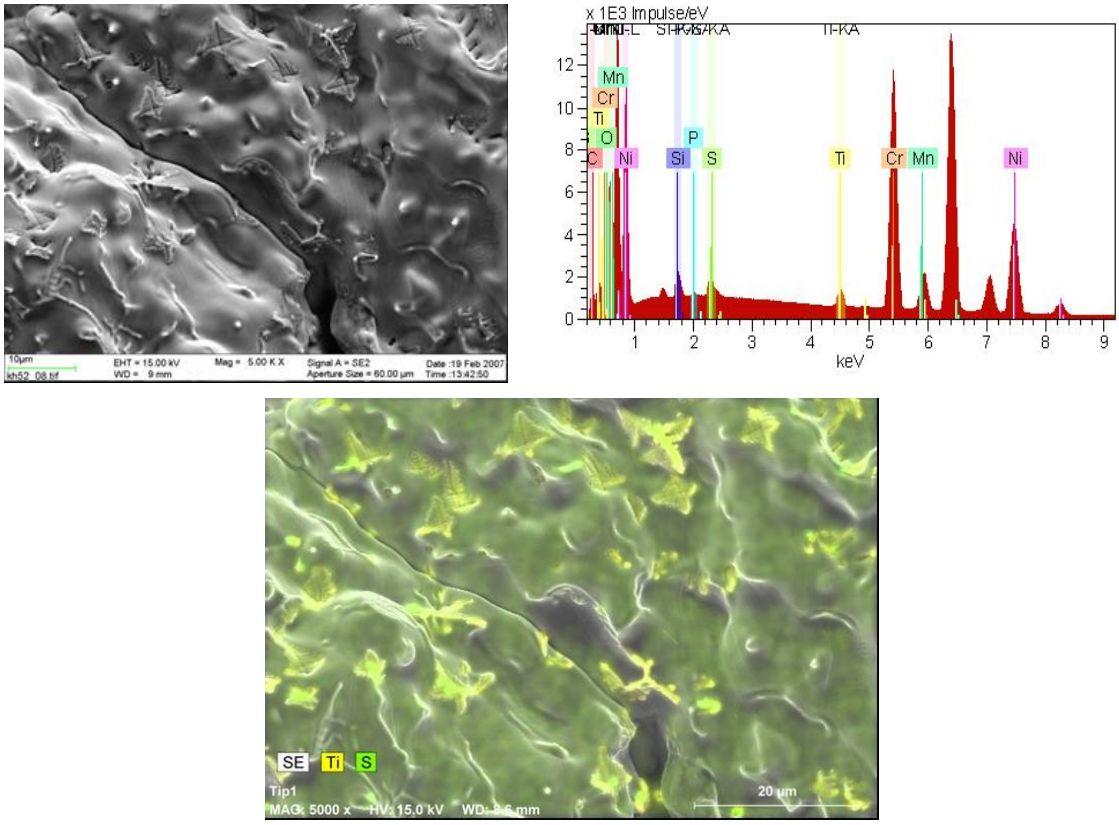

Figure 2.172. EDS analysis of the opened fracture surface shows enrichment of Ti in the precipitates on the fracture surface.

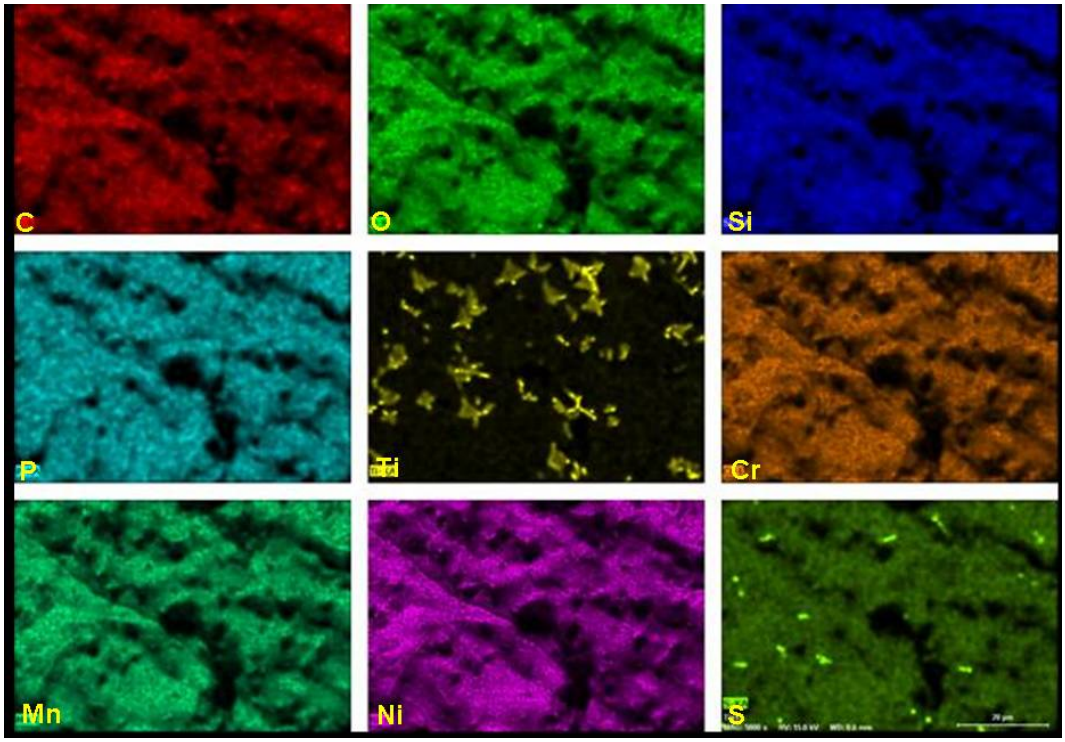

Figure 2.173. X-ray element maps of the opened fracture surface (Figure 2.172).

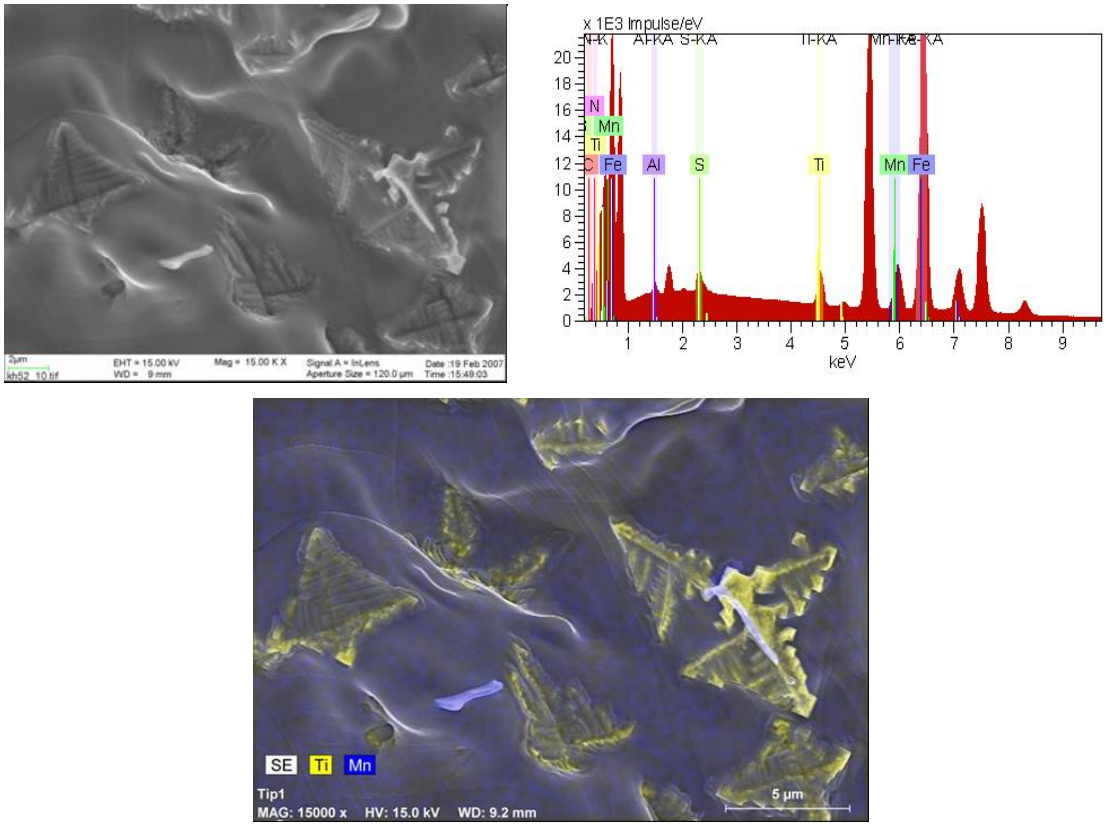

Figure 2.174. EDS analysis of the opened fracture surface.

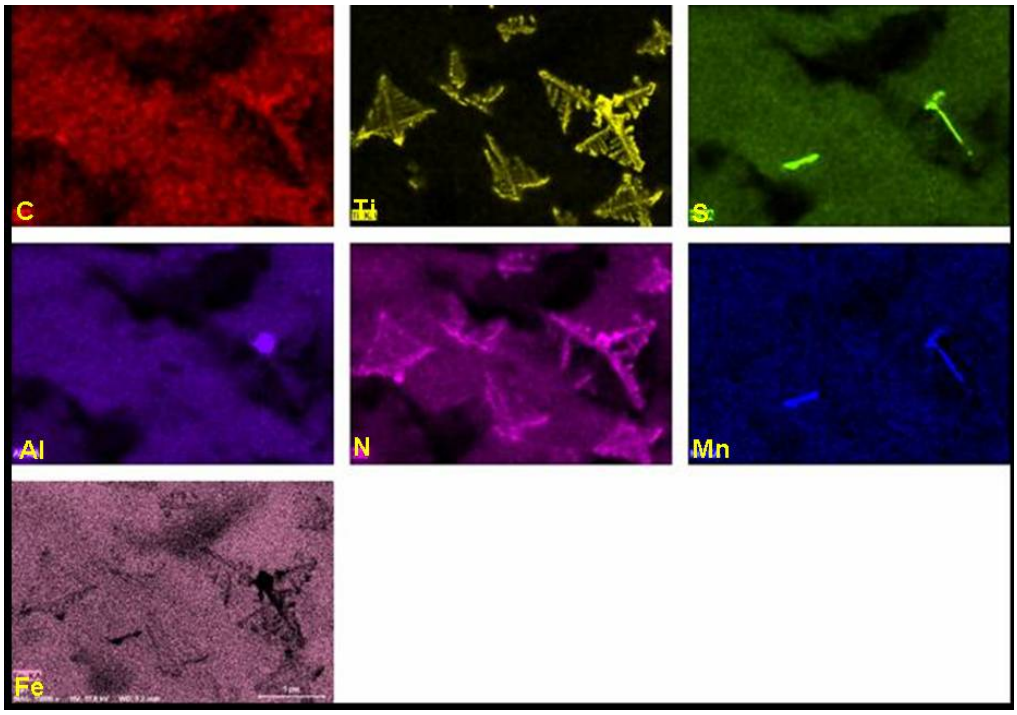

Figure 2.175. X-ray element maps of the opened fracture surface (Figure 2.174).

Hot cracking of alloy 52 does not show any indications of the Nb-rich white phase observed in the earlier cases with alloys 182, 82 and 152, since alloy 52 does not contain Nb. Alloy 52 contains Ti, and therefore a lot of precipitation of TiN(C) was observed both in the cross-sections along the dendrite boundaries, as well as on the fracture surfaces of the hot cracks, where the coverage of the fracture surface by TiN(C) can be quite extensive. The large dendritic TiN(C) phase particles are presumed to have formed in the melt prior to final solidification of the weld. On the fracture surface MnS phase particles are also observed as separate phases. The possible enrichment of Si and Mn (both very low in the alloy) and P would require Auger electron spectroscopy studies for their observation. Thus, in alloy 52, the only marked phase on the hot crack surfaces is TiN(C).

2.6.6 Mock-up 3 case (TU3)

Figure 2.176 presents a cross-section of the mock-up 3 dissimilar metal weld before the Varestraint test.

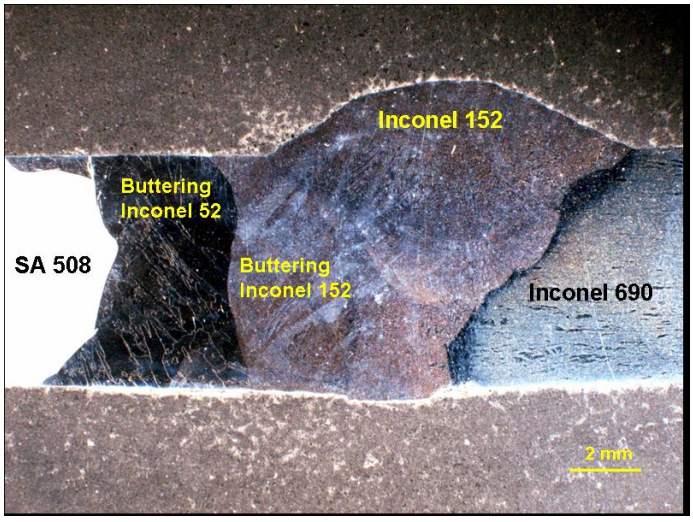

Figure 2.176. Cross-section of the mock-up 3 dissimilar metal weld before Varestraint test.

Figures 2.177–2.180 present microstructures of weld metal and base material interfaces.

a) b)

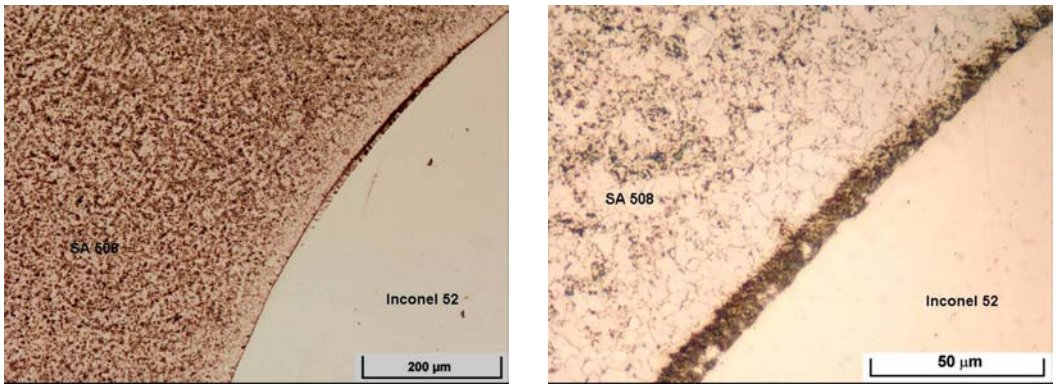

Figure 2.177 (a and b). Fusion line between pressure vessel steel SA 508 and Inconel 52 buttering weld metal.

a) b)

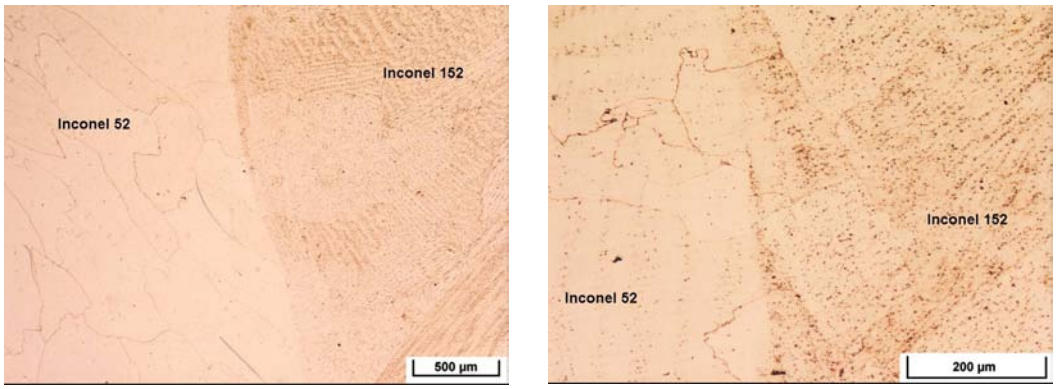

Figure 2.178 (a and b). Fusion line between Inconel 52 and 152 buttering weld metals.

a) b)

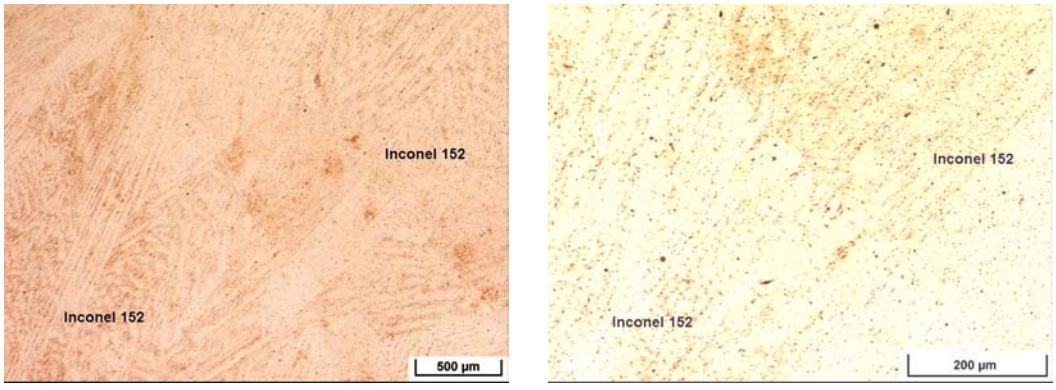

Figure 2.179 (a and b). Fusion line between Inconel 152 buttering (left side) and Inconel 152 weld (right side) metals.

a) b)

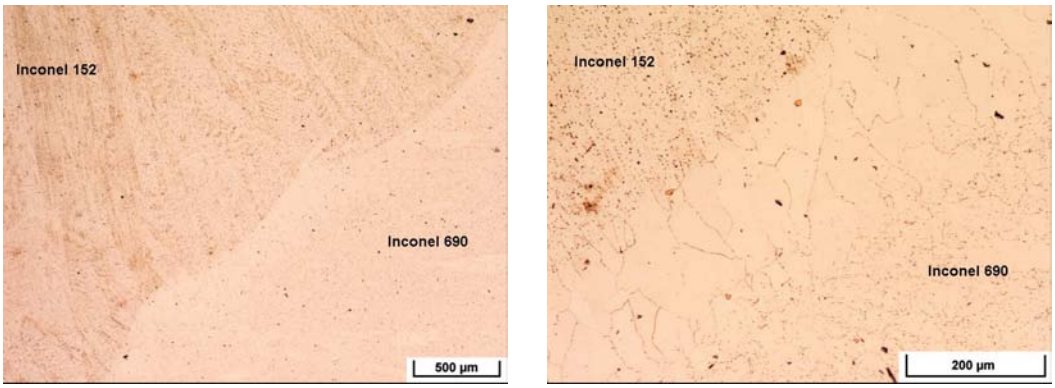

Figure 2.180 (a and b). Fusion line between Inconel 152 weld metal and Inconel 690 base material.

Figure 2.181 presents the cutting line of the cross-section of mock-up 3 sample for microstructural examinations.

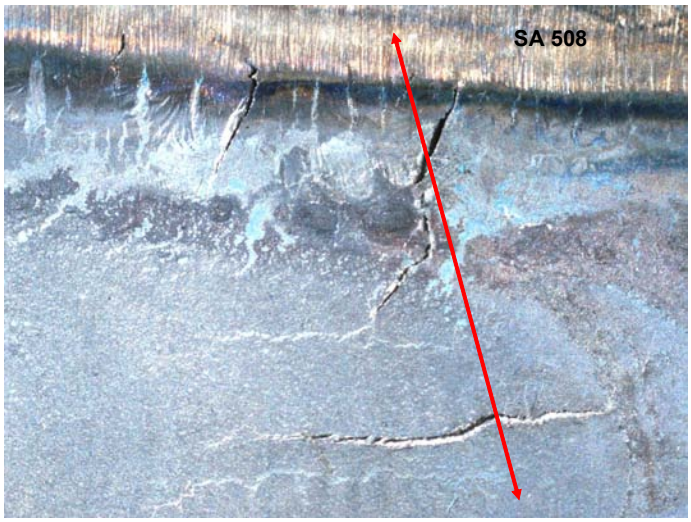

Figure 2.181. Cutting line of cross-section of mock-up 3 sample for microstructural examinations after Varestraint test.

Figure 2.182 presents cross-sections of mock-up 3 weld cracks after Varestraint testing.

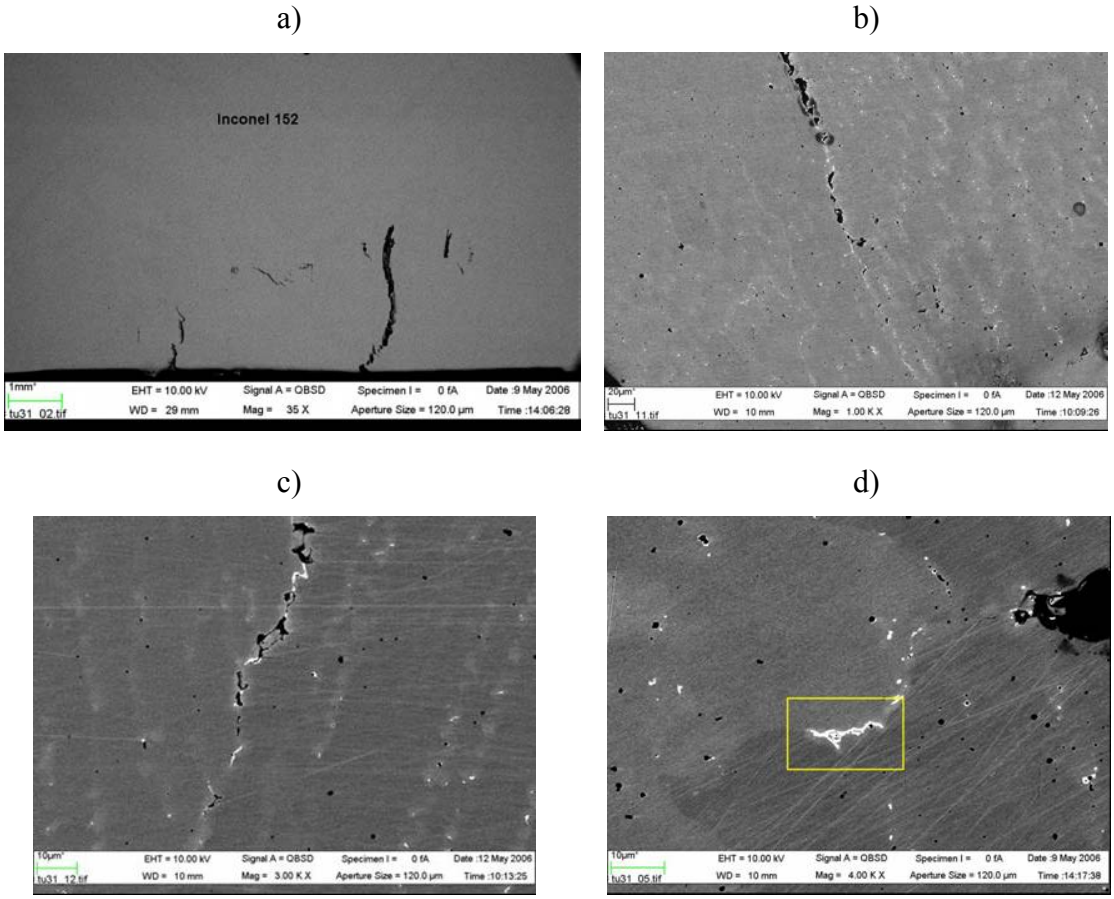

Figure 2.182 (a–d). Cross-section of mock-up 3 weld cracks after Varestraint test.

Figure 2.183 presents scanning electron microscopy (SEM) of white phase area marked with a rectangle in Figure 2.182 d).

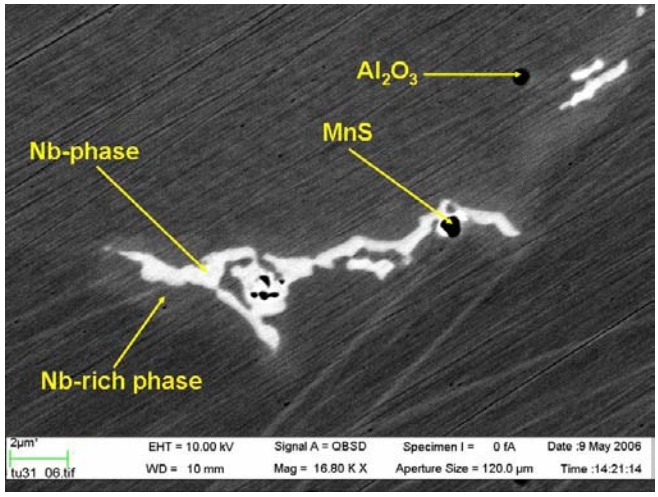

Figure 2.183. Scanning electron microscopy (SEM) of white phase area marked with a square in Figure 2.182 d).

Figure 2.184 and Table 2.6 present EDS analyses of the matrix (yellow) and of the light area (blue) along the dendrite boundary next to the white phase.

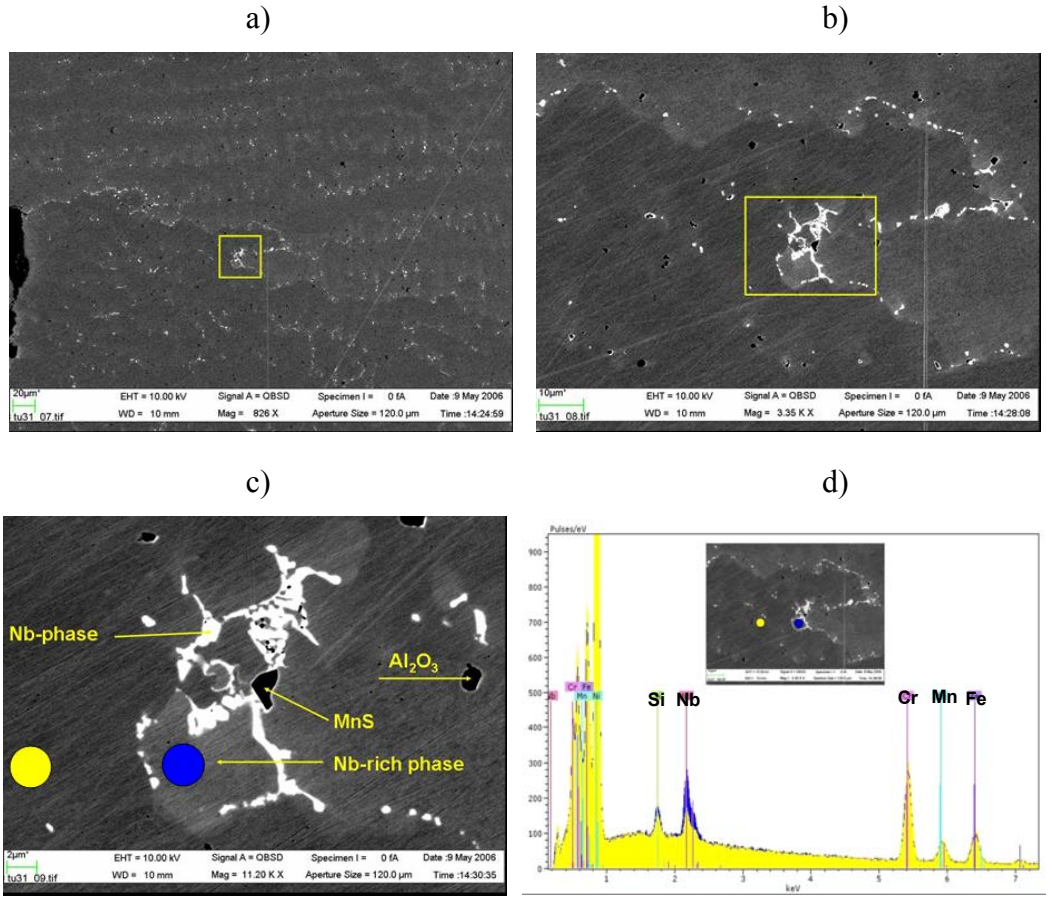

Figure 2.184 (a–d). EDS analyses of the matrix (yellow) and of the light area (blue) next to the white phase.

Table 2.6. Compositions of the areas marked by blue and yellow.

Element	Si	Cr	Mn	Fe	Ni	Nb
Blue area (wt.-%)	0,8	25,8	4,9	19,1	43,9	5,5
Yellow area (wt.-%)	0,6	27,5	5,1	21,1	43,4	2,4

Comparing to the composition of the dendrite matrix, the light area along the dendrite boundaries close to the white Nb-rich phase contains increased amounts of Nb, Si, and depletion of Cr occurs in the area. The light area along the dendrite boundaries represents the segregation during the solidification process, but is the matrix γ phase in which the white phase has formed.

2.6.7 Summary of microstructural observations

The metallography and fractography of the hot cracks revealed that, in Nb-containing alloys 182, 82, and 152, hot cracking is connected to the white phase along dendrite boundaries, which is rich in Nb, Si, Mn and P and depleted in Ni, Cr and Fe. In alloy 52, which does not contain Nb, but contains Ti (0.51 wt.-%), the only abundant phase along the dendrite boundaries and on the fracture surfaces of the hot cracks was TiN(C). These kinds of eutectic-type constituents in the vicinity of the hot cracks have formed from the terminal liquid phase, which existed in the interdendritic regions just before the solidification was complete. The amount and morphology of these constituents provides the information on the distribution of elements between solid and liquid phases in the final stages of solidification. The present observations are new findings for these weld metal alloys, and therefore the results can only be compared to the existing literature with other Nb-containing superalloys, namely Inconel 718 and 625, where the comparable white phase connected to hot cracking has been observed in the microstructure (Knorovsky et al., 1989; Cieslak et al., 1988; Dupont et al., 1998; Dupont, 1996). However, in these alloys the Nb-contents are typically much higher, up to 5 wt.-% of Nb.

In the literature on Inconel 718 and 625 superalloys, the white phase has been characterized by a Laves phase (a particular class of intermetallic phases having an ideal composition of AB_2). The typical compositions of the Laves phase in Inconel 718 have been about 22 wt.-% Nb, while the eutectic concentration is about 19 wt.-% Nb and maximum solid solubility about 9 wt.-% Nb at eutectic temperature (about 1180 °C) for Inconel 718 alloy. In the various studies, the chemical composition of the Laves phase of Inconel 718 is $(Ni, Cr, Fe)_2(Nb, Mo, Ti, Si, Mn)$.

Solidification of Nb-bearing superalloys (Inconel 718 and 625) has generally been observed to occur by a three-step solidification process: (1) primary L => γ reaction, which enriches the interdendritic liquid in Nb and C until (2) an eutectic-type L => (γ + NbC) reaction occurs over a rather broad temperature range (around 1250 °C) and finally (3) solidification is terminated by a second eutectic-type reaction, L => (γ + Laves) (around 1200 °C), which occurs over a narrow temperature range.

Based on the observations made in this study, the solidified weld microstructure is heavily segregated and consists of Nb-rich interdendritic regions and Nb-lean dendrite core regions. The white (Laves) phase forms in the interdendritic regions and contains Nb as high as 15–30 wt.-%. The presence of the Laves phase is probably enhanced by the presence of Si, Mn and P, which were also markedly segregated to the white phase and/or interdendritic areas. Solidification cracking occurs during the terminal stages of solidification when a liquid film is distributed along the grain boundaries in the

interdendritic regions as a continuous film, and the shrinkage strains across these boundaries cannot be accommodated. The solidification temperature range and morphology of the interfacial liquid are the primary factors controlling the solidification cracking susceptibility. Solute redistribution affects the solidification temperature range and amount of terminal liquid (small amount of terminal liquid, less than 1 vol.-%, is most detrimental).

Minor variations in Nb, Si, and C content have a strong influence on the solidification temperature range, type and amount of secondary phases, which form during terminal stages of solidification and affect the solidification cracking susceptibility. All of these alloy additions decrease the liquidus and solidus temperatures, and also increase the solidification temperature range, Nb being most effective in this. Of the two types of the eutectic-type constituents, γ/NbC and γ/Laves, known to form as the Ni-base alloy welds solidify, the γ/Laves constituent is more deleterious in terms of hot cracking, as it forms at a lower temperature and thus extends the solidification temperature range. In dissimilar metal welds the studied alloys are used to join low alloy steels to stainless steels, and due to dilution, the weld metal can become significantly enriched in Fe, Si and C, which can significantly change the solidification behavior and associated cracking tendency. It is well known from Fe-base alloys and based on Fe additions to Nb-bearing, Ni-base alloys, that Fe promotes the formation of the γ/Laves constituent. Silicon addition has a similar effect. Niobium addition promotes higher amounts of total eutectic, and both eutectic-type structures (Laves and NbC) are highly enriched in Nb.

Solidification temperature ranges were measured by differential thermal analysis (DTA) by Wu and Tsai (1999) for alloy 82 (44 °C) and alloy 52 (13 °C). However, in the studied Ni-base alloys the γ/Laves constituent forms in very small amounts, which probably precludes the measurement of the L => (γ + Laves) reaction temperature by DTA. For alloys 718 and 625 weld overlay, a wide solidification temperature range (around 160 °C and 170 °C, respectively) and presence of interdendritic Laves phase is typical. The γ within the γ/Laves mixture in alloy 625 weld overlay has a composition of about 9,3 wt.-% Nb for the eutectic composition of 18,9 wt.-% Nb and Laves phase composition of 22,1 wt.-% Nb and respectively for alloy 718 9,3, 19,1 and 22,4 wt.-% Nb were found. In this study the composition of γ close to the white (Laves) phase in the interdendritic region was 5,5 wt.-% Nb and in the Laves phase even 30,8 wt.-% Nb content (alloy 152) was measured. In order to obtain reliable compositions for different phases and regions an analytical TEM study is required.

In alloys 182, 82 and 152 Nb segregation and consequent formation of Nb-rich intermetallic phase, most probably Laves phase $(Ni, Cr, Fe)_2(Nb, Si, Ti)$, took place in the interdendritic regions during weld solidification. The γ within the γ/Laves mixture was also enriched markedly with Nb in a few μm wide zone along the dendrite

boundaries. Laves phase is brittle and may be detrimental to weld mechanical properties, e.g., as it depletes the matrix in dendrite cores of useful alloying elements and may provide an easy crack initiation and propagation path. In the future also the ageing phenomena in these interdendritic regions are very important to study.

In order to avoid solidification cracking in Nb-bearing Ni-base alloys the solidification temperature range has to decrease and the terminal secondary constituents have to form in small quantities. Carbon addition may improve the resistance to hot cracking by decreasing the amount of Laves phase (promotes formation of γ/NbC), but especially Nb and Si seem to be detrimental. Niobium segregation is governed by the prevailing solidification conditions: the low weld metal cooling rate and high heat input increase Nb segregation and the amount of Laves phase. Thus, for controlling the Laves phase in the Nb-bearing Ni-base weld metals, the lowest possible heat input with high cooling rates have to be used. Additionally, control of dilution by Fe, Si, and C is very important, since they lower the liquidus and solidus temperatures, increase the solidification temperature range, and favour eutectic-type solidifications. It is also interesting to note that the segregation and Laves phase can be dissolved by homogenization heat treatments at high temperatures (up to 1150 °C), but may be unaffected even after extensive ageing at 600 °C.

2.7 Ring segment tests of weld metals Inconel 182 and Inconel 152

The ring segment test method is used for determining the hot cracking susceptibility of weld filler metals in arc welding of metallic materials, when welds need to meet high requirements. The test method has to be applied for austenitic weld filler metals with delta ferrite content of 3% or less, as well as for weld filler metals of nickel-base alloys. The test is applied for metal arc welding with rod electrodes as well as for metal and tungsten inert gas welding. Ring segment tests were made according to standards KTA 1408.2 (1985) and VdTÜF-Merkblatt Schweisstechnik 1153. The filler metals tested were electrodes Inconel 182 and Inconel 152.

2.7.1 Test specimen form

The test specimen consists of four square segments of equal size (thickness is 25 mm and edge length is 45 mm) into which a circumferential groove is machined on one side after tack welding is completed on both sides. Figure 2.185 presents the test specimen form used in these tests.

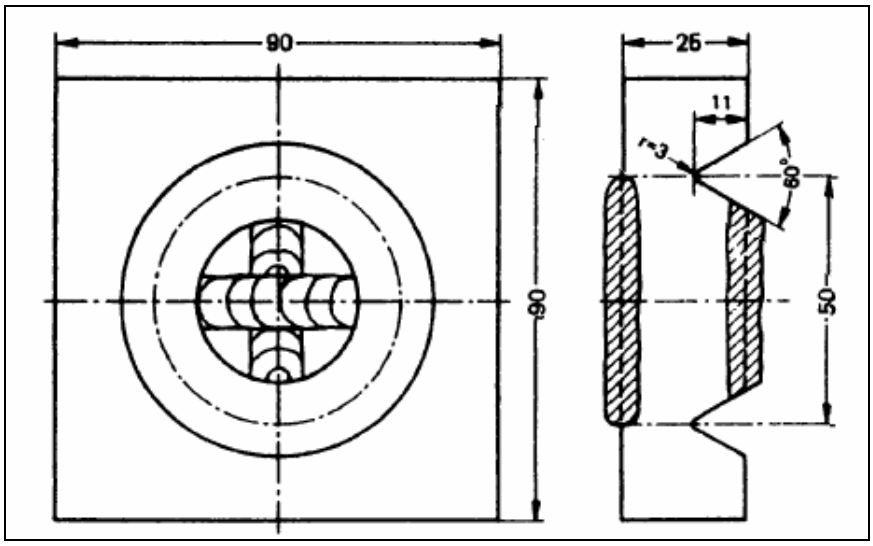

Figure 2.185. Ring segment test specimen form.

For the test specimen, the base metal material number 1.4550 (AISI 347) in accordance with DIN 17 440 shall be used, unless another material is specified in the order sheet. In these tests the base material was AISI 316 stainless steel.

Preparation of the test specimen

Four square parts of thickness of 25 mm and an edge length of 45 mm were prepared in such a way that they could be used to produce the test specimen shown in Figure 2.185 after tack welding. The rolling skin surface needs not to be removed. The touching surfaces were ground prior to tack welding. In Figure 2.186 is presented the preparation of the ring segment test specimen.

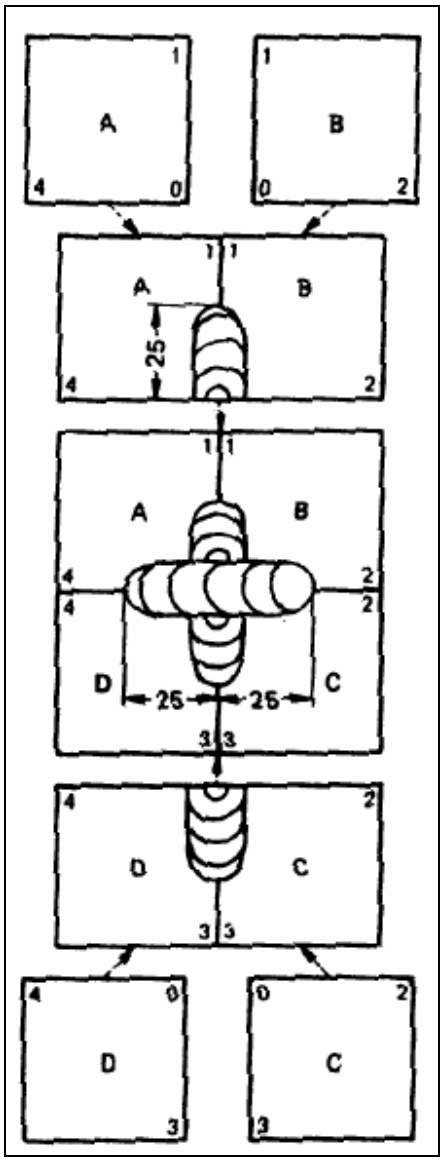

Figure 2.186. Preparation of the ring segment test specimen.

The work sequence of preparation of the ring segment test specimen is as follows:

1. Grind surfaces 1-0 of parts A and B as well as surfaces 3-0 of parts C and D.
2. Clamp parts A and B as well as C and D together.
3. Join parts A and B as well as C and D by tack welds on both sides (25 mm long).
4. Grind surfaces 4-0-2 of tack-welded parts A-B and C-D.
5. Clamp tack-welded parts A-B and C-D together.
6. Join tack-welded parts A-B and C-D by tack welds on both sides (50 mm long).

In Figure 2.187 is presented the ring segment test specimen after tack welding.

Figure 2.187. Ring segment test specimen after tack welding.

After tack welding of the ring segment test specimen, a circumferential groove was machined on one side of it (Figure 2.188). The dimensions of the groove are shown in Figure 2.185. No cooling liquids are allowed during machining.

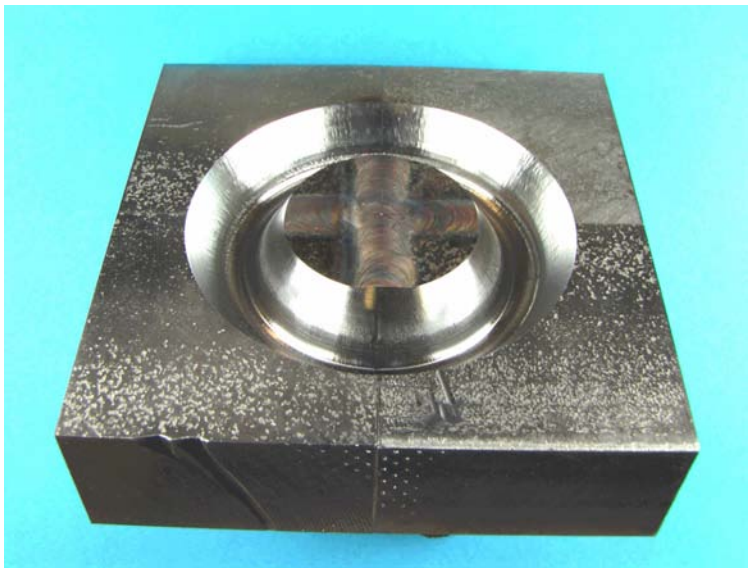

Figure 2.188. The ring segment test specimen after tack welding and machining of circumferential groove.

2.7.2 Welding of the test specimen

The ring segment test specimen was welded in the flat position as required. Welding was carried out clockwise from point X (see Figure 2.189) to point Y without weaving and in an uninterrupted process. After the specimen was cooled down to approximately room

temperature and the weld surface and groove were cleaned, welding was resumed clockwise from point Y to point X, again without weaving and in an uninterrupted process.

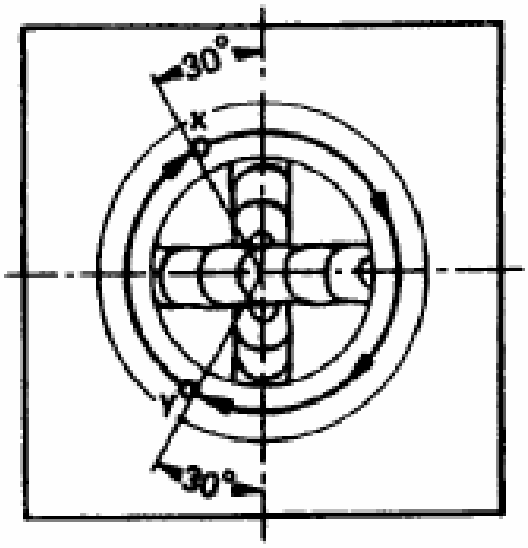

Figure 2.189. Welding of the test specimen.

In Figure 2.190 is presented specimen after the first weld and in Figure 2.191 specimen after the second weld is presented.

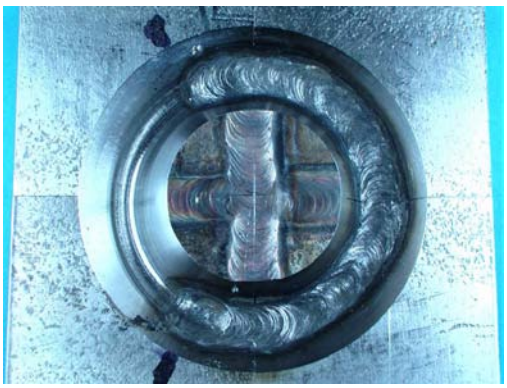

Figure 2.190. Specimen after the first weld.

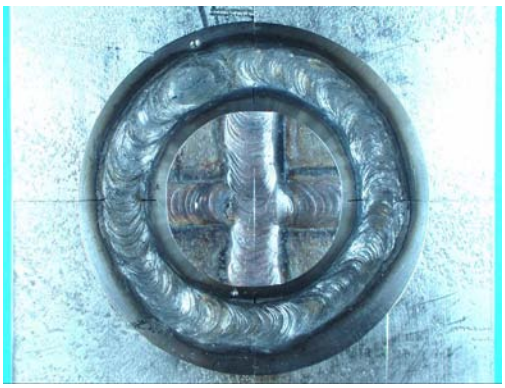

Figure 2.191. Specimen after the second weld.

2.7.3 Evaluation of the ring segment test

After the ring segment test specimen has cooled to room temperature, the cleaned annular weld is examined for surface cracks by the liquid penetrant method. Figure 2.192 presents the Inconel 182 specimen after the liquid penetrant testing and Figure 2.193 shows the Inconel 152 specimen, respectively.

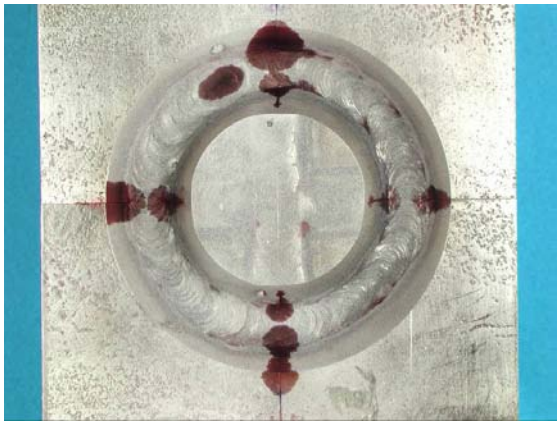

Figure 2.192. Inconel 182 after liquid penetrant testing.

Figure 2.193. Inconel 152 after liquid penetrant testing.

After the surface crack examination, the specimen shall be broken at separation points in order to be able to verify the root fusion. Figure 2.194 presents a cross-section of the Inconel 182 test specimen.

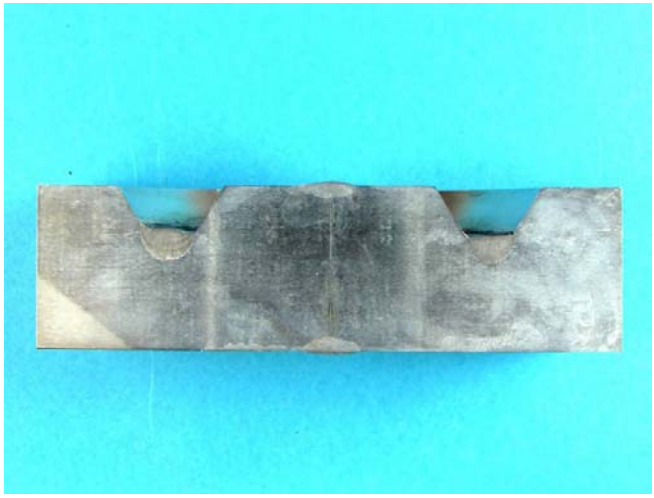

Figure 2.194. Cross-section of the Inconel 182 test specimen.

If no cracks are found, the filler metal is not susceptible to hot cracking. If cracks are found, information on position, direction, number and length of the cracks is to be reported. Figures 2.195 and 2.196 present two cracks found in the Inconel 182 weld.

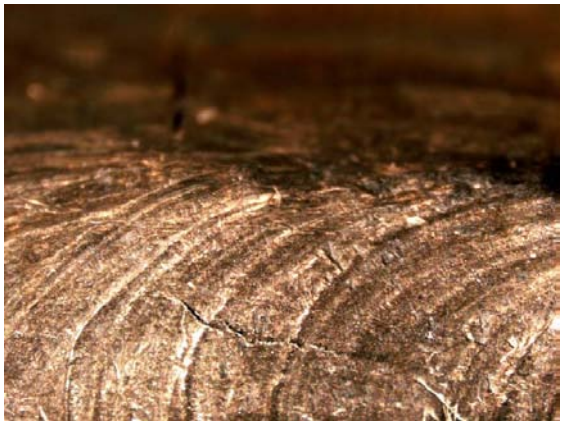

Figure 2.195. Crack 1 in Inconel 182 weld.

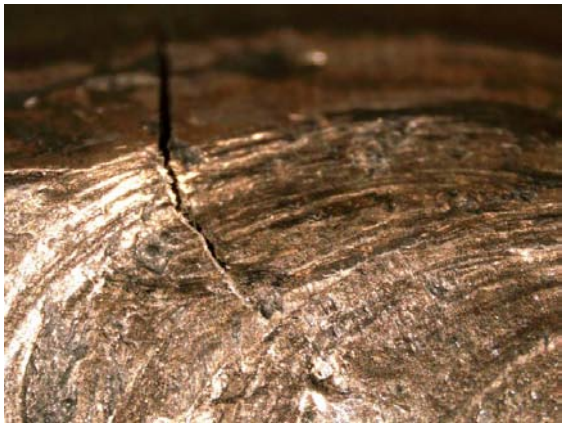

Figure 2.196. Crack 2 in Inconel 182 weld.

Figure 2.197 presents the crack found in the Inconel 152 weld.

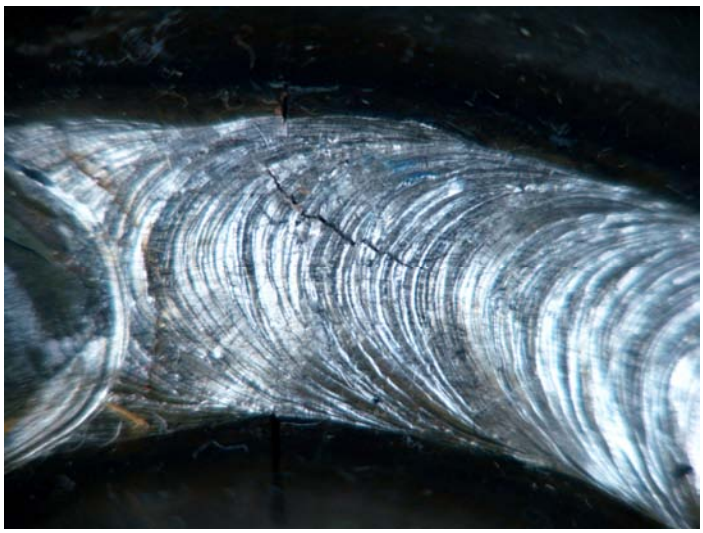

Figure 2.197. Crack in Inconel 152 weld.

All three cracks found in Inconel 182 and 152 welds were related to the interface between the tack-welded segments. The information value of the test is very small. Improper preparation of the sample and welding performance can cause hot cracks that cannot be attributed to the filler metal used. In the future European Standard prEN 14532 dealing with qualifying examinations of filler metals, this test method is not considered. It has to be carried out only if mandatory (production in compliance with standard KTA 1408).

2.8 Welding of full size Neste Oil mock-up

A full-scale dissimilar metal weld mock-up pipe was made. The pipe material was pressure vessel steel 2,25Cr1Mo0,25V, ASME code case 2098 (diameter 405 mm, wall

thickness 35 mm and length 1000 mm). The pipe was clad with AISI 309 and AISI 347 steel. The second pipe material was stainless steel AISI 347 (diameter 405 mm, wall thickness 40 mm and length 280 mm). Figure 2.198 presents the pressure vessel steel pipe with cladding.

Figure 2.198. Pressure vessel steel pipe with cladding.

A 300 mm long piece was cut from the pressure vessel steel pipe. A welding groove was machined into this piece of pipe and the stainless steel pipe according to the technical drawing in Figure 2.199.

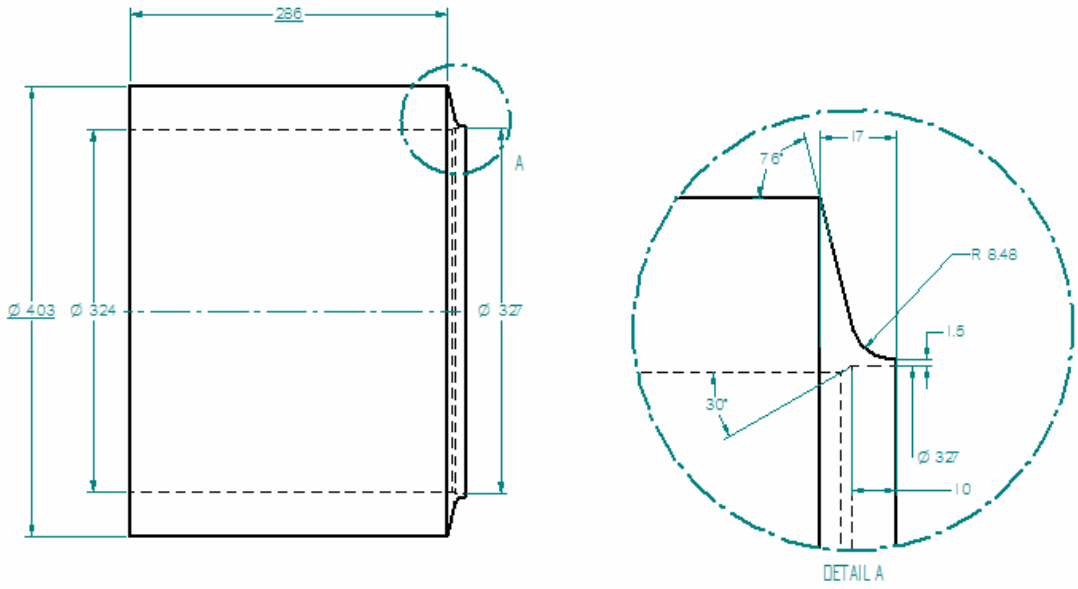

Figure 2.199. Technical drawing of the welding groove.

The machined pressure vessel steel side groove was buttered with welding electrode Inconel 182. Minimum requirement for the thickness of the buttering layer was 7 mm. Minimum requirement for the preheating temperature was 105 °C and maximum temperature was 250 °C. Preheating was done with a petroleum gas torch to temperature 200 °C, and the upper side of the mock-up was sealed. The preheating temperature was measured during welding by a thermocouple from the upper side of the pipe (see Figure 2.200) and from the surface of the buttering layer with a surface thermometer. Buttering was made in the flat position. Figure 2.200 presents the pressure vessel steel pipe fastened at the turning table, ready for buttering.

Figure 2.200. Pressure vessel steel pipe fastened to the turning table ready for buttering.

Figure 2.201 presents the pressure vessel steel pipe after the first buttering layer. Thickness of the layer was approximately 5 mm. Requirement for the layer thickness was at least 7 mm, and therefore two layers were welded to achieve a 10 mm thickness.

Figure 2.201. Pressure vessel steel pipe after first buttering layer.

Figure 2.202 presents the weld pass sequence and welding parameters of the buttering of the pressure vessel steel pipe groove.

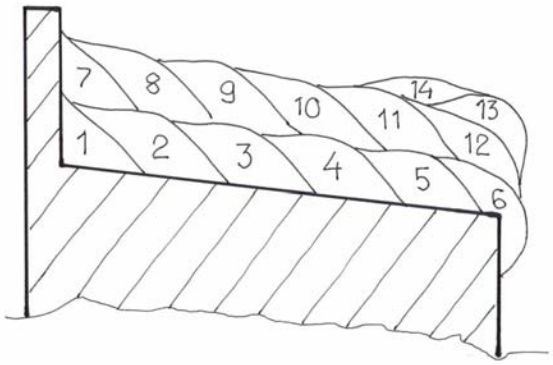

Pass no.	Current [A]	Electrode dia. [mm]	No. of electrodes
1	130	4	8
2	160	5	6
3	160	5	6
4	160	5	6
5	160	5	6
6	130	4	5
7	130	4	5
8	160	5	5
9	160	5	6
10	160	5	6
11	160	5	6
12	90	3,2	5
13	95	3,2	8
14	95	3,2	9

Figure 2.202. Weld pass sequence and welding parameters of the buttering of the pressure vessel steel pipe groove.

After buttering, the pipe was heat treated at 700 °C for 8 h with slow cooling. Then the welding groove was machined to the buttering side as shown in Figure 2.199. The thickness of the buttering after machining was approximately 8,5 mm, as shown in Figure 2.203.

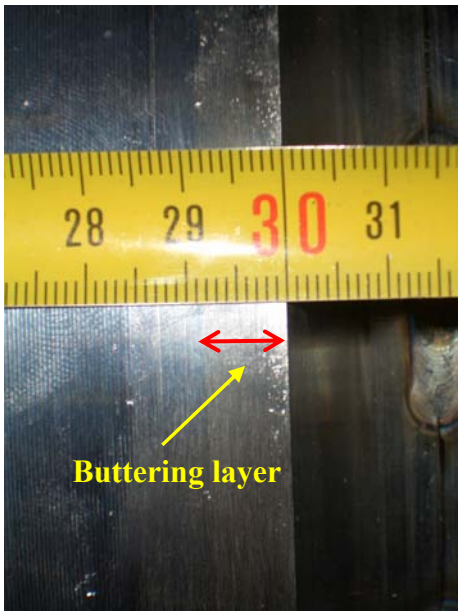

Figure 2.203. Buttering layer after machining.

The machined surface of the buttering layer was inspected with liquid penetrant testing, shown in Figure 2.204.

a) b)

Figure 2.204 (a and b). Liquid penetrant testing of the buttering after application of a) penetrant and b) developer.

One indication of a small defect in the buttering surface was found shown in Figure 2.205 a) and b). The length of the indication was 2,5 mm and depth was approximately 0,2 mm, and it was ground away with caution.

a) b)

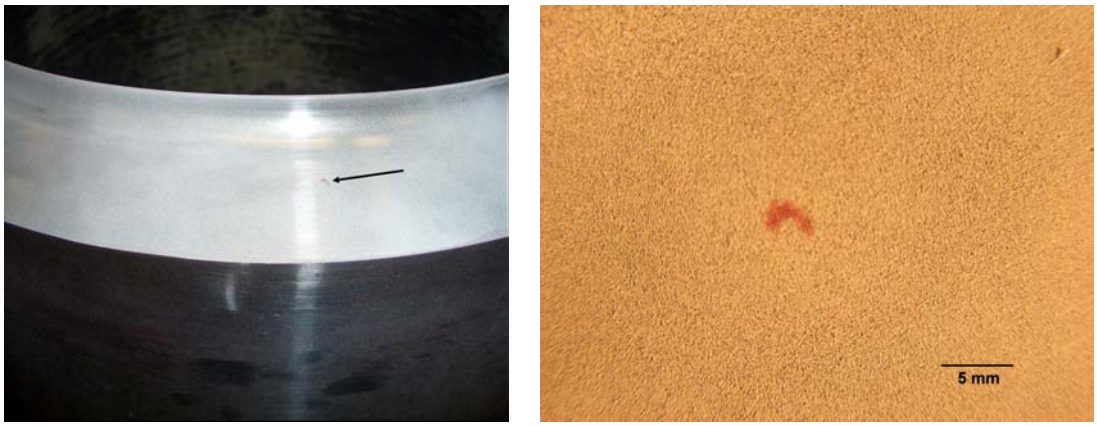

Figure 2.205 (a and b). Defect in the buttering surface.

The pressure vessel steel pipe with buttering was tack welded to stainless steel AISI 347. A shielding gas covering box was used for protection of the weld root side from oxidation during the welding process (Figure 2.206).

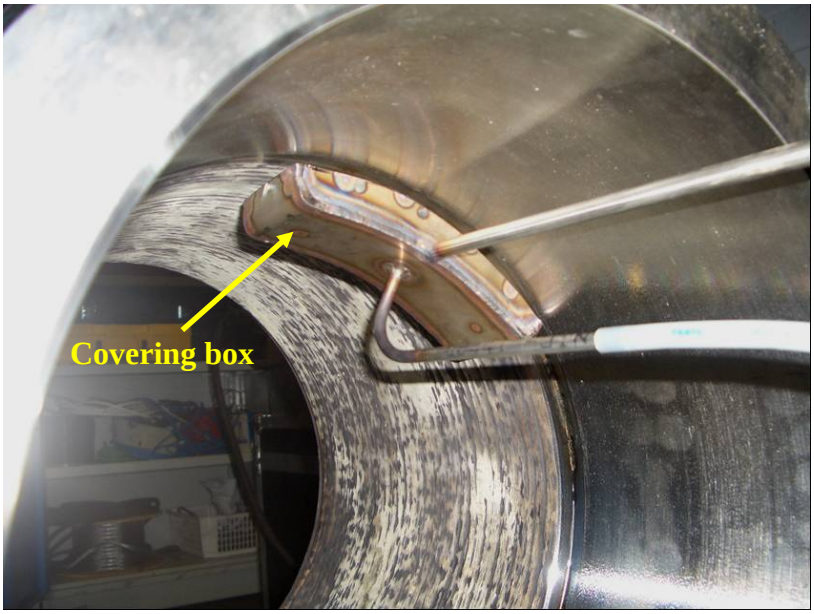

Figure 2.206. Weld root shielding gas covering box.

Figure 2.207 presents a general view of the welding of the mock-up. A is the mock-up to be welded. B is the welding power source. Turning rolls are marked as C. D is the video camera for monitoring the weld root via mirror E (Figure 2.208). F is the video camera for monitoring each weld bead from the surface side (Figure 2.209).

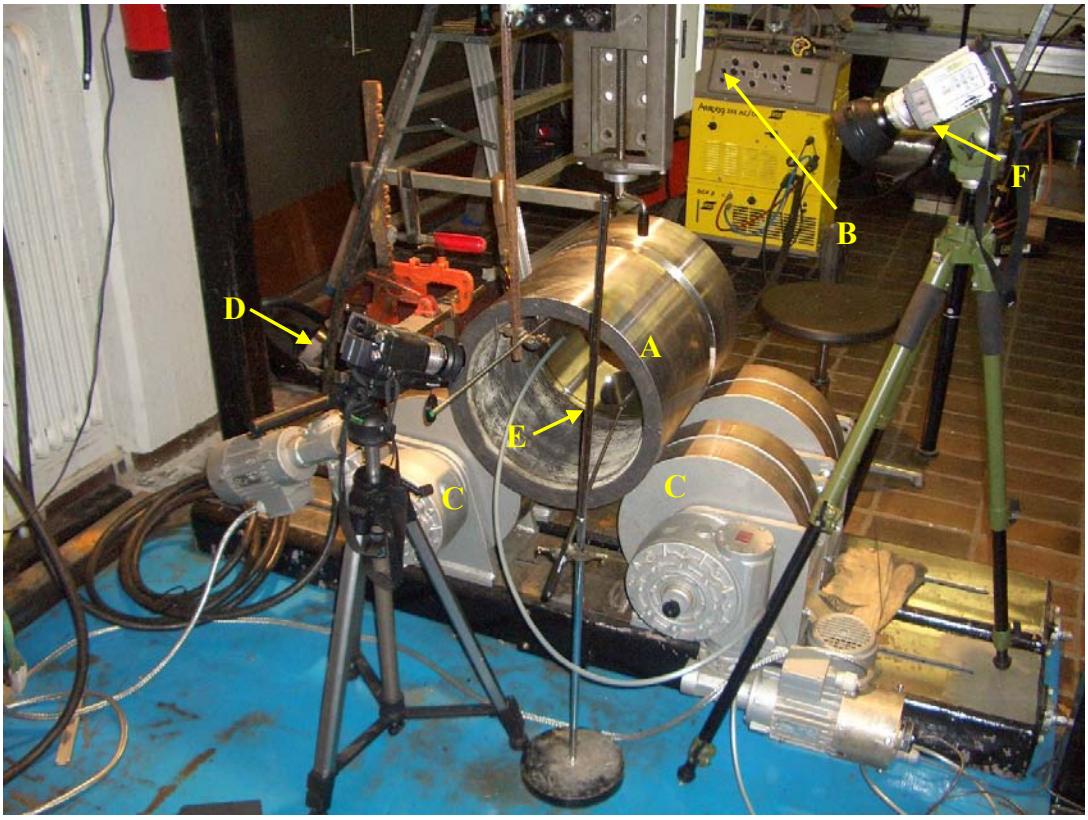

Figure 2.207. General view of the welding of the mock-up.

Figure 2.208. Weld root side monitoring via mirror by video camera.

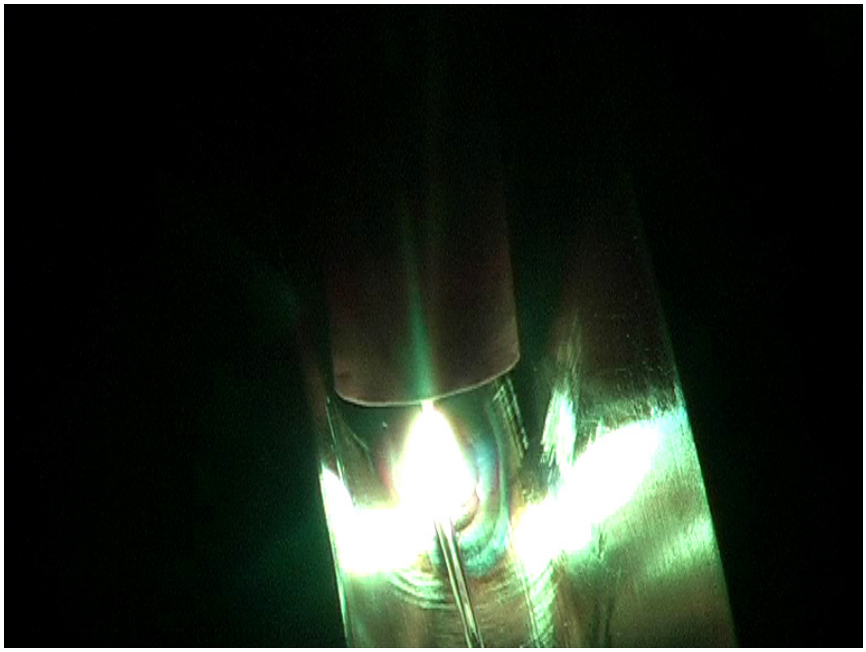

Figure 2.209. Surface side monitoring by video camera.

Figure 2.210 presents the weld pass sequence of the Neste Oil mock-up and Table 2.7 the welding parameters of the mock-up. The total amount of the welding electrodes used was 174.

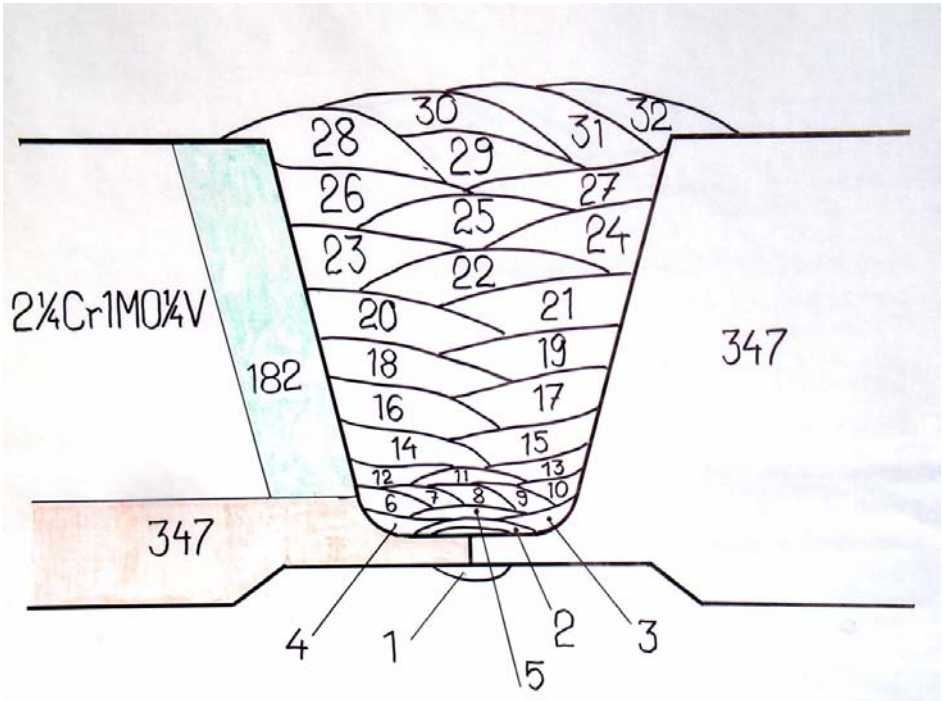

Figure 2.210. Weld pass sequence of the Neste Oil dissimilar metal weld mock-up.

Table 2.7. Welding parameters of the Neste Oil dissimilar metal weld mock-up.

Pass no.	Filler metal	Current [A]	Electrode dia. [mm]	No. of electrodes
1	347 Si	75-80	1,6	
2	347 Si	85-90	1,6	
3	347 Si	120	2	
4	347 Si	110	2	
5	347 Si	100-105	1,6	
6	Inconel 82	120	2	
7	Inconel 82	100	1,6	
8	Inconel 82	110	1,6	
9	Inconel 82	120	1,6	
10	Inconel 82	130-140	2	
11	Inconel 82	140	2	
12	Inconel 82	140-145	2	
13	Inconel 82	110-120	1,6	
14	Inconel 182	130	4	7
15	Inconel 182	130	4	8
16	Inconel 182	160-150	5	9
17	Inconel 182	150	5	10
18	Inconel 182	160	5	10
19	Inconel 182	160	5	10
20	Inconel 182	155	5	9
21	Inconel 182	155	5	8
22	Inconel 182	155	5	8
23	Inconel 182	155	5	8
24	Inconel 182	155	5	9
25	Inconel 182	155	5	10
26	Inconel 182	95	3,2	13
27	Inconel 182	95	3,2	16
28	Inconel 182	155	5	7
29	Inconel 182	95	3,2	10
30	Inconel 182	155	5	6
31	Inconel 182	155	5	7
32	Inconel 182	155	5	9

Figure 2.211 presents the finished Neste Oil dissimilar metal weld mock-up and Figure 2.212 the surface of the mock-up.

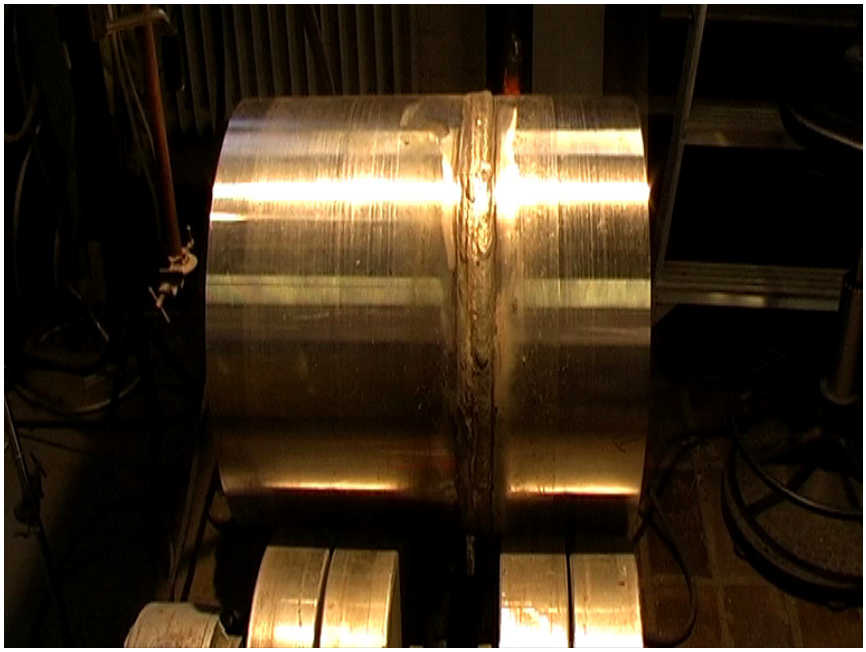

Figure 2.211. Finished Neste Oil dissimilar metal weld mock-up.

Figure 2.212. Surface of the Neste Oil dissimilar metal weld mock-up after welding.

NDE was conducted for the shop fabricated Neste Oil dissimilar metal weld mock-up for refinery applications. The requirements of the specifications for radiographic examination and liquid penetrant examination were applied. The butt-welded pipe joint of pressure vessel steel to stainless steel with Inconel 182 filler metal met the requirements set in the ASME Section 8, Div. 1 inspection procedure. However, the

classification of radiographic films was made based on EN-standard. Liquid penetrant inspection revealed two surface indications exceeding the quality requirements.

2.9 TIG and MMA welding of Inconel materials, practical considerations

Welding procedures for nickel-base alloys are similar to those used for stainless steels. The thermal expansion characteristics of the alloys are approximately similar to that of carbon steels, and essentially similar shrinking or distortion can be expected during welding.

In TIG welding the torch should be held at nearly 90° to the work piece. Slight inclination into the forehand side during manual welding may be necessary for good visibility. Too much leaning can cause aspiration of air into the shielding gas. The electrode extension beyond the gas cup should be as short as possible. To ensure a sound weld, the arc length must be maintained as short as possible. The arc length can be longer when feeding the filler metal. The filler metal should be fed carefully to the leading edge of the molten pool to avoid contact with the electrode. The hot weld must be kept in the protective atmosphere. A full penetration weld must be protected from the root side with the shielding gas.

In manual metal arc welding (MMA), electrodes should remain sealed in their moisture-proof containers in a dry storage area. The flux coating is hygroscopic and absorbs excessive moisture if exposed to normal humidity. Opened containers of electrodes should be stored in a dryer. Electrodes that have absorbed moisture can be baked to remove the absorbed moisture by heating at 300 ±25 °C for 2–3 h in a vented oven. Groove surfaces must be clean. Brushing with stainless steel brush and removal of grease has to be done.

Welding current should be selected in the optimum range for each electrode diameter, or otherwise the arc becomes unstable and the amount of spatter increases remarkably. Nickel-base alloy weld metals do not flow and spread like steel weld metals. The welder must direct the flow of the pool so that the weld metal wets the sidewalls of the groove. Small amounts of weaving can be used to help this. Inconel electrodes are more difficult to ignite than the stainless steel electrodes, and the arc is more unstable than in the case of stainless steel electrodes. The arc length must be maintained as short as possible to avoid spattering. Flux-covered electrodes form a thick and mobile slag that easily goes under the arc and extinguishes it, and can cause slag inclusions. Therefore, welding is good to perform in a slightly uphill position. In multi-pass welding, careful slag removal is important after welding of every bead.

2.10 References

CEN ISO/TR 17641-3. 2005. Destructive Tests on Welds in Metallic Materials. Hot Cracking Tests for Weldments. Arc Welding Processes. Part 3: Externally Loaded Test. 17 p.

Cieslak, M.J., Headley, T.J., Kollie, T. & Romig Jr., A.D. 1988. A Melting and Solidification Study of Alloy 625. Met. Trans., 19A, 9, pp. 2319–2331.

Dupont, J.N. 1996. Solidification of an Alloy 625 Weld Overlay. Met. Trans., 27A, 11, pp. 3612–3620.

Dupont, J.N., Robino, C.V. & Marder, A.R. 1998. Solidification and Weldability of Nb-Bearing Superalloys. Welding J., 77, pp. 417-s–431-s.

Heuser, H. 2005. Value of Different Hot Cracking Tests for the Manufacturer of Filler Metals. In: Böllinghaus, T. & Herold, H. (Eds.). Hot Cracking Phenomena in Welds. Springer, Germany. ISBN 3-540-22332-0. Pp. 305–327.

Hänninen, H., Aaltonen, P., Brederholm, A., Ehrnstén, U., Gripenberg, H., Toivonen, A., Pitkänen, J. & Virkkunen, I. 2006. Dissimilar Metal Weld Joints and their Performance in Nuclear Power Plant and Oil Refinery Conditions. VTT Research Notes 2347. Espoo: VTT. 208 p. http://www.vtt.fi/inf/pdf/tiedotteet/2006/T2347.pdf.

Knorovsky, G.A., Cieslak, M.J., Headley, T.J., Romig Jr., A.D. & Hammetter, W.F. 1989. Inconel 718: A Solidification Diagram. Met. Trans., 20A, 10, pp. 2149–2158.

KTA 1408.2. 1985. Safety standards KTA 1408.2. Quality Assurance of Weld Filler Materials and Weld Additives for Pressure and Activity Retaining Systems in Nuclear Power Plants, Part 2: Manufacture, pp. 17–18.

Prime, M.B. 2001. Cross-Sectional Mapping of Residual Stresses by Measuring the Surface Contour after a Cut. Journal of Engineering Materials and Technology, 123, pp. 162–168.

VdTÜF-Merkblatt Schweisstechnik 1153. Prüfung der Rissanfälligkeit von Schweisszusätsen: Ring Segment Probe. 4 p.

Wu, W. & Tsai, C.H. 1999. Hot Cracking Susceptibility of Fillers 52 and 82 in Alloy 690 Welding. Met. Trans., 30A, 2, pp. 417–426.

3. Crack initiation tests

3.1 Background

A limited amount of laboratory results is available for the new material combinations of dissimilar metal welds of nuclear power plants. In the national ERIPARI project the crack initiation in good quality weld metals, as well as in a few weld metals having weak dendrite boundaries, was studied using a so-called “doped steam test”.

According to Staehle and Gorman (2004), the doped steam test was developed to simulate the steam phase in heat transfer crevices, where impurities are known to condensate. According to Staehle and Gorman (2004), Dehmlow conducted the first experimental tests using Inconel 600 and 690 base metals and two weld metals at 400 °C in hydrogenated steam doped with sodium sulfate, nitrate and chloride. Tests were conducted by using pre-cracked C(T) specimens and constant displacement loading.

According to Staehle and Gorman (2004), the initiation time for low potential stress corrosion cracking (LPSCC) follows a monotonic 1/T dependence from hydrogenated steam to water. This suggests that the mechanistic processes in water and steam are the same, at least for pure water. However, the influence of the doped impurities on the mechanism is not clear, since many of the relevant dopant impurities are not well soluble in steam.

As crack initiation takes very long time in actual LWR water at relevant operating temperatures (years or decades), the tests were conducted at 400 °C in steam doped with hydrogen, chloride, sulphate and fluoride. The doped steam environment is known to accelerate the crack initiation process. The approach of Jacko et al. (2003) with some modifications was adopted for this work.

Jacko et al. (2003) performed an accelerated laboratory test series in an environment consisting of hydrogenated 400 °C steam doped with fluoride, chloride and sulphate anions. Comparison tests were performed using alloy 600 and alloy 182 weld metal. Alloy 52M welds, prepared to simulate the Ringhals 4 field repairs of the reactor pressure vessel outlet nozzle, exhibited complete resistance to stress corrosion crack initiation in laboratory exposure times exceeding 45 efpy equivalent service times. Stress corrosion cracks initiated in alloy 182 welds in exposure times less than one-fifth of the total exposure time of the alloy 52M specimens. Crack initiation was also observed in specimens of alloy 600 CRDM nozzle material in the doped steam environment. The specimens used by Jacko et al. (2003) were prepared as flat plates and they were bolt loaded in specially designed four-point bending fixtures. The alloy 52M

weld specimens, as provided by Uddcomb, were 180 mm long x 40 mm wide x 9 mm thick plates, in which the welds were transverse to the long dimension. Alloy 600 reference specimens were 102 mm long x 19 mm wide x 3.8 mm thick plates. Analysis of Jacko et al. (2003) indicated that the degradation observed after 89000 effective full-power hours (efph) at 317 °C in Ringhals 4 was duplicated with 289 h exposure at 400 °C to sulphate, chloride and fluoride doped hydrogenated steam. This translates to an acceleration factor of 308 relative to primary water at 317 °C in Ringhals 4. For other temperatures Jacko et al. (2003) adjusted the acceleration factor using an activation energy of Q = 55 kcal/mole. The activation energy was estimated by assuming an Arrhenius type dependence for cracking probability between alloy 600 in Ringhals 4 and alloy 600 in laboratory tests at 400 °C in doped steam (Rao et al., 2002).

3.2 Experimental methods

3.2.1 Test environment and equipment

The crack initiation tests in the ERIPARI project were performed in steam at 400 °C and 150 bar. The steam was generated from de-ionized water doped with 30 ppb SO_4^{2-} (added as sulphuric acid), 30 ppb F^- (added as NaF) and 30 ppb Cl^- (added as NaCl). The target value for H_2 partial pressure was 0.56 bar, which, according to the Ellingham diagram, represents the Ni-NiO stability limit in these conditions.

The steam pressure was maintained using a HPLC (High Performance Liquid Chromatography) pump feeding replacement water to the autoclave. The pump can be operated under constant flow or constant pressure mode. The latter mode was used for steam pressure control.

H_2 partial pressure was measured using a Pd-membrane sensor inside the autoclave. Hydrogen diffuses through the Pd-membrane into a stainless steel tube filled with N_2. The inside pressure of the stainless steel tube was measured using a commercial pressure sensor.

The H_2 partial pressure was controlled by a West 6100 PID controller connected to the pressure sensor and a high pressure solenoid valve connected to the tube between the autoclave and the hydrogen bottle.

The autoclave temperature was controlled using a West 6100 PID controller and a commercial K-type thermocouple.

3.2.2 Test materials

Five different dissimilar metal welds were studied. The weld geometries are shown in Figure 3.1. The studied dissimilar metal welds contained Inconel weld metals 152 (TU1), 52 (TU2), both 52 and 152 (TU3), 182 (TV4) and, in one case simulating a repair weld of an Inconel 182 weld, both Inconel 82 and 182 weld metals (TV4K).

The applied thermal treatments were as follows:

- TU1 and TU2: 610 °C/16 h after welding and 550 °C/35 h after specimen preparation,
- TU3: for the side with the buttering (alloys 52 and 152) 610 °C/4 h, no heat treatment after joint welding,
- TV4: for the side with the buttering weld (alloy 182) 610 °C/6 h, no heat treatment after joint welding, and
- TV4K: the same treatment as for TV4.

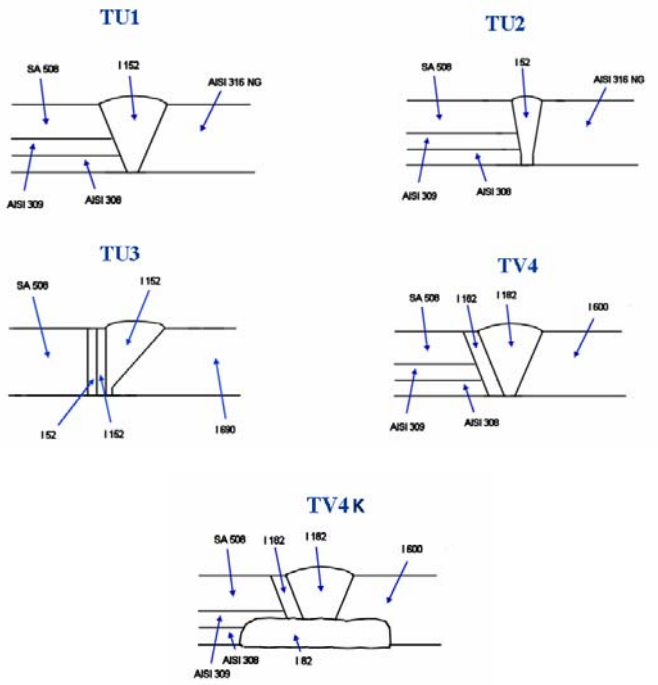

Figure 3.1. Different weld geometries used for the crack initiation tests. See details in Chapter 2. Weld codes TU1, TU2, TU3 and TV4 correspond to mock-ups 1, 2, 3, and mock-up TV weld, respectively. Weld TV4K was prepared from a piece of mock-up TV weld by machining a groove, which was filled with Inconel 82 weld metal.

3.2.3 Specimens

The specimens were 80 x 15 x 3 mm^3 plates cut from the root side of the welds. The specimen dimensions and cutting location are schematically shown in Figure 3.2 (TU2 weld used as an example). The dissimilar metal weld was in the middle of the specimen with its orientation either transverse (orientation "T") or parallel (orientation "P") to the longitudinal axis of the specimen.

The specimens were prepared by plane milling from the blocks prepared for Varestraint tests. A smooth mechanical grinding by 600 grit emery paper was performed after milling in order to remove the roughness of the specimen surfaces.

Three specimens contained hot cracks formed during the Varestraint tests. Augmented strain in the Varestraint tests was 3%. The surface with the hot cracks was not plane milled.

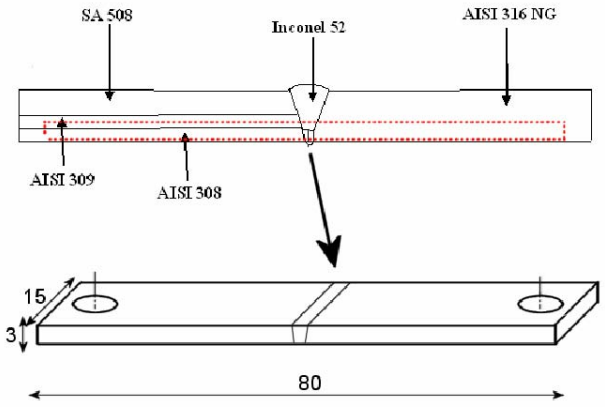

Figure 3.2. Schematic specimen cutting location (transverse orientation) and specimen dimensions.

3.2.4 Loading of the specimens

The specimens were bolt-loaded in a fixture producing four-point bend loading, Figure 3.3 a). Strain was calculated from the bending radius of a 3 mm thick plate. This radius, and thus strain, was calibrated experimentally to the change of the distance (i.e., displacement) between the outer surfaces of the adjacent specimens. However, the bending radius was difficult to determine accurately, especially under small displacement levels, and a theoretical dependence for the displacement and radius was formulated. The experimental and theoretical dependencies between the displacement and bending radius are shown in Figure 3.3 b). The theoretical dependence between the displacement and strain for a 3 mm thick plate is shown in Figure 3.3 c). The theoretical solution was used for specimen loading.

The nominal target strains for the specimens were 0.35 and 1%. The ε = 0.35% specimens were loaded directly to the desired strain. The 1% specimens were first loaded to a negative strain (–1%) and then to the final 1% (i.e., final ε = +1% in the root side of the dissimilar metal weld) using a rigid bending fixture in order to simulate cyclic straining resulting from multiple weld passes.

The strain calibration and strain profile do not apply to the specimens with the pre-existing hot cracks, because the hot cracks resulted in strain concentration and local bending of the specimens. The specimens with the hot cracks were loaded under an optical microscope until the crack mouth opening displacement (CMOD) of some of the cracks were in the range of 0,01 mm.

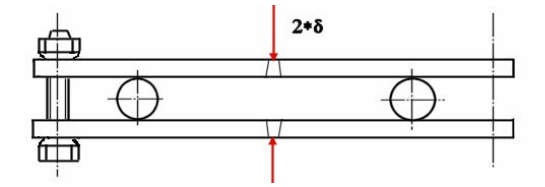

a)

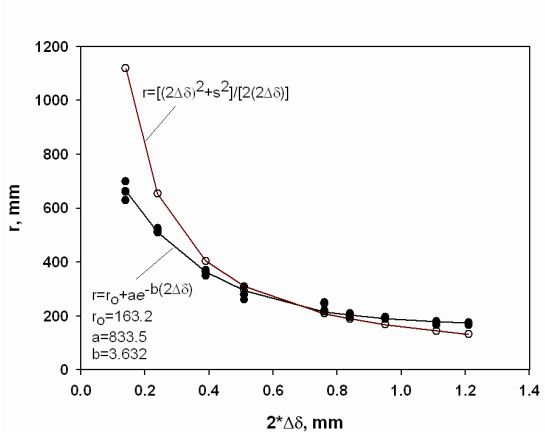

b)

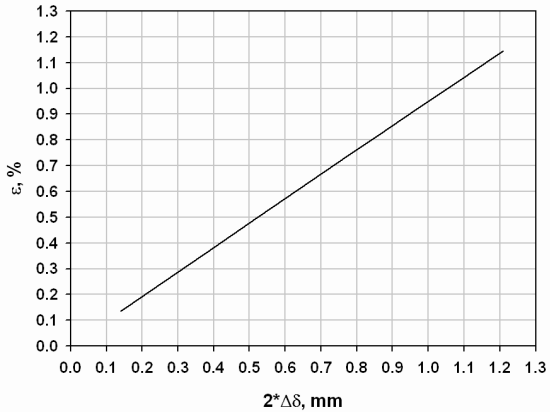

c)

Figure 3.3 (a–c). Loading geometry with displacement measurement location indicated by two red arrows a), experimental and theoretical displacement vs. bending radius calibration curves b), and theoretical strain vs. displacement curve for a 3 mm thick plate c).

3.2.5 Test matrix

All tested specimens are shown in Table 3.1. The first specimens put into the autoclave were those with 0.35% strain. Other specimens were not yet prepared at this stage, so they were put into the autoclave later. The number of the exposures experienced by each specimen is shown in Table 3.1. The total number of exposures was 5 (1460 h). The weld from which each specimen was prepared is shown in column 1, the specimen code in column 2, the orientation in column 3, the applied strain in column 4 and the number of exposures in column 5.

Table 3.1. Test matrix for the crack initiation tests performed in doped steam at 400 °C.

Weld	Specimen code	Orientation	Strain, %	Number of exposures
Mock-up 1	TU1-1	T	0.35	5
	TU1-2	T	0.35	5
	TU1-3	T	1	4
	TU1-4	T	1	4
	TU1-5	L	0.35	5
	TU1-6	L	0.35	5
	TU1-7	L	1	4
	TU1-8	L	1	4
Mock-up 2	TU2-1	T	0.35	5
	TU2-2	T	0.35	5
	TU2-3	T	1	4
	TU2-4	T	1	4
	TU2-5	L	0.35	5
	TU2-6	L	0.35	5
	TU2-7	L	1	4
	TU2-8	L	1	4
Mock-up 3	TU3-1	T	0.35	5
	TU3-2	T	0.35	5
	TU3-3	T	1	4
	TU3-4	T	1	4
	TU3-5	L	0.35	5
	TU3-6	L	0.35	5
	TU3-7	L	1	4
	TU3-8	L	1	4
Mock-up TV	TV4-1	T	0.35	5
	TV4-2	T	0.35	5
	TV4-3	T	1	4
	TV4-4	T	1	4
	TV4-5	L	0.35	5
	TV4-6	L	0.35	5
	TV4-7	L	1	4
	TV4-8	L	1	4
Mock-up 1	TU1C1	T	0.01 mm*	3
Mock-up 2	TU2C1	T	0.01 mm*	3
Mock-up 3	TU3C1	T	0.01 mm*	3
Mock-up TV	TV4K-1	T	1	1
	TV4K-2	T	1	1

* Crack mouth opening displacement (CMOD).

3.2.6 Post-test investigations

The specimens were investigated after the first exposure using a stereo microscope (i.e., the specimens with 0.35% strain). After the subsequent exposures, the specimens were investigated using liquid penetrant testing. All liquid penetrant indications were further studied using the stereo microscope.

After all 5 test series were concluded, the specimens were further loaded a small amount (about 0.1–0.3% strain increment) in order to open the possible very narrow cracks indicated by the liquid penetrant test but not observed by the stereo microscope. Further studies were also performed using an SEM. Some selected cracks were opened and specimens were sliced in order to study the crack propagation paths in the microstructure.

Before the specimens were further loaded after all 5 test series, some of the specimens were unloaded in order to estimate the stress levels in the specimen surfaces during the exposure. The elastic strain was estimated from the amount of unloading measured, using the same calibration curve as when the specimens were initially loaded.

3.3 Results

The measured autoclave temperature, steam pressure and hydrogen partial pressure are shown in Figure 3.4. Table 3.2 shows the total exposure time of each specimen, exposure time after which the first indications were observed by liquid penetrant testing method, and locations where cracks were observed in post-test examination by either optical microscopy or SEM.

The results of the post-test strain relaxation measurements are shown in Table 3.3. The measurements showed an elastic relaxation of 0.13–0.34%, when the specimens were unloaded. This indicates that a considerable stress remained on the specimen surfaces throughout the test series (i.e., stress close to the 0.2% proof stress).

Figure 3.5 a) shows the number of 0.35% strained specimens with a liquid penetrant indication as a function of exposure time. Corresponding data is shown for 1% strained specimens in Figure 3.5 b). Liquid penetrant testing was started after 2nd exposure, i.e., it is not possible to tell whether there were any features that could have resulted in liquid penetrant indications before that. Figure 3.5 c) shows the average number of cracks observed by optical microscopy or SEM after the tests. In the case of weld TV4, the number of cracks was more than 10 in each specimen except one. In the case of the cracked TV4 specimens, every crack could not be distinguished from others.

Figures 3.6–3.24 show photographs of cracks in each specimen observed by optical microscopy or SEM. The first photograph a), in each case, is a macrograph after liquid penetrant test, the second photograph b) is in most cases a micrograph taken by a stereo microscope, and the subsequent photographs are taken by an SEM. Only those specimens showing both liquid penetrant indications and crack-like features observed by SEM were photographed.

Micrographs taken from sliced, polished and etched specimens TU2-4 and TV4-3 are shown in Figures 3.25–3.26. The specimens were sliced in axial and through-thickness direction. Figure 3.25 a) shows a micrograph of a part of the weld in a section cut from the weld region of specimen TU2-4. AISI 316 NG steel is seen on the right hand side of the Inconel 182 weld. Figure 3.25 b) shows a higher magnification of the same Inconel 182 weld. Figure 3.25 c) shows a higher magnification micrograph from the same area as Figures 3.25 a) and b). After further grinding this indication seems to be more a result of dissolution of a slag inclusion than a real EAC crack.

Figure 3.26 a) is a macrograph from the axially sliced surface of specimen TV4-3 after polishing but before etching. The etched surface is shown in Figure 3.26 b). The locations of the subsequent micrographs c)–f) are shown in Figure 3.26 a). As can be seen, the largest crack is in the middle of the weld. Smaller cracks are located both in the weld metal and alloy 600 base metal.

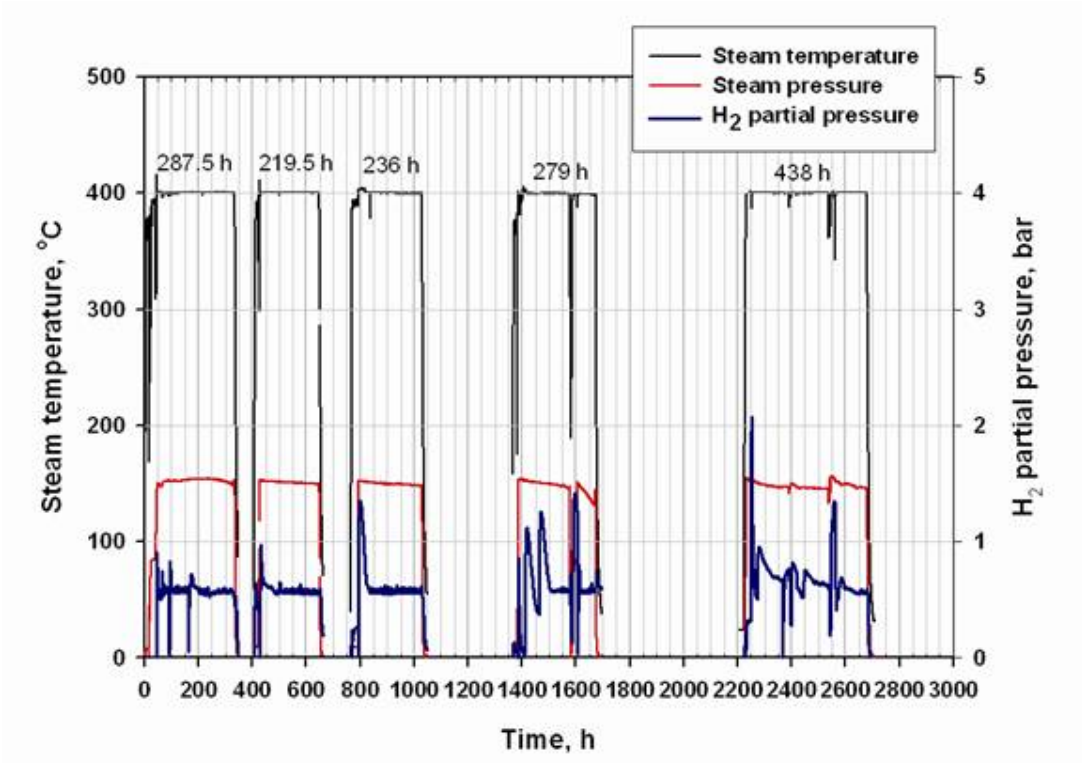

Figure 3.4. Temperature, autoclave pressure and hydrogen partial pressure during the 5 test exposures.

Table 3.2. Specimen ID, orientation, strain, total exposure time of each specimen, exposure time after which the first indications were observed by liquid penetrant method (LP) and locations of cracks observed after the tests by optical microscopy or SEM.

Specimen code	Orientation	Strain, %	Total exposure time, h	First LP indication, h	Crack locations (post-test microscopy examination)	Number of cracks	Max. crack length, mm
TU1-1	T	1[a]	1460	507[b, d]			
TU1-2	T	0.35[a]	1460				
TU1-3	T	1	1172.5				
TU1-4	T	1	1172.5	734.5[d]			
TU1-5	L	0.35	1460				
TU1-6	L	0.35	1460	507[b, d]			
TU1-7	L	1	1172.5	219.5[b, d]			
TU1-8	L	1	1172.5	734.5[d]			
TU2-1	T	0.35	1460				
TU2-2	T	0.35	1460				
TU2-3	T	1	1172.5	219.5[b]	Weld	3	0.3
TU2-4	T	1	1172.5	455.5	Weld	1	3
TU2-5	L	0.35	1460	507[b, d]			
TU2-6	L	0.35	1460	1022[d]			
TU2-7	L	1	1172.5	734.5	Weld	3	0.4
TU2-8	L	1	1172.5	219.5[b]	Weld	2	0.15
TU3-1	T	0.35	1460	507[b, d]			
TU3-2	T	0.35	1460	743	Weld	1	1
TU3-3	T	1	1172.5	219.5[b]	Weld, 52 butter	2	0.5
TU3-4	T	1	1172.5	734.5	52 butter	1	0.4
TU3-5	L	0.35	1460	507[b]	Weld	2	2
TU3-6	L	0.35	1460	743[d]			
TU3-7	L	1	1172.5	219.5[b]	Weld	1	2
TU3-8	L	1	1172.5				
TV4-1	T	0.35	1460	1460	Weld, butter	>10	5
TV4-2	T	0.35	1460	1460	Weld, butter	>10	8
TV4-3	T	1	1172.5	734.5	Base (I600), weld, butter	>10	9
TV4-4	T	1	1172.5	219.5[b]	Base (I600), weld	>10	15
TV4-5	L	0.35	1460	743	Base (I 600), weld, butter	>10	1
TV4-6	L	0.35	1460	1460	Weld, butter	>10	1.5
TV4-7	L	1	1172.5	734.5	Base (I600), weld, butter	>10	4
TV4-8	L	1	1172.5	1172.5[d]			
TV4K-1	T	1	438				
TV4K-2	T	1	438	438[d]			
TU1C1	T	0.01 mm[c]	953	Not relevant			
TU2C1	T	0.01 mm[c]	953	Not relevant			
TU3C1	T	0.01 mm[c]	953	Not relevant			

[a] The specimen pair TU1-1 and TU1-2 was bent unevenly. [b] Liquid penetrant test performed for the first time. [c] Crack mouth opening displacement (CMOD). [d] No cracks observed in microscopy examination.

Table 3.3. Results of post-test stress evaluation.

Weld	Spec. no.	Relaxation, mm*	Original ε, %	Δε, %**
TU1	1	0.23	0.35	-0.22
TU1	2			
TU2	3	0.22	1	-0.21
TU2	4			
TU2	5	0.31	0.35	-0.29
TU2	6			
TU2	7	0.30	1	-0.28
TU2	8			
TU3	3	0.14	1	-0.13
TU3	4			
TU3	5	0.36	0.35	-0.34
TU3	6			
TV4	5	0.17	0.35	-0.16
TV4	6			
TV4	7	0.31	1	-0.29
TV4	8			
TV4K	1	0.22	1	-0.21
TV4K	2			

*$-\Delta(2*\delta)$ or $-2\Delta\delta$ in Figure 3.3.

** Strain relaxation in outer surface, when the specimens were unloaded after the autoclave exposures.

a)

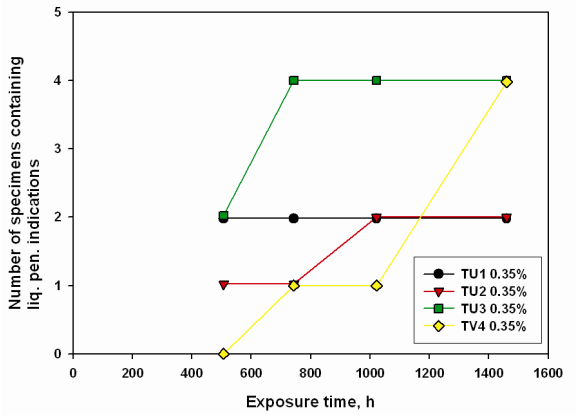

b)

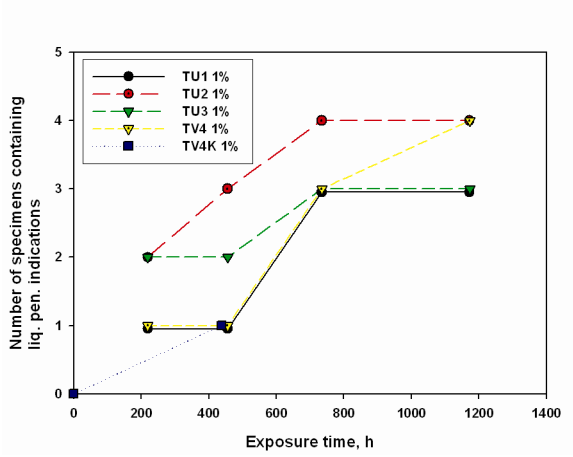

c)

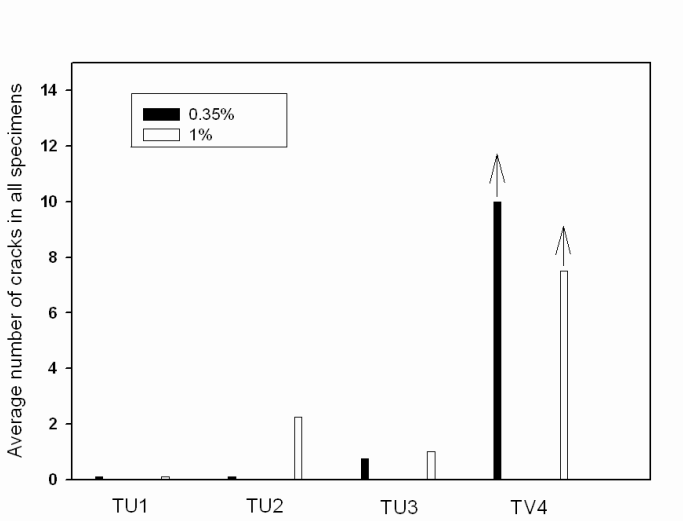

Figure 3.5 (a–c). Number of 0.35% strained specimens with a liquid penetrant indication shown as a function of exposure time a), corresponding data for specimens with 1% strain b). Liquid penetrant testing was started after 2nd or 1st exposures (0.35% and 1% strained specimens, respectively), so it is not possible to tell what was the starting level of indications in each case except for 1% strained TV4K (TV4K specimens were exposed only during the last test period and the number of specimens was 2). Figure 3.5 c) shows the average number of cracks in the specimens observed by optical microscopy or SEM.

a) b)

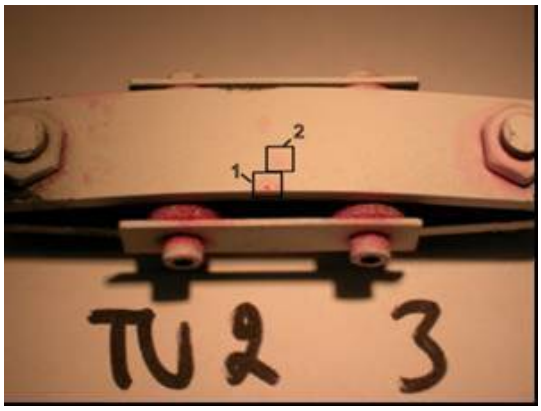

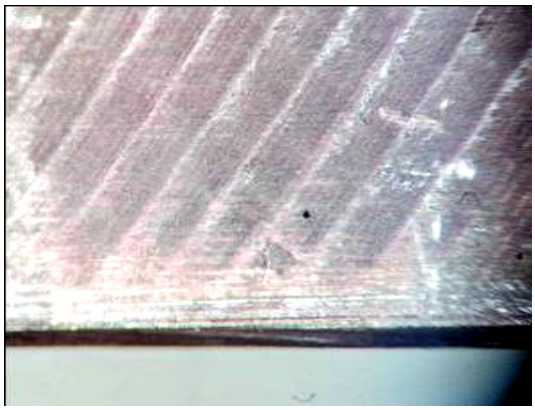

c) d)

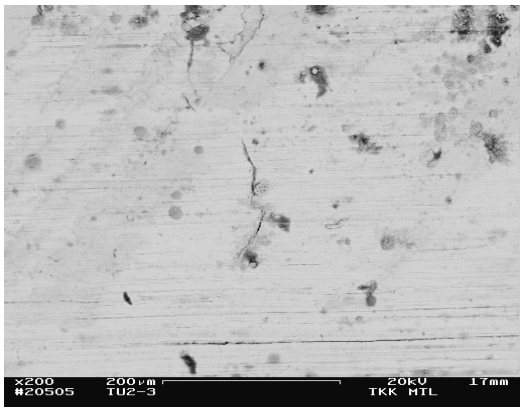

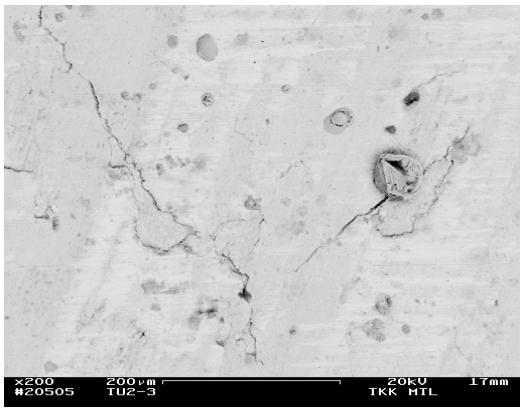

Figure 3.6 (a–d). a) Post-test liquid penetrant indications in specimen TU2-3. The locations of the subsequent photographs are shown with numbered squares. b) A photograph taken by optical microscope from location 1 in a). c)–d) SEM backscattering electron images (BEI) from locations 1 and 2 showing small crack-like features.

a) b)

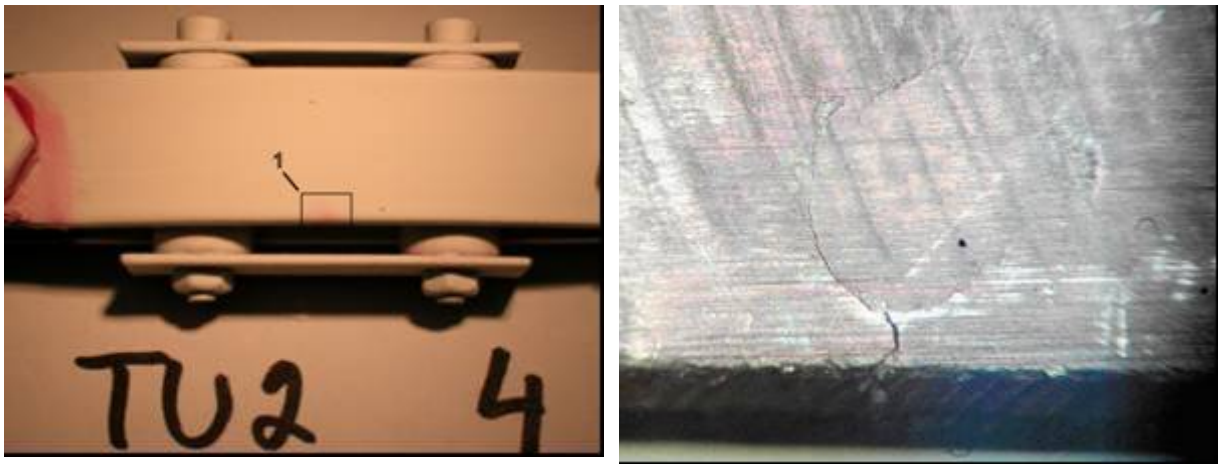

c)

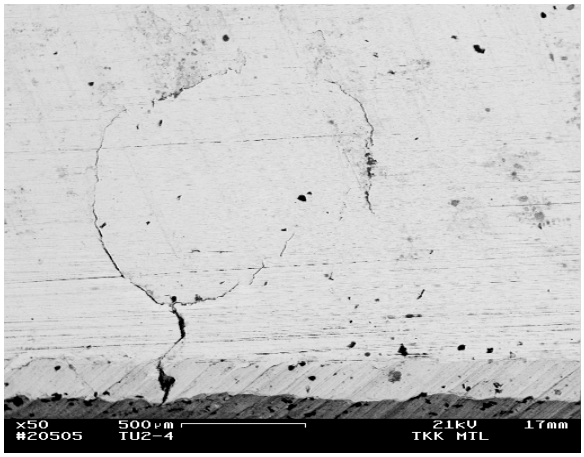

Figure 3.7 (a–c). a) Post-test liquid penetrant indication in specimen TU2-4. b) A photograph taken by optical microscope from the location of the liquid penetrant indication. c) An SEM (BEI) photograph from the same location showing a branching crack on the edge of the specimen.

a)

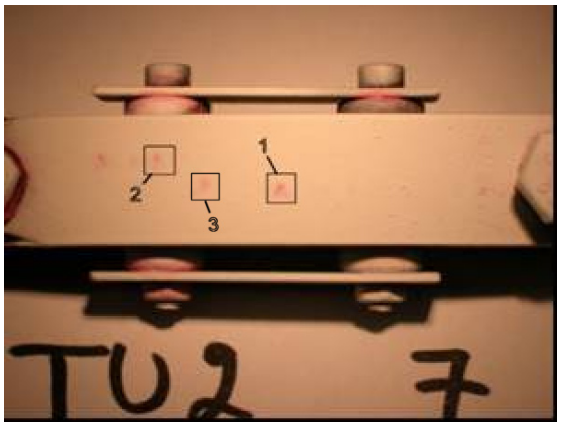

b)

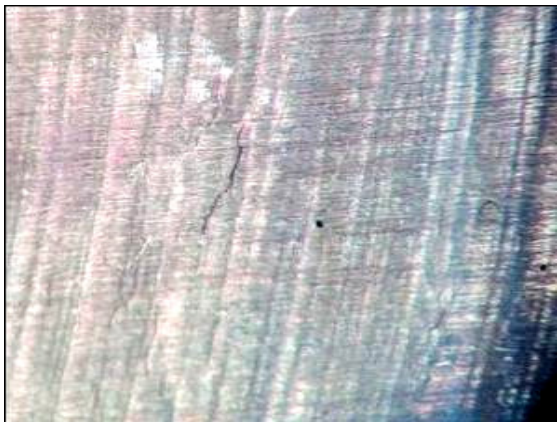

c)

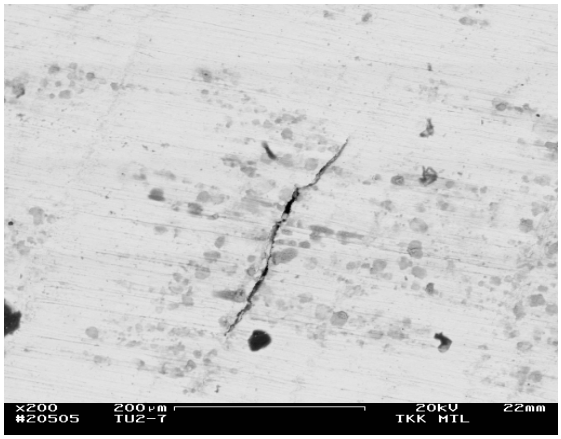

d)

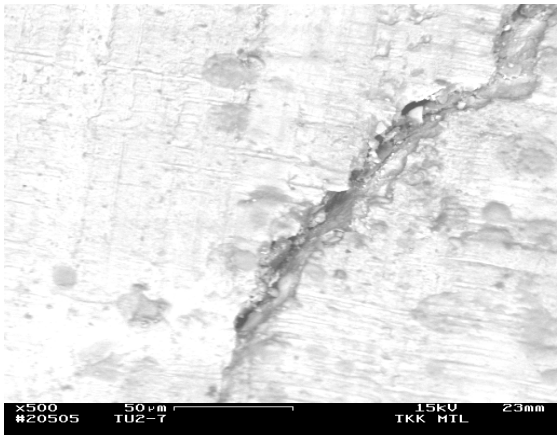

e)

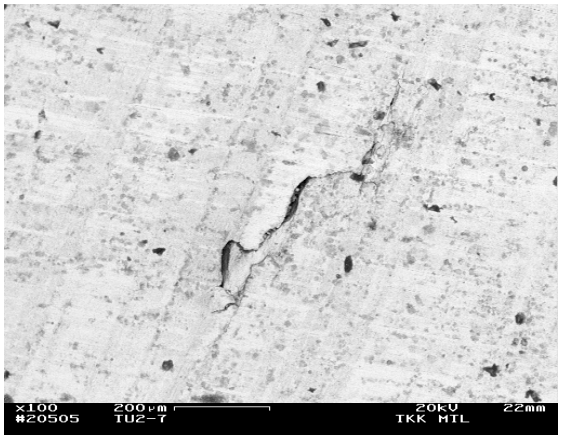

f)

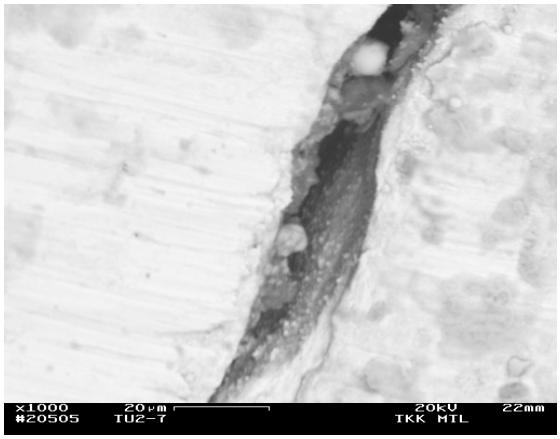

Figure 3.8 (a–f). a) Post-test liquid penetrant indications in specimen TU2-7. The locations of the subsequent photographs are shown with numbered squares. b) A photograph taken by optical microscope from location 1. c) An SEM (BEI) photograph from the same location showing a small crack. d) An SEM (BEI) photograph taken from location 2. e) An SEM (BEI) photograph taken from location 3. f) A higher magnification photograph taken from the same location as e) showing the crack-like appearance of the indication.

a) b)

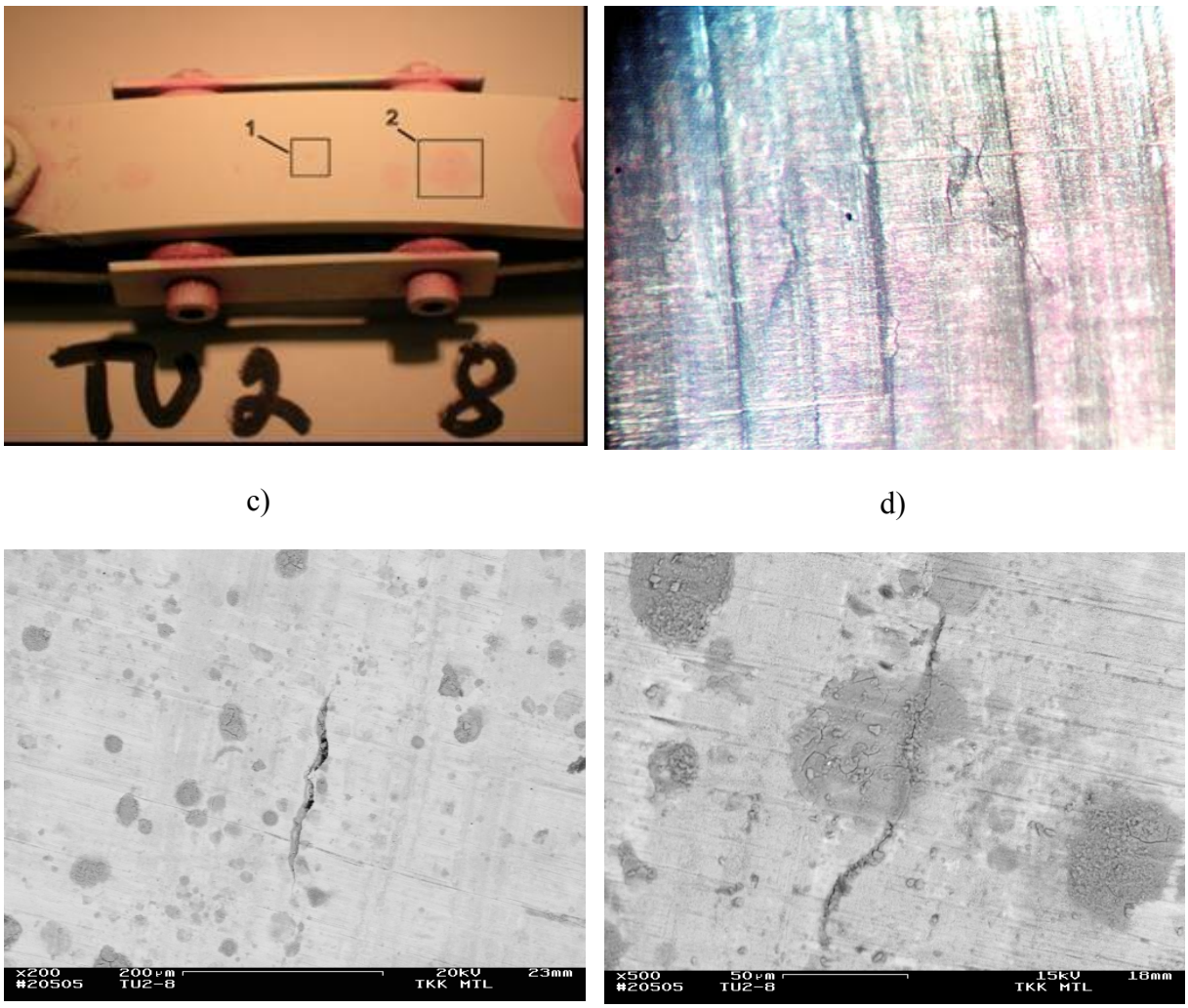

c) d)

Figure 3.9 (a–d). a) Post-test liquid penetrant indications in specimen TU2-8. The locations of the subsequent photographs are shown with numbered squares. b) A photograph taken by optical microscope from location 1. c) An SEM (BEI) photograph from the same location showing a small crack. d) An SEM (BEI) photograph taken from location 2.

a)

b)

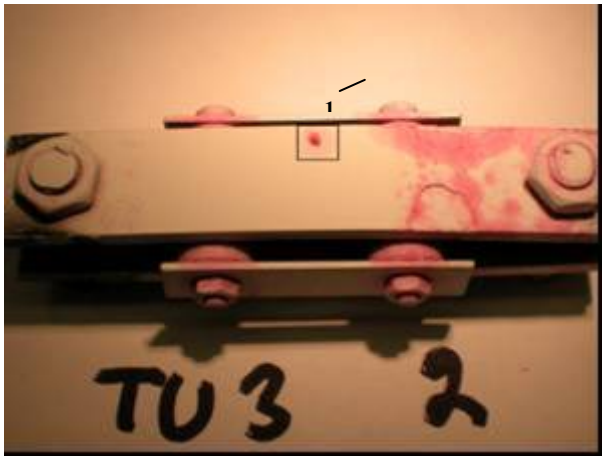

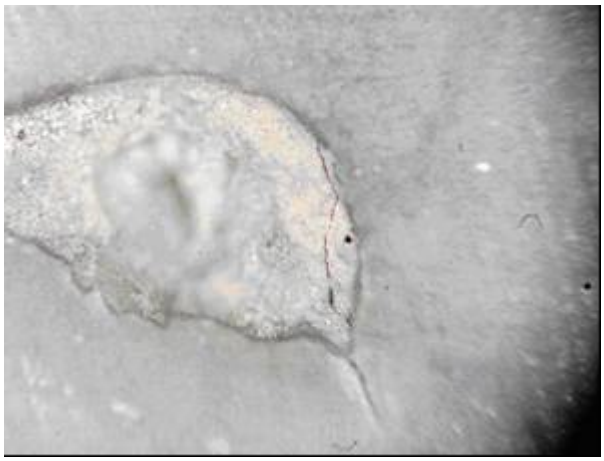

c)

d)

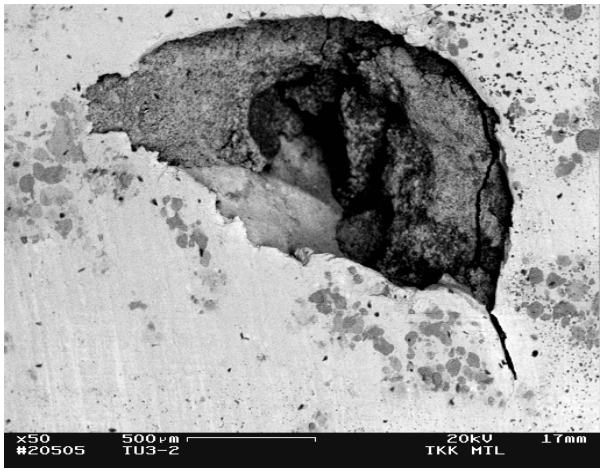

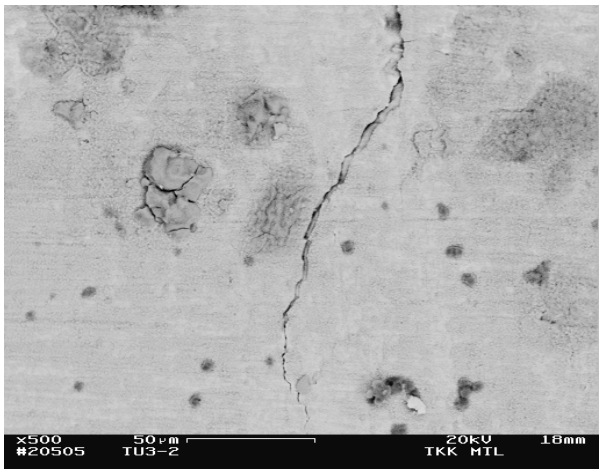

Figure 3.10 (a–d). a) Post-test liquid penetrant indications in specimen TU3-2. The location of the subsequent photographs is shown with the square. b) A photograph taken by optical microscope from location 1. A crack associated with a pit can be seen. c) An SEM (BEI) photograph from the same location showing the crack more clearly. d) An SEM (BEI) photograph taken from the tip of the same crack.

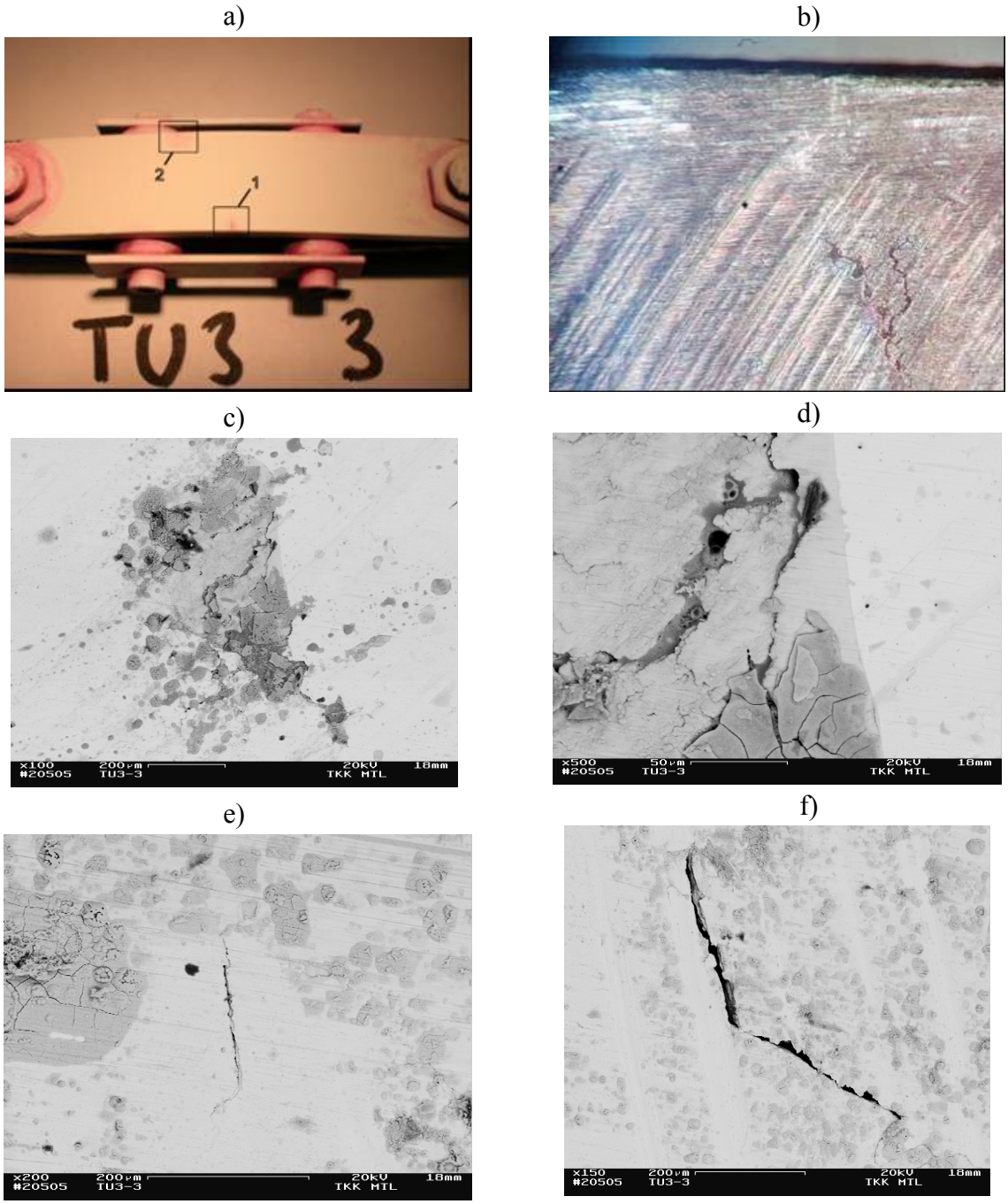

Figure 3.11 (a–f). a) Post-test liquid penetrant indications in specimen TU3-3. The locations of the subsequent photographs are shown with numbered squares. b) A photograph taken by optical microscope from location 1 (Inconel 52 buttering layer). c) An SEM (BEI) photograph from the same location showing cracked oxide layer which is different from the general surface of the specimen. d) A higher magnification SEM (BEI) photograph taken from the same location. The cracks in the oxide can be seen more clearly. e) and f) SEM (BEI) photographs taken from location 2 showing crack-like features (Inconel 152 weld).

a) b)

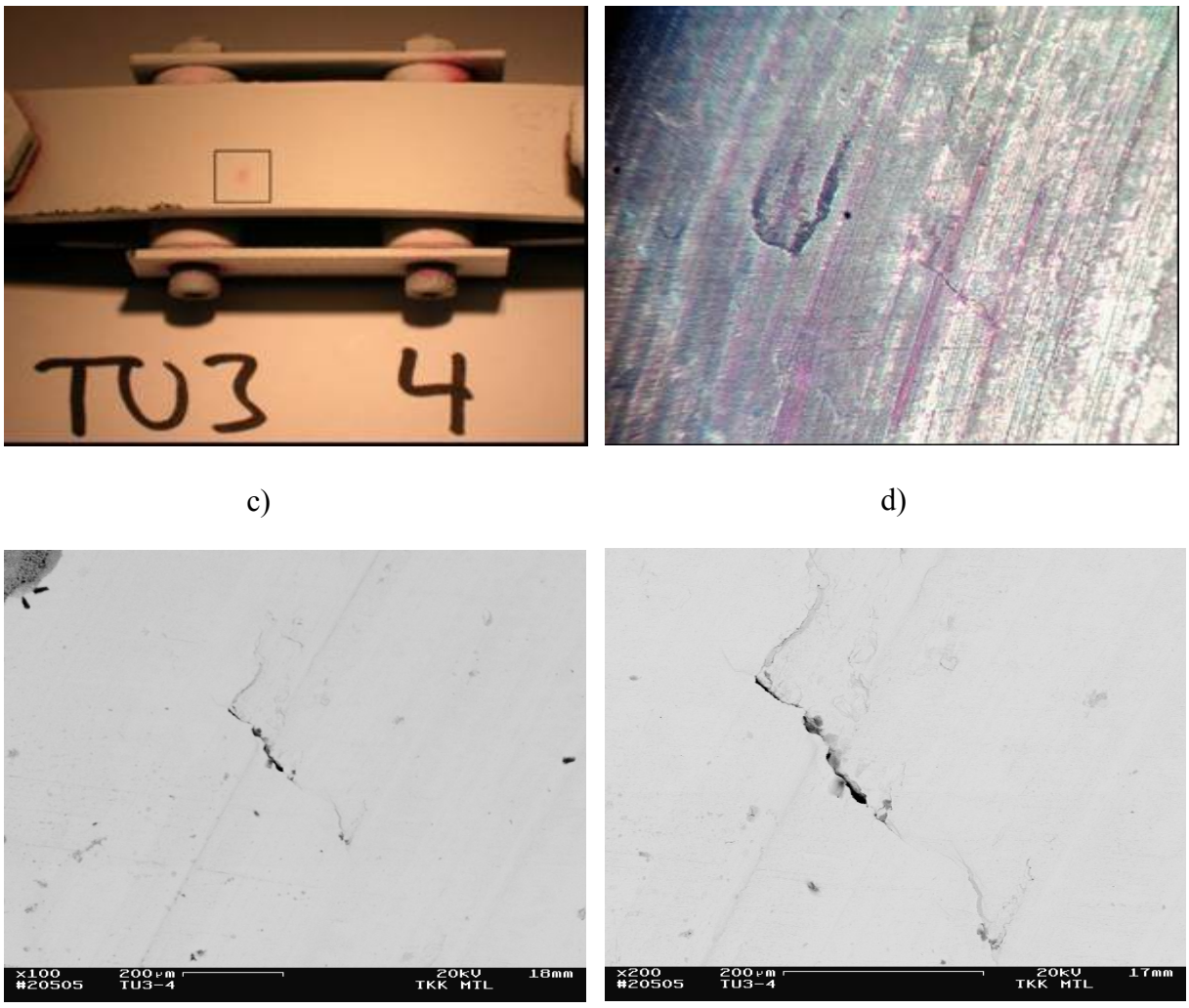

c) d)

Figure 3.12 (a–d). a) Post-test liquid penetrant indication in specimen TU3-4 in Inconel 52 buttering layer. b) A photograph taken by optical microscope from the indication. c) and d) SEM (BEI) photographs from the same location showing a small crack-like feature.

a) b)

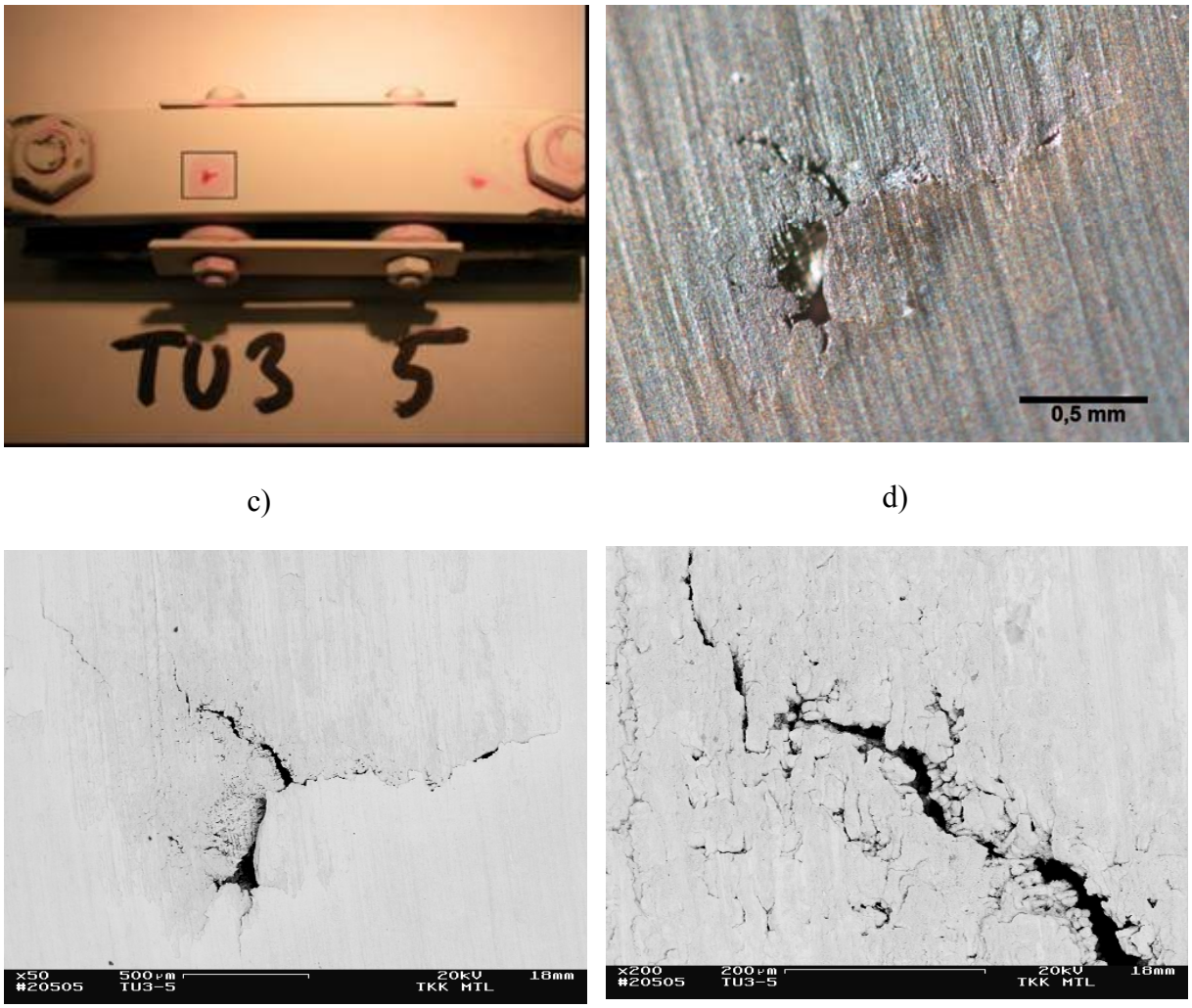

c) d)

Figure 3.13 (a–d). a) Post-test liquid penetrant indications in specimen TU3-5. The location of the subsequent photographs is shown with a square. b) A photograph taken by optical microscope from the indication. c) and d) SEM (BEI) photographs from the same location showing a branching crack and local dissolution of slag inclusion.

a)

b)

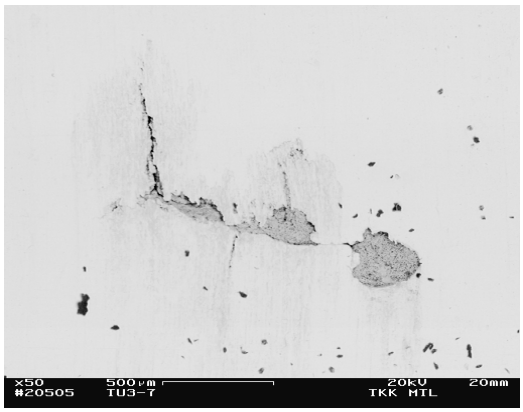

c)

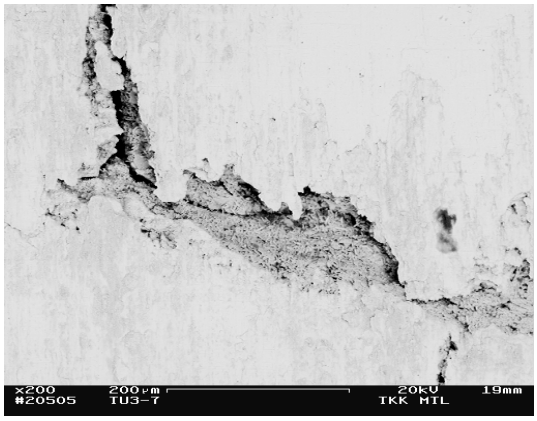

d)

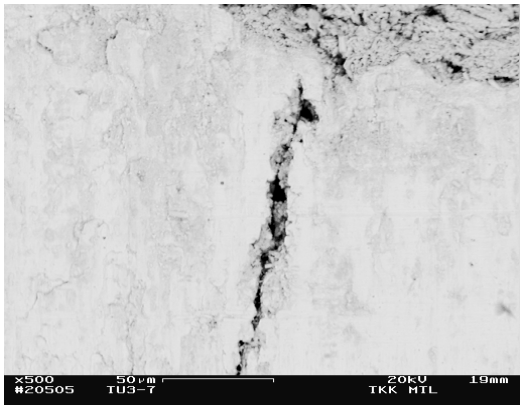

Figure 3.14 (a–d). a) Post-test liquid penetrant indications in specimen TU3-7. The location of the subsequent photographs is shown with a square. b)–d) SEM (BEI) photographs showing that the indication is a branched crack associated with a wider area where the surface layer (probably a slag inclusion) has cracked or dissolved away.

a) b)

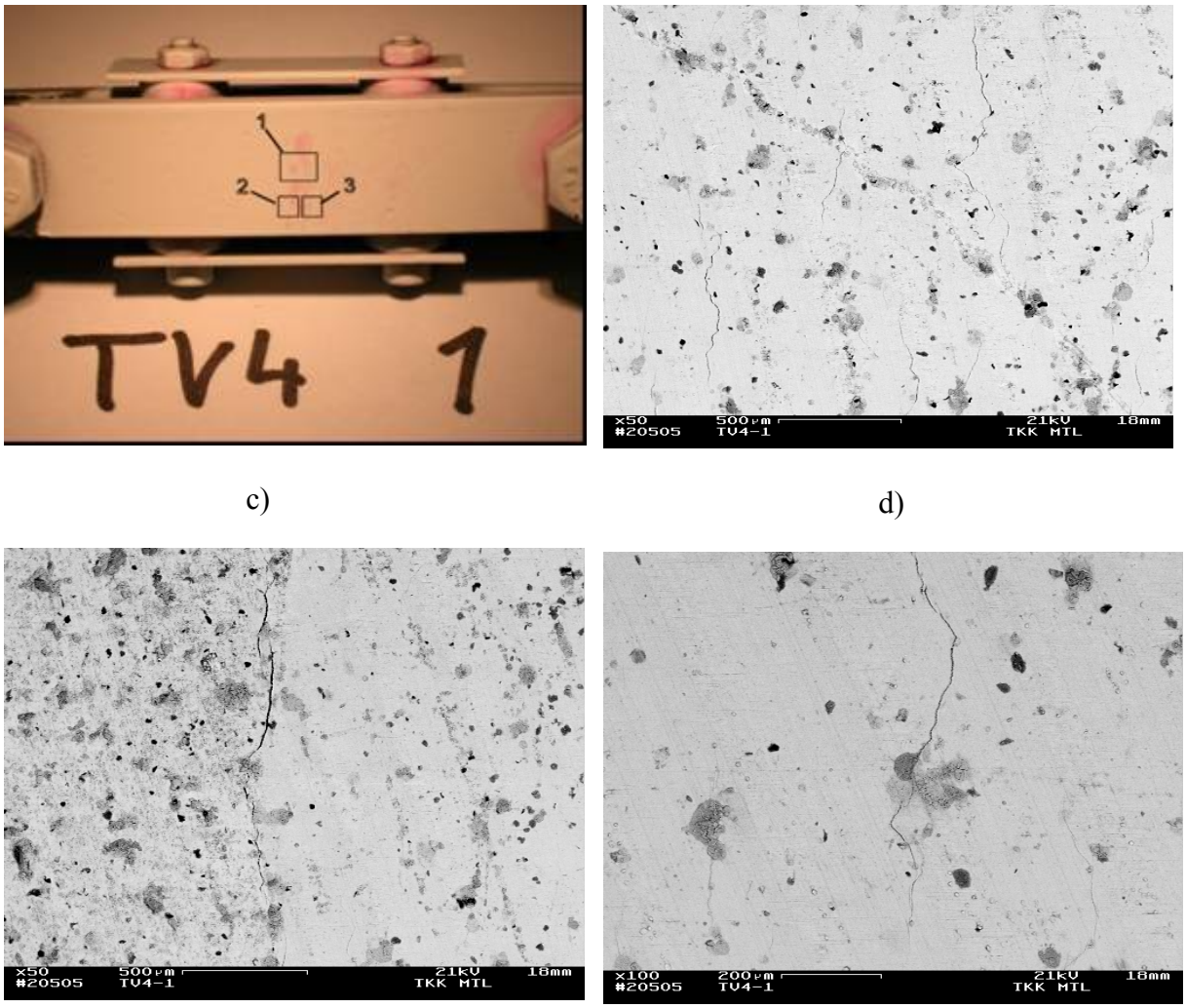

c) d)

Figure 3.15 (a–d). a) Post-test liquid penetrant indications in specimen TV4-1. The locations of the subsequent photographs are shown with squares. b) An SEM (BEI) photograph taken from location 1. c) An SEM (BEI) photograph taken from location 2. d) An SEM (BEI) photograph taken from location 3. All SEM photographs show one or several long but narrow cracks. The crack in image c) is located in the weld-Inconel 600 base metal interface. Other cracks are both in weld buttering (Inconel 182) and weld joint (also Inconel 182).

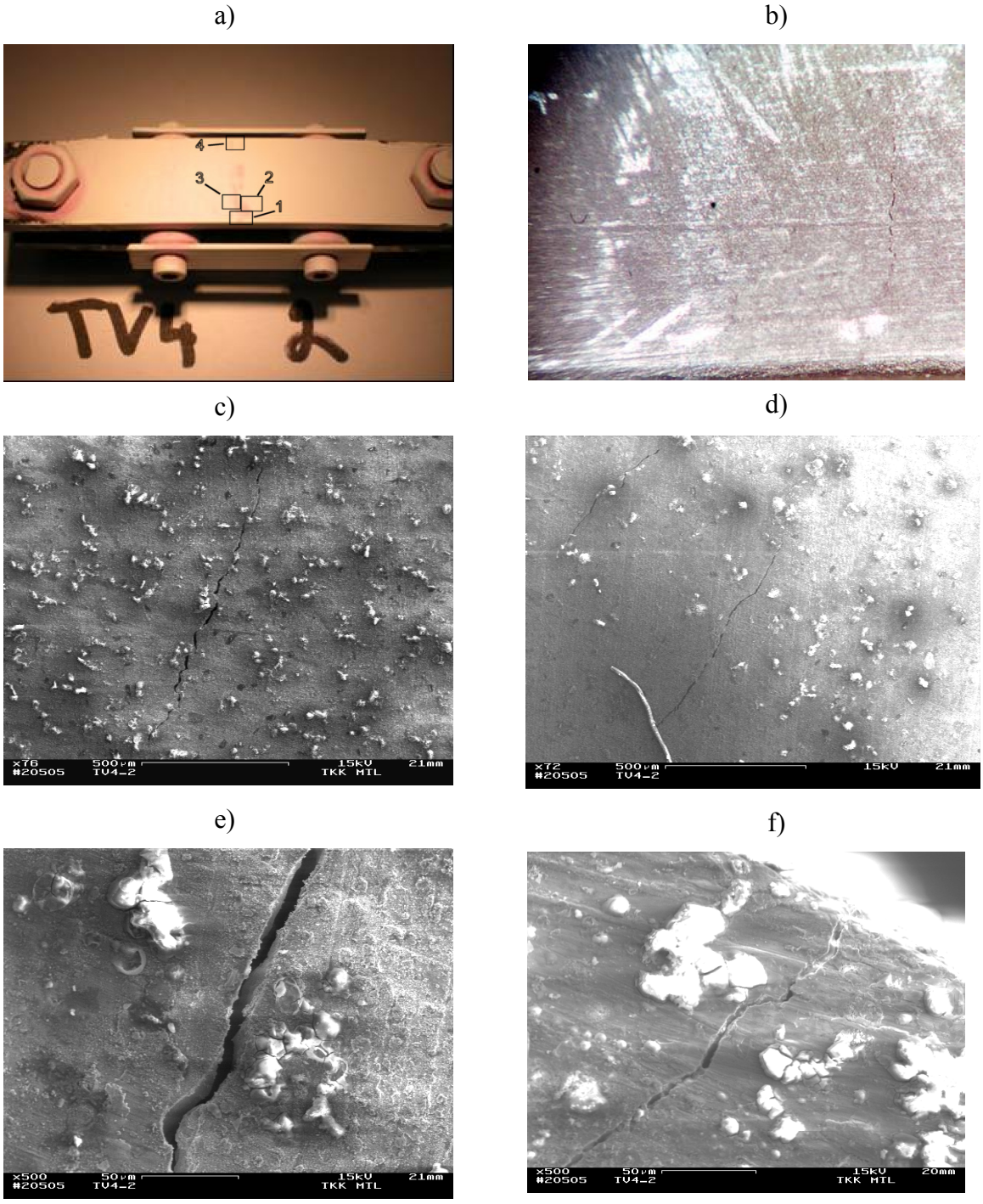

Figure 3.16 (a–f). a) Post-test liquid penetrant indications in specimen TV4-2. The locations of the subsequent photographs are shown with squares. b) A photograph taken by optical microscope from the indication in location 1 close to the specimen side surface. c) An SEM (secondary electron image, SEI) photograph taken from the same location. d)–f) SEM (SEI) photographs taken from locations 2–4, respectively. Cracks exist both in weld buttering and weld joint.

a) b)

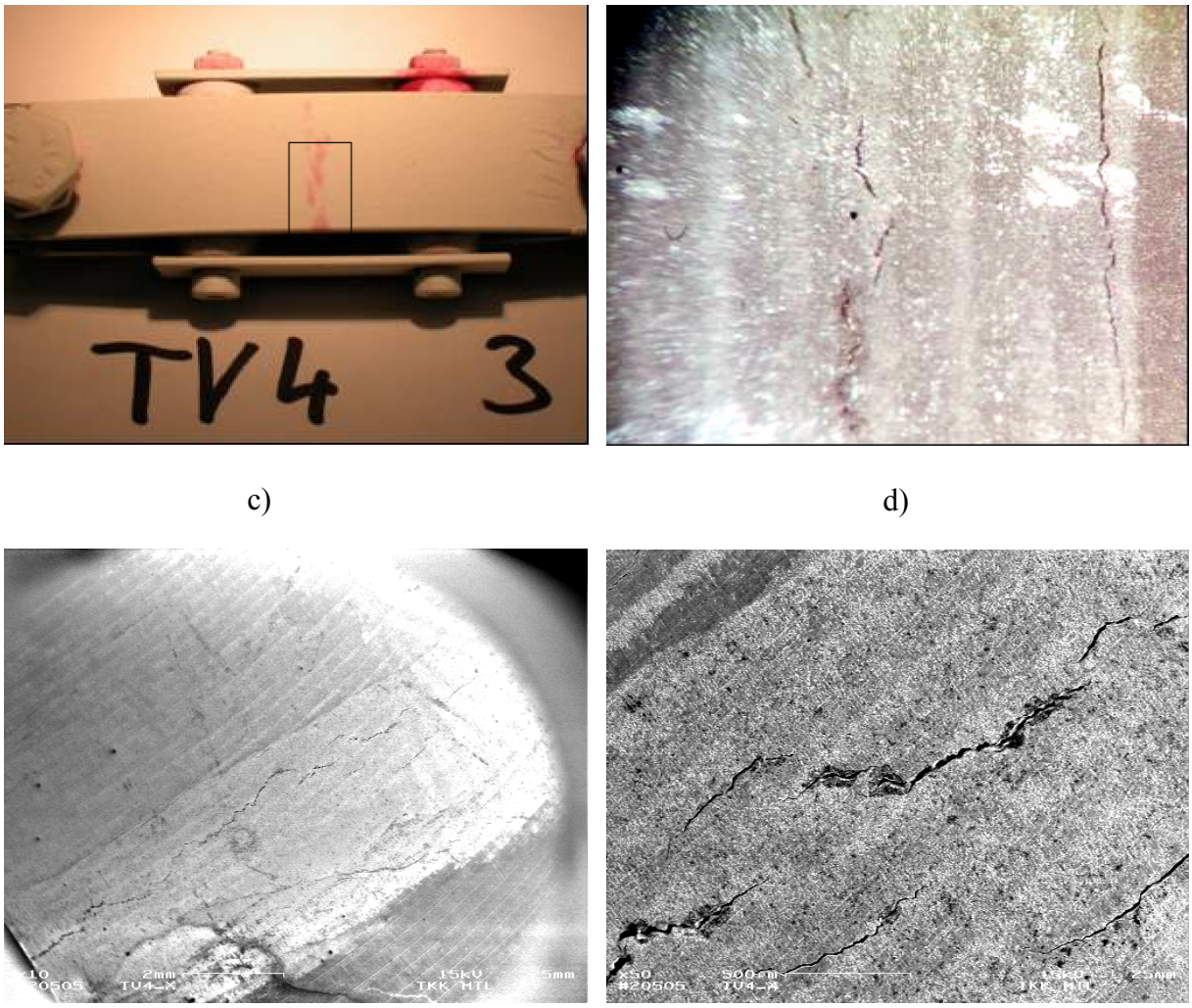

c) d)

Figure 3.17 (a–d). a) Post-test liquid penetrant indications in specimen TV4-3. b) A photograph taken by optical microscope from the area marked with the square in image a). c) and d) SEM (BEI and SEI, respectively) photographs taken from the same location. Cracks are located in the weld buttering, weld joint and smaller ones also in Inconel 600 base metal.

a)

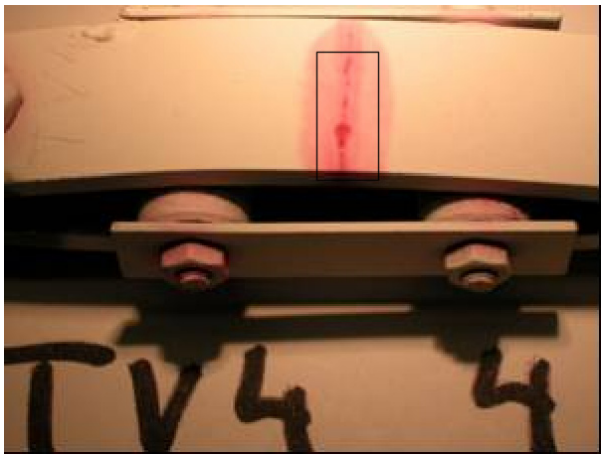
TV4 4

b)

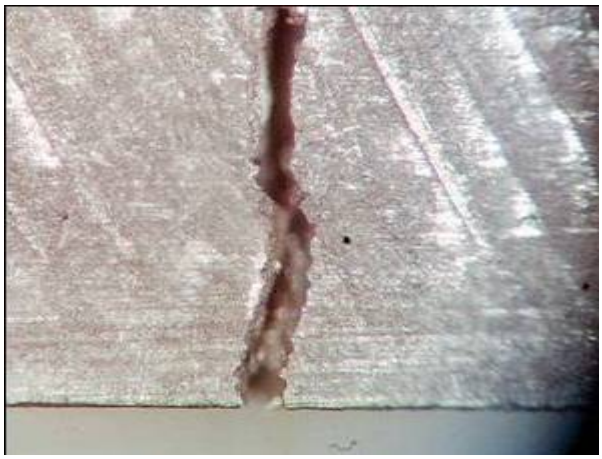

c)

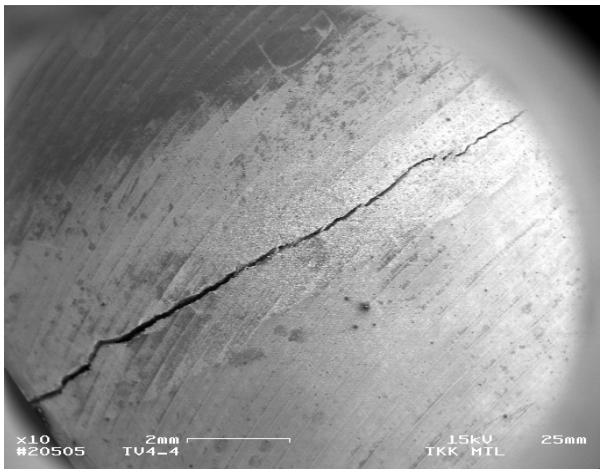
x10 2mm 15kV 25mm
#20505 TV4-4 IKK MIL

d)

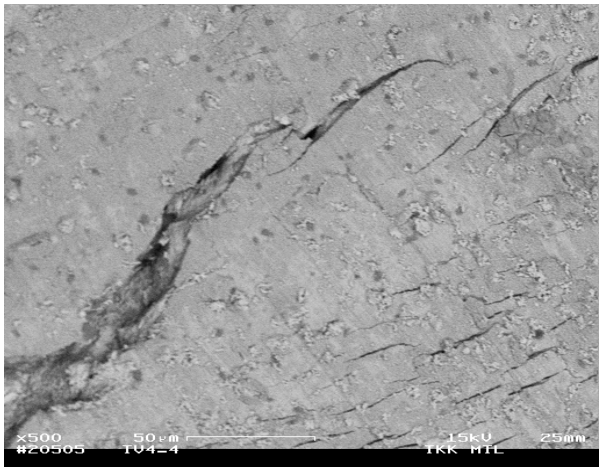
x500 50 µm 15kV 25mm
#20505 TV4-4 IKK MIL

e)

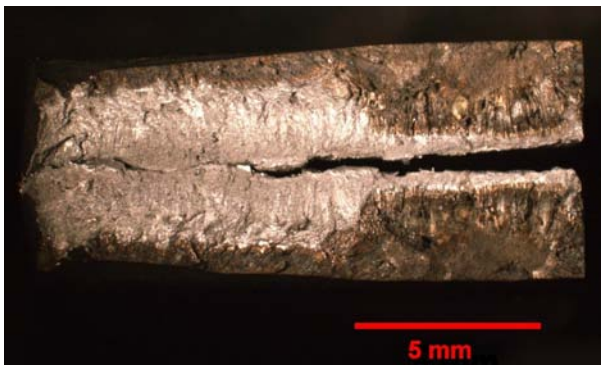
5 mm

f)

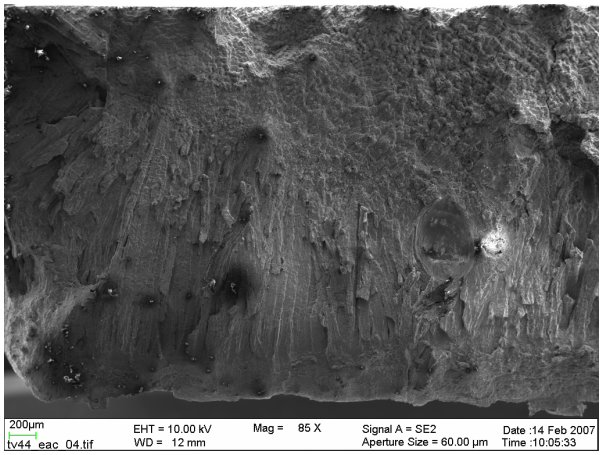
200µm
tv44_eac_04.tif
EHT = 10.00 kV
WD = 12 mm
Mag = 85 X
Signal A = SE2
Aperture Size = 60.00 µm
Date :14 Feb 2007
Time :10:05:33

g) h)

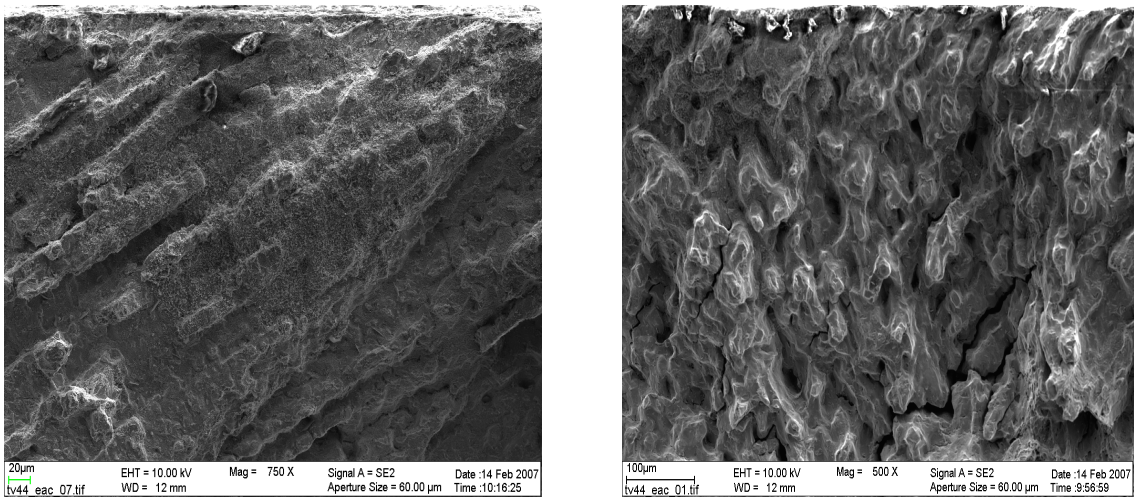

Figure 3.18 (a–h). a) Post-test liquid penetrant indications in specimen TV4-4. b) A photograph taken by optical microscope from the main crack. c) An SEM (BEI) photograph taken from the same location as image b). d) An SEM (BEI) photograph taken from an area close to the area in the middle of image b) from a secondary crack. A number of smaller cracks can also be seen. The main crack is in Inconel 182 weld joint. Smaller cracks are also in Inconel 182 buttering. e) Opened fracture surface. The main crack formed during the test series is seen as dark brown (both halves of the specimen are shown). f), g) and h) SEM (SEI) photographs showing the interdendritic nature of the cracking.

a) b)

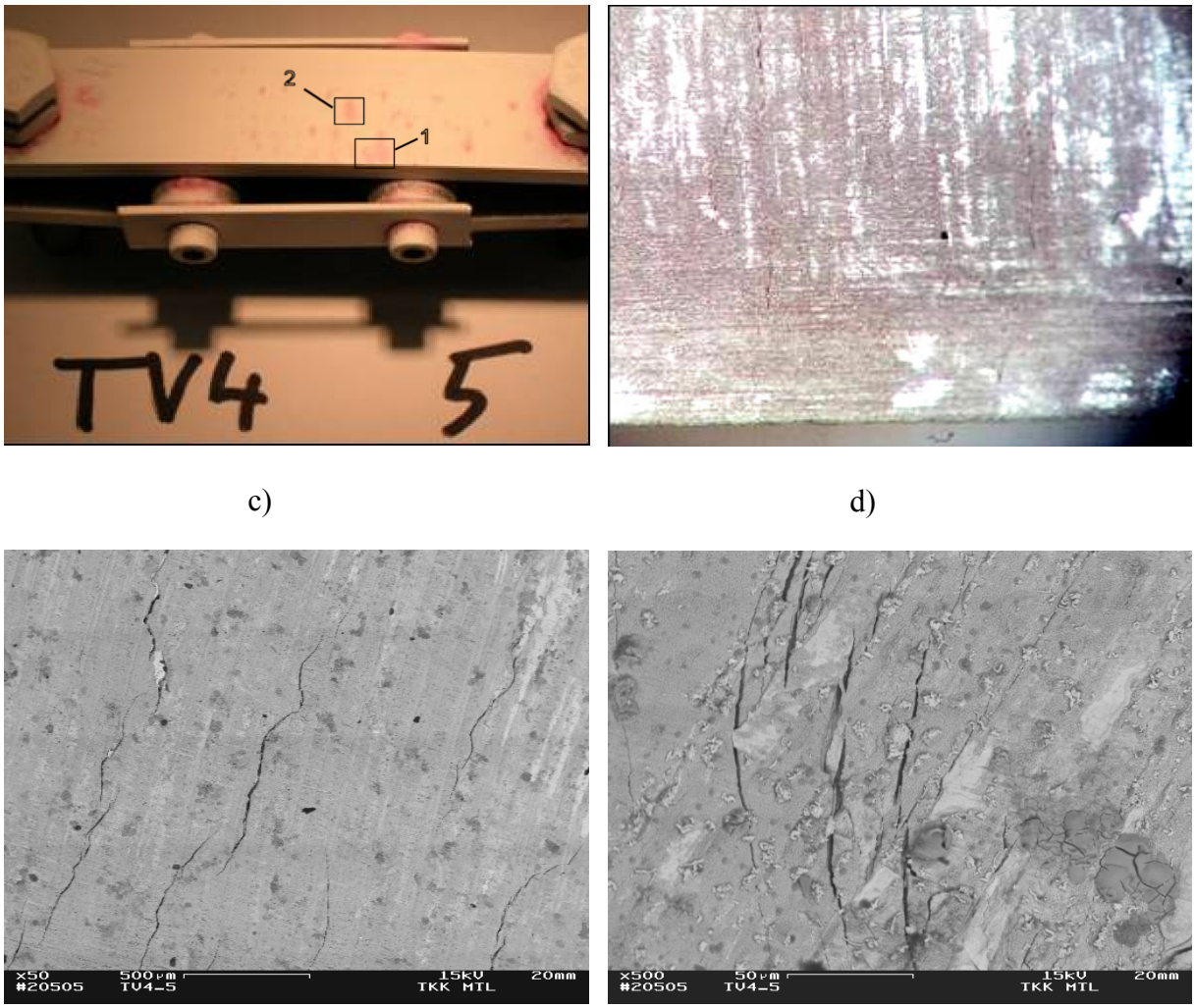

c) d)

Figure 3.19 (a–d). a) Post-test liquid penetrant indications in specimen TV4-5. b) A photograph taken by optical microscope from location 1 (Inconel 600 base metal). c) An SEM (BEI) photograph taken from the same location as image b). d) An SEM (BEI) photograph taken from location 2 (Inconel 182 weld metal). The cracks were located in Inconel 182 buttering layer, weld joint and Inconel 600 base metal.

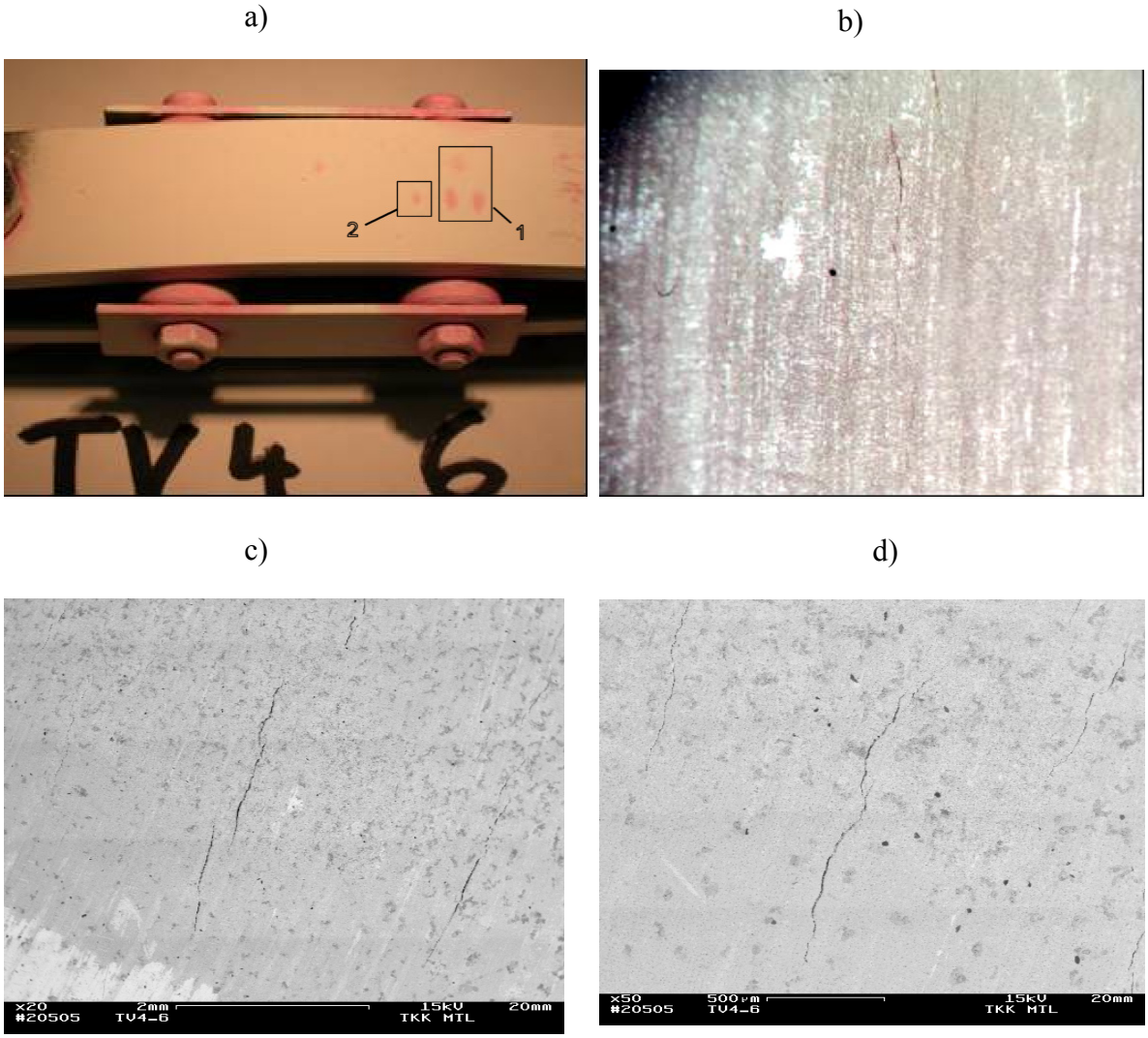

Figure 3.20 (a–d). a) Post-test liquid penetrant indications in specimen TV4-6. b) A photograph taken by optical microscope from location 1 (Inconel 182 buttering and weld joint). c) An SEM (BEI) photograph taken from the same location as image b). d) An SEM (BEI) photograph taken from location 2 (Inconel 182 weld metal). The cracks were located in Inconel 182 buttering layer and weld joint. No cracks were observed in Inconel 600 base metal.

a)

b)

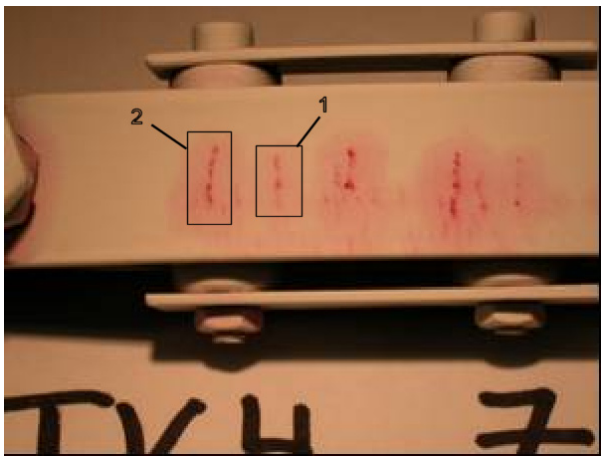

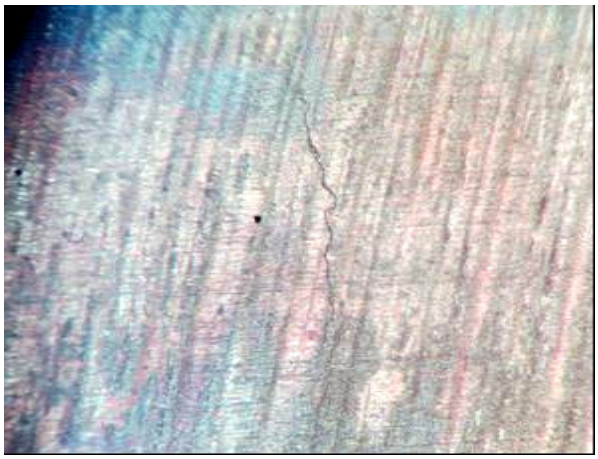

c)

d)

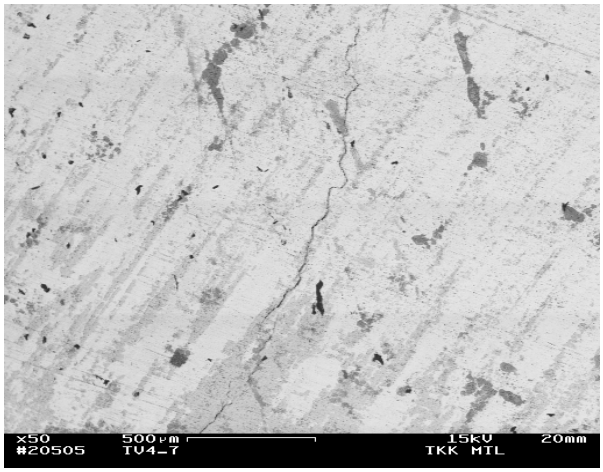

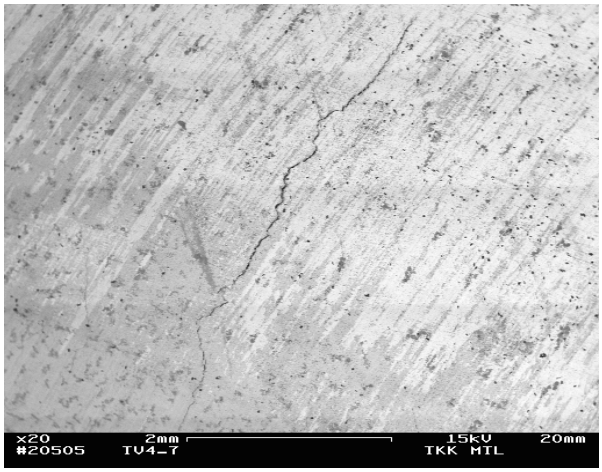

Figure 3.21 (a–d). a) Post-test liquid penetrant indications in specimen TV4-7. b) A photograph taken by optical microscope from location 1 (Inconel 182 buttering and weld joint). c) An SEM (BEI) photograph taken from the same location as image b). d) An SEM (BEI) photograph taken from location 2 (Inconel 182 buttering and weld joint). Some of the cracks extend into Inconel 600 base metal.

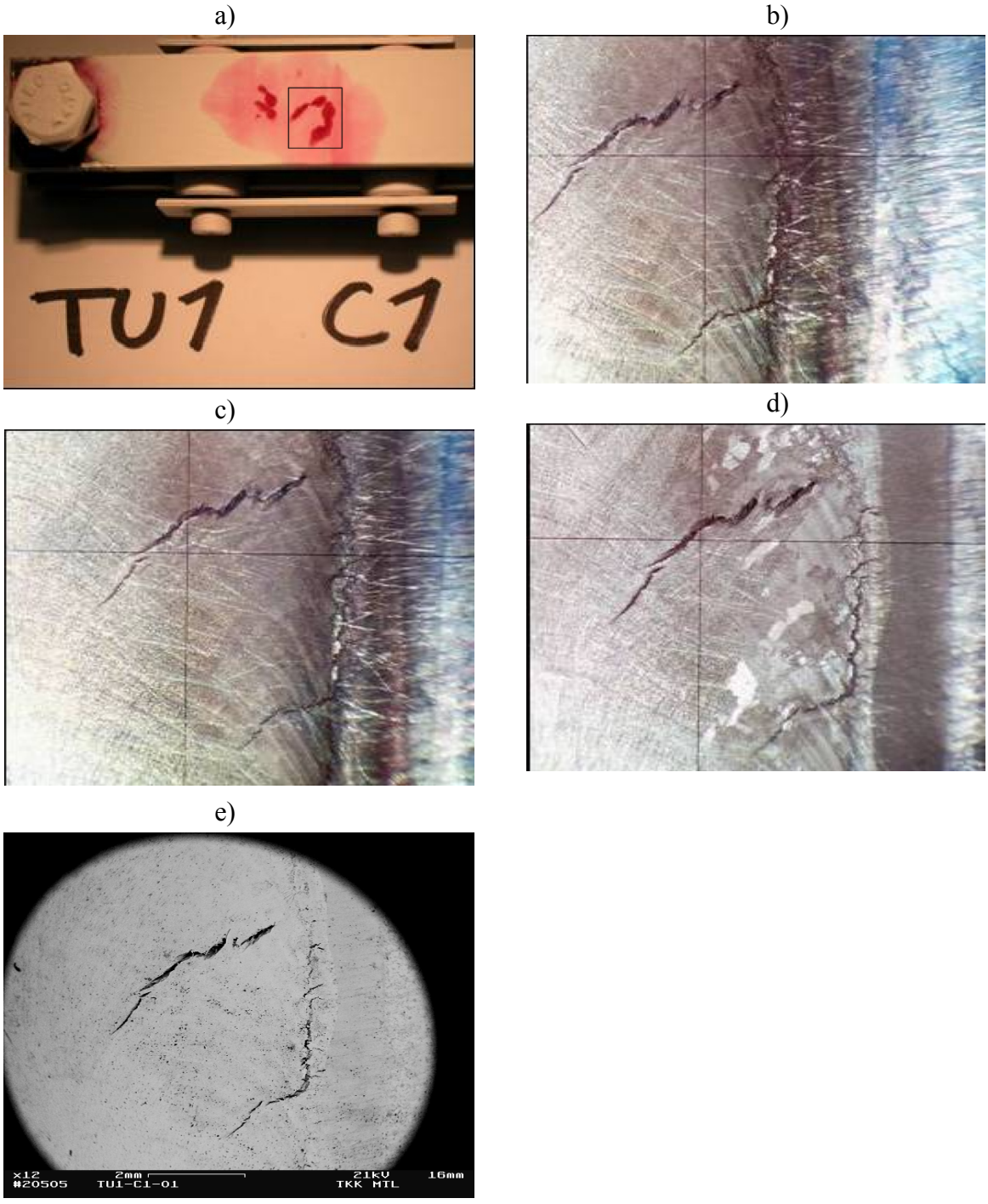

Figure 3.22 (a–e). a) Liquid penetrant indications in hot cracked specimen TU1C1. b) A photograph taken by optical microscope from the location indicated in image a) by a rectangle after Varestraint test. Image c) is the same crack as in image b) but after loading. Image d) is the same crack as in images b) and c) but after exposure to doped steam. e) Post-test SEM (BEI) photograph of the same location. The hot cracks are located in Inconel 152 weld metal and weld metal/AISI 316NG base metal interface.

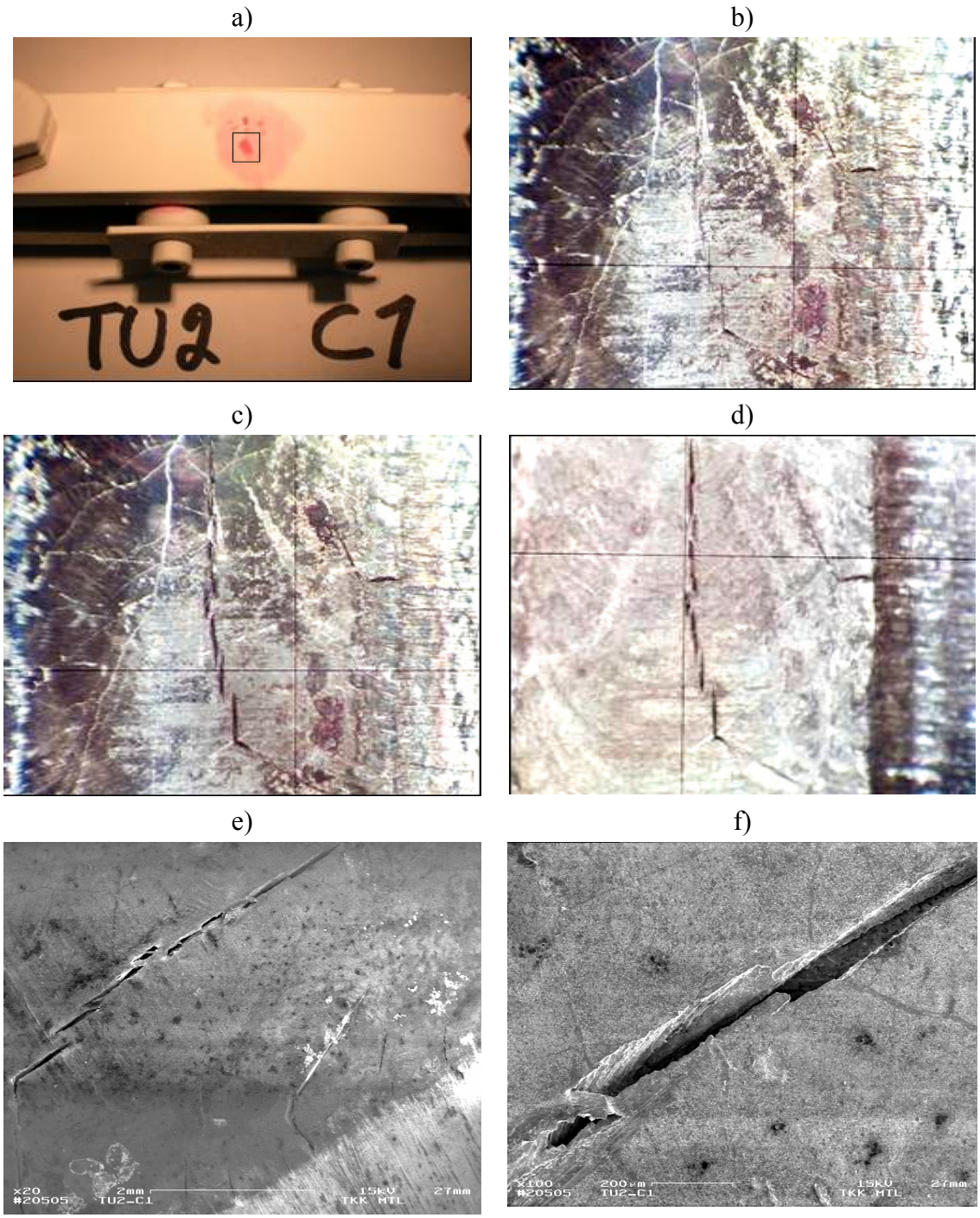

Figure 3.23 (a–f). a) Liquid penetrant indications in hot cracked specimen TU2C1. b) A photograph taken by optical microscope from the location indicated in image a) by a rectangle after Varestraint test. Image c) is the same crack as in image b) but after loading. Image d) is the same crack as in images b) and c) but after exposure to doped steam. Images e) and f) are post-test SEM (SEI) photographs of the same location. The hot cracks are located in Inconel 52 weld metal.

a) b)

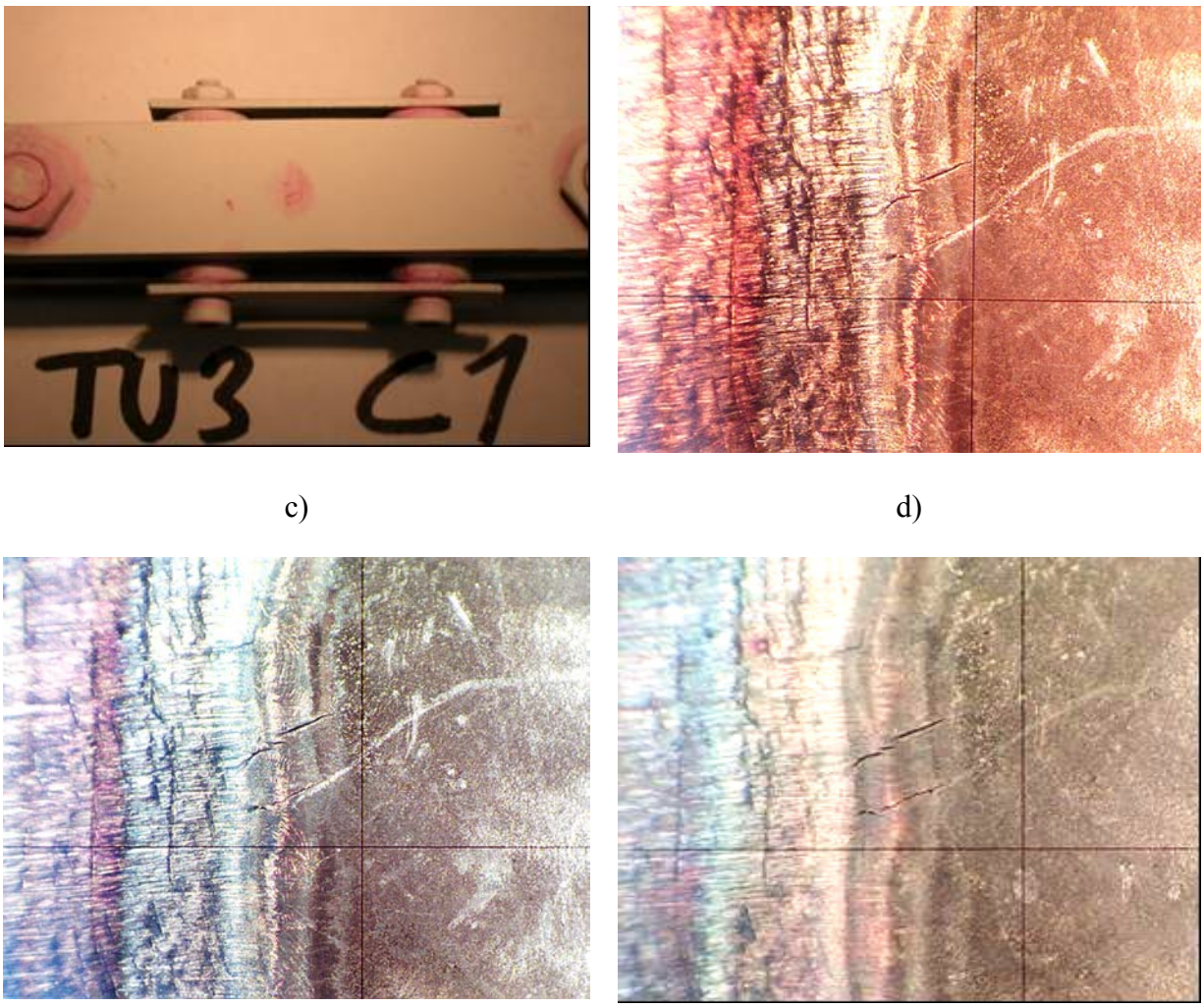

c) d)

Figure 3.24 (a–d). a) Liquid penetrant indications in hot cracked specimen TU3C1. b) A photograph taken by optical microscope from the liquid penetrant indication after Varestraint test. Image c) is the same crack as in image b) but after loading. Image d) is the same crack as in images b) and c) but after exposure to doped steam. The hot cracks are located in Inconel 152 weld metal (not in alloy 152 or 52 buttering layers).

a) b)

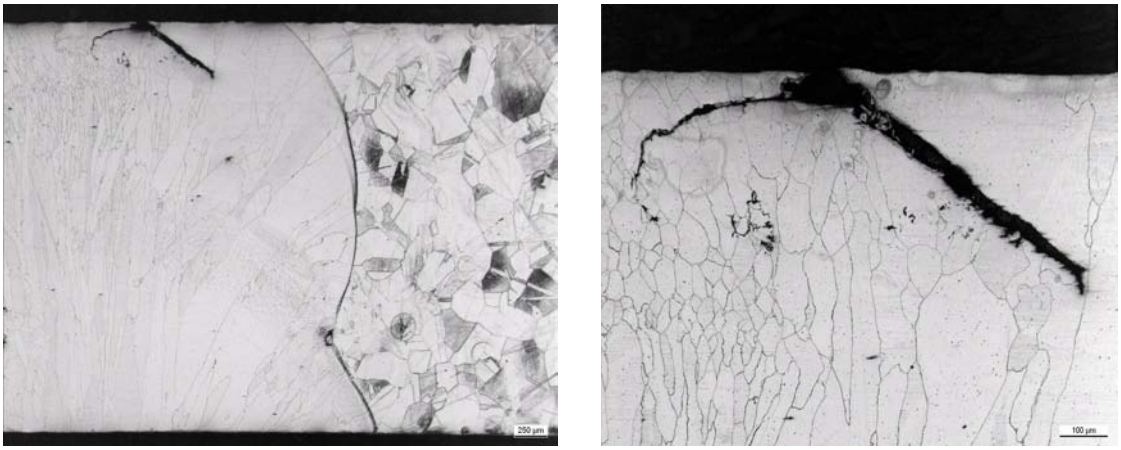

c)

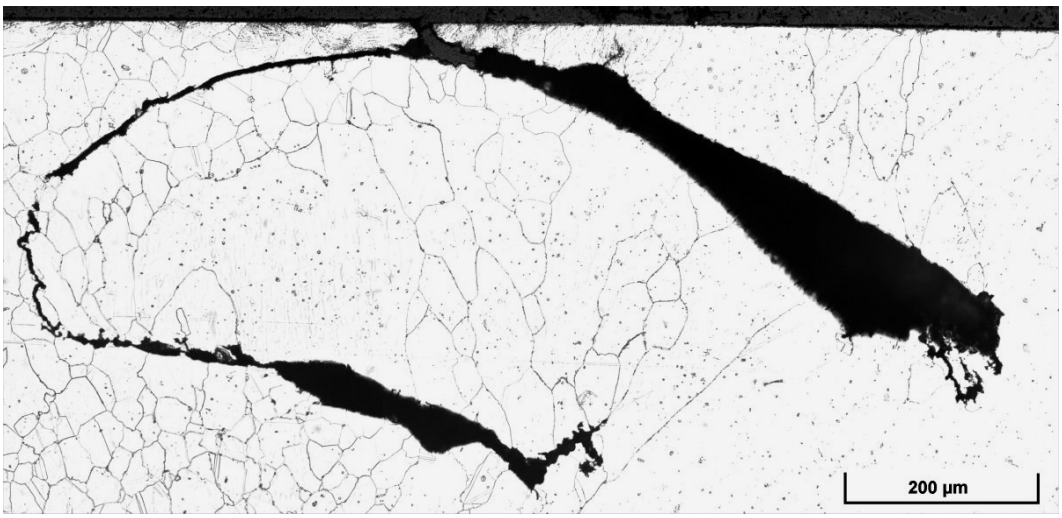

Figure 3.25 (a–c). a) A micrograph showing a part of the weld with a crack in a section cut from the weld region of specimen TU2-4. AISI 316 NG base metal is seen on the right hand side of the Inconel weld (as polished and etched). b) A higher magnification micrographs from a) (as polished and etched). c) The same location, but after ~0.5 mm further grinding (after etching).

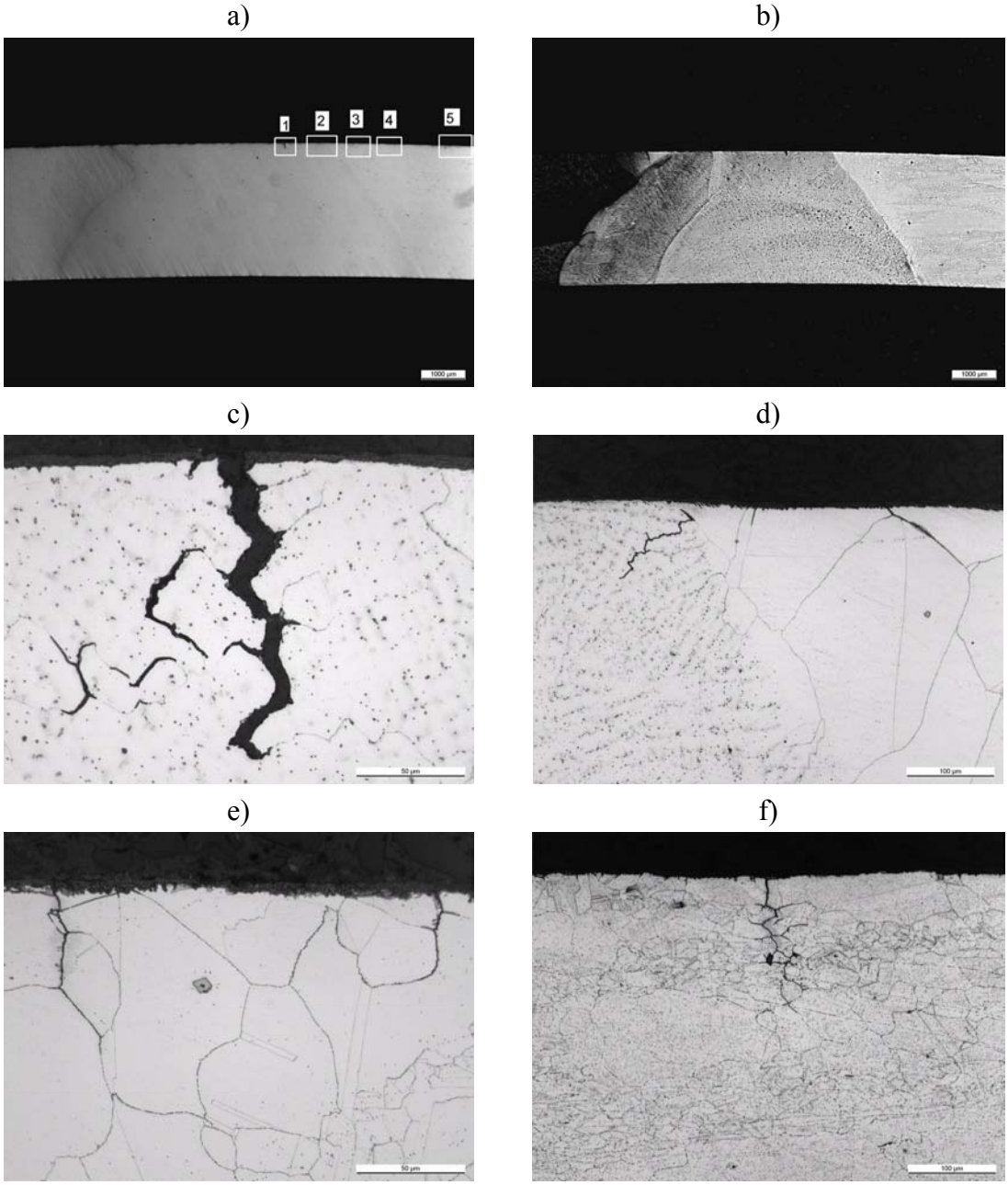

Figure 3.26 (a–f). a) A macrograph of a section cut from the weld region of specimen TV4-3. The locations of the micrographs c)–f) are shown in the photograph. b) The same section as in a) in etched condition. c) Micrograph taken from location 1 (cracks in the weld). d) Micrograph taken from location 2 (cracks in weld and Inconel 600 HAZ). e) Micrograph taken from location 3 (cracks in HAZ). f) Micrograph taken from location 4 (a branching crack in Inconel 600 base metal).

Figure 3.27 shows an EDS analysis of the cross-section of the crack shown in Figure 3.26 c), close to the crack mouth so that the outer surface can also be seen. It can be seen that the outer surface and the fracture surface have oxidized, and the sideways penetrations of the crack are full of oxide. The X-ray element maps of Figure 3.28 show that the oxide is enriched in Cr and Mn and that Ni is only as isolated areas on the surface of the oxide layer. Niobium can only be seen in the Nb(C, N) particles.

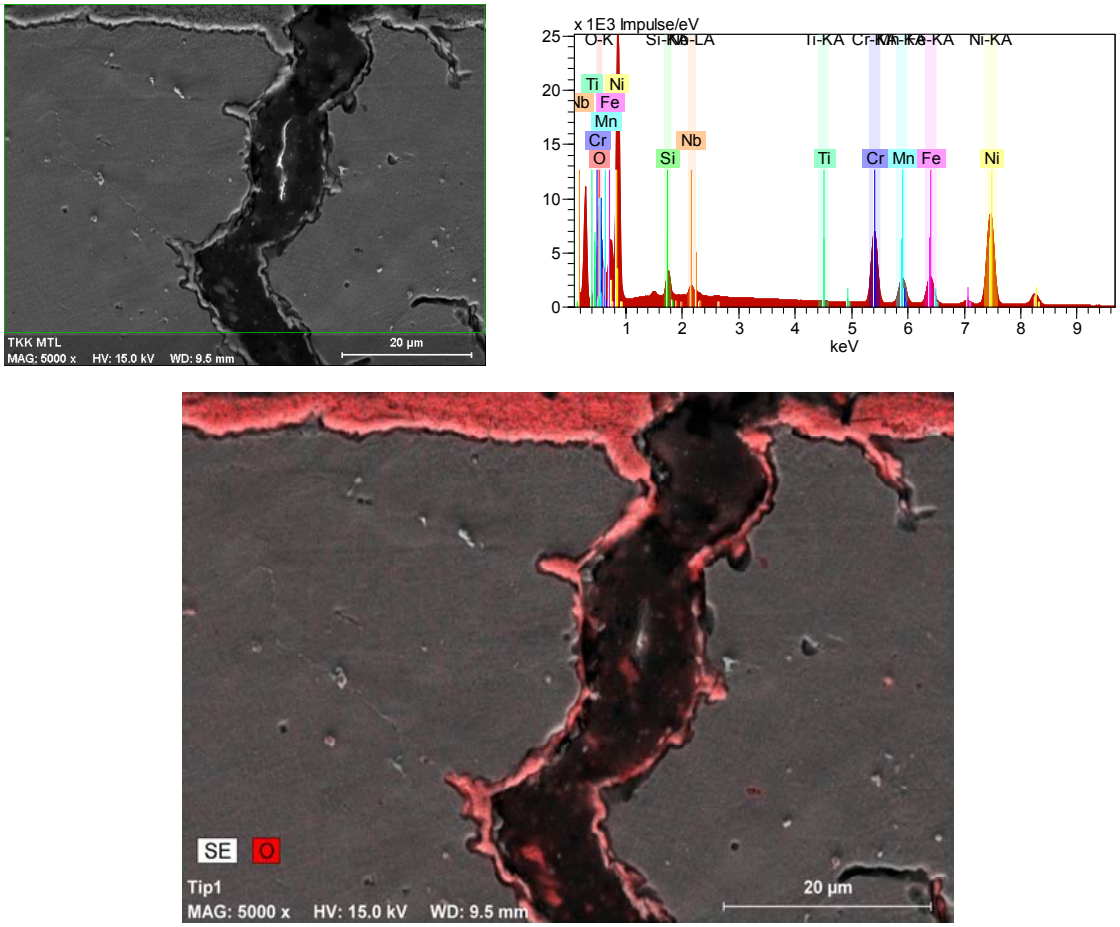

Figure 3.27. EDS analysis of cross-section of an EAC crack of specimen TV4-3 showing oxidation of the fracture surface and the outer surface of the specimen in the doped steam test.

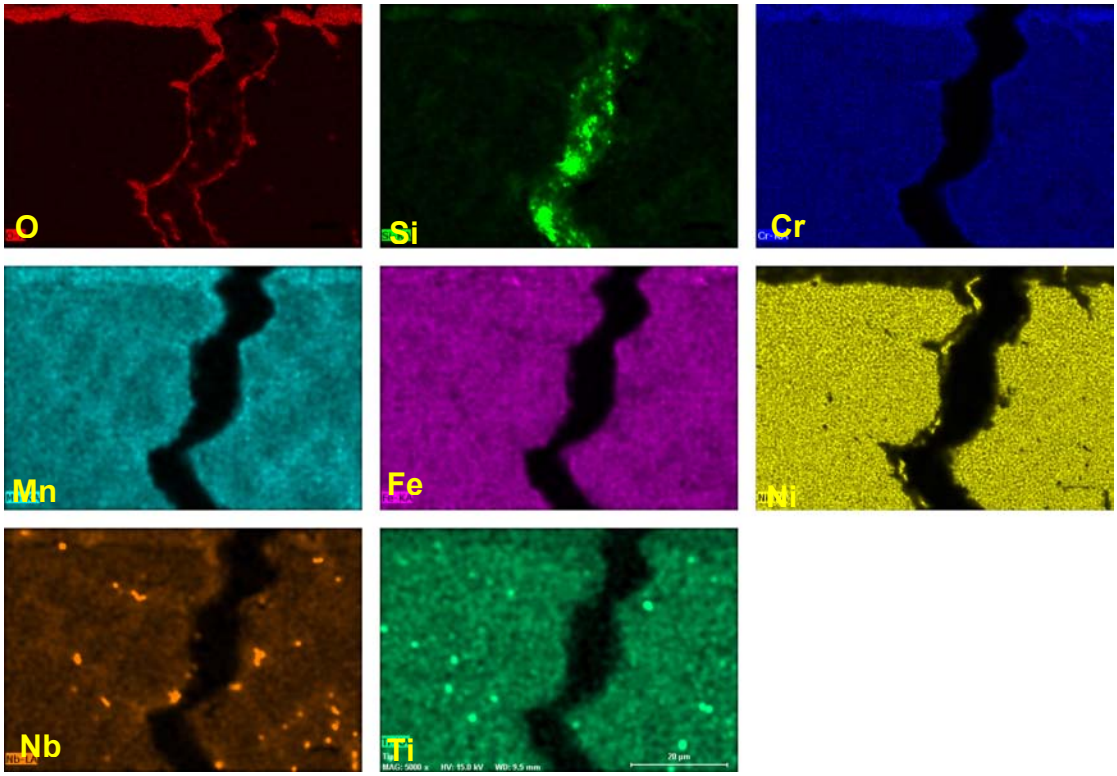

Figure 3.28. X-ray element maps of cross-section of an EAC crack of specimen TV4-3 showing element distribution in the oxide layer.

The opened fracture surface of the main crack in alloy 182 weld metal of specimen TV4-4 shown in Figure 3.18 e) was studied by FEG-SEM in the same way as the hot cracking fracture surfaces presented in Chapter 2. Figures 3.18 f)–h) show the interdendritic macroscopic nature of EAC cracking, which has different features depending on the orientation of dendrites. Microscopically the fracture surface is intergranular, as can be observed in Figure 3.18 h). On the fracture surface, especially close to the outer surface of the specimen, a lot of NiO oxide particles are present, Figure 3.29. As the X-ray element maps of Figure 3.28 showed, NiO is as particles on the surface of the Cr- and Mn-rich thin oxide layer on the fracture surface. The intergranular features of the fracture surface can be seen under the deposited NiO particles.

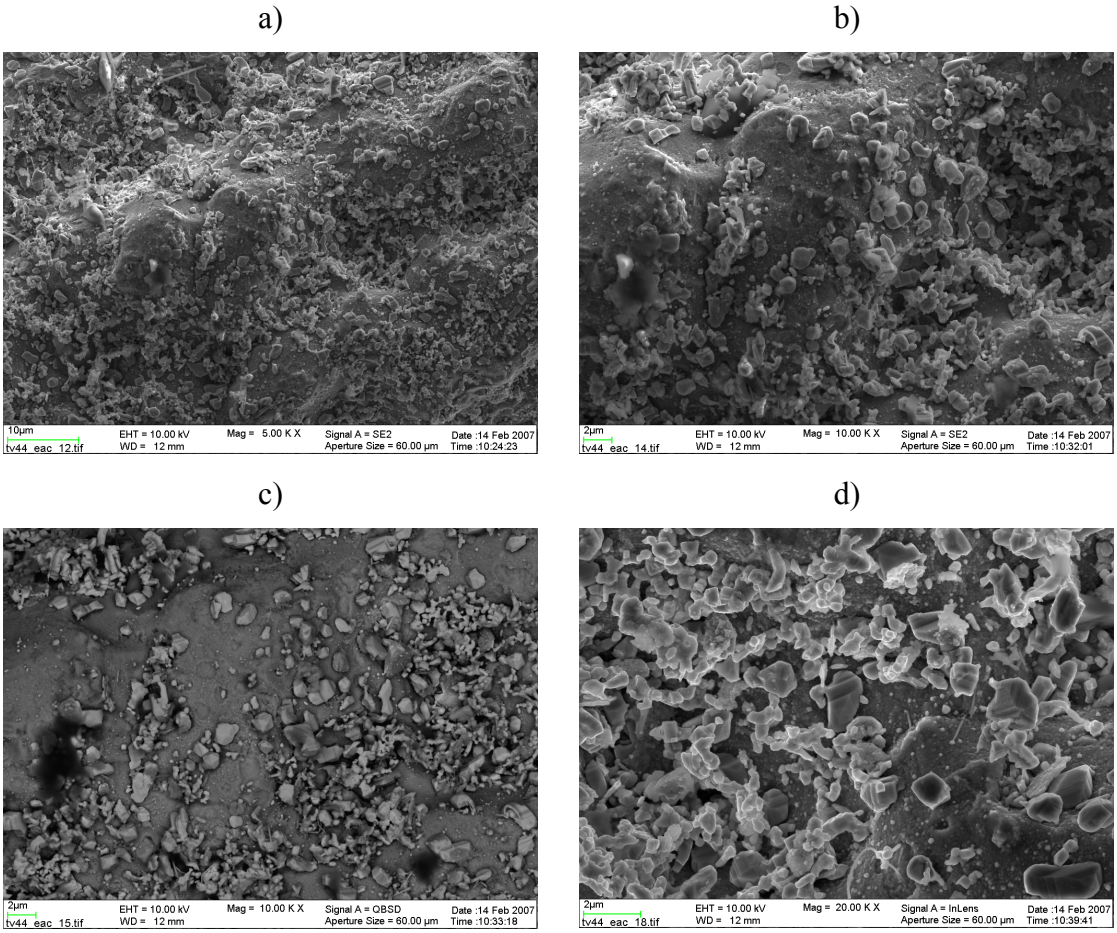

Figure 3.29 (a–d). Fracture surface of the main EAC crack of specimen TV4-4 close to the outer surface is covered by NiO particles.

The fracture surface close to the crack tip is presented in Figure 3.30. The fracture surface shows typical intergranular features, and smooth facets where Nb(C, N) particles are present. No NiO particles are seen on the fracture surface close to the crack tip. Locally the smooth facets change to a rough corroded-like surface, but the chemical composition of these more rough areas, shown, e.g. in Figure 3.30 d), was the same as that of the smooth areas. Thus, they are not representing other phases in the material as was seen on the hot cracking fracture surfaces of alloy 182. Figure 3.31 shows more detailed observations of these more rough areas on the EAC fracture surface. It is clear that part of the roughness comes from an elevated corrosion attack at those areas of the fracture surface (Figure 3.31 c)), but small pit-like corrosion attack is also seen on the smooth areas of the fracture surface connected to the small precipitate particles. Figure 3.31 d) reveals that there is a thin oxide film on the fracture surface close to the crack tip. This film is probably the Cr-rich oxide seen closer to the outer surface of the specimen under the deposited NiO particles. Close to the crack tip regions no deposited NiO particles are present.

a) b)

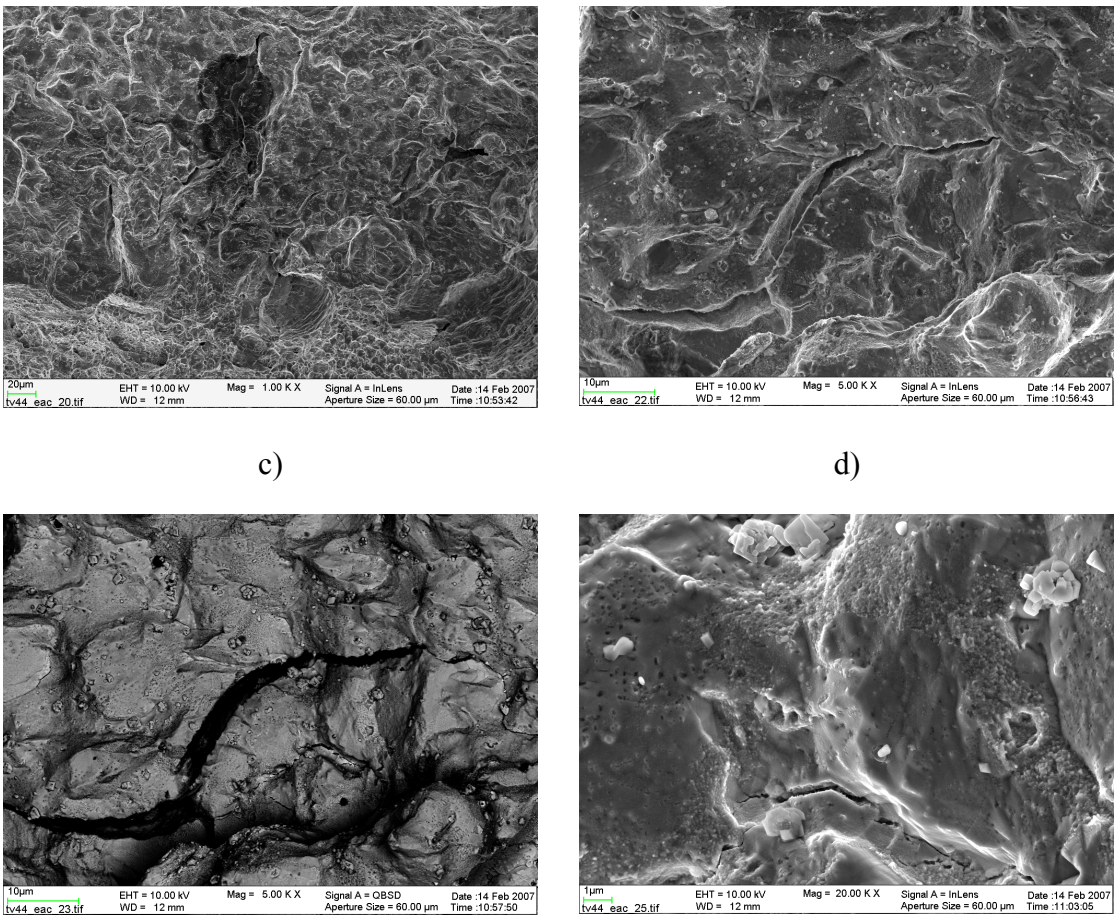

Figure 3.30 (a–d). Fracture surface of the main EAC crack of specimen TV4-4 close to the crack tip shows particles of Nb(N, C) but no NiO particles.

a) b)

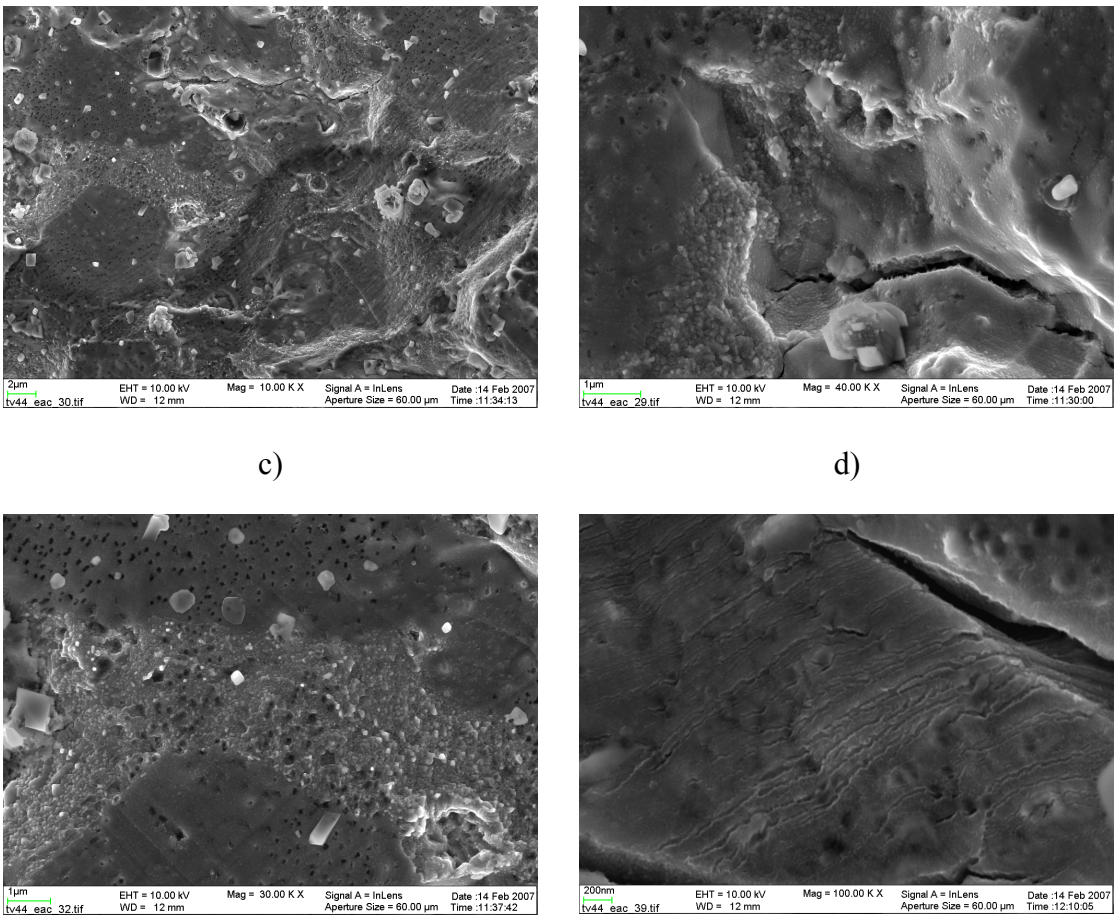

Figure 3.31 (a–d). Fracture surface of the main EAC crack of specimen TV4-4 close to the crack tip shows areas which are more rough than the otherwise smooth intergranular fracture surface. A thin oxide layer is on the fracture surface visible in d).

In the middle of the fracture the formation of NiO particles on the fracture surface was clearly visible, Figure 3.32. Figures 3.32 c) and d) show that NiO particles grow through the thin (probably Cr-rich) oxide layer on the fracture surface and cover locally by growing laterally almost the whole fracture surface, Figure 3.32 a) and b).

a) b)

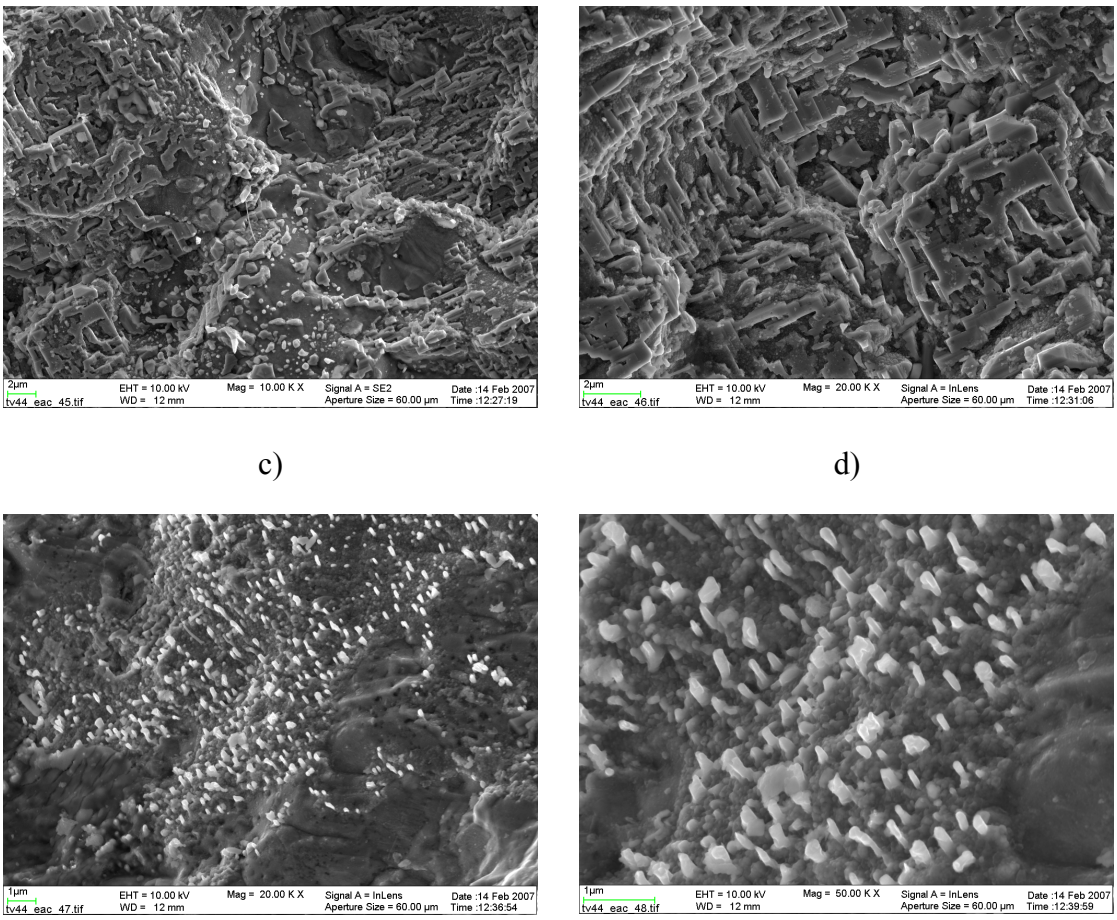

c) d)

Figure 3.32 (a–d). Fracture surface of the main EAC crack of specimen TV4-4 in the middle of the fracture shows growth of NiO particles through the thin oxide layer and their subsequent lateral growth on the fracture surface.

High magnification examination, Figure 3.33, of the EAC fracture surface close to the crack tip region shows that the fracture surface is generally smooth, and contains the large particles of Nb(C, N) and a large number of small precipitates that could not be analysed with FEG-SEM. The smooth features without any dendrite-like details, and the small precipitates, separate the EAC fracture surface clearly from the hot cracking fracture surfaces presented in Chapter 2 of this publication.

a) b)

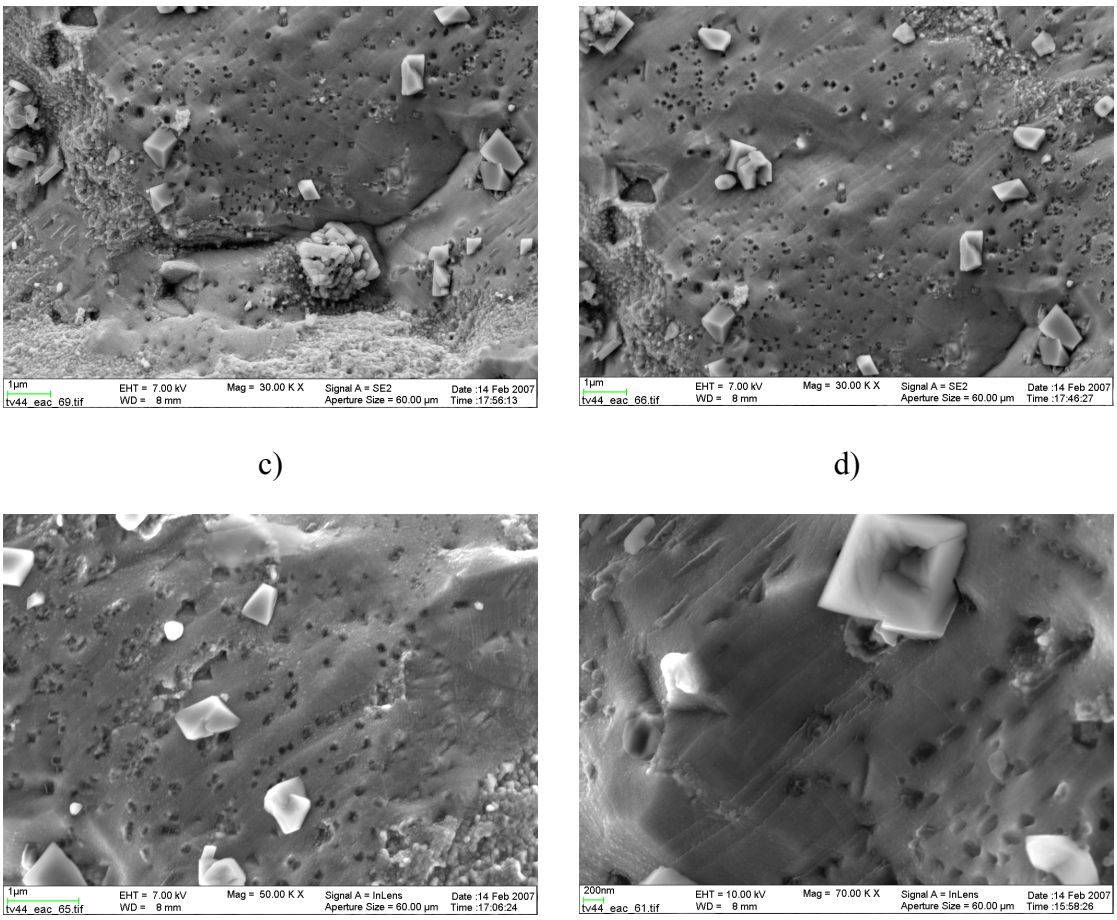

Figure 3.33 (a–d). Fracture surface of the main EAC crack of specimen TV4-4 close to the crack tip shows smooth intergranular features with large Nb(C, N) particles and a large amount of small precipitates.

A lot of effort was put into searching for the Nb-rich Laves phases on the EAC fracture surfaces to be able to compare the hot cracking fracture surfaces to EAC fracture surfaces. However, the Nb-rich Laves phases were not found from the studied EAC fracture surface. Figure 3.34 shows an EDS analysis of the region on the fracture surface where the growth of NiO particles is just starting. Figure 3.34 a) shows also lamellar features similar to Laves phase on the EAC fracture surface, but Figure 3.35 indicates that these features are rich in P, Mn and O, and depleted in Ni, Cr and Fe. However, no indications of Nb or Si enrichment can be seen. The lamellar features show additionally their brittle nature by exhibiting cracks. If these lamellar feartures were originally the Laves phase, only selective dissolution of Nb and Si can explain the observations.

a)

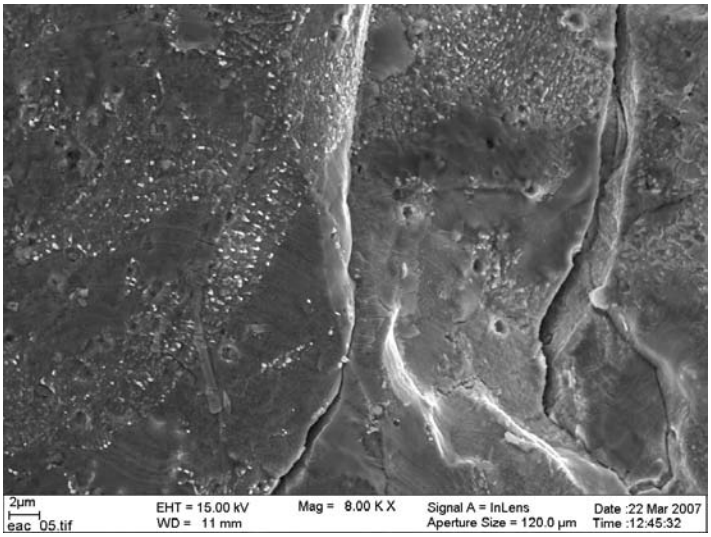

b)

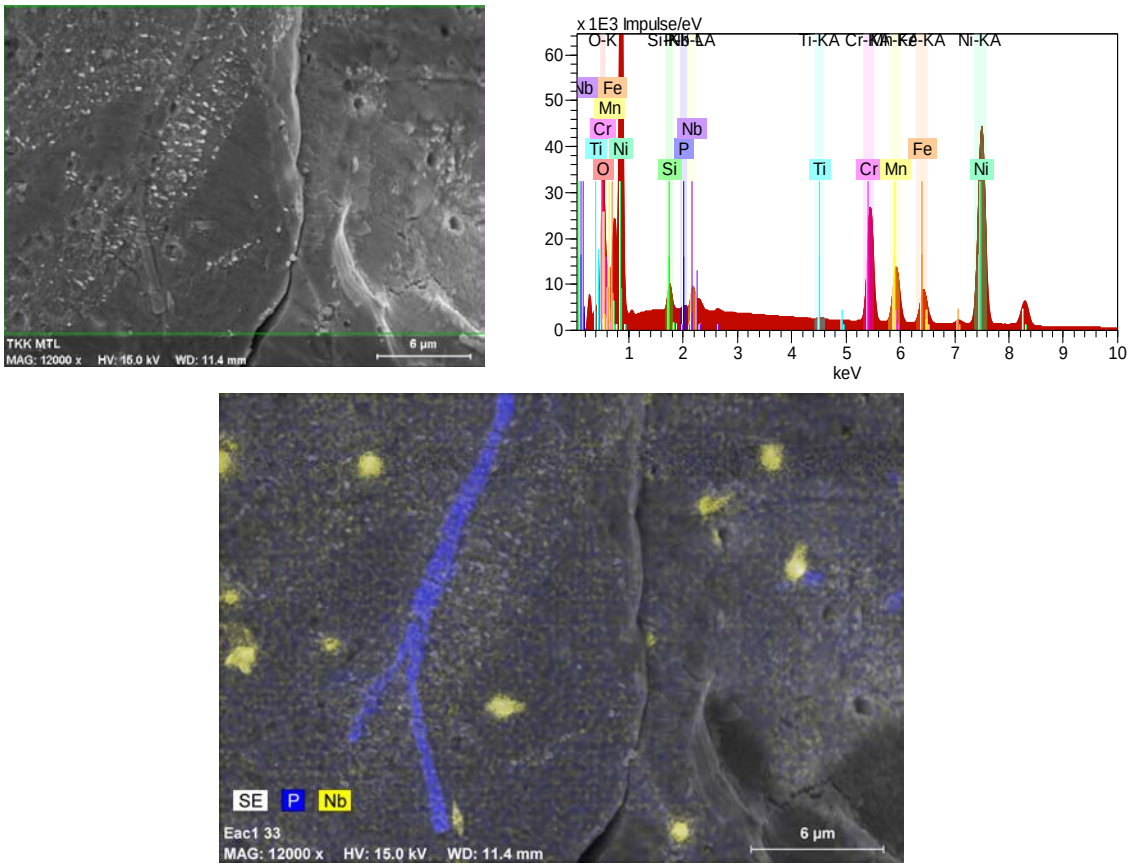

Figure 3.34 (a and b). Fracture surface of the main EAC crack of specimen TV4-4 in the area where NiO particle growth is starting shows also some lamellar features similar to the Laves phase seen on the hot cracking fracture surfaces of alloy 182. a) Fracture surface, and b) EDS analysis of the fracture surface showing P-rich lamellar phase and Nb-rich Nb(C, N) particles.

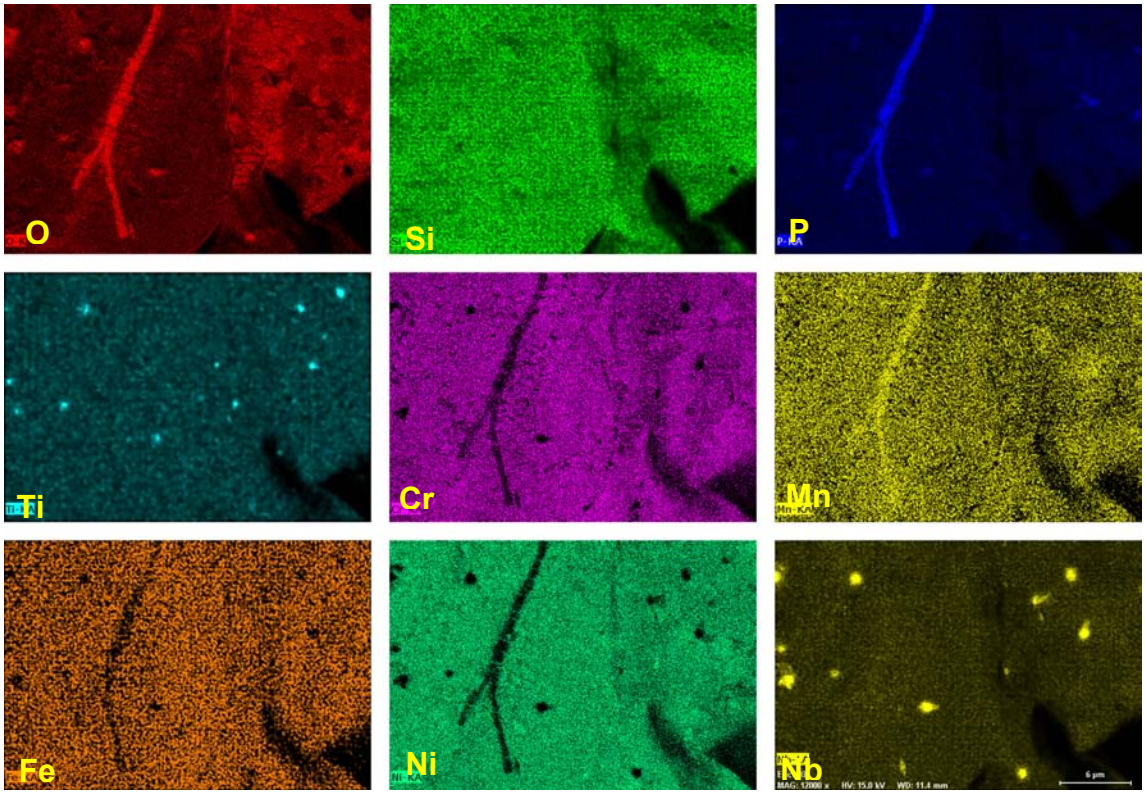

Figure 3.35. X-ray element maps of the fracture surface of the main EAC crack of specimen TV4-4 showing enrichment of P, Mn, and O as well as depletion of Ni, Cr, and Fe in the lamellar phase and Nb-rich Nb(C, N) particles.

3.4 Discussion

Liquid penetrant tests

Liquid penetrant indications were found in specimens fabricated from all of the studied weld combinations. In specimens prepared from weld mock-up 1 (i.e., TU1-x specimens, x = 1, 2, 3…8), liquid penetrant indications were in 5 of the 8 specimens. In mock-up 2 specimens (TU2-x), indications were present in 6 of 8 specimens, in mock-up 3 specimens (TU3-x) in 7 of 8 specimens and in every mock-up TV weld specimen (TV4-x). In the repair welded (alloy 82) mock-up TV weld specimens (TV4K-x) indications were present in one of the two tested specimens (note: TV4K-x specimens were present only in the last exposure).

However, since the liquid penetrant tests were started in a later stage of the test series, it is not possible to tell whether some of the features causing the indications were already present in the as-fabricated specimens. Some indications which appeared after the first liquid penetrant test could be attributed to a crack or cracks in post-test SEM or stereomicroscope studies. On the other hand, some of the indications were associated

with detached slag particles, local dissolution, or a feature resulting from specimen machining. In 16 of the 34 specimens (specimens without hot cracks), the liquid penetrant indication could be attributed to one or more cracks or crack-like features.

The number of 0.35% strained specimens showing liquid penetrant test indications, Figure 3.5 a), indicates a dependence between the exposure time and the number of indications. However, the dependence is not very strong, and does not exist at all in one case; in specimens prepared from mock-up 1 sample (specimens TU1-x), the number of specimens with indications did not change as the exposure time increased. The most clear effect of the exposure time is seen in the case of specimens prepared from the mock-up TV weld (specimens TV4-x). The apparent effect of the exposure time on the specimens prepared from mock-up 2 and 3 samples falls between that of mock-up 1 sample and the mock-up TV weld.

On average, the effect of the exposure time on the number of liquid penetrant indications is clearer in specimens with 1% strain, Figure 3.5 b). On the other hand, the number of specimens with indications increases with increasing exposure time in a similar manner in all specimens, i.e., the number of liquid penetrant indications is not a good parameter if benchmarking of the susceptibility to EAC is of interest.

Post-test SEM and stereomicroscope studies

No cracks were observed in specimens prepared from the mock-up 1 sample. In post-test examination of the specimens prepared from the mock-up 2 sample, no cracks could be associated with the indications in the 0.35% strained specimens, but in 3 of the 4 specimens strained to 1%, several very small crack-like features were observed on the specimen surfaces. A narrow crack was observed in one of the specimens prepared from the mock-up 3 sample and strained to 1%. This crack was associated with a pit, probably resulting from the dissolution of a slag particle, Figure 3.10. One of the 0.35% strained specimens exhibited a crack, around which was a zone looking like dendrite boundary corrosion attack, indicating possible segregation, Figure 3.13. An almost similar crack was in the low strained region close to the loading bolt in one of the 1% strained specimens, Figure 3.14. In this case, however, the zone around the crack looks like there has been a thin layer of material that has been dissolved or cracked away. In other specimens prepared from the mock-up 3 sample, the cracks were small.

The mock-up TV weld was apparently the most susceptible of the welds. In 7 of the 8 specimens a large number of cracks were observed by optical microscopy and SEM. In one of the specimens the main crack extended almost through the specimen (specimen TV4-4, Figure 3.18). In addition to the weld joint itself, cracks were observed in the

alloy 182 buttering and also in the alloy 600 base metal. No exact features were observed to which the cracks or their initiation could be associated.

The repair welded (alloy 82) specimens prepared from the mock-up TV weld did not show cracking during 438 h exposure. On the surface of the other one of the two specimens, one liquid penetrant indication was found. However, the results on these specimens are not comparable to the results on the other specimens, because the exposure time was short, 438 h as compared to 953–1460 h of the other specimens.

The specimens containing hot cracks (originating from Varestraint tests) and prepared from the mock-up 1, 2 and 3 samples (specimens TU1C1, TU2C1 and TU3C1, respectively) were exposed for a longer time than the repair welded mock-up TV weld specimens (TV4K1 and TV4K2), but for a shorter time than all the other specimens. The loading condition was also different than in the other specimens, as described in Chapter 3.2.4, i.e., it was based on the crack mouth opening instead of strain on the specimen surface. No new cracks or growth of the pre-existing hot cracks were observed in these specimens. However, these specimens were not sliced for microstructural examination, and thus it is not possible to conclude if the crack depth had grown during the exposure or not.

The average number of cracks in the specimens is a better parameter in benchmarking of the different welds than the number of liquid penetrant test indications is, as seen in Figure 3.5 c). The most susceptible weld is the mock-up TV weld (alloy 182 weld with alloy 182 buttering). The differences between mock-ups 2 and 3 are small. Cracks or crack-like features were observed in specimens prepared from both mock-ups, but the number of cracks in them is clearly smaller than that in specimens prepared from the mock-up TV weld. The most resistant weld was apparently mock-up 1, as no cracks or crack-like features were observed by SEM or stereomicroscope.

Microstructural investigations

A clear branching crack was observed on the side surface of the longitudinally-sliced mock-up 2 specimen TU2-4 strained to 1%, Figure 3.25. This crack was not present when the first liquid penetrant test was performed in the early stage of the test series. Microstructural examination after cutting, polishing and etching revealed that the crack depth was ~0.5 mm, Figure 3.25. Regions along the crack indicate local dissolution of material at the dendrite boundaries, probably associated with slag or segregation during welding.

One of the specimens prepared from the mock-up TV weld, TV4-3, was sliced in order to study the crack morphology and locations, Figure 3.26. The cracks in Inconel 182

weld metal were interdendritic and had initiated both in the middle of the weld and also close to the alloy 182/alloy 600 fusion line. The latter crack had grown towards the center of the weld after initiation. No cracks were in the Inconel 182 buttering in this longitudinal cut, but there are several cracks in Inconel 600 base metal. These cracks are intergranular, and in some cases branching. In this cut, the cracks are shallow, under 0.2 mm, but in the case of specimen TV4-4, the main crack extended almost through the specimen in the thickness direction, in addition to the width direction (see the macrograph of the opened specimen shown in Figure 3.18). The images in Figure 3.26 do not reveal any features acting as initiation sites for cracking.

Fractography of alloy 182 specimen TV4-4 showed that the outer surface and fracture surface are covered with an oxide layer. On the fracture surface NiO forms on the top of the thinner oxide layer and covers almost completely the fracture surface close to the outer surface. In the middle of the fracture surface the formation of NiO was observed as small particles growing laterally on the thin oxide-covered surface. Close to the crack tip no NiO was observed, and the fracture surface was covered only by a very thin oxide layer that was not possible to analyse with FEG-SEM/EDS. Close to the crack tip the intergranular nature of the fracture surface is clear (see, e.g., Figures 3.30 and 3.33) and its morphology is quite different from the interdendritic morphology of the hot crack fracture surface, where the wavy structure of the solidified final melt is also visible (see, e.g., Figure 2.133). The differences in the fracture mechanisms are marked; hot cracks form by separation in the liquid phase while EAC occurs by fracture in the solid phase. Close to the crack tip the dual distribution of carbonitrides is present on the fracture surface, i.e. large blocky Nb(C, N) particles together with small particles, which are probably $M_{23}C_6$ carbides. The images of the small $M_{23}C_6$ particles indicates that they may have started dissolving or oxidizing, since their appearance changes and they are not clearly observed by FEG-SEM further away from the crack tip. Presence of the Laves phase on the fracture surface was especially studied, but only weak indications of the possible lamellar Laves phase, clearly visible on the fracture surfaces of the hot cracks, were observed. The studied features were rich in P, Mn and O (and depleted in Ni, Cr and Fe), but no enrichment of Nb or Si was observed. If the observed features are remnants of the Laves phase which has oxidized, the dissolution behavior of Nb and Si has to be explained in the further studies. Based on the fractographical findings, the mechanistic studies in the future should include high temperature electrochemical studies of the segregated elements (especially Nb, Si and Mn in addition to base alloying elements) as well as interdendritic/-granular phases (Laves-phase and various carbonitrides, Nb(C, N), Ti(N, C) and $M_{23}C_6$). Related to this, the compositions and structures of the oxide films and their stabilities should be understood in the test environments used both on the outer surface and at the crack tip.

3.5 Conclusions

The tests demonstrated that differences in the EAC susceptibility between different weld geometries and weld metals can be distinguished by the doped steam test method. LWR safe-end weld metal alloy 182 was clearly more susceptible to EAC than weld metals of alloy 82, 152 and 52. Some cracking was also observed in the latter weld metals, but the difference between their EAC susceptibility and that of alloy 182 was clearly established.

Since eventual hot cracks in the welds may act as initiation sites for EAC, three specimens with hot cracks in the weld metal were exposed to the doped steam. However, no conclusive EAC crack growth was observed in these specimens, probably due to the small number of test specimens, short exposure time and, possibly, relatively imprecise loading condition.

3.6 References

Jacko, R.J., Gold, R.E. & Kroes, A. 2003. Accelerated Corrosion Testing of Alloy 52M and Alloy 182 Weldments. Proceedings of the 11th International Conference on Environmental Degradation of Materials in Nuclear Systems – Water Reactors, Stevenson, WA, USA, 10–14 August 2003. CD-ROM.

Rao, G.V., Jacko, R.J. & McIlree, A.R. 2002. An Assessment of the CRDM Alloy 600 Reactor Vessel Head Penetration PWSCC Remedial Techniques. Proceedings of Fontevraud 5, Contribution of Materials Investigation to the Resolution of Problems Encountered in Pressurized Water Reactors, SFEN, Fontevraud, France, 23–27 September 2002. CD-ROM.

Staehle, R.W. & Gorman, J.A. 2004. Quantitative Assessment of Submodes of Stress Corrosion Cracking on the Secondary Side of Steam Generator Tubing in Pressurized Water Reactors: Part 2. Corrosion, 60, 1, pp. 5–63.

4. Summary

This study is part of the national Dissimilar Metal Welding (ERIPARI) project, where the main objective was to first review the field experience related to the nickel-base materials and components where degradation has occurred in the light water reactor (LWR) systems, and secondly, to carry out an extensive study on hot cracking and EAC crack initiation susceptibility of the existing nickel-base alloy weld metals. The selection of new materials relies mainly on the existing laboratory results and short-term service experience. The long-term behavior of these materials and their performance in the plant has still to be demonstrated.

Weldability of the studied nickel-base materials was evaluated based on the results obtained with various mock-up welds of real components or anticipated weld designs of future plants, and weld metals of different chromium contents. The susceptibility to hot cracking was examined based on the Varestraint test results, but also other types of tests allowing ranking of the materials were examined. The mechanistic understanding of the hot cracking behavior of nickel-base weld metals is still largely missing, so careful metallurgical studies of the solidification mechanisms were carried out with a modern FEG-SEM/EDS instrument. Marked segregation of alloying elements such as Nb, Si and Mn to the last liquid to solidify at dendrite boundaries was observed, and in Nb-bearing alloys an eutectic Laves phase formed in the interdendritic regions. Hot cracking occurred along these dendrite boundaries, and the susceptibility to hot cracking in the weld mock-up samples was observed to follow the order: Alloy 152 > Alloy 52 > Alloy 182 > Alloy 82. The observed differences in hot cracking susceptibility between the studied alloys are explained mechanistically.

The PWSCC susceptibility in reactor primary water is strongly affected by the chromium level of the nickel-base weld metals, and is also based on the metallurgical properties of the nickel-base alloys. The microstructure and microchemistry in the multi-pass nickel-base alloy welds is very different than in the wrought and recrystallized nickel-base materials, but the details of the EAC susceptibility and mechanisms are still open. Weld residual stresses and their role in PWSCC are considered to play very important role in cracking susceptibility. The novel Contour method was studied for the first time in the DMW application, with promising results.

The EAC susceptibility of nickel-base alloys was studied in the doped steam test environment, and the crack initiation susceptibility of the various alloys was obtained. The results showed the markedly higher susceptibility to EAC of alloy 182 weld metal as compared to the other studied alloys, i.e., alloy 152, 52 and 82.

Acknowledgements

The project ERIPARI (dissimilar metal welds), launched in 2004, deals with dissimilar metal weld issues in nuclear power and the oil refinery industry. The three-year project is funded by Tekes – the Finnish Funding Agency for Technology and Innovation, TVO, Fortum Nuclear Service, Metso, Fortum Oil & Gas, Helsinki University of Technology and VTT Technical Research Centre of Finland, which is gratefully acknowledged. The objectives of the project are to develop reliable methods to measure and evaluate the manufacturing, properties and performance of new dissimilar metal welds. A main objective is also to understand the aging of Ni-base weld metals and the failure causes of dissimilar metal welds in nuclear power plants, and to develop non-destructive examination techniques for them.

Series title, number and
report code of publication

VTT Research Notes 2399
VTT-TIED-2399

Author(s)

Hänninen, Hannu; Brederholm, Anssi; Saukkonen, Tapio; Gripenberg, Hans; Toivonen, Aki; Ehrnstén, Ulla & Aaltonen, Pertti

Title

Hot cracking and environment-assisted cracking susceptibility of dissimilar metal welds

Abstract

The operating experience of major nuclear power plant (NPP) pressure boundary components has recently shown that dissimilar metal weld joints can markedly affect the plant availability and safety because of increased incidences of environment-assisted cracking (EAC, PWSCC) of alloy 600 and corresponding weld metals (alloys 182/82). Alloy 690 and associated weld metals (alloys 152/52) are widely used for repair and replacement of the affected thick-section components. The selection of new materials relies mainly on laboratory results and short-term service experience. The long-term behavior of these materials and their performance in the plant has still to be demonstrated.

Weldability and susceptibility to hot cracking of the studied nickel-base materials was evaluated based on the Varestraint test results obtained with weld metals of different chromium contents. The microstructures and microchemistry of the multi-pass nickel-base alloy welds was studied by FEG-SEM/EDS techniques and were found to be very different from those of the wrought and recrystallized nickel-base materials. Additionally, the weld residual stresses were measured and analyzed by a novel Contour method suitable for through-thickness residual stress determination.

The studied nickel-base material welds were exposed to doped steam test environment and crack initiation susceptibility of them was studied. The results showed the markedly higher susceptibility to EAC of alloy 182 weld metal as compared to the other studied alloys, i.e., alloy 152, 52 and 82.

ISBN
978-951-38-6952-6 (soft back ed.)
978-951-38-6953-3 (URL: http://www.vtt.fi/publications/index.jsp)

Series title and ISSN	Project number
VTT Tiedotteita – Research Notes 1235-0605 (soft back ed.) 1455-0865 (URL: http://www.vtt.fi/publications/index.jsp)	631

Date	Language	Pages
September 2007	English	182 p.

Name of project	Commissioned by
ERIPARI	Tekes, TVO, Fortum Nuclear Service, Metso, Fortum Oil & Gas, HUT, VTT

Keywords	Publisher
hot cracking, environment-assisted cracking, nuclear power plants, nickel base alloys, carbon steels, austenitic stainless steels, weldability, dissimilar metal welds, Varestraint tests, residual stress measurement, microstructural analysis, crack initiation, crack growth	VTT Technical Research of Finland P.O. Box 1000, FI-02044 VTT, Finland Phone internat. +358 20 722 4404 Fax +358 20 722 4374

The operating experience of major nuclear power plant pressure boundary components has recently shown that dissimilar metal weld (DMW) joints can markedly affect the plant availability and safety because of increased incidences of environment-assisted cracking (EAC, PWSCC) of Alloy 600 and corresponding weld metals (Alloys 182/82). Alloy 690 and associated weld metals (Alloys 152/52) are widely used for repair and replacement of the affected thick-section components. Weldability of the nickel-base materials was evaluated based on the Varestraint test results obtained with weld metals of different Cr-contents. In addition to the susceptibility to hot cracking in welding, EAC susceptibility in the doped steam test was evaluated based on the metallurgical properties of the nickel-base alloy weld metals. Weld residual stresses of DMWs were measured and analyzed with the Contour method, suitable for through-thickness residual stress determination.

Julkaisu on saatavana
VTT
PL 1000
02044 VTT
Puh. 020 722 4404
Faksi 020 722 4374

Publikationen distribueras av
VTT
PB 1000
02044 VTT
Tel. 020 722 4404
Fax 020 722 4374

This publication is available from
VTT
P.O. Box 1000
FI-02044 VTT, Finland
Phone internat. + 358 20 722 4404
Fax + 358 20 722 4374

ISBN 978-951-38-6952-6 (soft back ed.)
ISSN 1235-0605 (soft back ed.)

ISBN 978-951-38-6953-3 (URL: http://www.vtt.fi/publications/index.jsp)
ISSN 1455-0865 (URL: http://www.vtt.fi/publications/index.jsp)